UNIVERSIDADE DE LISBOA
FACULDADE DE CIÊNCIAS
Departamento de Engenharia Geográfica,
Geofísica e Energia

UNIVERSITÉ DE TOULOUSE
ÉCOLE DOCTORALE SDU2E
Sciences de l'Univers, de
l'Environnement et de l'Espace

Magnetic studies of the Late Cretaceous magmatism in Portugal: from Iberian plate kinematics to magnetic fabrics

Marta Maria de Almeida Neres

DOUTORAMENTO EM CIÊNCIAS GEOFÍSICAS E DA GEOINFORMAÇÃO
(GEOFÍSICA)

2013

UNIVERSIDADE DE LISBOA
FACULDADE DE CIÊNCIAS
Departamento de Engenharia Geográfica,
Geofísica e Energia

UNIVERSITÉ DE TOULOUSE
ÉCOLE DOCTORALE SDU2E
Sciences de l'Univers, de
l'Environnement et de l'Espace

Magnetic studies of the Late Cretaceous magmatism in Portugal: from Iberian plate kinematics to magnetic fabrics

Marta Maria de Almeida Neres

Tese orientada pelos Profs. Eric Font e Jean-Luc Bouchez

DOUTORAMENTO EM CIÊNCIAS GEOFÍSICAS E DA GEOINFORMAÇÃO
(GEOFÍSICA)

2013

Université de Toulouse

THÈSE

En vue de l'obtention du

DOCTORAT DE L'UNIVERSITÉ DE TOULOUSE

Délivré par :

Université Toulouse 3 Paul Sabatier (UT3 Paul Sabatier)

Cotutelle internationale avec Universidade de Lisboa

Présentée et soutenue par :

Marta Maria de Almeida Neres

le 20 décembre 2013

Titre :

Études magnétiques du magmatisme Crétacé Supérieur du Portugal: de la cinématique de la plaque Ibérique aux fabriques magnétiques

---

École doctorale et discipline ou spécialité :
ED SDU2E : Géophysique, Magnétisme, Géologie

Unité de recherche :
Géosciences Environnement Toulouse

Directeur(s) de Thèse :

Prof. Eric Font
Prof. Jean-Luc Bouchez

Jury :

à Maria e à Inês

Table of Contents

Abstract **i**

Resumo **iii**

Résumé **vii**

Acknowledgements **xi**

1 Introduction **1**

1.1 Motivation . . . 3

1.2 Iberian Kinematics: the State of the Art . . . 4

1.2.1 Previous paleomagnetic studies in Iberia . . . 4

1.2.2 Marine magnetic anomalies and kinematic models . . . 5

Magnetic record offshore Iberia . . . 5

Kinematic models from marine magnetic anomalies . . . 7

The model of Olivet [1996] . . . 8

The model of Srivastava et al. . . . 9

Constraints imposed by the kinematics of Central Atlantic . . . 11

1.3 Late Cretaceous Magmatism in West Iberia . . . 12

Offshore . . . 13

Onshore . . . 13

1.4 Objectives . . . 16

2 Theoretical and Methodological Principles **17**

2.1 Rock Magnetism . . . 19

2.1.1 Magnetism . . . 19

Ferromagnetism (*s.l.*) . . . 20

2.1.2 Magnetic minerals . . . 21

2.1.3 Magnetic energy, anisotropy and stability . . . 22

2.1.4 Types of remanence . . . 27
Thermal remanent magnetization . . . 28
Demagnetization techniques . . . 28
Viscous remanent magnetization . . . 29
Chemical remanent magnetization . . . 29
Detrital remanent magnetization . . . 29
Isothermal remanent magnetization and hysteresis cycle . . . 29
IRM unmixing . . . 31
Lowrie test . . . 32
Day diagrams . . . 32
First Order Reversal Curves . . . 33
2.2 Anisotropy of the Magnetic Susceptibility . . . 35
2.2.1 Magnetic Susceptibility of rocks . . . 35
2.2.2 AMS and magnetic fabric . . . 35
2.2.3 Magnetic fabric of magmatic rocks . . . 36
2.3 Paleomagnetism and Plate Kinematics . . . 38
2.4 Euler rotations applied to Plate Kinematics . . . 41

3 Reconciling Cretaceous paleomagnetic and marine magnetic data for Iberia: new Iberian paleomagnetic poles 43
Résumé . . . 45
Abstract . . . 47
3.1 Introduction . . . 48
3.2 Geological settings . . . 50
3.3 Sampling and methods . . . 52
3.4 Results . . . 54
3.4.1 Paço de Ilhas (PI) . . . 54
PI Paleomagnetism . . . 54
PI Rock Magnetism . . . 54
PI SEM and optical microscopic analyses . . . 58
3.4.2 Foz da Fonte (FF) . . . 60
FF Paleomagnetism . . . 60
FF Rock Magnetism . . . 60
FF SEM and optical microscopic analyses . . . 65
3.5 Discussion . . . 67
3.5.1 New paleomagnetic poles for Iberia at 88 and 94 Ma . . . 67
3.5.2 APWP of Iberia during the Mesozoic . . . 68

3.6 Conclusions . . . 74
3.7 Appendix: Supplementary tables . . . 75

4 Testing Iberian Kinematics at Jurassic-Cretaceous times 83
Résumé . . . 85
Abstract . . . 87
4.1 Introduction . . . 88
4.2 Method . . . 91
4.3 Results . . . 92
4.4 Discussion . . . 92
4.4.1 Testing Iberian Paleomagnetic Poles . . . 92
4.4.2 New Reconstruction of Iberia at 150 Ma . . . 96
4.5 Conclusions . . . 98
4.6 Appendix: About the method . . . 99
4.6.1 Comparison of results using BC02, SS05, KI10 and T12 . . . 99
4.6.2 Evaluation of the implied paleogeographic solutions . . . 100

5 Magnetic fabric in a Cretaceous sill (Foz da Fonte, Portugal): magmatic flow model and implications for regional magmatism 105
Résumé . . . 107
Abstract . . . 109
5.1 Introduction . . . 110
5.2 Geological setting . . . 112
5.3 Sampling and methods . . . 114
5.4 Petrographic features . . . 115
5.5 Magnetic mineralogy . . . 117
5.6 AMS results . . . 119
5.6.1 Bulk magnetic data . . . 119
5.6.2 Along profile variations . . . 121
5.7 Discussion . . . 125
5.7.1 Mineralogical variability . . . 125
5.7.2 Linking AMS with direction and sense of magma flow . . . 125
5.7.3 Linking the magnetic lineation with the shape fabric of the opaque grains . . . 127
5.7.4 Interpreting the along-profile variations . . . 129
5.7.5 Implications for regional tectonics and magmatism . . . 132
5.8 Conclusions . . . 134

5.9 Appendix 1: Tables 135
5.10 Appendix 2: AMS from other sills of the Lusitanian Basin 139
Paço de Ilhas sill 139
Lomba dos Pianos sill 139
Anços sill 139

6 Final Synthesis and Conclusions **143**
6.1 Iberian kinematics 145
6.2 Magmatic flow 146
6.3 Iberian Late Cretaceous Magmatism 146

7 Suggestions for Future Work **149**
7.1 Iberian kinematics 151
7.2 Magmatic flow 151
7.3 Iberian Late Cretaceous Magmatism 152

List of Figures **154**

List of Tables **155**

References **171**

Abstract

The Jurassic-Cretaceous Iberian kinematics is still not well understood, mainly due to limitations on reconstructions based on marine magnetic anomalies (uncertainties about the nature of the crust and presence of the Cretaceous Normal Superchron) and on paleomagnetic data (insufficient and sometimes low-quality data, low age resolution, tectonic influences and remagnetizations).

In this thesis, we first provide new high-quality paleomagnetic poles for the Late Cretaceous of Iberia, calculated from two mafic sills (Foz da Fonte, ∼88 Ma et Paço de Ilhas, ∼94 Ma), which enable better calibrating the Iberian apparent polar wander path (APWP) at the Late Cretaceous. A detailed study of magnetic mineralogy and microscopic observations (electronic and optic) confirm a primary magnetization carried by titanomagnetite. We then present a new compilation of the published paleomagnetic data for the Late Jurassic-Cretaceous of Iberia from which we calculate mean poles for six time periods. By rotating these mean poles to the African frame using Euler rotation poles from kinematic models we evaluate their position with respect to the global APWP in African coordinates. We verify that while post-rift mean poles (from 70 to 120 Ma) are in agreement with the APWP, poles corresponding to pre-rift times (older than 120 Ma) do not fit the APWP, revealing an incompatibility between the different types of data.

We next seek for the cause of this incompatibility, which may be due to the APWP (we show that this is unlikely since differences between different APWPs are not significative), euler poles (we show that a discard is verified using both end-member models of Olivet [1996] and Vissers & Meijer [2012]) and/or paleomagnetic data. We solve the inverse problem of finding the Euler poles that fit the pre-rift mean paleomagnetic poles with the GAPWP and then test their implications on Iberian reconstructions. We find that Iberian poles from the Early Cretaceous (mean poles for 123 and 130 Ma) are incompatible with the GAPWP, bringing into question their validity. Contrarily, Late Jurassic data (mean pole at 151 Ma) are compatible with the GAPWP and thus can be considered reliable. These results enable us to constrain a reconstruction of Iberia and surrounding plates at ∼150 Ma. These results highlight that more high-quality paleomagnetic data are needed

for the Iberian plate particularly at the Early Cretaceous, and that kinematic models based on the interpretation of marine magnetic anomalies should be reviewed.

In the last part of this thesis we present a study of the anisotropy of magnetic susceptibility of the Foz da Fonte sill, ∼7-8 m width. A detailed vertical sampling of the sill allowed us to distinguish three domains with respect to the magnetic fabric, which we relate with distinct regimes of magma flow. The chilled margins, ∼50 cm apart from the margins, where low anisotropies suggest low velocity gradients and heterogeneous flow paths during initial emplacement stages; in the center of the sill, where undisturbed magma flow is expected, low anisotropies suggest low shear gradients and magma displacement close to pure translation; and intermediate zones, where high anisotropy values are ascribed to maximum shear gradient zones. A mean orientation at ∼N310° of the magnetic lineation agrees with the direction of elongation of vesicles and is interpreted as magma flow direction. In addition, a sense of flow toward the southeast is inferred from the mirror imbrication of the magnetic foliation and lineation at the borders. Implications of these results are discussed with respect to the West Iberian Late Cretaceous magmatism, by integrating magnetic anomalies, isotope chronology and tectonics. The Cabo Raso anomaly is proposed as the magmatic source of the Foz da Fonte sill, and a ∼350 km long magmatic structure is proposed to connect the region of Sintra-Cabo Raso to the Tore seamount.

Keywords plate kinematics; anisotropy of magnetic susceptibility; Iberia; paleomagnetism; Cretaceous; magnetic mineralogy.

Resumo

O conhecimento actual sobre a cinemática e a paleogeografia da placa Ibérica desde a abertura da Pangeia até ao Cretácico Superior é ainda limitado. Em particular, há ainda questões essenciais a resolver no que diz respeito à compatibilidade entre os modelos cinemáticos, os dados paleomagnéticos e as evidências geológicas. As limitações das reconstituições magnéticas são devidas quer à incerteza sobre a natureza da crosta mais antiga, quer à presença do Superchron de Polaridade Normal do Cretácico, entre 125 e 84 Ma. Diversos factores limitam também a análise através de dados paleomagnéticos: escassa quantidade de polos paleomagnéticos existentes, cuja qualidade nem sempre é assegurada por critérios de referência, baixa resolução de idade, incerteza sobre correcções ligadas a eventos tectónicos pós-formação da rocha, e eventual presença de remagnetização. Esta tese tem como primeiro objectivo contribuir para uma melhor compreensão da cinemática Ibérica no Jurássico-Cretácico, por um lado contribuindo com novos dados, e por outro avaliando diferentes tipos de dados existentes e a sua compatibilidade.

Começamos por apresentar novos dados paleomagnéticos para o Cretácico Superior da placa Ibérica, determinados a partir de duas soleiras básicas (Paço de Ilhas, ∼88 Ma e Foz da Fonte, ∼94 Ma). Estas soleiras encontram-se na Bacia Lusitaniana, em contextos tectonicamente estáveis. Através de um estudo detalhado de mineralogia magnética e observações de microscopia electrónica e óptica mostramos que a a magnetização característica é primária e portada por titanomagnetite. Uma discussão sobre a validade dos nossos dados tendo em conta a variação secular do campo geomagnético levou-nos a concluir os pólos determinados são representativos do pólo magnético, e não de um pólo virtual, para as idades consideradas. Estes novos pólos permitiram pois melhor definir a trajectória de deriva aparente do pólo (TDAP) da Ibéria durante o Cretácico Superior. Em seguida, seleccionamos e discutimos os dados paleomagnéticos cretácicos publicados para a Ibéria. Para esta análise, calculamos pólos médios para seis períodos de tempo e transportamo-los para o referencial África utilizando pólos de rotação Ibéria-África dos modelos cinemáticos das anomalias magnéticas marinhas. Verificamos que os pólos médios correspondentes essencialmente ao período pós-rift (de 120 a 70 Ma) estão em acordo com

a TDAP. No entanto, os pólos de idades anteriores à abertura oceânica (mais antigos que 120 Ma; paleopólos médios para 123, 130 e 151 Ma) afastam-se largamente da TDAP, o que revela uma incompatibilidade entre os diferentes tipos de dados para as idades pré-rift.

Na segunda parte deste trabalho procuramos a causa para esta inconsistência, para a qual três causas são possíveis: má calibração da TDAP ou pólos de Euler e/ou pólos paleomagnéticos mal constrangidos. Começamos por justificar a escolha da TDAP global de Torsvik et al. [2012] como referência argumentando que em geral, as diferenças que existem entre as várias TDAP não são significativas para a nossa análise. Seguidamente, comparamos a utilização de pólos de rotação Ib-Af respectivos aos dois modelos cinemáticos "end-member", Olivet [1996] e Vissers & Meijer [2012], e mostramos que a incompatibilidade se mantém independentemente do modelo considerado, o que deixa como possíveis causas para o problema a qualidade dos pólos paleomagnéticos ou o rigor dos modelos cinemáticos. Para responder a esta questão, concebemos e aplicamos um novo método: (1) resolvemos o problema inverso de encontrar os pólos de Euler Ib-Af capazes de transportar os pólos paleomagnéticos médios (para 123, 130 e 151 Ma) de forma a fazê-los coincidir com os pólos respectivos da TDAP; (2) verificamos quais as implicações de utilizar estes pólos de rotação para determinar a posição da Ibéria nas idades correspondentes. Os resultados obtidos permitiram concluir que: (1) os pólos paleomagnéticos ibéricos do Cretácico Inferior (123 e 130 Ma) são incompatíveis com a TDAP, o que põe em causa a qualidade dos dados paleomagnéticos correspondentes. Sugerimos que a validade limitada dos testes de confiança aplicados e a complexidade das histórias tectónicas das regiões envolvidas podem ser a justificação para este facto. (2) O paleopólo do Jurássico Superior (151 Ma) é compatível com a TDAP.Os dados paleomagnéticos correspondentes podem então ser considerados válidos. Esta compatibilidade permite-nos apresentar uma nova reconstituição da paleoposição da Ibéria há ∼150 Ma. Uma importante conclusão que se retira desta análise a necessidade por um lado, de adquirir novos dados paleomagnéticos, especialmente para o Cretácico Inferior, e por outro, de proceder a uma reinterpretação cuidadosa das anomalias magnéticas marinhas.

Numa última parte desta tese, abordamos um outro aspecto dos estudos magnéticos, aqui aplicado a soleiras Cretácicas: a caracterização de algumas das suas propriedades reológicas através do estudo da anisotropia da sua susceptibilidade magnética (ASM). O nosso objecto de estudo foi a soleira de Foz da Fonte, uma das muitas (mas ainda pouco estudadas) ocorrências do magmatismo alcalino do Cretácico Superior em Portugal. Esta soleira, datada de cerca de 88 Ma e de 7 a 8 m de espessura, revelou-se um excelente laboratório natural, permitindo-nos obter uma amostragem vertical completa e detalhada.

Um estudo de ASM de grande resolução foi conduzido afim de melhor compreender o escoamento do magma durante a intrusão da soleira e de reposicionar esse escoamento no quadro do magmatismo regional. Variações significativas dos valores dos parâmetros de ASM permitiram-nos definir cinco zonas paralelas às margens da soleira, correspondentes a três domínios caracterizados pela sua fábrica magnética. Interpretamos estas zonas como correspondendo a diferentes regimes de fluxo magmático durante a intrusão. Estes domínios são: (1) as margens "congeladas", que correspondem aos primeiros ∼50 cm a partir das extremidades do sill (base e topo). São caracterizadas por fraca anisotropia, sugerindo fracos gradientes de velocidade e um fluxo magmático irregular ao longo das margens durante os primeiros estadios da intrusão. (2) o interior do sill, onde fraca anisotropia e grande dispersão direccional são observados. Nesta zona, o magma escoou mais livremente, sob baixo gradientes de cisalhamento e sofrendo um transporte essencialmente translativo. (3) as zonas intermédias, entre as margens "congeladas"e o interior, onde se verificam os mais fortes índices de anisotropia, atribuídos à existência de fortes gradientes de cisalhamento. Para justificar estas interpretações, várias análises foram conduzidas, permitindo concluir que: (1) os portadores da susceptibilidade magnética são essencialmente titanomagnetites multi-domínio com teor em titânio variável. (2) a ASM pode neste caso ser interpretada como um indicador da direcção do escoamento magmático (verificámos uma correlação entre a lineação magnética e a direcção de alongamento das vesículas carbonatadas, marcadores macroscópico do fluxo). (3) a lineação magnética corresponde estatisticamente à orientação preferencial deforma dos minerais opacos, determinado por análise de imagens. OS resultados direccionais de ASM permitiram determinar a direcção do escoamento magmático: direcção ∼310° (orientação média da lineação) e sentido para o Sudeste (inferido através da imbricação da foliação magnética em relação aos planos da base e do topo. Este resultado, que sugere que a fonte magmática estaria localizada a Noroeste do local de amostragem, é então ejnquadrado no magmatismo alcalino do Cretácico Superior da margem ocidental portuguesa. Integrando dados de anomalias magnéticas marinhas, cronologia isotópica, sísmica e tectónica, sugerimos que a anomalia do Cabo Raso (fortemente positiva) é a fonte magmática do sill de Foz da Fonte. Os mesmos tipos de dados levam-nos a especular que uma estrutura magmática (do tipo falha ou dique) de cerca de 350 km de extensão, liga a margem portuguesa (anomalias da zona Sintra-Cabo Raso) à montanha submarina Tore.

Palavras-chave cinemática de placas; anisotropia da susceptibilidade magnética; Ibéria; paleomagnetismo; Cretácico; mineralogia magnética.

Résumé

La connaissance sur la cinématique et la paléogéographie de l'Ibérie depuis l'ouverture de la Pangée jusqu'au Crétacé Supérieur restent encore limitée. En particulier, il y a des questions à résoudre concernant la compatibilité entre les modèles cinématiques, les données paléomagnétiques et la géologie. Les reconstitutions magnétiques sont handicapées, à la fois par les incertitudes sur la nature de la croûte pour les périodes les plus anciennes, et par la présence du Superchrone Normal du Crétacé entre 125 Ma et 84 Ma. Du côté du paléomagnétisme, les données sont limitées à cause de plusieurs facteurs : faible quantité de pôles paléomagnétiques satisfaisant les critères de qualité de référence, faible résolution sur les âges, incertitudes sur les corrections liées aux mouvements tectoniques post-formation et à la présence éventuelle de phases de ré-aimantation. Cette thèse a pour premier objectif de contribuer à une meilleure compréhension de la cinématique Ibérique au Jurassique-Crétacé en fournissant des nouvelles données, et aussi en évaluant les differents données existantes et leur compatibilité.

Nous présentons d'abord de nouvelles données paléomagnétiques pour le Crétacé Supérieur de l'Ibérie, déterminées à partir de deux sills basiques (Paço de Ilhas, environ 88 Ma, et Foz da Fonte, environ 94 Ma), intrusifs dans le Bassin Lusitanien dans un contexte tectoniquement stable. Une étude détaillée de minéralogie magnétique et des observations de microscopie électronique et optique ont montré que l'aimantation caractéristique est primaire, portée par titanomagnétite. La validité de nos données est discutée en regardant la variation séculaire du champ géomagnétique. Cette discussion nous a permis de conclure que les pôles déterminés sont représentatifs du pôle magnétique et non d'un pôle virtuel (pour les âges considérés). En conséquence nous avons pu mieux calibrer la CDPA (courbe de dérive polaire apparente) de l'Ibérie au Crétacé Supérieur. La partie suivante de ce travail de paléomagnétisme était de sélectionner et de discuter les données paléomagnétiques publiées pour le Crétacé de l'Ibérie. Nous avons calculé des pôles moyens pour six périodes de temps et les avons transportés dans le référentiel Afrique en utilisant les pôles d'Euler Ibérie-Afrique issus des modèles cinématiques déterminés à partir des anomalies magnétiques marines. Nous vérifions que les pôles moyens correspondant plutôt

à la période post-rifting (de 120 Ma à 70 Ma) sont en accord avec la CDPA. Par contre, pour les âges antérieurs à l'ouverture océanique (plus anciens que 120 Ma ; paléopôles moyens à 123, 130 et 151 Ma), les pôles paléomagnétiques sont écartés de la CDPA, ce qui révèle une incompatibilité entre les différents types de données aux âges pré-rifting.

Dans la seconde partie de ce travail nous recherchons la cause de ce décalage. Trois causes sont possibles : mauvaise calibration de la CDPA, pôles d'Euler et/ou données paléomagnétiques mal contraints. Nous justifions d'abord le choix de la CDPA de Torsvik et al. [2012] comme référence. Puis, en utilisant les rotations d'Euler des modèles cinématiques "end-members" de Olivet [1996] et de Vissers & Meijer [2012], nous montrons que l'incompatibilité persiste indépendamment du modèle considéré. La cause du problème réside donc dans la qualité des pôles paléomagnétiques ou dans celle des pôles de rotation des modèles cinématiques. Pour répondre à cette question, nous concevons et appliquons une nouvelle méthode : (1) résoudre le problème inverse permettant de trouver quels sont les pôles d'Euler de Ibérie par rapport à l'Afrique (IB/AF) capables de faire migrer les paléopôles moyens (à 123, 130 et 151 Ma) jusqu'aux pôles correspondants de la CDPA dans le référentiel Afrique ; et (2) étudier quelles sont les implications d'utiliser ces pôles d'Euler pour déterminer la position de l'Ibérie aux âges correspondants. Nos résultats nous permettent de conclure que : (1) Les pôles paléomagnétiques de l'Ibérie au Crétacé Inférieur (123 et 130 Ma) sont incompatibles avec la CDPA globale. C'est donc la qualité (au sens large) des données paléomagnétiques qui est la source du problème. Nous identifions la validité limitée des tests de confiance pris et les histoires tectoniques complexes des régions concernées comme raisons pour cette faible qualité des données paléomagnétiques pour la période considérée. (2) Le paléopôle du Jurassique Supérieur (à 151 Ma) est compatible avec la CDPA : les données paléomagnétiques correspondantes peuvent être considérées comme valables. Cette compatibilité nous permet de présenter une nouvelle reconstitution de la position de la plaque Ibérique à environ 150 Ma. Une leçon importante issue de ce travail est que l'acquisition de nouveaux paléopôles, en particulier pour le Crétacé Inférieur, et la ré-interprétation soigneuse des anomalies magnétiques s'avèrent indispensables.

Dans la dernière partie de cette thèse, nous nous intéressons à un autre aspect des études magnétiques, ici appliqué à des sills d'âge Crétacé : la caractérisation de certaines de leurs propriétés rhéologiques par l'étude de l'anisotropie de leur susceptibilité magnétique (ASM). Les roches que nous avons étudiées sont les magmas basiques (ou diabases) formant le sill de Foz da Fonte, daté d'environ 94 Ma, et de 7 à 8 m d'épaisseur. Affleurant dans la province magmatique portugaise du Crétacé Supérieur où plusieurs corps magmatiques intrusifs sont encore peu étudiés, ce sill constitue un véritable laboratoire naturel,

et nous a permis d'obtenir un échantillonnage vertical complet et détaillé. Nous avons conduit une étude fine d'ASM afin de mieux comprendre l'écoulement du magma lors de la mise en place du sill, et de replacer cette mise en place dans le cadre du magmatisme régional. Des variations significatives des valeurs des paramètres d'AMS nous ont permis de définir cinq "couches" parallèles aux épontes du sill, correspondant à trois domaines caractérisés par leur fabrique magnétique. Nous relions ces "couches" aux différents régimes de flux magmatique qui existent pendant l'intrusion. Ces domaines sont : (1) les zones figées, qui correspondent aux premiers ∼50 cm le long des épontes supérieure et inférieure (ou mur et toît) du sill, caractérisées par un faible degré d'anisotropie, suggérant de faibles gradients de vitesse et un flux magmatique irrégulier le long des parois au cours des premiers stades de mise en place ; (2) le cœur du sill, où de faibles anisotropies et grande dispersion directionnelle sont observées, correspondant à la zone où le magma s'est écoulé plus librement, sous de faibles gradients de cisaillement et donc suivant un transport plutôt translatif ; et (3) les zones intermédiaires entre zones figées et cœur du sill, où on trouve les plus forts degrés d'anisotropie, attribués aux zones où se développent les plus forts gradients de cisaillement. Pour justifier ces interprétations, nous avons conduit plusieurs analyses qui nous ont permis de conclure que : (1) les porteurs de la susceptibilité magnétiques sont essentiellement des titanomagnétites multi-domaines avec un contenu variable en titane ; (2) l'ASM peut être interprétée dans ce cas comme indicateur de la direction de l'écoulement magmatique (nous avons trouvé une corrélation entre la linéation magnétique et l'axe long des vésicules carbonatées, marqueurs macroscopique du flux) ; et (3) la linéation magnétique correspond statistiquement à l'orientation préférentielle de forme des opaques, déterminé par l'analyse d'images. Les résultats directionnels de l'ASM nous ont permis de déterminer la direction de l'écoulement magmatique : direction ∼N310° (orientation moyenne de la linéation) et sens vers le Sud-Est (donné par le pincement observé entre la foliation magnétique et les épontes du sill), ce qui suggère que la source magmatique est localisée au Nord-Ouest du site de prélèvement. Ce résultat est interprété dans le cadre du magmatisme alcalin du Crétacé Supérieur de la marge ouest du Portugal, en intégrant les données issues des anomalies magnétiques, de la chronologie isotopique, de la sismique et de la tectonique. Nous suggérons que l'anomalie du Cabo Raso est la source magmatique du sill de Foz da Fonte et qu'une structure magmatique (de type faille ou dyke) d'environ 350 km de long, relie la marge portugaise (anomalies de la zone Sintra-Cabo Raso) au Tore Seamont.

Mots-clées cinématique de plaques ; anisotropie de la susceptibilité magnétique ; Ibérie ; paléomagnétisme ; Crétacé ; minéralogie magnétique.

Acknowledgements

I should say that this part of the thesis was very difficult for me to write: it is very hard to put in words all the importance that many people had to me during this time. Someone once said me that he doesn't take many photos, but instead keeps memories of people and moments in mind. I feel something similar about this: maybe I will not be able to justly express here all my gratefulness, but I always remember all the importance that many people had during this time!

I start acknowledging my supervisor Eric Font and my co-supervisor Jean-Luc Bouchez, who guided and encouraged me during these four years. I thank you both for always being wise advisers, for transmitting me lots of knowledge on rock magnetism and on the scientific procedures, and for helping me being now something much more similar to "a scientist" than I was four years ago. Eric, your patience, enthusiasm, comprehension and friendship were essential to overpass many difficult moments and to always re-find my way during this work. Jean-Luc, your calm and pragmatism taught me to hold on and focus on which is more important at each moment. I thank you and Anne for your great hospitality during my stays in Toulouse.

I also owe a great acknowledge to Miguel Miranda, who wisely guided me on some parts of this work, making me learn the nuts and bolts of plate kinematics and boosting me toward new and ambitious objectives, always telling me something like "Why shouldn't you be able to do that?".

Great special thanks also to Pedro Terrinha, my main guide to the geology of Portugal and surroundings and the trigger to our studies on the Late Cretaceous magmatism. Thank you for being always so supportive and heartening.

I am indebted to all co-authors of the papers here presented: Pierre Camps, José Mirão, Mário Moreira, Rui Miranda, Patrick Launeau and Claire Carvallo. This work would not be the same without your help and collaboration!

I also thank the editors and reviewers of these papers, whose constructive comments and suggestions improved the final published results: Rob Van der Voo (with a nice hat-trick!), Jaume Dinarèz-Turell, Stuart Gilder, Juan José Villalaín, Eduard Petrovsky,

Craig Magee and Edgardo Cañon-Tapia.

I acknowledge many people for help, teachings, discussions, support and company: Mário Moreira, Pedro Silva, Joaquim Luís, Rob Van der Voo, Anne Nédélec, Jacques Rey, Nassrrddine Youbi, Mohamed Bensalah, Maryline Moulin, Rui Miranda, José Carlos Kullberg and Carine Lezin. And also Luis Alva-Valdivia, Thierry Aigouy, Helena Sant'Ovaia and Sr. Alberto Verde for technical support.

Financially, I acknowledge the Fundação para a Ciência e Tecnologia for my Ph.D. grant, Fundação Calouste Gulbenkian for the award Prémio Gulbenkian de Estímulo à Investigação 2010, Instituto Dom Luiz (PEst-OE/CTE/LA0019/2013) and the projects PAUILF and PESSOA (collaboration Portugal-France), IMPACTO (PTDC/CTE-GIX/117298/2010), TOPOMED (TOPOEUROPE/0001/2007) and TECTAP (PTDC/CTE-GIN/68462/2006). I also thank the University of Lisbon (Department of Geophysics), Instituto Dom Luiz and the University of Toulouse (Géosciences Environnement Toulouse) for scientific support and workspace.

Special thanks also to Célia Lee, Ana Sousa, Anabela Martins and Mme Marie-Claude Cathala for your essential administrative support.

I thank the rapporteurs Vicente Carlos Ruíz-Martínez and Charles Aubourg for having accepted judging this work.

Pedro Silva, Susana Fernandes, Ana Lopes, Jorge Ponte, Francisca Ferrão, Francisco Almeida, thank you for your all the days we were together at the Paleomag laboratory. Work is much easier when we are in good company! Susana, thank you specially for your help in the field (and for, since then, making me always remember not to be so fearless...).

I also acknowledge the support and friendship from all the Font family, specially Mme. Jeannette and Malu.

Filipa Varino and Joana de Medeiros, thank you for your friendship and support during these years, and for being there for me on good and bad moments. And of course, for introducing me very important people...

Thanks also to my other friends, specially Sara, Gilda and Flor, for your support and solicitude when I most needed.

My final and greatest acknowledge must be to my family.

Muito do que consegui fazer e ultrapassar devo ao apoio incondicional de toda a minha família. Tenho a sorte de pertencer a uma família em que há sempre alguém que ajuda quando é preciso, e o valor disto é incomensurável. Obrigada aos meus pais: Rosa e Joaquim, por tudo o que me proporcionaram, e também aos meus irmãos: Rita, Ana e João, cunhados: Henrique e Fernando e sobrinhos: Francisco, Manuel, André, Tiago e Madalena. E uma dedicação especial à memória da minha avó Maria.

Ademar, companheiro em tudo e em todos os momentos, obrigada pelo teu apoio incondicional, calma infinita e palavras sábias sempre que necessário.

Maria e Inês, este trabalho, assim como tudo o que faço, é por vocês. Obrigada por serem as filhas mais lindas, fortes, amorosas e compreensivas do mundo! Sei que vão continuar sempre a descobrir os vossos "basaltos", e o meu maior objectivo é ajudar-vos a seguir esse caminho.

1. Introduction

1.1 Motivation

Plate tectonics is a well-established paradigm since the end of the 60's. The comparison between the paleomagnetic record of rocks from different continents and the discovery of striped magnetic anomalies on the seafloor were essential to the acceptance of the continental drift predicted by Wegener and the seafloor-spreading antevised by the Vine-Matthews-Morley hypothesis. The combination of these two geophysical approaches - paleomagnetism and oceanic magnetic kinematics - has allowed a good comprehension of the breakup of the Pangaean supercontinent and subsequent kinematic evolution of major plates during the Mesozoic. However, some lithospheric regions still resist to a clear kinematic interpretation, in particular some small plates for which angular constraints are difficult to obtain.

The Iberian plate in particular, represents a challenging piece on the tectonic puzzle, for which several factors difficult a consensual understanding of its evolution. Having occupied a strategic, pivotal position during the opening of the Atlantic Ocean and Bay of Biscay, a comprehension of its tectonic history is important for many reasons, such as the assessment of resources and natural hazards [e.g., Omira et al., 2011; Cloetingh et al., 2011] and global plate kinematics [e.g., Torsvik et al., 2008, 2012].

Specially controversial in Iberian history is the Jurassic-Cretaceous period. The interpretation of marine magnetic data has raised many (inconclusive) discussion and the paleomagnetic data are not sufficient (in amount and quality) for definitive evaluation. Meanwhile, during this period the Iberian plate underwent several processes: an important rifting phase and subsequent continental breakup, the opening of the Bay of Biscay, the Pyrenean orogeny and small cantabrian subduction, and at least three magmatic events. Among the latter, the Late Cretaceous Magmatic pulse is especially relevant. It consists on a voluminous, long-lived magmatic event of intrusive and extrusive sub-lithospheric magmas that spread on- and offshore along the West Iberian Margin. Its genesis is intrinsically related with the geodynamic evolution of Iberia [e.g., Merle et al., 2006; Miranda, 2010], and therefore a better comprehension on its geometry and emplacement mode would be insightful.

The geodynamical causes and relations between some of these processes are still unclear. This work aims to contibute to a better understanding of the Jurassic-Cretaceous geodynamics of the Iberian plate.

1.2 Iberian Kinematics: the State of the Art

A quelque cause qu'on doive attribuer l'ouverture du golfe de Gascogne et l'origine de ses grandes profondeurs (...) il faut que la France et l'Espagne, sur l'emplacement actuel du golfe, aient été d'un seul tenant.

Emile Argand, Congrès Géologique International,10 Oût 1922

Argand [1924] was the first to highlight the correspondence of geological features between France and Iberia. Carey [1958] showed that a simultaneous origin for the Bay of Biscay and Pyrenees could be accomplished by a rotation around a pivot point in western Pyrenees and Bullard et al. [1965] assumed a similar movement in the first numerical fit of circum-Atlantic continents. Since then, the fit of Iberia with surrounding plates and subsequent kinematics have been extensively investigated by several geological and geophysical approaches. Paleomagnetism and interpretation of seafloor magnetic anomalies are the two most important geophysical methods for this assessment, but despite the large amount of publications, no consensual model has yet been achieved, particularly for the Jurassic and Cretaceous.

1.2.1 Previous paleomagnetic studies in Iberia

The first paleomagnetic evidence of a rotation of Iberia with respect to Europe came in 1969, with the landmark and book-example work of Van der Voo [1969]. This study, that comprised rocks from the Paleozoic (Ordovician) till the Cretaceous, showed evidences for a 35° counterclockwise rotation of the stable Iberian Meseta with respect to stable Europe, between the Late Triassic and the Late Cretaceous. Since then, most of paleomagnetic works in Iberia have focused on better constraining of the mode and timing of this rotation. A later paleomagnetic study on sediments of the Lusitanian Basin near Lisbon by Galdeano et al. [1989] suggested that a total absolute anticlockwise rotation of 41° took place on two stages: a rapid phase of 27° during Hauterivian-Aptian (∼125-112 Ma) and a slower phase of 14° Aptian-Campanian (∼112-80 Ma), equivalent to a total 34° relative rotation with respect to Europe. From studies on Algarve basin sediments, Moreau et al. [1997] proposed a fast anticlockwise rotation of 22±14° with respect to Europe during the Barremian (130-125 Ma). Other studies [Storetvedt et al., 1990, 1987] suggested a more complex evolution comprising an anticlockwise rotation of ∼40° followed by a clockwise rotation of ∼70°, before the coupling of Iberia to Europe. More recently, Gong et al. [2008b], based on paleomagnetic data from the Organyà Basin (South Pyrenees), defended a single rotation event of ∼35° limited to the Aptian.

However, most of these interpretations have the severe limitation of being based on a low resolution and low quality paleomagnetic database. Main problems arise from the lack of precise radiometric dates, low age resolution of sampling, insufficient sampling statistics (low number of sites and/or samples), the absence of field tests, unknown paleo-horizontal corrections in the case of igneous rocks, poorly defined inclination corrections for sedimentary rocks. Moreover, many rock units in Iberia were reported to have been remagnetized [e.g., Galdeano et al., 1989; Dinarès-Turell & Garcia-Senz, 2000; Gong et al., 2009; Juárez et al., 1998; Soto et al., 2008; Moreau et al., 1992; Villalain et al., 2003]. In many of these studies, a main remagnetization event is referred, and assigned to be related with the Cretaceous Normal Superchron. Given these problems with paleomagnetic data, a re-examination of the Iberian paleomagnetic data, as well as the acquisition of new paleomagnetic poles, preferentially from igneous rocks, is necessary.

1.2.2 Marine magnetic anomalies and kinematic models

Magnetic record offshore Iberia

The magnetic anomalies of the North Atlantic domain around Iberia present several distinct situations (Fig. 1.1):

- The period **between the present and 84 Ma** (till C33 anomaly) is well recorded by striped oceanic magnetic anomalies, the C-series. Therefore their interpretation is free of major ambiguities and only small differences exist between kinematic models [e.g., Luis & Miranda, 2008]. By contrast, reconstructions for periods older than 84 Ma may always be subjected to some degree of speculation.

- The period corresponding to the **Cretaceous Normal Polarity Superchron** (CNPS; chron C34) cannot be studied using magnetic isochrones due to the lack of geomagnetic reversals: it is not possible to fit magnetic lineations or to establish a credible chronology for the seafloor. Moreover, as will be discussed next, it is likely that the CNPS is only partly represented in this domain.

- The **J anomaly**, the eastern boundary of the CNPS domain, was since the decade of 70 considered to correspond to a M3-M1 sequence [Rabinowitz et al., 1978; Srivastava et al., 1990a, 2000; Sibuet et al., 2004; Olivet, 1996]. However, Bronner et al. [2011] recently suggested that the J anomaly may not result from seafloor spreading, but from a voluminous magmatism that triggered the crustal breakup before seafloor spreading. The age assigned for this event in the IAP is 112 Ma. Consequently, the assumption of the J anomaly as the beginning of the M-series

Figure 1.1: Map of magnetic anomalies of the Iberian plate and surroundings (compilation from Luis & Miranda [2008]). To the west of C33 isochron, the C-series is clearly recorded and allow well-constrained magnetic reconstructions. However, during the CNS and for older times the interpretation of anomalies is far from consensual, in particular the existence of chrons belonging to the M-series in west Iberian margin and in the Bay of Biscay, and the nature of the respective seafloor. Note that a different situation is found in the African coast: the CNS shows oceanic fracture zones, the M-series is clear, and coastal anomalies (African Blake Spur magnetic anomaly and West African coast magnetic anomaly) are identifiable [cf. Labails et al., 2010]. Several strong positive magnetic anomalies are identified in west Iberian margin as Cretaceous magmatic events, such as along the Tore-Madeira rise; across the limit between TAP and IAP toward the coast (Estremadura Spur), and the onshore plutons of Sintra, Sines and Monchique. CNS: Cretaceous Normal Superchron; IAP: Iberia Abissal Pain; TAP: Tagus Abissal Plain; AGFZ: Azores-Gibraltar Fault Zone. The identification of J anomaly follows Bronner et al. [2011].

and the existence of an M0 isochron, are strongly challenged. This may have severe implications on the accuracy of magnetic reconstructions based on M0 identification.

- A vast debate exists about the origin of magnetic anomalies and the nature of the respective seafloor **to the east of the the J anomaly**, in Tagus Abissal Plain (TAP) and in Iberia Abissal Plain (IAP) [e.g., Srivastava et al., 2000; Sibuet et al., 2007; Afilhado et al., 2008; Whitmarsh et al., 1996; Russell & Whitmarsh, 2003]. Most authors agree with the existence of a transitional domain instead of a simple continent-ocean boundary, but models vary between the existence of oceanic crust, thinned continental crust and exhumed mantle. Some authors propose to identify chrons up to M20 (∼150 Ma) in the TAP, either as resulting from ultraslow oceanic spreading [Srivastava et al., 2000] or as ridges of serpentinized peridotite [Sibuet et al., 2007].

- North of Iberia in the **Bay of Biscay**, the interpretation of magnetic anomalies is difficult, despite high-quality magnetic data exist since 1973 [Choukroune et al., 1973]. The only clear isochron is C33, which prolongates from IB-NAM and EUR-NAM domains, witnessing the existence of a paleo triple point. Different interpretations of the older seafloor support different processes and ages for the opening. According to Cande & Kristoffersen [1977], Rosenbaum et al. [2002] and Olivet [1996], the M0 isochron is not represented in the Bay. By contrast, Sibuet et al. [2004] propose the direct identification of the M0-M3 sequence in the northern half of the Bay, and suppose the southern part of this sequence to have subducted during the Cantabrian thrust.

Kinematic models from marine magnetic anomalies

The existing kinematic models for Iberia (for pre-C33 anomaly times) result essentially from two "end-member schools". The school of Olivet defends a dialectical approach between magnetic and geological data, and a large-scale interpretation in terms of major plate reorganization periods [Olivet, 1996]. The school of Srivastava and Sibuet privileges the direct interpretation of magnetic anomalies, and infers afterwards about necessary compatible geological processes [e.g., Sibuet et al., 2004; Srivastava et al., 2000].

Main differences between these two visions come from different identification of J anomaly and consequent different kinematics inferred for the Pyrenean domain. Note that due to the large width of the J anomaly, and uncertainties about its nature (see Section 1.2.2), reconstructions based on the identification of J anomaly have associated large degrees of freedom [Olivet, 1996; Bronner et al., 2011]. Geological data from the

Pyrenees suggest a maximum extension of 100 to 150 km in the eastern part of the range and 80 km in the west. This maximum extension corresponds to the phase of higher thermal metamorphism, dated radiometrically at ∼100 Ma [Vergés et al., 2002, and references therein].

For consistency, ages assigned for the kinematic stages were redefined according to the Gradstein et al. [2004] timescale.

The model of Olivet [1996]

Olivet [1996] describes the northern IB-EU border as a composite frontier, where distensional, compressive and strike-slip movements succeeded in space and time until the attachment to EU in the Oligocene. The Pyrenean chain is viewed as a segment of this border, which reached more than 2000 km. The same nature is attributed to the southern IB-AF border, with the important difference of being still active. The western boundary has been limited by the medium-Atlantic accretion axis since separation of Newfoundland (NAM plate).

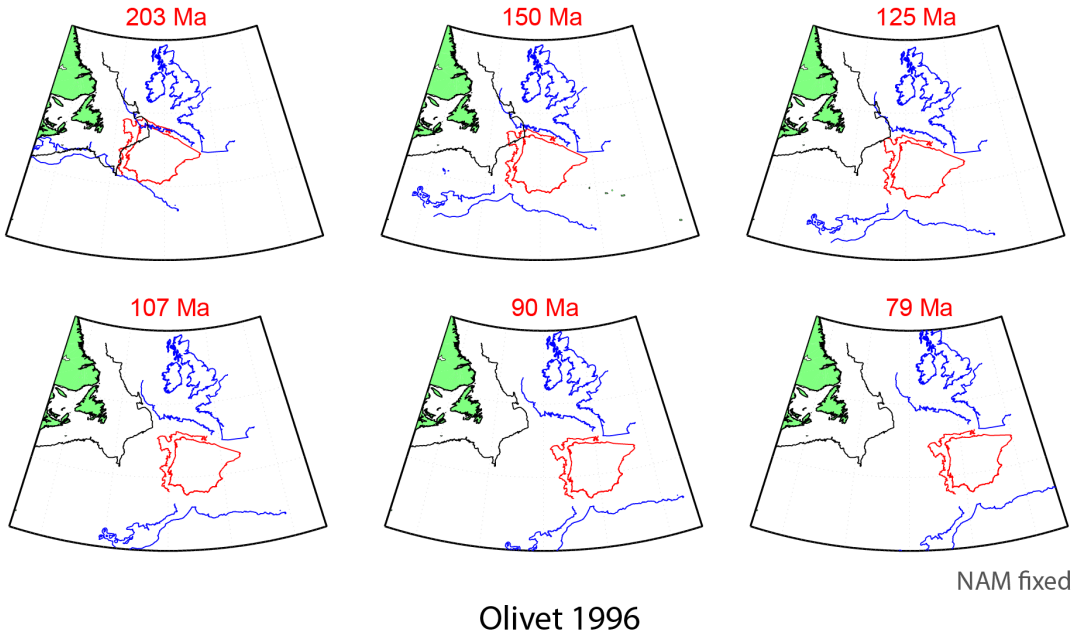

Figure 1.2: The kinematic model of Olivet [1996] for Iberia.

The kinematic model of Olivet [1996] is represented in Fig. 1.2. It agrees with the main tectonic features assigned to the Pyrenees: Cretaceous extension or transtensional setting followed by convergence onset in Campanian-Maastrichtian. It is based on:

- Two reconstructions corresponding to continental fits (ages were here assigned for these reconstructions, as they were not originally defined):

203 Ma: post-hercynian stage with maximum closing of the North Atlantic basins.

150 Ma: partial closing of peri-Iberian basins after major Jurassic rifting.

- Two independent post-rift reconstructions based on fit of anomalies:

  79 Ma (Campanian): fit of C33 chron.

  125 Ma: J anomaly. The width of the Pyrenean domain is less than 100 km.

- And two intermediate reconstructions, achieved by interpolation between stages correponding to J and C33 anomalies, assuming constant velocity and direction of spreading:

  107 Ma: (Middle Albian) maximum distension in the Pyrenean domain: 170 km at east and 100 km at west.

  90 Ma: (Turonian-Coniacian) Since the previous stage, Iberia moved away from NAM much faster than EU, and the opening of the Bay of Biscay, which is now almost complete, is viewed as a consequence of this difference in plate velocity. In the Pyrenean domain, a left-lateral strike-slip of ∼120 km along the north Pyrenean fault since the last stage (∼107 Ma) is implied. This stage marks the beginning of the ∼N-S compression between Africa and Eurasia that lasts until present.

The model of Srivastava et al.

The model of Srivastava et al result from several published works and is based on the direct identification of conjugate magnetic anomalies. Srivastava et al. [2000] proposed the identification of M-series in Iberia-Newfoundland. However, only Sibuet et al. [2004] later explored the consequences of this for the IB-EUR relative motion, namely for the opening of the Bay of Biscay and Pyrenean orogeny. In order to justify a gap of 400 km in the Pyrenean domain, they suggest that this correponded to a Neo-Tethys ocean that would have formed during Jurassic-Early Aptian and subducted during Aptian-Albian, forming an independent slab in Iberian Ranges region.

More recently, Vissers & Meijer [2012] reviewed the model of Srivastava et al., seeking for an alternative geodynamic scenario, more compatible with the observable Pyrenean geology and with paleomagnetic data from Gong et al. [2008b]. This model is represented in Fig. 1.3. It consists of four main phases of Pyrenean and IB-EUR tectonics:

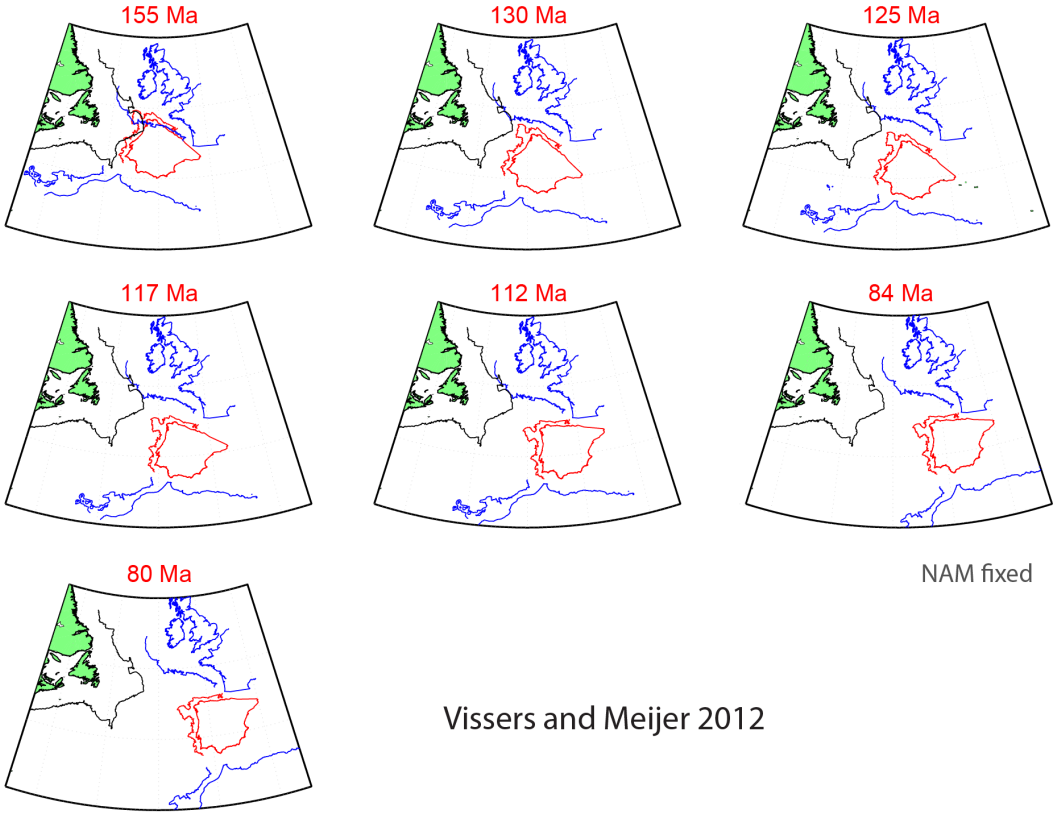

Figure 1.3: The kinematic model of Vissers & Meijer [2012], synthetizing several works by Srivastava et al.

- From Late Jurassic to Barremian (155-125 Ma; M25-M0): rifting and ultra-slow spreading resulting in the formation of a ∼320 km Neotethys oceanic domain north of Iberia.
- During the Aptian (125-112 Ma): rotation of Iberia with respect to Europe, resulting in major opening of the Bay of Biscay and subduction of Neotethys.
- From Albian to Campanian (112-84 Ma): stagnant stage.
- Campanian: onset of continental collision between Iberia and Europe.

In Fig. 1.4 the models of Olivet [1996], Vissers & Meijer [2012] and Sibuet et al. [2012] can be compared. Only stages stages allowing a direct comparison are represented. Note that the model of Sibuet et al. [2012], also representive of the Srivastava et al model, is mostly equivalent to Vissers & Meijer [2012] despite slight differences between compilations.

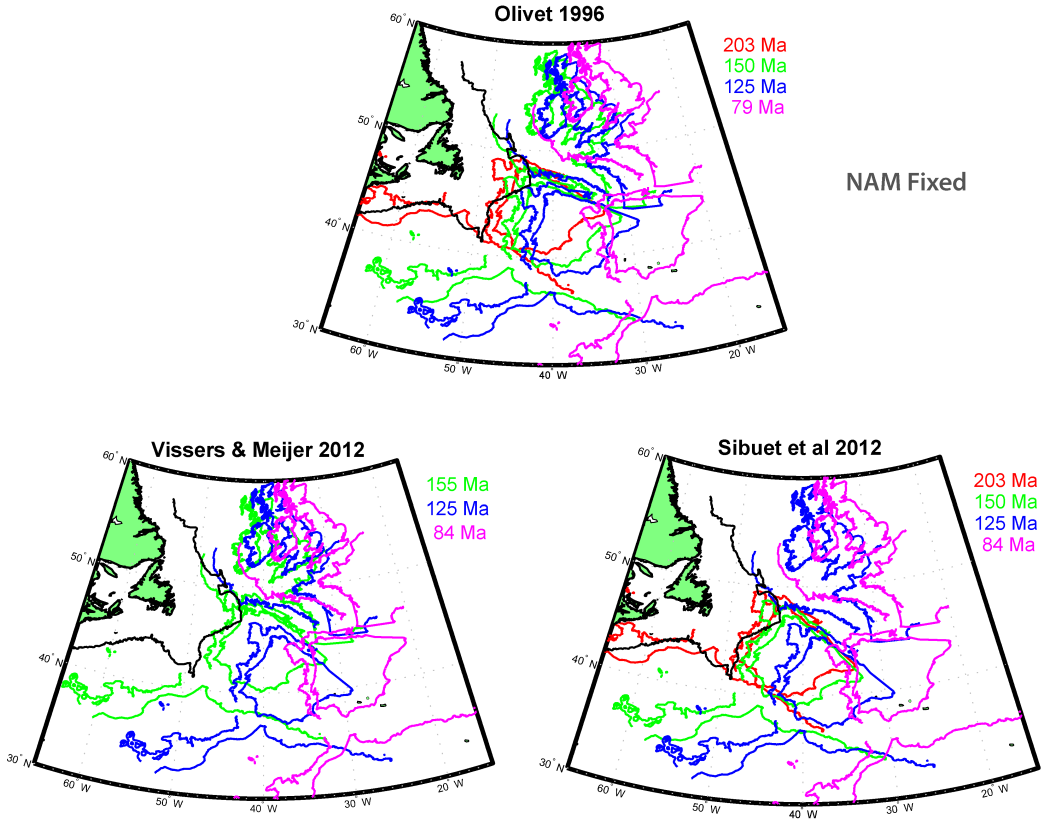

Figure 1.4: Comparison between the kinematic models of Olivet [1996], Vissers & Meijer [2012] and Sibuet et al. [2012]. The represented ages were chosen in order to allow a direct comparison between models.

Constraints imposed by the kinematics of Central Atlantic

The Central Atlantic, between Africa (AF) and North America (NAM), was the embryonic zone for the Pangean breakup. Seafloor spreading started at ∼200 Ma and persisted for long restricted to this domain. The kinematic history of Central Atlantic is well documented by seafloor magnetic anomalies since then: from initial opening to M0 anomaly (125 Ma) [Sahabi et al., 2004; Labails et al., 2010] and from M0 till present [e.g., Klitgord & Schouten, 1986]. This also implies severe constraints to the kinematics of North Atlantic, since NAM-AF fit determines the location of NAM further north than the IB-AF frontier. While NAM can be regarded as a solid block until the Labrador Sea, AF is separated from Iberia (IB) by a discontinuous tectonic frontier that suffered many tectonic events. This is illustrated in Fig. 1.5. AF is kept as fixed frame and the AF-NAM Euler poles from Labails et al. [2010] were used to rotate NAM (coastlines and -3000 m isobaths) for each indicated age. Given the Paleozoic age of Newfoundland Basin (reference), the -3000 m isobath can be considered as a first-order indicator of the continental

lithosphere of NAM. Therefore, paleogeographic configurations of Iberia are limited by the paleoposition of Newfoundland, for each age.

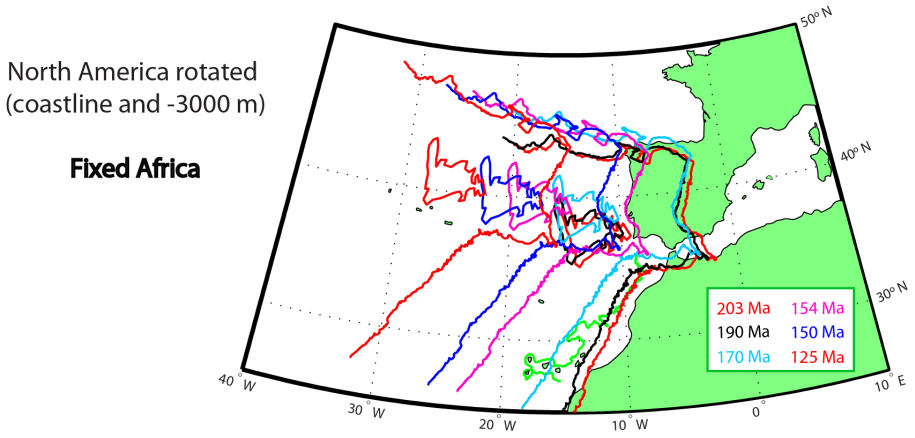

Figure 1.5: Central Atlantic kinematics and constraints imposed in North Atlantic domain. North America (coastline and -3000 m isobath) is rotated with Euler parameters from Labails et al. [2010]. Africa is the fixed frame; Iberia and Europe are only represented for reference.

1.3 Late Cretaceous Magmatism in West Iberia

The west Iberian Late Cretaceous magmatism is a key episode in the geodynamic history of this passive margin: it took place in a post-rift setting, about 20 Ma after the oceanic breakup, partially contemporaneous with the opening of the Bay of Biscay, the Pyreneen continental collision and the onset of tectonic inversion on the Mesozoic basins. It occurred both off- and onshore and lasted for at least 20 Ma [Miranda, 2010].

It is the third and last cycle of Mesozoic magmatic activity in Portugal, as described by Martins [1991]. The first two cycles comprised: tholeiitic volcanism of earliest Jurassic age (∼200 Ma), attributed to a northernmost manifestation of the Central Atlantic Magmatic Province [Martins et al., 2008; Verati et al., 2007]; and a magmatic pulse of transitional composition occurring as scattered small-scale plugs and sills of Late Jurassic age (∼130-146 Ma) [Grange et al., 2008; Martins, 1991]. Rock (1982) grouped the Portuguese Late Cretaceous alkaline magmatism along with other occurrences of similar age and composition located around the Pyrenees in what he named the Iberian Late Cretaceous Alkaline Igneous Province.

Both onshore and offshore occurrences of the Late Cretaceous west Iberian magmatism have isotopic signatures that call for a sub-lithospheric source for the magma, sometimes associated with some metasomatic contamination on the way to the surface [Grange et al.,

2010; Miranda, 2010].

Offshore

In the west Iberian margin (Fig. 1.6), a series of previously unknown igneous alkaline seamounts have been identified, sampled and studied during the last decades. Main occurrences are associated with the **Tore-Madeira rise**, which extends over about 1000 km in SW–NE direction, and roughly matches the J anomaly. Its origin was initially attributed to the Madeira hotspot, with the seamounts representing its hotspot trail, and later to a period of intense volcanism in the mid-Atlantic ridge [cf. Miranda, 2010, and references therein]. However, the most recent studies revealed that some of the seamounts that constitute the Madeira-Tore rise have ages more recent than the J anomaly, which calls for a different generation mechanism.

Geldmacher et al. [2006] proposed that all the observed magmatism in the offshore WIM could be explained by the activity the Madeira and Canaries hotspots and their interaction with the late Cretaceous mid Atlantic Ridge. Merle et al. [2009, 2006] proposed that the Madeira-Tore seamounts would be the result of a long-lived and wide mantle thermal anomaly present in the region during the Cretaceous that emitted several magmatic pulses: the first, 103-80.5 Ma (which coincides with the ages of onshore Late Cretaceous events) in the northern and central part of the rise; the second, c. 68 Ma and randomly located; the third, 28-0 Ma, restricted to the south of the Azores-Gibraltar fault zone. The space–time distribution of this magmatism would have resulted from the interaction between these pulses and the complex kinematics of the Iberian plate [Merle et al., 2009].

Other seamounts and volcanoes not associated with the Tore-Madeira rise were identified in west Iberian margin, such as the Ormonde seamount in the Goringe bank and the Fontanelas seamount [Miranda, 2010]. Furthermore, a series of magnetic anomalies forming a WNW-ESE alignment from the Sintra complex to the Tore seamount (Fig. 1.1) may correspond to further alkaline igneous activity [Miranda, 2010].

Onshore

Onshore occurrences (Fig. 1.7) comprise the **intrusive complexes** of Sintra, Sines and Monchique, the Lisbon **volcanic complex** and several scattered **sub-volcanic intrusions** emplaced into Lower Cretaceous shallow marine sediments, mainly in the Lusitanian Basin: **sills** (e.g., Paço d'Ilhas, Foz da Fonte, Anços, Lomba dos Pianos), **dykes** (e.g., Mafra radial dyke complex, Oeiras-Cascais dykes, Algarve dykes), **plugs** and **necks**; and also some minor occurrences in the Algarve Basin [cf. Miranda, 2010].

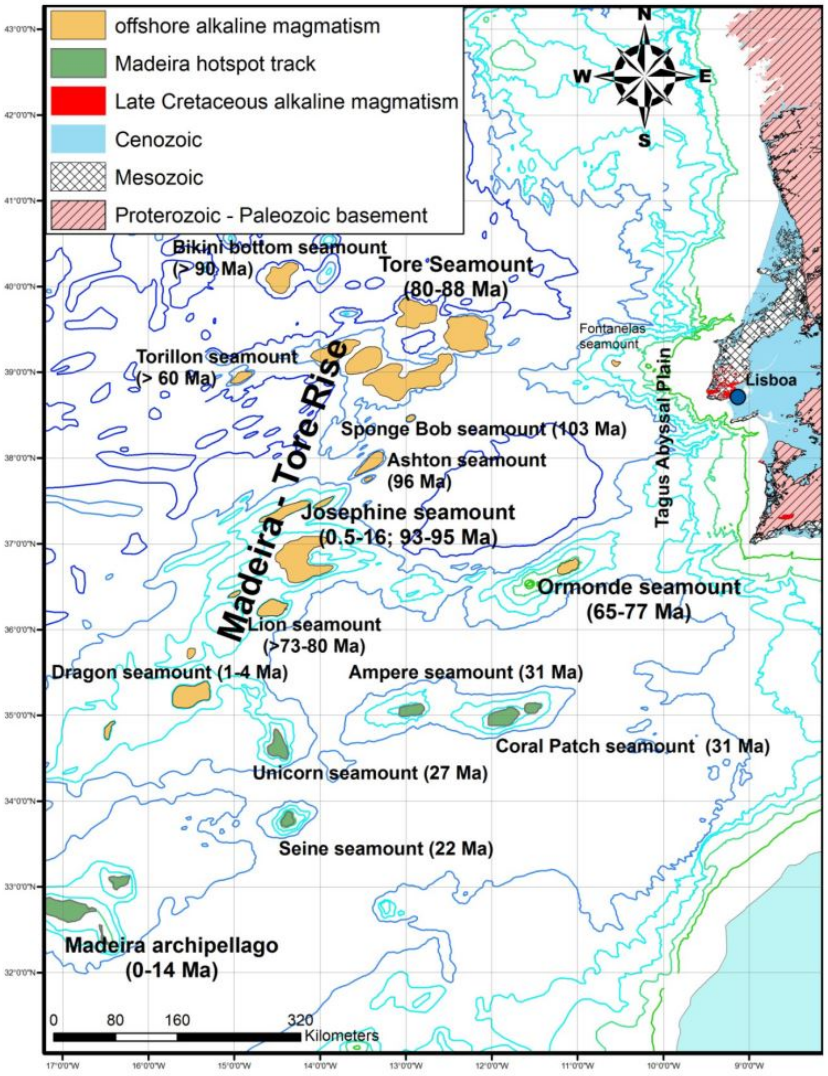

Figure 1.6: Alkaline magmatic occurrences offshore the west Iberian margin. Ages from Geldmacher et al. [2006] and Merle et al. [2006, 2009]. From Miranda [2010].

Geochronological studies [Miranda et al., 2009; Grange et al., 2010] dated this event between 100 and 72 Ma, thus lasting more than 20 Ma. Miranda [2010] proposed two pulses of magmatic activity and linked them with distinct geodynamical scenarios: the first, (94-88 Ma) more restricted to the Lusitanian Basin around Lisbon area and lacking metasomatic signature, attributed to a rapid magma ascent in a more extensional stress regime during the rotation of Iberia; the second (75-72 Ma), in which Sines and Monchique plutons are included, with metasomatic signature attributed to higher interaction with the subcontinental lithosphere during ascent in a less favorable stress regime after initiation of the Africa-Iberia continental collision.

Apart from geological and geochemical studies, some studies have applied geophysi-

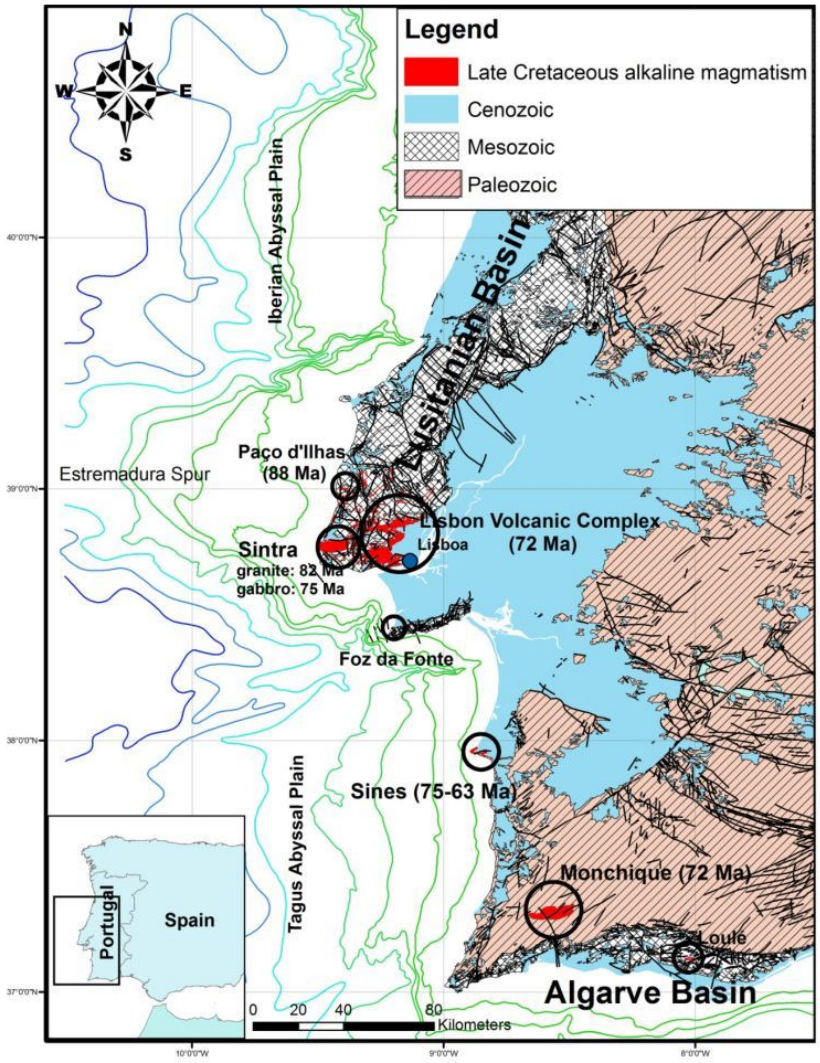

Figure 1.7: The Late Cretaceous alkaline magmatism in the onshore sector of the west Iberian margin. From Miranda [2010].

cal methods to assess the origin and emplacement mechanisms of some Late Cretaceous magmatic intrusions, for example gravimetry and anisotropy of the magnetic susceptibility of the Sintra igneous complex [Terrinha et al., 2003] and anisotropy of the magnetic susceptibility on dykes of the Mafra Radial Dyke Complex [Nogueira, 2008] and on Foz da Fonte sill [Miranda et al., 2006]. In fact, many onshore magmatic occurrences show excellent outcropping conditions, making them promising targets for studies aiming not only a better understanding of this magmatic event, but also of the mechanisms governing magmatic emplacement in general. In particular, some sills show total or partial vertical profiles and/or wide horizontal exposure, making them excellent natural laboratories for detailed studies, in particular of anisotropy of magnetic susceptibility.

1.4 Objectives

The following objectives were addressed during this thesis:

1. Acquisition of good-quality paleomagnetic data with the aim of improving the Iberian APWP.
2. Compilation and critical selection of Iberian paleomagnetic data
3. Evaluation of the compatibility between Iberian paleomagnetic data, existing kinematic models and global APWP
4. Use the paleomagnetic data to constrain paleogeographic reconstructions for the cases where data are proved to be reliable.
5. Study the AMS of sills from the Late Cretaceous magmatic event, with the aim of unraveling magma flow directions during their emplacement.
6. Explore implications for the Late Cretaceous magmatism, in particular inferring about location of magmatic sources and relation with offshore events.

Objectives 1 and 2 are addressed in Chapter 3, objectives 3 and 4 in Chapter 4 and objectives 5 and 6 in Chapter 5. These chapters are in paper format, as published (Chapters 3 and 4) or submitted (Chapter 5) to ISI journals.

2. Theoretical and Methodological Principles

2.1 Rock Magnetism

2.1.1 Magnetism

The origin of magnetism lies in the orbital and spin motions of electrons and how the electrons interact with one another. Therefore, all materials are magnetic, but some are much more magnetic than others. The main reason for this is the existence or not of a collective interaction between atomic magnetic moments. The induced magnetization resulting from an induced field is given by $M_i = \chi H_i$, where χ, the magnetic susceptibility of the material, the ability of the material to respond to an applied field. There are three classes of magnetic behavior: diamagnetism, paramagnetism (which do not exhibit collective magnetic interactions and are not magnetically ordered) and ferromagnetism (which exhibits long-range magnetic order below a certain critical temperature).

Diamagnetism is an intrinsic property of all materials, due to the non-cooperative behavior of orbiting electrons when exposed to an applied magnetic field. Diamagnetic substances are composed of atoms which have no net magnetic moments (i.e., all the orbital shells are filled and there are no unpaired electrons). However, when exposed to a field **H**, the precession of the electronic orbits about **H** creates an induced magnetic moment opposite to **H**, and thus the diamagnetic susceptibility is negative. Diamagnetism is temperature independent and usually very weak. It is usually surpassed by other magnetic behaviors coexisting in materials. Some minerals exhibit a diamagnetic behavior, e.g.,quartz (SiO_2) and calcite ($CaCO_3$).

Paramagnetism is a property of materials in which some of the atoms or ions have a net magnetic moment due to unpaired electrons in partially filled orbitals. Each unpaired electronic spin behaves as a dipole magnetic moment **m** with magnitude m_B and is subjected to a competition between the magnetic ($E_m = -\mathbf{m} \cdot \mathbf{B}$) and the thermal energy ($E_T = k_B T$). In the absence of an applied field, or in the absence or the ordering influence of neighboring spins (exchange interactions) the electronic spins are randomly oriented. Under an applied field, the magnetic moments tend to align, creating a net magnetization parallel to the field, and reaching a saturation magnetization when all magnetic moments are aligned with the field. If the field is removed, as the magnetic moments are independent, any small thermal perturbation will cause them to oscillate and to be randomly distributed, giving rise to a null resultant magnetization. Paramagnetic susceptibility is thus positive and, to first order, inversely proportional to the temperature (Curie's law). One of the most important atoms with unpaired electrons is iron, and for example most ferromagnesian minerals (e.g. olivine, pyroxenes, amphiboles...) exhibit a paramagnetic behavior.

Ferromagnetism (*s.l.*)

Unlike paramagnetism, in which magnetic moments are independent from each other and magnetizations are generally low, ferromagnetism characterizes materials in which neighboring spin moments interact, giving rise to strong magnetizations. In ferromagnetic materials, magnetic spins cooperate through the mechanism of **exchange interaction**. This cooperation is originated by the superposition of electronic orbitals from neighboring ions through significant regions of the crystalline structure. The energy associated with this interaction is the **exchange energy**. Exchange energies are very large, equivalent to the energy associated with the same moment in a field of the order of 1000 T. As a consequence of the Pauli Exclusion Principle from quantum mechanics, exchange energy is minimized when the spins are aligned parallel or antiparallel, depending on the details of the crystal structure (Fig. 2.1).

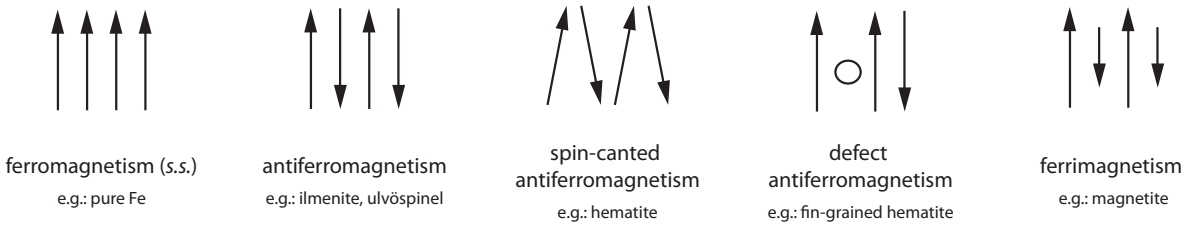

Figure 2.1: Types of spin alignment in ferromagnetism (*s.l.*). Adapted from Tauxe [2010].

In **ferromagnetism (*sensu stricto*)** a direct parallel coupling between spins exists, and magnetizations are very strong. In **antiferromagnetism**, the antiparallel coupling between spins results in a null net magnetization. However, if some deviation in spin alignment (canted antiferromagnetism) or some lattice defects (defect antiferromagnetism) occur, a low net magnetization will appear. In **ferrimagnetism**, spins are antiparallel coupled, but the magnitudes of moments in each direction are unequal, which results in a significant net magnetic moment.

The 3d electronic orbital of the transition elements (e.g. Fe, Co, Ni) is particularly susceptible to exchange interactions due to its shape and prevalence of unpaired spins. In oxides, oxygen can mediate this interaction forming a bridge between neighboring cations which would otherwise be too far apart from direct overlap, a phenomenon named **super-exchange**. In iron oxides, which are particularly important for rock magnetism, oxygen shares its 2p electrons with the 3d shells of iron ions (Fig. 2.2).

Thermal pertubations affect the ferromagnetic coupling by weakening the exchange interaction as the crystal expands and orbital overlaps vanish. For each crystal, there is a

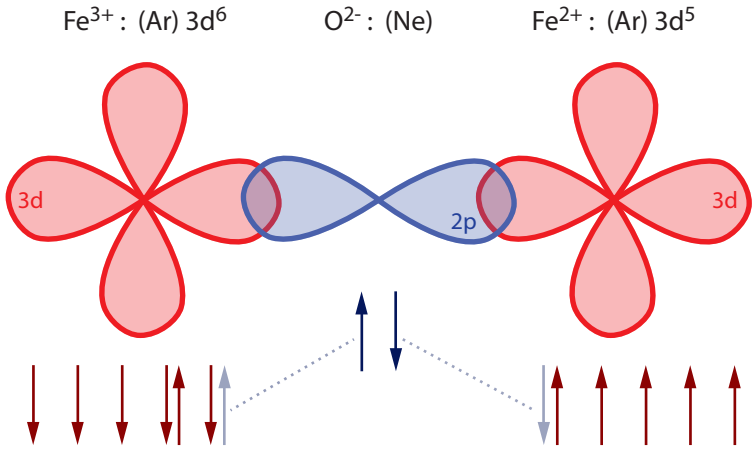

Figure 2.2: Super-exchange between the 3d electronic orbitals of Fe^{2+} and Fe^{3+} cations, mediated by the 2p orbital of oxygen anion. An antiparallel coupling between the two cations is necessary in order to respect the Pauli Exclusion Principle. Redrawn from Tauxe [2010] and Miranda [2011].

characteristic temperature that is enough to completely destroy the spin coupling, named **Curie temperature**, or Néel temperature in the case of antiferromagnetic materials. Above this temperature, the crystal assumes a paramagnetic behavior. In particular, its susceptibility rapidly drops to values close to zero, given the paramagnetic $1/T$ dependence of susceptibility. In measurements of magnetic susceptibility versus temperature (thermomagnetic curves), different susceptibility drops are associated with Curie temperatures of different minerals.

2.1.2 Magnetic minerals

The **ferromagnetic minerals** that most contribute to the rock magnetism at the Earth's crust belong to the ternary diagram of iron oxides FeO-TiO_2-Fe_2O_3, particularly the solid solutions magnetite-ulvöspinel (**titanomagnetites**, spinel structure) and hematite-ilmenite (titanohematites, rhombohedral structure) (Fig. 2.3). **Solid solutions** are crystallographic series in which one or more types of atoms may be substituted without changing the original crystal structure. In **iron oxides**, titanium commonly substitutes iron in the crystal structure. **Substitution of iron to titanium** in titanomagnetites is represented by the variation of the parameter x ($0 < x < 1$): $Fe_{3-x}Ti_xO_4$, from Fe_3O_4, magnetite, and Fe_2TiO_4, ulvöspinel. As Ti^{4+} has no unpaired spins and is of a different size, magnetic properties vary along the series (Fig. 2.3b).

When exposed to environmental conditions different from those of their formation,

minerals tend to alter in order to re-achieve equilibrium. Usually, the new conditions are more oxidized and compositions alter by diffusion of Fe^{2+} cation to the mineral's surface, where it converts to Fe^{3+}. In (titano)magnetite, this process gives rises to a cation-deficient spinel structure named (titano)maghemite (Fig. 2.3c). **Maghemitization** is thus a low-temperature oxidation process.

When magnetic minerals form from cooling magma (above 1300°C), all solid solution compositions are allowed. However, as temperature decreases crystals seek compositions in equilibrium with the new conditions. This leads to diffusion of cations through the lattice, leaving titanium-poor and titanium-rich regions within the crystal, a process named **exsolution**. The existence of oxygen in the melt usually associates a high-temperature oxidation with this process, named **deuteric oxidation**.

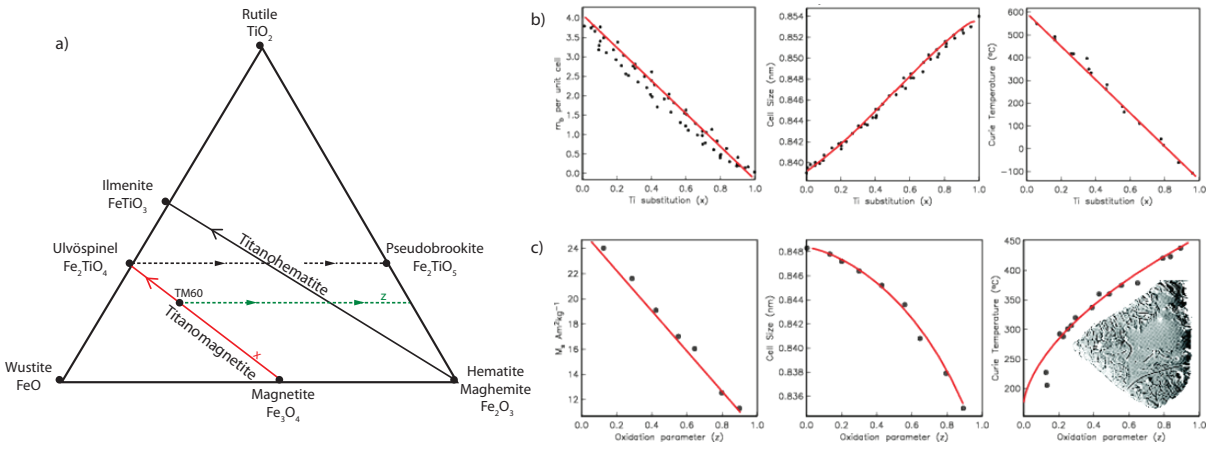

Figure 2.3: (a)Ternary diagram for iron oxides. The solid lines are the magnetite-ulvöspinel and hematite-ilmenite solid-solution series, in which titanium content increases. The dashed lines indicate example paths of increasing oxidation. (b) Variation of intrinsic parameters with titanium substitution (x parameter) in the lattice of titanomagnetites (magnetization per unit cell, cell size and Curie temperature). (c) Variation of intrinsic parameters with oxidation (z parameter) in TM60. Inset show a magnetite crystal undergoing maghemitization: the crystals crack due to the decrease in volume. Adapted from Tauxe [2010].

2.1.3 Magnetic energy, anisotropy and stability

The magnetization (and its stability) of ferromagnetic particles is controlled by magnetic energy, which is a sum of several contributing terms. Any magnetic grain will seek the magnetization configuration that minimizes its total energy, and certain directions within crystals (the easy-directions) are at lower energies than others. So, to shift the magnetization vector from one easy-direction to another always requires overcoming an energy barrier. If this barrier is sufficiently large, the magnetization may remain for long time

Mineral	Composition	Magnetic Order	T_c (°C)	M_s (kAm^{-1})	$H_{c,max}$ (T)
		Oxides			
Magnetite	Fe_3O_4	ferrimagnetic	580	480	0.3
Ulvospinel	Fe_2TiO_2	AFM	-153	-	-
Hematite	αFe_2O_3	canted AFM	675	2	1.5 - 5
Ilmenite	$FeTiO_2$	AFM	-233	-	-
Maghemite	γFe_2O_3	ferrimagnetic	∼600	420	0.3
		Sulfides			
Pyrrhotite	Fe_7S_8	ferrimagnetic	320	<60	0.5 - 1
Greigite	Fe_3S_4	ferrimagnetic	∼333	75	
		Oxyhydroxides			
Goethite	αFeOOH	AFM, weak FM	∼120	<3	>5
		Metals			
Iron	Fe	FM	770	∼1000	$<10^{-4}$
Nickel	Ni	FM	358	∼200	-

Table 2.1: Magnetic properties of some common minerals: Curie or Néel temperature (T_c), saturation magnetization (M_s), maximum coercivity (H_c). Adapted from Moskowitz [1991].

in the same direction. The main contributions to the magnetic energy of ferromagnetic materials are the following.

- **Exchange energy**. Due to the coordination of neighboring spins, in order to respect the Pauli's Exclusion Principle. It is the cause for the remanent magnetization of ferromagnetic materials.

- **Magnetostatic interaction energy**. It represents the interaction between the flux lines of the magnetic field and the magnetic moments of electronic spins: $E_m = -\mathbf{M} \cdot \mathbf{B}$. It is minimized when the spins are aligned (parallel or antiparallel) with the magnetic field.

- **Anisotropy energy**. It represents the energy terms that depend on the crystal itself, constraining the direction of magnetization. Ultimately, it is anisotropy energy that allows paleomagnetic studies. It creates energy barriers within the crystal that prevent the free rotation of magnetic moments and lead to the existence of preferred directions for the magnetization. It is due to different causes, being the most important:

  - **Magnetocrystalline anisotropy**. It is an intrinsic property of the crystalline structure, independently of grain size and shape, and is especially important on particles with low saturation magnetization. Magnetocrystalline anisotropy

is defined by parameters K_i named **magnetocrystalline anisotropy constants**, and is minimum at chrystallographic directions. It determines the energy necessary to deflect the magnetic moment from one easy direction. The easy and hard directions arise from the interaction of the spin magnetic moment with the crystal lattice (spin-orbit coupling). Two important types of magnetocrystaline anisotropy are the cubic (e.g. magnetite) and the uniaxial (e.g. hematite). Magnetocrystalline anisotropy strongly depends on temperature because electronic interactions (that determine the shape of the energy surface of the crystal) strongly depend on the interatomic spacing.

- **Magnetostriction**. It is due to the state of stress within the crystal. Straining a crystal results in changing the physical interaction between orbitals of neighboring atoms (by modifying their exchange energy and shape). Conversely, changing the magnetization of a crystal may also change the shape of the crystal by altering the shapes of the orbitals. Magnetostriction may be physically equivalent to a uniaxial anisotropy, giving rise to a single easy-axis of magnetization.
- **Magnetostatic (shape) anisotropy**. Shape is the more important source of magnetic anisotropy. A magnetized body produces an external field that is equivalent to the field produced by a set of free poles distributed over its surface. These surface poles also produce an internal field that is shape-sensitive and proportional to the magnetization: it is called the **internal demagnetizing field** $\mathbf{H}_d = \mathbf{N} \cdot \mathbf{M}$, where $\mathbf{N}$, the **demagnetizing tensor**, depends on the shape of the magnetized body (Fig. 2.4). The magnetostatic energy can thus be seen as $E_m = \mathbf{M} \cdot \mathbf{B}$, where $\mathbf{B}$ includes both the external field $B_e = -\mu_0 H_e$ and the internal demagnetizing field $B_i = \mu_0 \mathbf{N} \cdot \mathbf{M}$. Thus, $E_m = -\mu_0 \mathbf{M} \cdot \mathbf{H}_e - \frac{1}{2}\mu_0 \mathbf{M} \cdot \mathbf{N} \cdot \mathbf{M}$. Here, the first term is the magnetostatic energy related to the external field and the second one is the **magnetostatic self-energy** or **demagnetizing energy**.

Given that the internal demagnetizing energy varies with M^2, the magnetic anisotropy of strongly magnetized particles (such as magnetite, with strong saturation magnetization) is largely dominated by shape anisotropy, even for slightly elongated grains. By contrast, the magnetic anisotropy of weakly magnetized particles such as hematite will not prone to be dominated by shape anisotropy, but will rather be controlled by magnetocrystalline anisotropy.

The magnetic anisotropy thus controls the stability of the acquired magnetization, determining the energy barriers that are necessary to overpass in order to flip the magne-

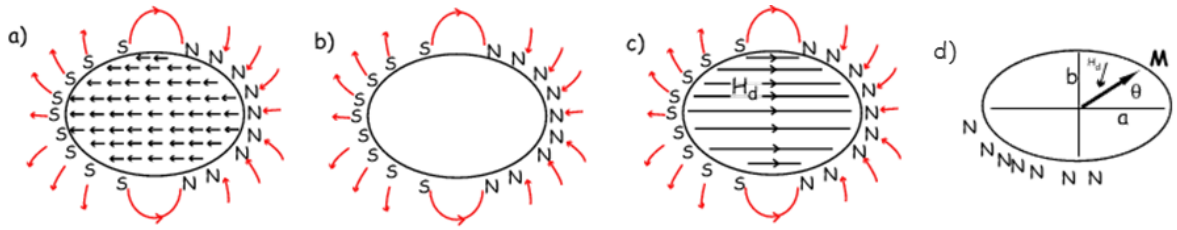

Figure 2.4: Internal and external magnetic fields in an elliptic ferromagnetic crystal. (a) The exchange energy between electronic spins produces a magnetization distribution within the crystal which generates an external magnetic field. (b) This external field is equivalent to the field generated by a series of monopoles distributed along the crystal's surface and (c) generates an internal field $\mathbf{H}_d$, named internal demagnetizing field which is opposite to the direction of the magnetization (d) An induced magnetization along an angle θ with the long axis a will change the surface pole distribution and flip the internal demagnetizing field. Adapted from Tauxe [2010].

tization vector. One way to accomplish this is to apply a magnetic field sufficiently large so that its magnetic energy exceeds the anisotropy energy. The magnetic field able to flip the magnetization of uniformly magnetized particles at saturation over the magnetic anisotropy energy barrier is the **microscopic coercivity** H_c. For the simple case of a uniaxial grain, it is related to the magnetocrystalline anisotropy constant K and to the saturation magnetization M_s as $H_c = \frac{2K}{\mu_0 M_s}$.

The mechanisms described above apply to uniformly magnetized particles, in which all spins act in concert. This is the case for very small particles, called **single-domain** (SD) particles (<40 nm for magnetite grains). For larger particles (>80 nm), the self-energies rapidly become large due to the squared dependence on the magnetization. Therefore, large particles tend to internally reorganize their magnetic moments in order to achieve configurations of lower magnetostatic energy. At first stage, neighboring spins diverge from strict parallelism forming non-uniform magnetization configurations with increasing complexities (**pseudo-single domain**, PSD). As particles grow larger, the minimum energy configuration is achieved by the formation of **magnetic domains**: regions in which spins are parallel aligned (**multi-domain**, MD particles). Domains are separated by **domain walls** (Fig. 2.5). Both the number of domains and the width of domain walls are controlled by energy balance. The division in domains stops when the energy necessary to create a new wall is higher than the energy gained with the new configuration. In domain walls, a rapid transition (thin walls) have a high exchange energy price, while a more gradual switch (thick walls) is more unfavorable for magnetocrystalline energy (Fig. 2.5e,f).

In fact, the size at which domain walls appear in magnetite is poorly constrained because it depends on the exact shape of the particle, its state of stress, and even its

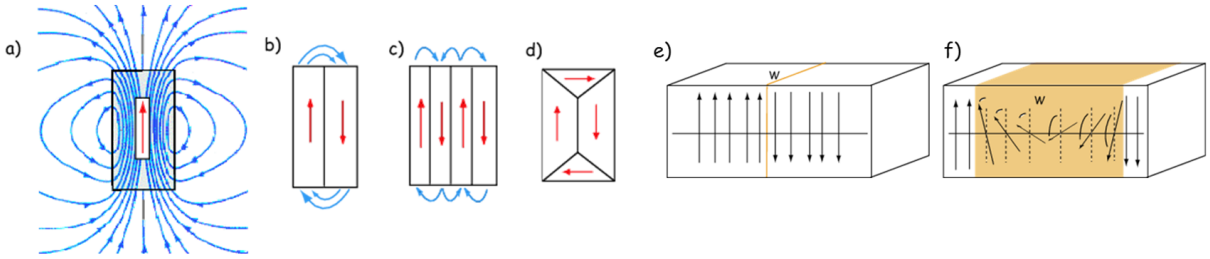

Figure 2.5: Some magnetic domain structures and associated external fields. (a) Uniformly magnetized particle (single-domain). (b) Two domains. (c) Four domains in a lamellar pattern. (d) Closure domains. (e) Instantaneous domain wall, with a 180° switch from one atom to another. This wall has a very high cost of exchange energy. (f) Thicker domain wall with gradual transition along the wall width w. The exchange price is lower, but the configuration is less favorable for magnetocrystalline energy. Adapted from Tauxe [2010].

history of exposure to past fields. In the literature the higher estimates are of 100 nn, therefore truly SD magnetite is unlikely to be common in nature. Nonetheless, given the difficulty to theoretically model more complicated states, most of the theory supporting paleomagnetic studies is based on SD theory.

Most of the remanent magnetization of rocks is carried by grains containing a small number of magnetic domains. Large grains containing a large number of domains have very small and unstable net magnetization, thus have lower coercivities. In the absence of external fields, the domains rest in the lowest magnetostatic configuration. When a field is applied, domains parallel to the field extend, crossing magnetocrystalline energy barriers. In the case of low fields, the barriers crossed are low and the wall may come back to the initial position after removing the field. However, if the field is high enough for high barriers to be crossed, it becomes impossible to go back to the initial wall position and the remanence is lost.

Another very important factor controlling the stability of magnetization (or equivalently the **magnetic viscosity**) in non-applied field conditions is related to **thermal energy**. Anisotropic magnetic energy E_a and the thermal energy E_T compete to maintain or destroy the alignment of magnetic moments in a grain. This is described by statistical physics through the probability density function $P = \exp(E_a/E_T)$. It allows calculating the probability to find a grain with thermal energy enough to overcome the anisotropy energy and flip the net magnetization vector from one easy axis to another. With increasing temperatures, it becomes easier to find grains in such conditions and the net magnetic moment will decrease. For a random assemblage of uniaxial SD grains the magnetization will exponentially vanish according to

$$M = M_0 \exp(t/\tau)$$

where M_0 is the initial magnetization and τ, the decay constant, is the relaxation time and depends on the competition between magnetic anisotropy energy and thermal energy:

$$\tau = \frac{1}{C} \exp(\frac{E_a}{E_T}) = \frac{1}{C} \exp(\frac{Kv}{k_B T})$$

where $C \simeq 10^{10} s^{-1}$ and v is the volume of the grain. Two important dependences of the relaxation time can be here seen: it increases exponentially with the volume and decreases exponentially with the temperature. In constant temperature, small grains will have low relaxation times, and a limit grain volume exists below which these grains become unstable at laboratory time-scale. This volume is named the **blocking volume** and grains with those characteristics are called **superparamagnetic** (SP) grains, because their magnetic moments rapidly randomize and align with the field. However, they still differ from paramagnetism because much larger fields are necessary to saturate them. Conversely, for a given grain volume there is a temperature above which the net magnetization will rapidly vanish, named the **blocking temperature** T_B. It is a property of the grain and not of the mineral constituting it, so that different blocking temperatures (or even a spectrum of T_B) can be expected for one sample.

If the particle is subjected to an external field, the energy barrier to flip its magnetic moment will be lower, as well as the relaxation time, as reflected by the Néel equation:

$$\tau = \exp\left(\frac{Kv}{k_B T}\right)\left(1 - \frac{H}{H_c}\right)^2$$

When considering the Earth's magnetic field $H << H_c$ and this additional factor can be neglected.

2.1.4 Types of remanence

As previously described, the principle of acquisition and stability of a magnetization is related to the ability of grains to retain their magnetization along time. This is dependent on the nature of the grains, their volume, temperature and time. Each of these mechanisms represents a different type of **natural remanent magnetization** (NRM), i.e. remanence naturally acquired, in the presence of natural ambient fields.

Thermal remanent magnetization

The NRM acquired by cooling a material magnetic to values below its TC is named thermal remanent magnetization (TRM). This is the main mechanism of remanence acquisition in igneous rocks. When the temperature decreases below T_C it will pass through the various T_B corresponding to the various grains existing in the rock. Thus, the TRM is not simultaneously acquired to the whole rock. Instead, the total TRM is the vectorial sum of partial TRMs (pTRM) acquired at distinct T_B windows (**law of additivity of pTRM** for SD grains):

$$TRM = \sum_{i}^{n} pTRM(T_{Bi})$$

Below T_B the grain will have a stable TRM. Above T_C the molecular ferromagnetic coupling is destroyed and the grain assumes paramagnetic behavior. Above T_B but below T_C the grain will be superparamagnetic.

Demagnetization techniques

Thermal demagnetization allows determining the T_B spectrum within a sample and the pTRM respective to each T_B intervals. In practice, the following procedure is repeated for increasing temperatures T: the sample is heated to a given temperature T and then cooled in zero field. Grains with relaxation times that are SP at that temperature become randomized. The resultant magnetization vector, which will only include contributions from grains with $T_B > T$, is measured.

Similarly, the technique of **alternating field (AF) demagnetization** allows determining the coercivity spectrum and the different magnetization components carried by populations with different coercivities. It takes advantage from the variation of relaxation times with coercivity: components with short τ also have low H_c. In this technique the following steps are repeated for increasing H: an oscillating field with peak H is applied and then progressively decreased under null ambient field. Grains with coercivity below the AF peak will be randomly oriented and will have a final net contribution for the remanence. The resultant magnetization will only be due to grains with $H_c > H$.

During demagnetization, the remanence vector changes from the initial NRM until the most stable component has been isolated; at this point the vector decays in a straight line to the origin. This final component is the **characteristic remanent magnetization** (ChRM).

Viscous remanent magnetization

The continuous exposure of rocks to the ambient magnetic field may lead to partial or total remagnetization. Low-coercive, large MD grains as well as SP grains are particularly prone to be continuously remagnetized by the ambient field. This gives rise to a magnetization component of the Earth's crust that coincides with the present-day Earth's magnetic field direction. This component is named viscous remanent magnetization (VRM).

Chemical remanent magnetization

New magnetic minerals formed in presence of a magnetic field and above T_C acquire a chemical remanent magnetization (CRM). This is the case for minerals that nucleate and progressively increase their size (and reach their blocking volume) and for minerals that result from the alteration of other pre-existing minerals. This process usually takes place later than the rock formation, so that CRM leads to secondary magnetization.

Detrital remanent magnetization

The NRM acquired by sediments is due to a very different process. The detrital magnetic grains are already magnetized, therefore the NRM results from the mechanical alignment of grains with the magnetic field, a process named depositional magnetic remanence (DRM).

Isothermal remanent magnetization and hysteresis cycle

Diamagnetic and paramagnetic particles have a linear $M(H)$ variation, with negative and positive slope, respectively. In ferromagnetism, $M(H)$ follows a more complex trend. The magnetic susceptibility corresponds to the slope of the $M(H)$ curve. When a ferromagnetic particle is subjected to an applied magnetic field **H**, it will gain a certain magnetization. For a random set of SD uniaxial particles, the variation of the magnetization with the intensity of the applied field, under isothermal conditions, will give rise to a curve similar to Fig. 2.6. This curve is called a **hysteresis curve**.

Consider an initial null net magnetization. With increasing applied field the magnetization increases linearly through the brunch a. To low H intensities, the curve is still reversible, i.e. the magnetization will vanish if the field is removed. This initial slope corresponds to the **low-field susceptibility** χ_{lf}. If the field is increased until some point in branch b, say until point P, the curve becomes irreversible: if the field is decreased the magnetization will follow the branch c, and once reached null field an **isothermal remanent magnetization** (IRM) of value M_r will have been acquired. If the field continues

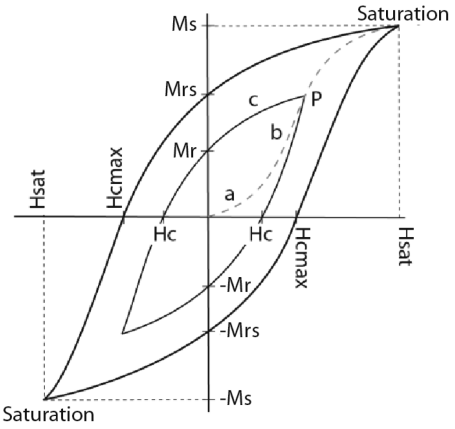

Figure 2.6: Hysteresis curve for a ferromagnetic material. A minor hysteresis loop and an outer loop are indicated, together with their main hysteresis parameters. From Miranda [2011].

to increase in the opposite direction the IRM continues to decrease. The field necessary to reduce the net moment to zero is the **coercive field** or **coercivity** H_c. The described path is in fact a minor hysteresis loop. If the maximum applied field is enough to align all the magnetic moments with the field, the magnetization will reach a maximum, the **saturation magnetization** M_s, and the resulting hysteresis curve is named the outer loop. The remanence acquired in this case is named the **saturation remanent magnetization** M_{rs}, also called saturation isothermal remanence sIRM. The respective coercivity is the **maximum coercivity** $H_{c,max}$.

Another hysteresis property is the **coercivity of remanence** (H_{cr}). This is the reverse field which, when applied and then removed, reduces the saturation remanence to zero (Fig. 2.7). H_{cr} is always larger than the coercive field. Snapshots of magnetization states corresponding to some points on the hysteresis curve are also illustrated in Fig. 2.7.

The various hysteresis parameters are not solely intrinsic properties but are dependent on grain size, domain state, stresses, and temperature. The dependence on grain size make them particularly useful for magnetic grain sizing of natural samples. For example, MD particles have much lower coercivity and saturation magnetization than SD grains, because it is easier to move domains around than to coherently flip the magnetization of an entire particle. The ratio parameters M_{rs}/M_s and H_{cr}/H_c have a particular importance in grain size analysis. For SD uniaxial particles, M_{rs}/M_s =0.5 and H_{cr}/H_c =1.09.

Several rock magnetism methods are based on IRM and hysteresis.

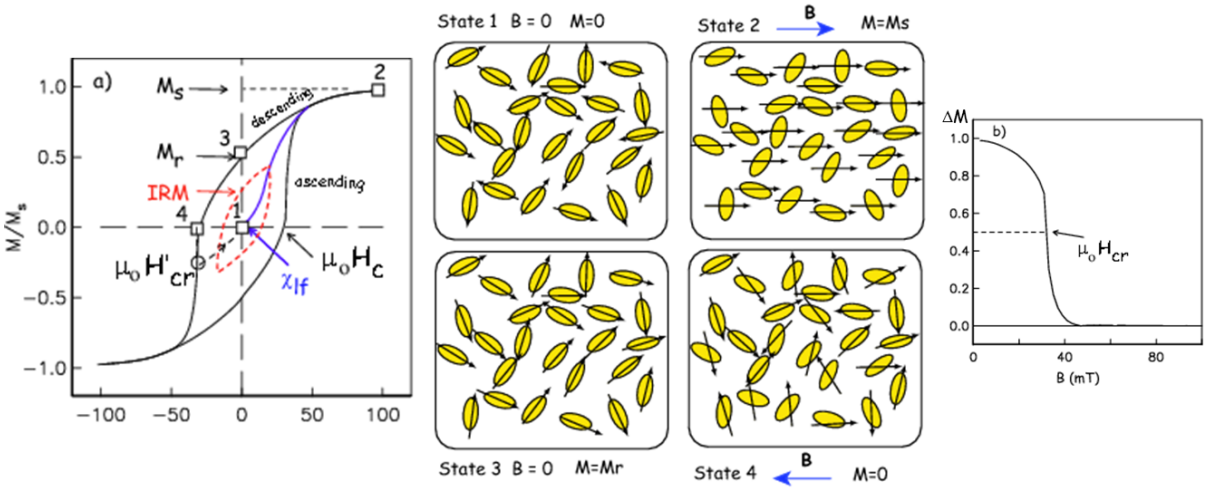

Figure 2.7: (a) Hysteresis curve for a random assemblage of uniaxial SD particles, with respective snapshots of magnetization states. State 1 is the initial demagnetized state. The initial slope is the low-field susceptibility χ_{lf}. Saturation M_s is reached when all moments are parallel to the applied field (State 2). Saturation remanence M_r is the remanence retained after returning from saturation to zero field (State 3). When the field is applied in the opposite direction and has remagnetized half M_s, it corresponds to the bulk coercive field H_c. The net magnetization is then null (State 4), but if the field is switched off at this stage, the grains will still conserve some net remanence. For the remanence to completely disappear it is necessary to increase a bit more the field intensity. The field at which this happens is the coercivity of remanence H'_{cr}. (b) Another measure of the coercivity of remanence. The curve is obtained by subtraction of the ascending curve from the descending curve. The maximum is M_r. Adapted from Tauxe [2010].

IRM unmixing

Based on the assumptions that (1) populations of magnetic minerals have log-normally distributed coercivity spectra; and (2) IRM is the linear sum of all the contributing grains, Robertson & France [1994] suggested that IRM acquisition curves can be unmixed into the contributing components. The IRM acquisition curve (LAP, linear acquisition plot [Kruiver et al., 2001]) can be differentiated in order to get the gradient acquisition plot (GAP). The latter can be unmixed in several Gaussian curves, from which the parameters of the contributing components can be taken, namely the mean $H_{1/2}$ and the standard deviation DP.

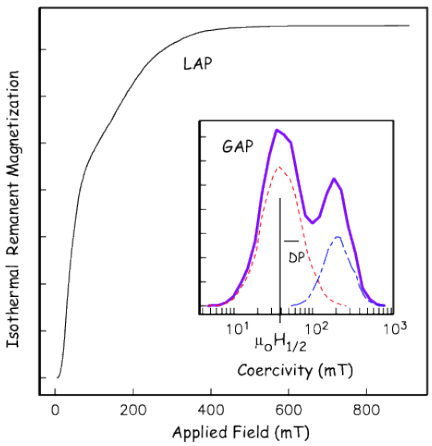

Figure 2.8: IRM unmixing of two magnetic components with different coercivity spectra. From Tauxe [2010].

Lowrie test

The Lowrie test is a 3D IRM unblocking technique [Lowrie, 1990] that combines isothermal and thermomagnetic analysis. It allows determining the blocking temperature spectra of different coercivity fractions. Each hard-, medium- and low-coercive fraction is magnetized along each orthogonal direction. The unblocking temperature spectra of each fraction are determined by stepwise thermal demagnetization on zero field.

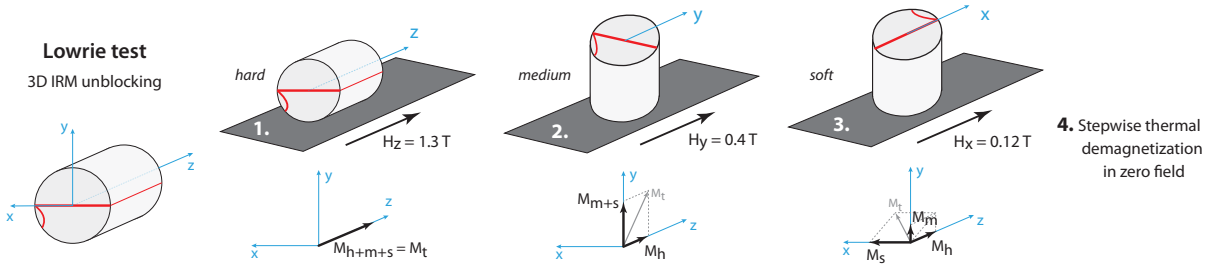

Figure 2.9: 3D orthogonal IRM inducing for Lowrie test. (1) A strong inducing field H_z (the largest field achievable in the laboratory) is applied in z direction saturating all minerals in the sample. The resulting total magnetization is along z direction. (2) A medium field is applied in y direction and saturates the minerals with coercivity lower than H_y. The total magnetization is the vectorial sum of $\mathbf{M}_h$ (magnetization of the hard fraction, along z) and $\mathbf{M_{m+s}}$ (medium and soft fractions, along y). (3) A soft field H_x is applied and flips the magnetic moments of the low-coercive phase toward the x direction. The final magnetization is the vectorial sum of the soft, medium and hard components. Afterwards, the sample is heated to successively larger temperatures and then cooled, in zero field. The magnitude of the remaining magnetization of each fraction is measured on each Cartesian axis and plotted versus the demagnetizing temperature.

Day diagrams

Day et al. [1977] built diagrams in which M_{rs}/M_s plot versus H_{cr}/H_c. They have defined quasi-theoretical bounds corresponding to SD, PSD, SP and MD particles. However, most of the paleomagnetic samples fall within the PSD region, therefore many research has been made in order to understand the real significance of this region of the Day diagram.

In particular, Dunlop [2002a,b] modeled theoretical curves for mixtures of SD-SP and SD-MD mixtures. These calculations are now thought to be oversimplified, and the interpretation of PSD behavior is now sought through modern micromagnetic modeling. Despite, the Day diagram and associated theoretical mixing curves are still extensively used in the literature as an indicator of the domain states present in samples.

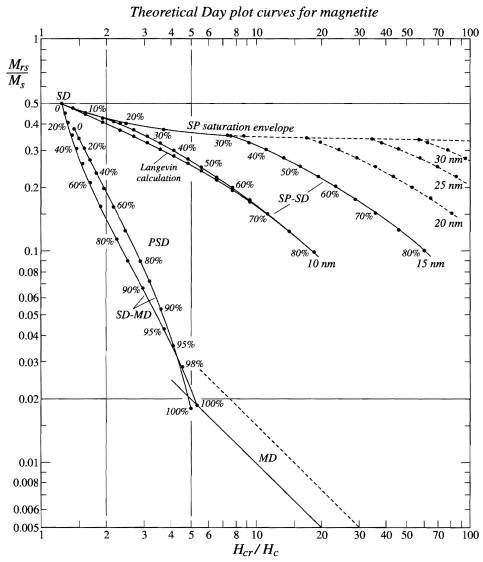

Figure 2.10: Day diagram for magnetite and theoretical mixing curves [Dunlop, 2002a].

First Order Reversal Curves

Another way to treat hysteresis data is the recent technique of **FORC diagrams** (Fig. 2.11). They are constructed by measuring a large number of partial hysteresis curves know as **First Order Reversal Curves**. The FORC experiment begins by saturating the specimen by a large positive applied field. The field is then reduced to a reversal field H_a, and the FORC is defined as the magnetization curve that results when the applied field is increased from H_a forward to saturation. This is repeated for several H_a values. The magnetization at the applied field Hb on the FORC with reversal point H_a is denoted by $M(H_a, H_b)$ and the FORC distribution is defined as the mixed second derivative:

$$\rho(H_a, H_b) \equiv -\frac{\partial^2 M(H_a, H_b)}{\partial H_a \partial H_b}$$

A coordinates change to $H_u = (H_a + H_b)/2$ and $H_c = (H_b - H_a)/2$ is made. The FORC diagram is the contour plot of a FORC distribution with H_u on the vertical and H_c on the horizontal axes. H_c is equivalent to a particle coercivity (thus related to its grain size) and H_u to a local interaction field (thus related to magnetostatic interactions).

An extended discussion on these analyses (theoretical basis and accuracy) can be found at [Tauxe, 2010].

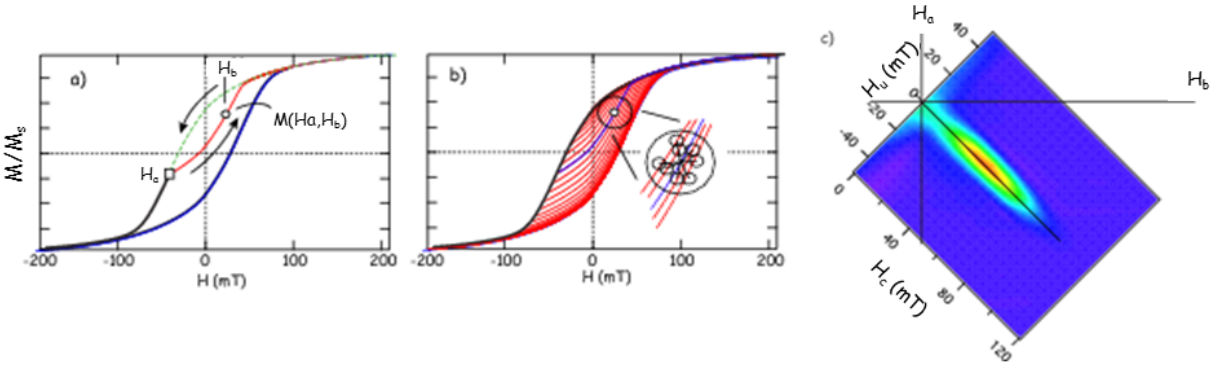

Figure 2.11: Illustration of construction of FORC diagrams. (a) Outer hysteresis loop and FORC for the H_a reversal point (red line). (b) A series of FORCs for a SD assemblage of particles. (c) FORC diagram for (b). From Tauxe [2010].

.

2.2 Anisotropy of the Magnetic Susceptibility

2.2.1 Magnetic Susceptibility of rocks

Magnetic susceptibility (MS) χ is defined by $\mathbf{M}_I = \chi\mathbf{H}$, where only the induced magnetization is considered. It results from the summed contribution of all phases that form the rock. At atomic level, the magnetic susceptibility results from the response of electronic orbits (diamagnetism) and/or unpaired spins (paramagnetism and ferromagnetism) to an applied field. The diamagnetic response is very weak when compared to the paramagnetic one, but a small fraction of ferroagnetic material is sufficient to dominate the magnetic response due to the high coupling energy from the exchange interactions. MS depends on the temperature and applied field. We here refer to the low-field (<1 mT) susceptibility (in the initial linear branch of the hysteresis cycle), measured in ambient temperature conditions (∼20°C).

Ferromagnetic minerals are usually dispersed in rocks within a matrix of diamagnetic (e.g. calcite, quartz) and paramagnetic (e.g. biotite, amphybole) minerals, and when ferromagnetic minerals represent more than 0.1% of the total volume of the rock, they dominate the observed magnetic properties because of their high MS. In the case of magmatic rocks, the ferromagnetic contribution is largely dominant over the other two (typically >5% of the total rock volume).

2.2.2 AMS and magnetic fabric

The bulk, scalar magnetic susceptibility has many applications in rock and environmental magnetism. However, the property that will be more considered in this work is the **anisotropy of magnetic susceptibility** (AMS): the dependence of the susceptibility on the direction of the applied field. In general, the anisotropic response of an induced magnetization to an applied field can be due to crystal shape, lattice structure, dislocation density, state of stress, etc. For highly magnetic materials such as magnetite, the AMS is dominated by the shape anisotropy.

When considering the anisotropy of magnetic susceptibility, both the inducing field $\mathbf{H}$ and induced magnetization $\mathbf{M}$ are vectors and their components are related by linear equations $M_i = \chi_{ij}H_j$ (in summation indexes), in an arbitrary system. The χ_{ij} coefficients define a second-rank symmetric tensor, the tensorial susceptibility $\boldsymbol{\chi}$. There exists a coordinate system in which the off-axis terms of $\boldsymbol{\chi}$ are zero. The eigenvectors are thus the principal axes $K_1 > K_2 > K_3$ that define the ellipsoid of anisotropy (Fig. 2.12a). The bulk susceptibility of an anisotropic sample is defined as the arithmetic mean of the three

directional susceptibilities: $K_m = (K_1 + K_2 + K_3)/3$. K_1 is the magnetic lineation and K_3 the pole to the foliation plane.

The AMS reflects the magnetic fabric of a sample and is evaluated terms of its magnitude and shape by the parameters:

- P, eccentricity of the ellipsoid (**total anisotropy**): $P = K_1/K_3$
- L, linear anisotropy (**lineation**): $L = K_1/K_2$
- F, planar anisotropy (**foliation**): $F = K_2/K_3$
- T, **shape parameter**: $T = (2 \ln K_2 - \ln K_1 - \ln K_3)/(\ln K_1 - \ln K_3)$

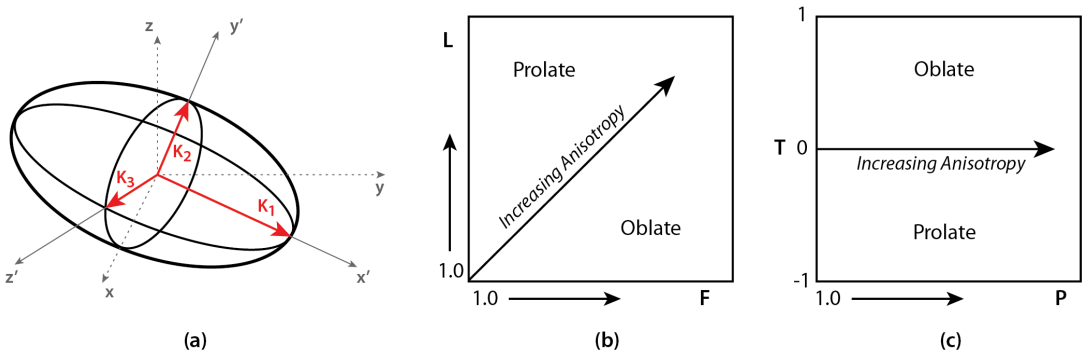

Figure 2.12: (a) AMS ellipsoid in an arbitrary system coordinates (x, y, z) and in a frame (x', y', z') defined by its eigenvectors, the principal axes K_1, K_2 and K_3. (b) Flinn diagram, which relates the linear and planar anisotropy parameters. (c) Jelinek diagram, relating the shape parameter with the total anisotropy.

2.2.3 Magnetic fabric of magmatic rocks

In **magmatic rocks**, the magnetic fabric is mainly determined by ferromagnetic iron oxides (mainly titanomagnetites). Some physical conditions are determinant for the characteristic igneous fabric, mainly: (i) magma has a viscous behavior up to 800°C, much higher than the Curie temperature of iron oxides; (ii) the fusion point for iron oxides is about 1300°C, so that they behave like solid particles during magmatic flow, as well as other dia- and paramagnetic phases such as olivines, pyroxenes and plagioclases. Therefore, it can be concluded that:

- The influence of the gravity and geomagnetic fields on the alignment of individual crystals is insignificant;

- The magnetic fabric is mainly influenced by the magmatic flux, either by the direct alignment of ferromagnetic grains (and therefore dominated by the shape anisotropy of individual grains) or by their clustering around paramagnetic minerals, mimicking their (flow) fabric (and in this case the anisotropy may be mainly due to distribution anisotropy due to magnetic interaction between grains, if they are sufficiently close to each other).

2.3 Paleomagnetism and Plate Kinematics

One of the most important consequences of the existence of ferromagnetic coupling in some materials is that they are able to retain a remanent magnetization after the inducing field is removed. Of special importance to Geophysics, the fact that some minerals constituting the Earth's crust are ferromagnetic enables us to open a window to explore past behaviors of the Earth's magnetic field. In particular, it is possible to determine the paleopositions of the Earth's magnetic pole. From that, and based on some assumptions, it is possible to infer the relative movements between tectonic plates and reconstitute past configurations of the Earth's crust. In fact, Paleomagnetism and Oceanic Magnetic Kinematics were the scientific bases for the validation of Plate Tectonic Drift theory and are intimately linked in the establishment of lithospheric kinematic models.

For the determination of paleomagnetic poles and derivation of tectonic implications for the studied plate, several field, laboratory and analytical work must be done. Most of these methods are described elsewhere in this work, and detailed for example by Tauxe [2010] and Butler [1992]. They can be briefly described as follows:

- **Selection of target rocks**, in function of their age, preservation state and geological stability
- **Sampling and orientation** in the field using appropriate devices and preparation of standard specimens in the laboratory
- **Demagnetization** of specimens by AF or thermal demagnetization techniques (cf. *Demagnetization techniques* in the previous section)
- Determination of the remanence components for each specimen, in particular the characteristic remanent magnetization (**ChRM**) and its angular coordinates **declination** D and **inclination** I, using principal component analysis and Fisher statistics
- Calculation of the respective **paleopole**

Paleomagnetic data are usually classified according to Van der Voo [1990] **Q factor**. This parameter evaluates the quality, i.e. the primary character of a paleomagnetic poles. It is based on seven reliability criteria: (1) Well-determined age and the assumption that the magnetization age equals the actual rock age; (2) Sufficient number of samples and adequate statistics; (3) Proper demagnetization techniques; (4) Field tests to constrain the age of the magnetization; (5) Structural control and tectonic coherence with the involved

craton or block; (6) Presence of reversals; (7) No resemblance to paleopoles of younger age.

Some concepts are essential to paleomagnetic analyses:

Geomagnetic pole: point of intersection between the magnetic dipole that best fits the Earth's magnetic field and the Earth's surface.

Virtual geomagnetic pole (VGP): the position, in present-day geographic coordinates, of the geomagnetic pole during the formation of a rock, justifying the acquired characteristic remanence.

Geocentric axial dipole (GAD) hypothesis: the assumption that the Earth's magnetic field is (and was) equivalent to a magnetic dipole centered on the Earth's rotation axis.

However, the magnetic axis is not coincident with the geographic axis but precesses about it, a phenomenon known as **secular variation** of the geomagnetic field. For the GAD to be a valid assumption it is thus necessary to assure that the rock sampling represents a time of acquisition of the remanence that is higher than the periodicity of this variation. This period is usually considered to be $10^4 - 10^5$ years, based on paleosecular variation data from the last 5 Ma. When this condition is verified, the paleopole coincides with the paleogeographic pole is named a **paleomagnetic pole**.

For a GAD magnetic field, the magnetic inclination I depends on the site latitude λ according to

$$\tan I = 2 \tan \lambda = 2 \cot \theta$$

where $\theta = 90 - \lambda$ is the colatitude. Thus, knowing the remanent magnetization of a rock placed on a given lithospheric plate and assuming the GAD hypothesis, it is possible to determine the latitude of the plate at the time the rock was formed (**paleolatitude**). However, its paleolongitude remains undetermined.

The position of the paleomagnetic pole (λ_p, ϕ_p) is calculated from the rock's geographic coordinates (λ_s, ϕ_s) and the local magnetic field components (D, I) by:

$$\lambda_p = \arcsin(\sin \lambda_s \cos \theta + \cos \lambda_s \sin \theta \cos D)$$

$$\phi_p = \begin{cases} \phi_s + \beta, & \text{if } \cos \theta \geqslant \sin \lambda_p \sin \lambda_s \\ \phi_s + (\pi - \beta), & \text{if } \cos \theta \leqslant \sin \lambda_p \sin \lambda_s. \end{cases}$$

Once the GAD hypothesis is assumed, a single magnetic pole is expected for all plates at a given time. Therefore, the difference existing between the paleopole positions of different plates at a given age is attributed to a different relative position of both plates in the past, and this is how paleomagnetism is able to reconstruct the past relative positions of continents.

If, for a given plate, the paleomagnetic poles corresponding to different ages are plotted, they will describe a path that reflects *how we would see the pole changing if we were standing on the plate through times*. This path is called the **apparent polar wander path** (APWP). The comparison of APWPs from different plates and continents is an essential tool to determine the relative positions of continents in the past, and to infer about paleolongitude. Note that the difference in APWP corresponds to the finite Euler rotations between plates at each age, which brings us to a straight link between paleomagnetic and kinematic approaches which has been extensively used in the last decades.

The main factors that can bias these analyses are the existence of **non-dipolar components** of the Earth's magnetic field and **true polar wander** (rotation of the entire Earth (including the mantle) with respect to the rotation axes).

2.4 Euler rotations applied to Plate Kinematics

Any motion of points, lines or rigid areas over the Earth's surface, either they are paleomagnetic poles, APWPs, lithospheric plates, etc., are all described by **finite Euler rotations**. In Chapters 3 and 4, it is made an intensive and extensive use of finite rotations. I here present the basic fundamentals and equations that are behind presented results and that support plate kinematics analyses in general. A complete description of plate tectonics methods can be found in Cox & Hart [1986].

The **Euler's fixed point theorem** states that any displacement of a rigid body in which one point remains fixed is equivalent to a single rotation about some axis that runs through the fixed point. In particular, any displacement on a sphere's (Earth's) surface can be described as a rotation about an axis passing through the center of the sphere (one can think of the rigid body as a "cone-slice" of the Earth containing the point or region of interest on its surface extremity and the center of the Earth on the other). The point where this axis intersects the Earth's surface is called the **Euler pole** of the rotation, **E**. Thus, any two points with position vectors **r** and $\mathbf{r}'$ are related by a rotation $(\mathbf{E}, \Omega)$, where Ω is the angular distance between **r** and $\mathbf{r}'$. The rotation is described by the 3×3 **rotation matrix R** so that $\mathbf{r}' = \mathbf{R} \cdot \mathbf{r}$, being R_{ij} elements defined as follows:

$$
\begin{aligned}
R_{11} &= {E_x}^2(1 - \cos\Omega) + cos\Omega \\
R_{12} &= E_x E_y(1 - \cos\Omega) - E_z \sin\Omega \\
R_{13} &= E_x E_z(1 - \cos\Omega) + E_y \sin\Omega \\
R_{21} &= E_y E_x(1 - \cos\Omega) + E_z \sin\Omega \\
R_{22} &= {E_y}^2(1 - \cos\Omega) + cos\Omega \\
R_{23} &= E_y E_z(1 - \cos\Omega) - E_x \sin\Omega \\
R_{31} &= E_z E_x(1 - \cos\Omega) - E_y \sin\Omega \\
R_{32} &= E_z E_y(1 - \cos\Omega) + E_x \sin\Omega \\
R_{22} &= {E_z}^2(1 - \cos\Omega) + cos\Omega.
\end{aligned}
$$

(E_x, E_y, E_z) are the Cartesian coordinates of the Euler pole.

Any unit position vector **A** is converted from its spherical components latitude λ and longitude ϕ to Cartesian coordinates according to:

$$A_x = \cos\lambda\cos\phi \ ; \ A_y = \cos\lambda\sin\phi \ ; \ A_z = \sin\lambda \ .$$

And conversely:

$$\lambda = \arcsin A_z \ ; \ \phi = \arctan(A_y/A_x) \ .$$

Plate circuits are chains of total reconstruction poles that are able to find the relative position of plates for which reconstruction poles cannot be directly inferred; for example, the circuit IB-NAM-AF can be used to calculate the IB-AF Euler poles. In practice, this corresponds to the addition of finite rotations, which is done by multiplication of rotation matrices. If $\mathbf{R}_1$ corresponds to the rotation IB-NAM and $\mathbf{R}_2$ to the rotation NAM-AF, $\mathbf{R}_{total} = \mathbf{R}_2\mathbf{R}_1$ represents the added rotation IB-AF.

Finally, we note that ideal plate reconstructions should be completely based on the assessment and direct interpretation of magnetic isochrones and fracture zones. This is only possible to accomplish on clearly striped seafloor and/or with transform faults. However, this approach is limited at different scales by several factors, for example: the oldest age of the oceanic crust is the furthest one can go; the quantity and quality of the magnetic data; the quality of the magnetic remanence of seafloor rocks; the existence of superchrons, eventually hampered by the lack of transforms; later tectonic imprints; difficulty on quantifying continental rifting and intraplate deformation. This leads to the fact that some reconstructions have a significant degree of speculation. Good quality paleomagnetic data can play an important role on solving some of these uncertainties. In particular, note that direct magnetic anomalies interpretation and reconstructions cannot go further than closing continental masses back to Pangean assemblage, so that pre-Pangean times are only quantitatively assessed by paleomagnetism.

3. Reconciling Cretaceous paleomagnetic and marine magnetic data for Iberia: new Iberian paleomagnetic poles

Résumé

Nos connaissances sur la cinématique et la paléogéographie de l'Ibérie depuis l'ouverture de la Pangée jusqu'au Crétacé Supérieur restent encore limitées. Les reconstitutions magnétiques sont handicapées, à la fois par les incertitudes sur la nature de la croûte pour les périodes les plus anciennes, et par la présence du Superchron Normal du Crétacé entre 125 Ma et 84 Ma. Du côté du paléomagnétisme, les données sont limitées à cause de plusieurs facteurs : faible quantité de pôles paléomagnétiques satisfaisant les critères de qualité de référence, faible résolution sur les âges, incertitudes sur les corrections liées aux mouvements tectoniques post-formation et à la présence éventuelle de phases de réaimantation.

Ce chapitre, présenté sous la forme d'un article publié au *Journal of Geophysical Research* (M. Neres, E. Font, J.M. Miranda, P. Camps, P. Terrinha and J. Mirão, 2012 : Reconciling Cretaceous paleomagnetic and marine magnetic data for Iberia : new Iberian paleomagnetic poles, J. Geophys. Res., 117, B06102) est ici brièvement résumé. De nouvelles données paléomagnétiques pour le Crétacé Supérieur de la plaque Ibérique sont calculées à partir de deux sills basiques (Paço de Ilhas et Foz da Fonte) récemment datés par chronologie isotopique à ∼88 et ∼94 Ma, respectivement. Le contexte régional est favorable au développement d'une étude paléomagnétique car ces deux sills sont intrusifs dans le Bassin Lusitanien, tectoniquement stable, et donc rattaché à l'Ibérie stable.

Afin de certifier l'origine primaire du signal magnétique, j'ai mené une étude détaillée de minéralogie magnétique de ces deux sills, basée sur l'acquisition de courbes d'IRM (Isothermal Remanent Magnetization), test de Fuller [Fuller et al., 2002], courbes thermomagnétiques, tests de Lowrie [1990], diagrammes FORC (First Order Reversal Curves), diagramme de Day et observations au microscopie électronique et optique en lumière réfléchie sur lames minces. Toutes ces mesures et observations montrent que, pour les deux sills, la minéralogie magnétique est magmatique (primaire), bien préservée, portée par titanomagnetite, ce qui suggère que l'aimantation caractéristique est primaire (contemporaine du refroidissement de la roche).

A partir des directions caractéristiques de l'aimantation, deux pôles paléomagnétiques ont été calculés : PLat = 73.4°, PLong = 204.6°, A95 = 1.3° pour le sill de Paço de Ilhas (∼88 Ma) et Plat = 73.8°, PLong = 217.1°, A95 = 3.3° pour celui de Foz da Fonte (∼94 Ma) (Fig. 3.2 et 3.8). Ces pôles sont classés au niveau 6 (pour un maximum de 7) suivant le critère de qualité Q de Van der Voo [1990].

Ces intrusions basiques étant des corps magmatiques dont la mise en place est relativement rapide (quelques centaines d'années ?), je discute de la validité des résultats en fonction de l'enregistrement de la variation paléoséculaire du champ magnétique (VPS) : a-t-on

un échantillonnage suffisant du champ pour justifier l'hypothèse du Dipole Géocentrique Axial (DGA) ? Je présente et discute les scénarios possibles. Je conclus qu'une minimisation de la VPS à l'échelle d'échantillons dans lesquels différentes températures de blocage coexistent (dû aux titanomagnétites à contenu variable en titane) et dans une période où l'intensité de la variation séculaire était plus faible (Superchrone Normal du Crétacé), est la raison la plus plausible pour expliquer la faible dispersion des directions magnétiques observées. J'ai vérifié par ailleurs que ces nouveaux pôles sont cohérents avec la Courbe de Dérive Polaire Apparente (CDPA) global publiée par Torsvik et al. [2008], ce qui renforce notre interprétation que les nouveaux pôles obtenues sur les sills basiques sont des pôles paléomagnétiques et non des pôles virtuels.

Dans ce travail sont également compilées, sélectionnées et discutées les données paléomagnétiques publiées pour le Crétacé de la plaque ibérique (Fig. 3.10). Nous avons calculé des pôles moyens pour six périodes de temps et les avons transporté dans le référentiel Afrique en utilisant les pôles d'Euler Ibérie-Afrique issus des modèles cinématiques déterminés à partir des anomalies magnétiques du fond océanique. Nous vérifions alors que les pôles moyens, correspondant plutôt à la période post-rifting (de 70 Ma jusqu'à 120 Ma) sont en accord avec la CDPA. Pour ces âges, la cinématique de l'Ibérie est raisonnablement connue à partir du moment où l'origine marine (i.e., basaltes médio-océaniques) des anomalies magnétiques est indiscutable et correspond aux isochrones C31 à C34 (70-84 Ma). Les pôles paléomagnétiques et les pôles d'Euler correspondant à cet intervalle de temps sont donc considérés comme valables. Par contre, pour les âges antérieurs à l'ouverture océanique (c'est-à-dire plus anciens que 120 Ma), un écart apparaît entre les pôles paléomagnétiques et la CDPA. Cet âge correspond aux périodes où l'origine des anomalies magnétiques reste encore très discutée. Par exemple, il reste des incertitudes sur la nature de la croûte océanique (serpentinisation, exhumation du manteau, croûte continentale étirée, etc...) et donc sur la fiabilité des isochrones magnétiques identifiés par certains auteurs (M0 à M29). A ce stade, l'origine de cette incompatibilité entre pôles paléomagnétiques et pôles d'Euler reste encore inconnue mais fait l'objet du chapitre suivant.

En conclusion, nous avons présenté de nouvelles données paléomagnétiques et lancé une nouvelle discussion sur l'origine du problème de la cinématique de l'Ibérie au Jurassique-Crétacé, période intrinsèquement liée à la formation de la chaîne pyrénéenne.

Reconciling Cretaceous paleomagnetic and marine magnetic data for Iberia: new Iberian paleomagnetic poles

M. Neres,[1] E. Font,[1] J. M. Miranda,[1] P. Camps,[2] P. Terrinha,[1,3] and J. Mirão[4]

(This chapter is presented in a paper format, as published in *Journal of Geophysical Research*, Neres et al., 2012, DOI: 10.1029/2011JB009067)

Abstract

The Cretaceous paleogeography and the kinematic evolution of the Iberian plate are poorly constrained. Especially problematic is to reconcile Iberian paleomagnetic data with paleomagnetic data of the neighboring plates and with Euler poles derived from seafloor magnetic anomalies. The first limitation arises from the Cretaceous Normal Polarity Superchron where paleogeographic reconstruction using marine magnetic anomalies is handicapped. The second arises from the paucity of reliable paleomagnetic poles with satisfactory statistical criteria and age. In order to address these shortcomings and provide new high quality paleomagnetic poles for Iberia, we conducted a detailed rock magnetic and paleomagnetic study of two Cretaceous magmatic sills, the Paço de Ilhas (PI) and Foz da Fonte (FF) sills, from the Lusitanian Basin, Portugal, recently dated at about 88 and 94 Ma, respectively. Our results show that the magnetic mineralogy of the sills is primary, i.e., acquired during magma cooling, and essentially represented by titanomagnetite. The corresponding paleomagnetic poles match the synthetic APWP from the African plate at 80 and 100 Ma. On the basis of a rigorous selection of Iberian Cretaceous poles, we then calculated mean paleomagnetic poles for different time intervals and found that Iberian paleomagnetic data fit well the global APWP between 70 and 120 Ma, but move far away from the APWP at pre-rift times. Our approach shows that new and better constrained paleomagnetic poles can aide in solving part of the contradiction between Iberian and African APWPs.

[1]Instituto Dom Luiz, Universidade de Lisboa, Lisbon, Portugal.
[2]Géosciences Montpellier, CNRS, Université Montpellier 2, Montpellier, France.
[3]Instituto Português do Mar e da Atmosfera, Portugal.
[4]Laboratório HERCULES, Évora, Portugal.

3.1 Introduction

The break-up of the Pangaean supercontinent and subsequent kinematic evolution of major plates during Mesozoic times are now well constrained by paleomagnetic data [Besse & Courtillot, 2002; Schettino & Scotese, 2005; Torsvik et al., 2008] and oceanic magnetic anomalies [Le Pichon & Sibuet, 1971; Luis & Miranda, 2008; Olivet, 1996; Russell & Whitmarsh, 2003; Sibuet et al., 2004; Srivastava et al., 2000, 1990a,b]. However, the positions of minor blocks, such as Iberia, are still poorly constrained [e.g., Márton et al., 2004; Osete & Palencia Ortas, 2006; Osete et al., 2011]. Nonetheless, the Iberian Plate occupies a strategic, pivotal position during opening of the Atlantic Ocean and the Bay of Biscay. Understanding its kinematic evolution is important for a number of reasons, including resource and natural hazard assessment [Cloetingh et al., 2011; Omira et al., 2011]. Several models based on oceanic magnetic anomalies have been proposed where the data are merged into a single rotation event of about 37° counterclockwise, and associated with Bay of Biscay seafloor spreading between the chrons M0 (125 Ma) and C33r (83 Ma) [Rosenbaum et al., 2002; Sibuet et al., 2004; Srivastava et al., 1990a; Vissers & Meijer, 2012]. A single rotation phase of Iberia is also supported by paleomagnetic data [Gong et al., 2008b; Van der Voo, 1969], while some favor a discontinuous two-stage counterclockwise rotation model [Galdeano et al., 1989; Moreau et al., 1997], and others a succession of clockwise and counterclockwise rotations [Storetvedt et al., 1990, 1987].

When evaluating proposed models, the major limitation resides in our incapacity to reconcile the paleomagnetic data with the corresponding eulerian finite rotation poles within a unique and consistent kinematic model. The relative motion between Iberia and Africa cannot be directly deduced from marine magnetic anomalies, so it must be deduced from the relative motion of each plate relative to the North American plate, data that can be readily obtained from the magnetic striping of the North and Central Atlantic [e.g., Labails et al., 2010; Luis & Miranda, 2008]. In spite of small differences mainly related to early drifting stages, the kinematics of the Central Atlantic are well known. However, identification of pre-M0 magnetic anomalies along the western Iberian margin has been the source of major uncertainties. Some authors have identified magnetic chrons up to M17 along the Iberian margin [e.g., Srivastava et al., 2000], with oceanic spreading beginning as early as 143 Ma. Others argue that only after chron M0r [Olivet, 1996], or chrons CM4n-M5r [Russell & Whitmarsh, 2003], was normal oceanic spreading initiated. In addition, the long-lived Cretaceous Normal Polarity Superchron (CNPS) prevented the development of normal and reverse magnetic periods during that time, thus limiting the study of plate kinematics with magnetic methods.

The Cretaceous paleomagnetic database for Iberia is still poorly constrained and re-

quires revisions in (1) age dating, (2) statistical criteria, (3) tilt or shallowing inclination correction in the case of records from sedimentary rocks, and (4) adjustments due to the influence of local/regional remagnetizations. Uncertainties in age result from low temporal resolution and outdated radiometric data. The reference paleomagnetic poles for the Lusitanian and Algarve basins, for example, are computed from a limited number of paleomagnetic sites for which the ages of the samples encompasses a large interval of time, particularly for those contemporaneous with a major rifting phase during the Barremian-Aptian and Aptian-Albian [Galdeano et al., 1989; Moreau et al., 1997]. In addition, misfits in paleopole ages and positions have resulted from outdated methods including K/Ar measurements on whole rock samples that can be biased by excess/loss of Ar during alteration. One serious problem is the widely documented remagnetization for northern Iberian sites [Dinarès-Turell & Garcia-Senz, 2000; Gong et al., 2008b, 2009; Juárez et al., 1994, 1998; Moreau et al., 1992; Schott & Peres, 1987; Steiner et al., 1985; Villalain et al., 2003], and sites in the Algarve and Lusitanian basins [Galbrun et al., 1990; Galdeano et al., 1989]. These remagnetized sites are usually found in Aptian-Albian times, during the final rifting phase that affected the west Iberian continental lithosphere. Except for late Cretaceous magmatic complexes (Sintra, Sines and Monchique [Van der Voo, 1969], and Lisbon Volcanics [Van der Voo & Zijderveld, 1971]), the Apparent Polar Wander Path (APWP) for Iberia is essentially based on sedimentary rocks, which are more sensitive to remagnetization effects and for which, in most cases, shallowing inclination corrections and field tests are lacking. Therefore, new reliable paleomagnetic poles, together with accurate radiometric ages, field tests, and evaluation of the magnetic mineralogy of samples are required to update and better constrain the Cretaceous Iberian APWP.

Here, we present a detailed paleomagnetic investigation of two large Cretaceous magmatic sills, the Paço de Ilhas and Foz da Fonte sills, in the Lusitanian Basin, which were dated by U-Pb and $^{40}Ar/^{39}Ar$ methods at ~ 88 and ~ 94 Ma, respectively [Grange et al., 2010; Mahmoudi, 1991; Miranda et al., 2009]. Detailed magnetic mineralogy analyses coupled to scanning microscopic observations suggest a primary (i.e., during cooling) origin for the characteristic magnetic remanence carried by these rocks. Our new, high quality paleomagnetic poles allow us to calibrate the APWP for Iberia during the late Cretaceous. We have compared these results to the recent global APWP of Torsvik et al. [2008], by rotating the new poles into African coordinates using late Cretaceous Euler poles that were deduced independently from seafloor marine magnetic anomalies for two plate pairs, Iberia-North America, and Africa-North America. The good agreement between our rotated poles and the global APWP can be considered a reliability test for the

paleomagnetic data, because the period under analysis is reasonably well constrained by identifiable seafloor magnetic chrons in the North and Central Atlantic. Implications for the kinematic evolution of Iberia during the Cretaceous are discussed.

3.2 Geological settings

The Paço d'Ilhas (PI; dated at 88 Ma) and Foz da Fonte (FF; dated at 94 Ma) sills were emplaced in the internal part of the Lusitanian Basin, the least extended domain of the West Iberia Margin that formed as a consequence of lithospheric rifting between Iberia and North America. According to various studies [e.g., Afilhado et al., 2008; Neves et al., 2009; Sibuet et al., 2007; Tucholke et al., 2007], the West Iberia Margin is a non-volcanic rifted continental margin that has been sub-divided into three zones that are characterized as (1) thinned continental crust (approximately 100 km wide), (2) a transitional zone (approximately 200 km wide), and (3) normal oceanic crust. From a structural and compositional point of view, Zone 1 displays the pinch-out of the lower crust and a series of upper crustal basement grabens and half-grabens filled with proximal and hemi-pelagic sediments resulting from significant vertical motion in the crust. Zone 2 was intruded during the early Cretaceous by late syn-rifting, and in the Late Cretaceous by post-rifting alkaline basalts. Zone 3 represents a highly stretched crust dominated by Mantle exhumation and serpentinization. The initial age of seafloor spreading is still debated. Sibuet et al. [2007] and Tucholke et al. [2007] favor two main rifting events: (1) widespread early rifting during Late Triassic and Early Jurassic times and (2) Late Jurassic through Early Cretaceous rifting and Continental Mantle exhumation localized in the transitional zone, and seafloor spreading starting sometime in the Aptian-Albian transition. However, Bronner et al. [2011] argue that alkaline volcanism in the transitional zone is syn-rifting and that the oceanic spreading is Late Cretaceous in age.

Studies of the Lusitanian and Algarve Basins have allowed the identification of the following three magmatic pulses: (1) Tholeiitic volcanism of earliest Jurassic age as the northernmost manifestation of the Central Atlantic Magmatic Province [Martins et al., 2008; Verati et al., 2007]; (2) A magmatic pulse of alkaline transitional composition occurs as scattered small-scale plugs and sills of Late Jurassic age [Grange et al., 2008; Martins, 1991]; (3) the Late Cretaceous alkaline magmatic event comprising the igneous intrusive complexes of Sintra (84-79 Ma) [Macintyre & Berger, 1982; Miranda et al., 2009; Storetvedt et al., 1987], Sines (75 Ma) [Miranda et al., 2009], Monchique (72 Ma) [Bernard-Griffiths et al., 1997; Miranda et al., 2009; Rock, 1982], and the Lisbon volcanic complex (73 Ma) [Ferreira & Macedo, 1979] (Fig. 3.1a). The PI and FF sills are two of several

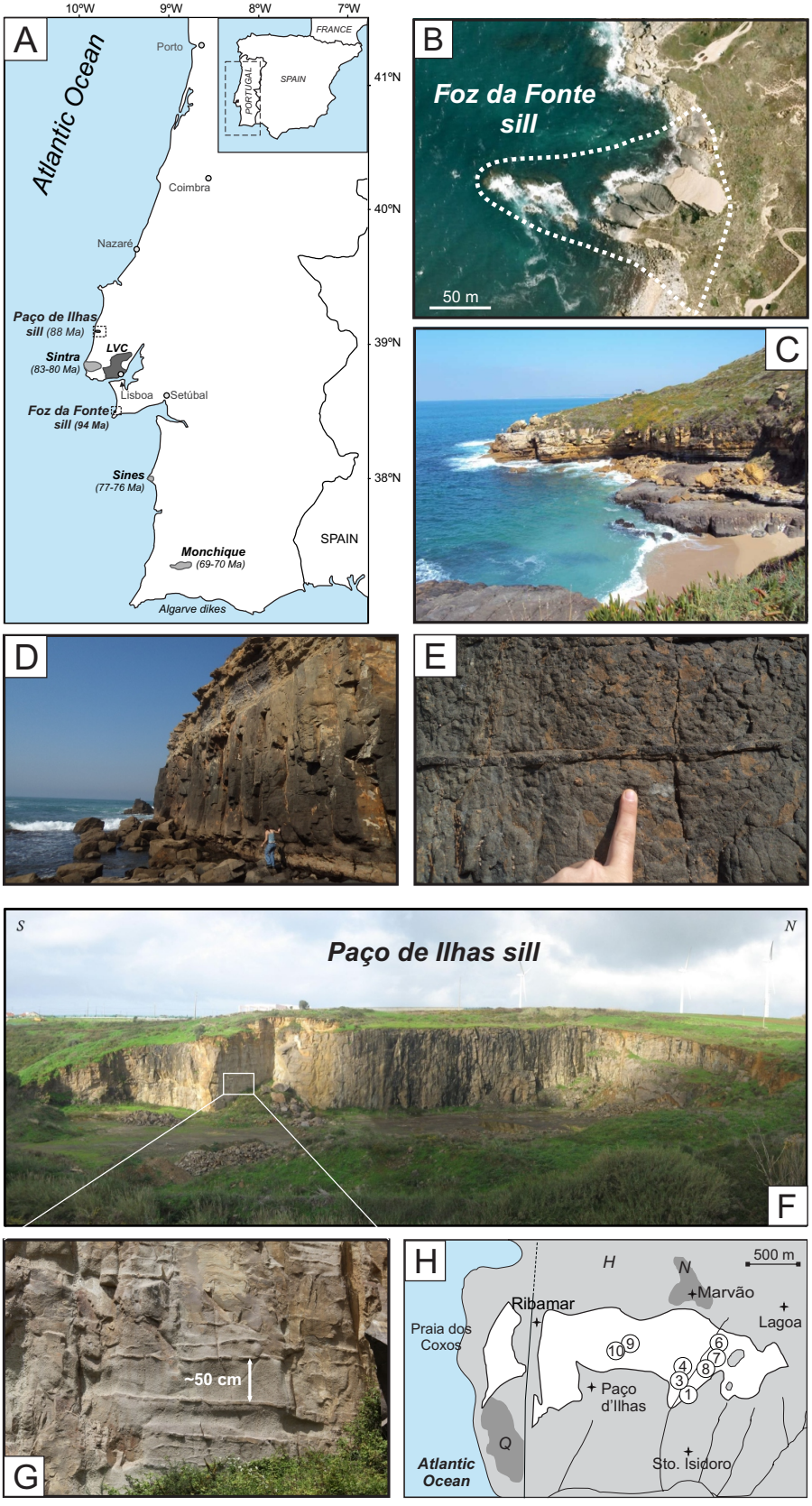
A
10ºW
9ºW
8ºW
7ºW
41ºN
40ºN
39ºN
38ºN
Atlantic Ocean
Porto
Coimbra
Nazaré
Lisboa
Setúbal
SPAIN
FRANCE
PORTUGAL
SPAIN
Paço de Ilhas sill (88 Ma)
Sintra (83-80 Ma)
LVC
Foz da Fonte sill (94 Ma)
Sines (77-76 Ma)
Monchique (69-70 Ma)
Algarve dikes
B
Foz da Fonte sill
50 m
C
D
E
S
N
Paço de Ilhas sill
F
G
~50 cm
H
H
N
500 m
Marvão
Ribamar
Lagoa
Praia dos Coxos
Paço d'Ilhas
Q
Atlantic Ocean
Sto. Isidoro

Figure 3.1

scattered sub-volcanic intrusions that belong to this third event [Miranda, 2010; Miranda et al., 2009], and were emplaced into Lower Cretaceous shallow marine sediments.

Revised radiometric ages were recently published for Late Cretaceous magmatism in the Lusitanian Basin and provide us with excellent candidates for new paleomagnetic investigations [Grange et al., 2010; Miranda, 2010; Miranda et al., 2009]. The Paço de Ilhas sill was dated at 88.0±2.7 Ma and 86.8±2.5 Ma, using K-Ar on biotite and K-feldspar respectively [Mahmoudi, 1991], and at 88.3±0.5 Ma based on U-Pb on zircon [Grange et al., 2010]. This sill is a kilometer-scale magmatic body that crops out near the town of Ribamar (Fig. 3.1f). It comprises monzogabbro and monzonite for which geochemical and petrographic features were extensively described by Miranda [2010]. The maximum thickness of the sill exceeds 20 m, although the contact with underlying sediments is not observable (Fig. 3.1d). The presence of syenitic sheets, that resulted from fractional crystallization, indicates several successive magmatic pulses (Fig. 3.1e) [Mahmoudi, 1991]. The PI sill intrudes upper Hauterivian (133-130 Ma) mixed sediments (carbonates and sandstone) [Dinis et al., 2008]. Because sills are intruded along the horizontal stratification plane of the host sediments, no tilt correction was done.

The Foz da Fonte sill was recently dated at 93.8±3.9 Ma using the $^{40}Ar/^{39}Ar$ method on amphibole [Miranda et al., 2009]. It is a massive 10 m thick dolerite, cropping out along Foz Beach, 4.5 km north of Cabo Espichel (Fig. 3.1b and 3.1c). It intrudes upper Albian (102-99.6 Ma) limestones and claystones [Dinis et al., 2008]. The geographic extension of the FF sill is difficult to evaluate in the field because it gently dips toward the NNW and is cut by a fault to the SSE (Fig. 3.1c). The structural surface (strike) of the sill is oriented N230° and gently dips ∼10° toward the north.

3.3 Sampling and methods

Samples were collected in the field with a gasoline-powered rock drill and oriented using a magnetic compass. In the PI sill, 80 oriented cylinders were collected at eight sites within an area of about 1 km (Fig. 3.1f). In the FF sill, 50 oriented cylinders were collected along

Figure 3.1: (a) Geological setting of the Paço de Ilhas (PI) and Foz da Fonte (FF) sills. Major Late Cretaceous magmatic events are also indicated. (b) Satellite photography (Google Earth) of the FF sill (white dashed lines show the emerged part of the sill). (c) Field photograph of the FF sill cropping out at Foz Beach (38°27′3.5″ / 9°12′5.5″). (d) Cross-section of the FF sill containing (e) magmatic joins. (f) PI sill (sites PI3 and PI4; 39°0′0″ / 9°24′3″). (g) Syenite levels indicating several magmatic injections. (h) Simplified geological map of the PI sill with location of the sampled sites (H indicates Hauterivian and Q Quaternary sediments).

the center and at the margin of the outcropping body. Geographical coordinates for the PI and FF sites are listed in Table 3.7. In the laboratory, samples were cut into standard paleomagnetic specimens, which then have been treated using thermal and alternating field (AF) demagnetization and measured with a JR6 spinner magnetometer. AF demagnetization results were processed with a LDA-3A demagnetizer (AGICO). Thermal treatments were performed within a prototype-shielded furnace. Characteristic Remanent Magnetizations (ChRM) were calculated by principal component analysis [Kirschvink, 1980] and Fisher statistics [Fisher, 1953] using the Remasoft software [Chadima & Hrouda, 2006].

Our understanding of the remanence carriers in the rocks is based on Isothermal Remanent Magnetization (IRM) analyses, triaxial IRM thermal demagnetization [Lowrie, 1990], temperature dependence of magnetic susceptibility, First Order Reversal Curve (FORC) measurements as well as petrographic and Scanning Electron Microscopic (SEM) observations coupled to Energy Dispersive Spectra analyses (SEM-EDS). IRM was induced at up to 1.2 T using an impulse magnetizer IM-10-30 (ASC Scientific) and data were subsequently treated by fit of cumulative log-Gaussian functions [Kruiver et al., 2001; Robertson & France, 1994]. IRM triaxial demagnetization [Lowrie, 1990] was performed after IRM acquisition at 1.4, 0.4 and 0.12 T fields along specimen z, y and x axis, respectively. Samples were then thermally demagnetized and remanence was measured at each step with a JR6 magnetometer. NRM:IRM data were developed after Fuller et al. [2002]. IRM was induced in a 100 mT peak field and subsequently demagnetized at the same steps as used during demagnetization of the natural remanent magnetization (NRM). Thermomagnetic susceptibility was measured at low and high temperature in an Ar atmosphere using a CS-L cryostat apparatus and a CS4 furnace in a MFK1 Kappabridge (AGICO). Hysteresis and FORC measurements were performed at room temperature on selected samples with the Micro Vibrating Sample Magnetometer at the Institute of Geophysic, UNAM, Mexico, and treated with the FORCinel software package [Harrison & Feinberg, 2008]. Microscopic observations in reflected light were performed on polished thin sections prepared from specimens cut from the cylinder cores. We used a Leitz orthoplan microscope located in the Laboratory of Géosciences, Montpellier (France), that allows maximum magnification under oil-immersion of 1250×. SEM observations and EDS analyses were performed on carbon-coated rock fragments using a Hitachi S-3700N coupled to an EDS Bruker XFlash® 5010 in the Hercules Laboratory, Évora (Portugal), and a Jeol JSM-6360LV coupled to a Noran EDS analyzer from in GET Laboratory, Toulouse (France).

3.4 Results

3.4.1 Paço de Ilhas (PI)

PI Paleomagnetism

A total of 280 specimens were analyzed, 208 of these were AF and 67 were thermally demagnetized. Of the samples treated, 275 yielded stable demagnetization patterns at high fields and high temperatures (Table 3.5). Zijderveld diagrams show two magnetic components with a viscous magnetic overprint that was removed below 4-6 mT or 100°C. What emerged was a stable RM component that trends to the origin (Fig. 3.2). After stepwise AF demagnetization until 30 mT, more than 90% of the NRM was removed, indicating that a low coercive phase is the principal magnetic carrier (Fig. 3.2). Unblocking temperatures vary from 150° to 500°C suggesting that this low coercive phase corresponds to titanomagnetite. The result is a positive (normal) and north directed RM with mean inclinations of 40-50°. A mean paleomagnetic pole was calculated using individual Virtual Geomagnetic Poles (VGPs) for each specimen (Fig. 3.2; Table 3.5). We chose this option because in the case of such a large intrusive layered-gabbroic complex (>3 km in length and more than 25 m in thickness), it is not possible to accurately identify different magmatic injection phases. No cut-off was applied to calculate the mean pole, because in that case we would be already assuming that the directional scatter reflects the PSV.

The result of these analyses yields a mean ChRM of D = 350.0° ; I = 42.2° (N = 275; α_{95} = 1.4° ; k = 39.6), a mean paleomagnetic pole located at Long = 204.6° ; Lat = 73.4° (A95 = 1.3° ; K = 42.7), and a paleolatitude of 24.5° (Fig. 3.2 and Table 3.1) for this data set. We attempted to apply a baked contact test to the host sediments (Hauterivian) that surround the PI sill, but results were inconclusive due to the limited thickness of the sediments (<2 m; Fig. 3.1d), which do not show typical hybrid and unbaked zones. Moreover, the high porosity of the Hauterivian sandstones may have facilitated fluid circulation and thermo-chemical magnetic overprinting during the emplacement of the sill.

PI Rock Magnetism

In order to study the composition and origin of the magnetic carriers and the nature of the remanent magnetization recorded in PI rocks, we measured coercivity and grain-size dependent magnetic properties of characteristic samples. Specifically, Isothermal Remanent Magnetization (IRM) acquisition curves were obtained at fields up to 1.2 T for eight samples (Fig. 3.3a). All samples reached saturation below 100 mT indicating a low

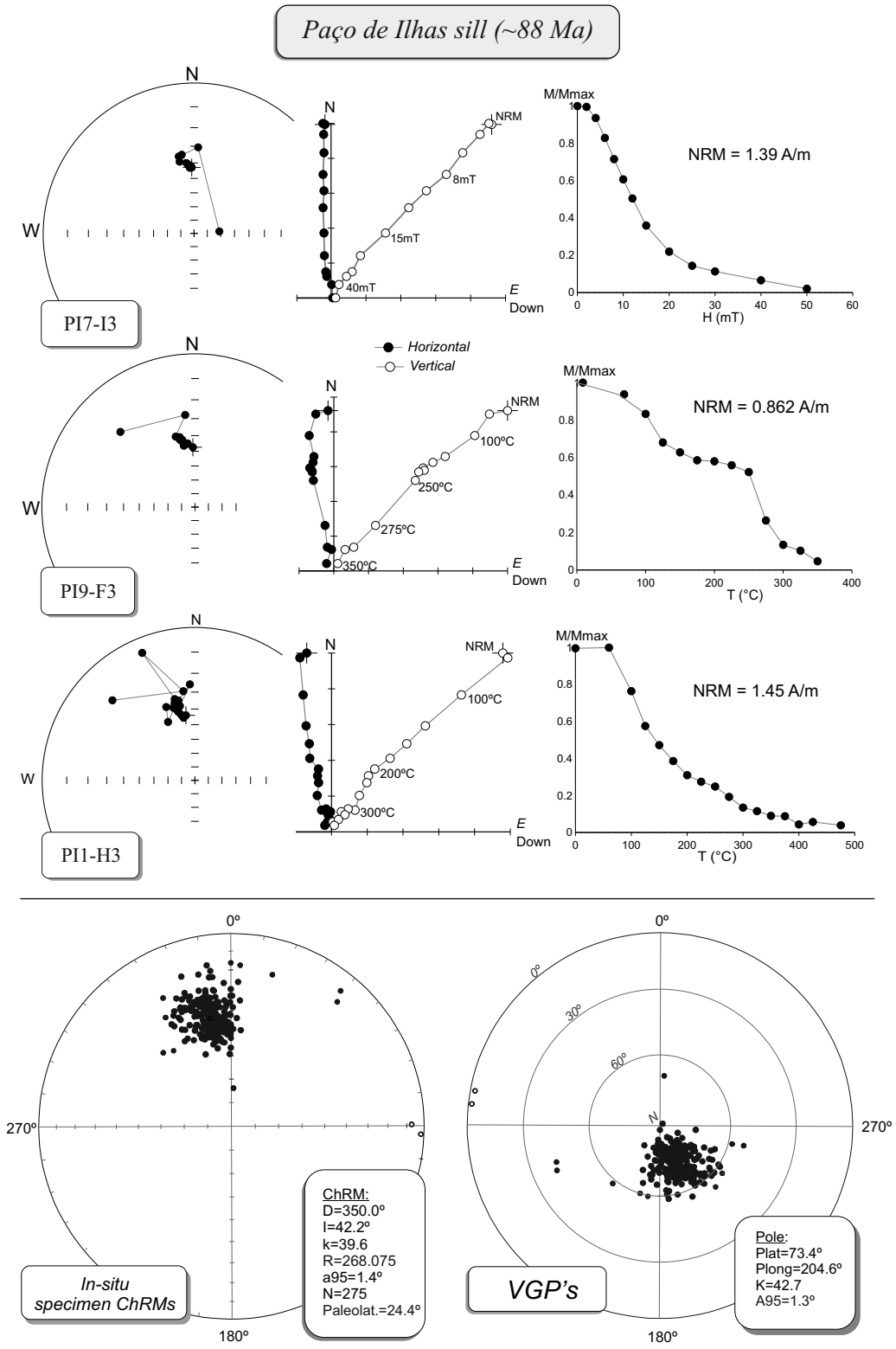

Figure 3.2: (top) Paleomagnetic results from the PI sill. Stereographic and orthogonal projections and remanence intensity versus AF demagnetizing field or demagnetizing temperature diagrams. (bottom) Characteristic Remanent Magnetization (ChRM) and corresponding Virtual Geomagnetic Poles (VGP's).

coercive phase as the dominant magnetic ferromagnetic mineral present in these samples. IRM data were analyzed assuming a cumulative log-Gauss function of the magnetizing field (CLG analysis) [Robertson & France, 1994], and then evaluated using the software developed by Kruiver et al. [2001] (Fig. 3.3a). This method has been recently challenged by Heslop et al. [2004], who demonstrated that the influence of the starting state of the magnetic system, magnetic interaction and thermal relaxation can produce IRM curves that fail the log normal assumption [Robertson & France, 1994], and therefore can lead to misleading interpretations. However, these effects are minimized when using an AF demagnetized state and for materials that contain well-separated coercivity distributions. We thus acquired IRM curves from AF demagnetized (100 mT) samples. In all cases, the curves showed a unimodal distribution of coercivity spectra (i.e., a single Gaussian curve), with saturation IRM (SIRM) values between 520 and 830 Am^{-1}, $B_{1/2}$ (the inducing field at which half of the SIRM is reached) between 30 and 45 mT, and dispersion parameter (DP, corresponding to one standard deviation of the logarithmic distribution) at $\sim$0.2 mT. SIRM and $B_{1/2}$ values are in the typically low- to medium-coercive range for minerals such as magnetite [Font et al., 2009, 2010; Gong et al., 2008a; Kruiver et al., 2001, 2003]. DP values are similar (0.20-0.25 mT) or all samples suggesting that magnetite grains in these samples have a homogenous grain-size distribution (Fig. 3.3c).

We compared the magnitude and demagnetization patterns of the NRM and SIRM [Fuller et al., 1988, 2002]. In rocks carrying a Thermal Remanent Magnetization (TRM) the NRM:IRM ratio is about 10^{-2}, whereas smaller values generally imply a secondary magnetization. All samples exhibit roughly straight-line behavior between 10^{-2} and 10^{-3}, indicating a primary TRM origin for the magnetization (Fig. 3.4a). The absence of typical concave-upward curves observed in remagnetized rocks, generally reflecting bimodal associations of soft and hard (secondary) fractions, further supports a primary TRM origin.

Thermomagnetic analyses at high (HT) and low (LT) temperatures under Argon-controlled and ambient atmosphere, respectively, were done on four samples from which two representative examples are illustrated in Fig. 3.5a. No major transitions are observed during LT analyses, while heating exhibited unblocking temperatures between 500 and 560°C (Fig. 3.5a), typical of titanomagnetite. In some samples (i.e., PI1_K; Fig. 3.5a), a typical Hopkinson peak near the Curie temperature indicates admixture of fine (SD to PSD) magnetic particles [Dunlop & Ozdemir, 1997]. During cooling below 700°C, HT curves are irreversible, indicating that authigenic magnetic minerals (probably magnetite) were created during the heating process. Consequently, AF demagnetization is more suitable than thermal demagnetization for these rocks.

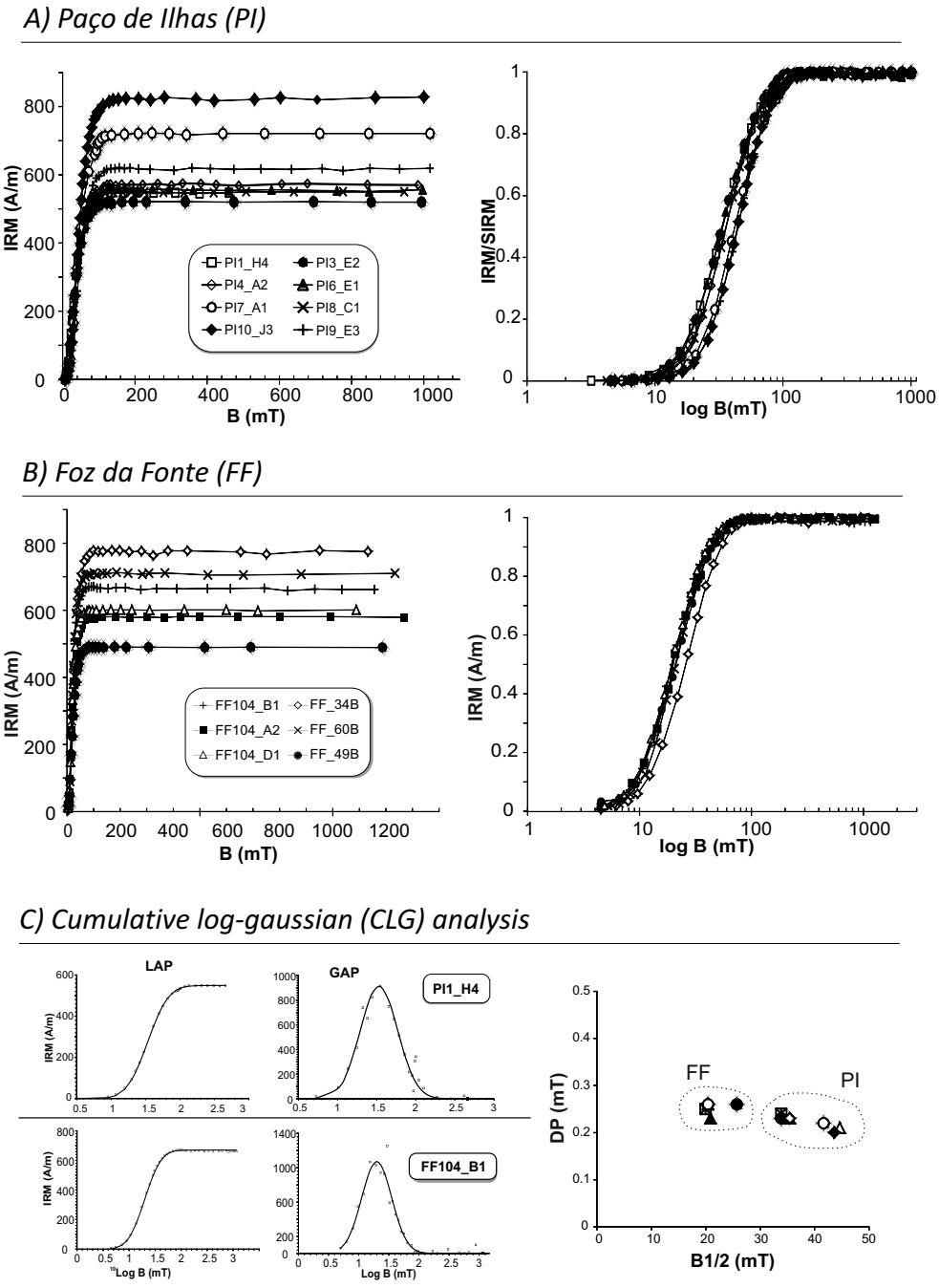

Figure 3.3: Isothermal Remanent Magnetization (IRM) acquisition of (a) PI and (b) FF samples. Normalized (IRM/SIRM) data are represented in horizontal logarithmic scale to enhance differences in the coercivity spectra. (c) Examples of IRM data treated by cumulative log-Gaussian analysis [Kruiver et al., 2001; Robertson & France, 1994]. LAP: Linear Acquisition Plot; GAP: Gradient Acquisition Plot, respectively; $B_{1/2}$: induced field corresponding to half SIRM.

Thermal demagnetization of tri-axial orthogonal IRM [Lowrie, 1990] was performed for eight representative samples and showed predominance of the softer magnetic fraction, whereas medium to hard fractions were weak (Fig. 3.5b). In the soft fraction, more than 90% of the imparted remanence is demagnetized during heating to 200°C, after which the RM decreases progressively until 520°C. Together with IRM and thermomagnetic analyses, these results indicate that titanomagnetite, with variable Ti-content, is the principal magnetic carrier in these rocks. FORC and analyses of hysteresis parameters were conducted for five samples. FORC diagrams show a clear contribution of two populations: a SD-like population with closed inner contours, and a second MD-like population with diverging outer contours (Fig. 3.6, top). Once titanomagnetite was identified as the main magnetic carrier, hysteresis ratios Mrs/Ms versus Hcr/Hc were plotted using a modified Day plot like those used by Dunlop [2002a]. Fig. 3.6 (bottom) illustrates the theoretical SD+MD mixing curves for grains of magnetite (TM0 and TM60) [Dunlop, 2002a] and experimental data from intrusive rocks (gabbro and dolerite) [Dunlop, 2002b]. The hysteresis ratios of PI samples are similar to those of gabbros that carry a primary magnetization.

PI SEM and optical microscopic analyses

The nature and origin of the ferromagnetic minerals in the PI sill were investigated on four samples using an SEM and these data are illustrated in Fig. 3.7. Chemical composition was obtained by EDS analysis. In all samples, iron oxides are ubiquitous and easily identified by the characteristic iron peaks at 6.40 and 7.06 keV (Fig. 3.7a). Crystals exhibited well preserved and euhedral shapes, with grain-sizes varying from 50 to 100 μm (Fig. 3.7b and 3.7c). Spinel-like and cubic morphologies, together with Ti in EDS spectra indicate that titanomagnetite as the principal magnetic carrier. Titanomagnetite grains occasionally show exsolved ilmenite lamellae, indicative of deuteric high temperature oxidation (i.e., during cooling). Dissociation between Ti and Fe is well illustrated by SEM Mapping (Fig. 3.7d).

Thin section analyses by optical ore microscopy have confirmed the presence of such simple two-phase assemblages, corresponding to oxidation stage C3-C4 of Haggerty [1991] (Fig. 3.7e). However, most of the ilmenite lamellae show an advanced stage of high temperature oxidation similar to the one described by Hoffman et al. [2008]. Moreover, the large euhedral ilmenite crystals present also show the same stage of oxidation (Fig. 3.7f). As interpreted by Hoffman et al. [2008], we also believe that these altered ilmenites host a SD population of titanohematite that disassociates above 500°C when heated in the KT experiment, producing an almost pure fine-grained magnetite. However, this interpreta-

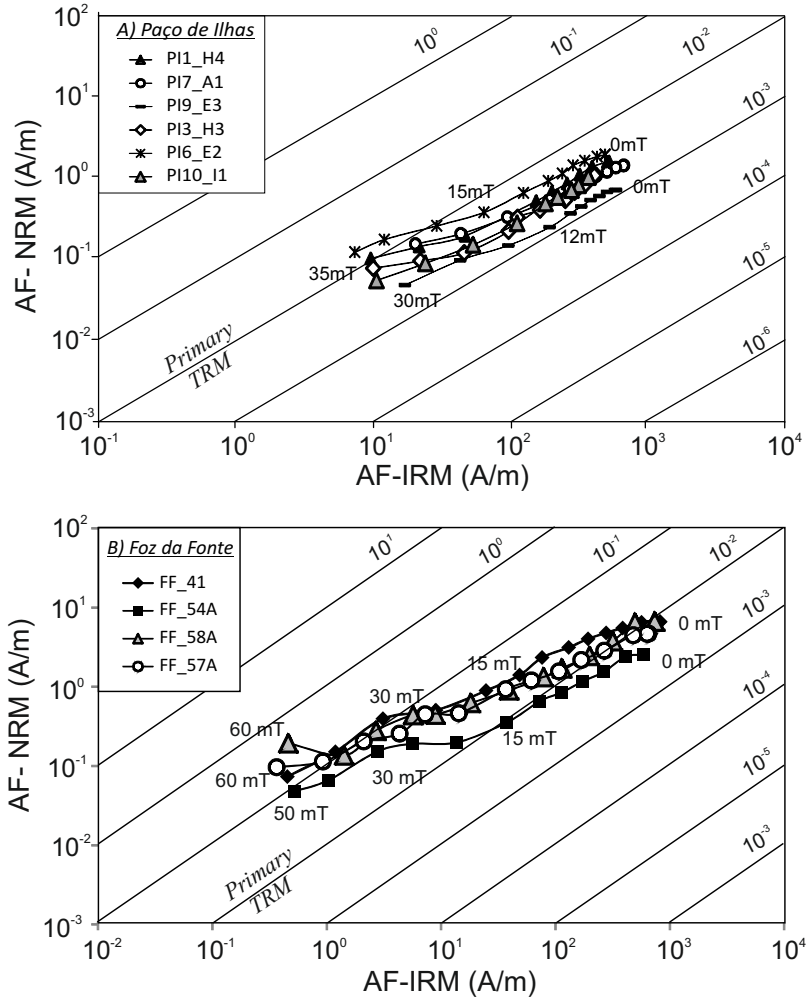

Figure 3.4: AF-IRM versus AF-NRM diagram [Fuller et al., 2002] from (a) PI and (b) FF samples. All samples show linear demagnetization patterns and AF-NRM:AF-IRM ratios near typical values for unremagnetized igneous rocks ($\sim 10^{-2}$).

tion is not fully supported by the FORC diagrams (Fig. 3.6, top); the peak of the FORC distribution occurs at a coercivity that seems too low (around 20 mT) for SD titanohematite. At present, we do not have a clear explanation to account for this discrepancy. To summarize, microscopic observations point to a well-preserved primary magnetic mineralogy, contemporaneous with the cooling time of the sill. This corroborates the magnetic analyses indicating a primary origin for the remanent magnetization exhibited by these rocks.

		Mean ChRM					Paleomagnetic Pole				
	N	Dec (°)	Inc (°)	k	R	α_{95} (°)	Pole Longitude (°)	Pole Latitude (°)	A95 (°)	K	Paleolatitude (°)
Paço d'Ilhas (PI)	275	350.0	42.2	39.69	268.075	1.4	204.6	73.4	1.3	42.7	24.4
Foz da Fonte (FF)											
In situ	73	352.0	53.0	30.3	70.623	3.1	226.9	82.8	3.7	20.8	33.6
Tilt corrected	73	346.5	44.3	30.3	70.623	3.1	217.1	73.8	3.3	26.0	26.0

In the case of the FF sill, results before and after tilt correction are indicated. Dec: declination; Inc: inclination; k: precision parameter of ChRM; R: intensity of resultant vector; PLong: pole longitude; PLat: pole latitude; K: precision parameter of paleopole; PaleoLat: paleolatitude. See text for details.

Table 3.1: Paleomagnetic results for PI and FF sills: mean characteristic remanent magnetizations (ChRM) and corresponding paleomagnetic poles.

3.4.2 Foz da Fonte (FF)

FF Paleomagnetism

A total of 86 specimens were demagnetized using AF (72) and thermal (14) treatment. Of these, 73 samples yield stable demagnetization patterns at high fields and/or high temperatures (Table 3.6). Zijderveld diagrams show two magnetic components with a viscous magnetic overprint removed below 4-6 mT and 150°C, and a high-field/temperature remanence projected to the origin (Fig. 3.8). After stepwise AF demagnetization to 15-3 0mT, more than 90% of the NRM was removed, indicating low coercive minerals as the principal magnetic carriers (Fig. 3.8). Unblocking temperatures around 550°C suggest that this low coercive phase corresponds to titanomagnetite with a low Ti-content (Fig. 3.8). *In situ* magnetic orientations are positive (normal) and north directed, with mean inclinations of 45-55°.

A structural orientation for this unit of 230° /10° (strike/dip) was measured for field exposures and this was used as a tilt correction to correct the specimen-based mean ChRM (Fig. 3.8). As was the case for PI samples, we calculated the mean ChRM and individual VGP using specimen-based mean directions. The coordinates of the mean ChRM are D = 346.5° ; I = 44.3° (N = 73, α95 = 3.1° ; k = 30.3). The mean paleomagnetic pole calculated from all VGPs is located at Long = 217.1° ; Lat = 73.8° (A95 = 3.3° ; K = 26.0). Paleolatitude is 26.0° (Fig. 3.8 and Table 3.1). We attempted to apply a baked contact test to the host sediments above FF sill. However, results were inconclusive because the age determined for these sediments is too close to the age of the sill.

FF Rock Magnetism

IRM acquisition curves obtained from six samples are s-shaped, typical of SD-PSD grain sizes, and show a single, low-coercive phase with 90% of saturation reached at 100 mT (Fig. 3.3b). All curves fit into a unimodal distribution of coercivity spectra, with SIRM

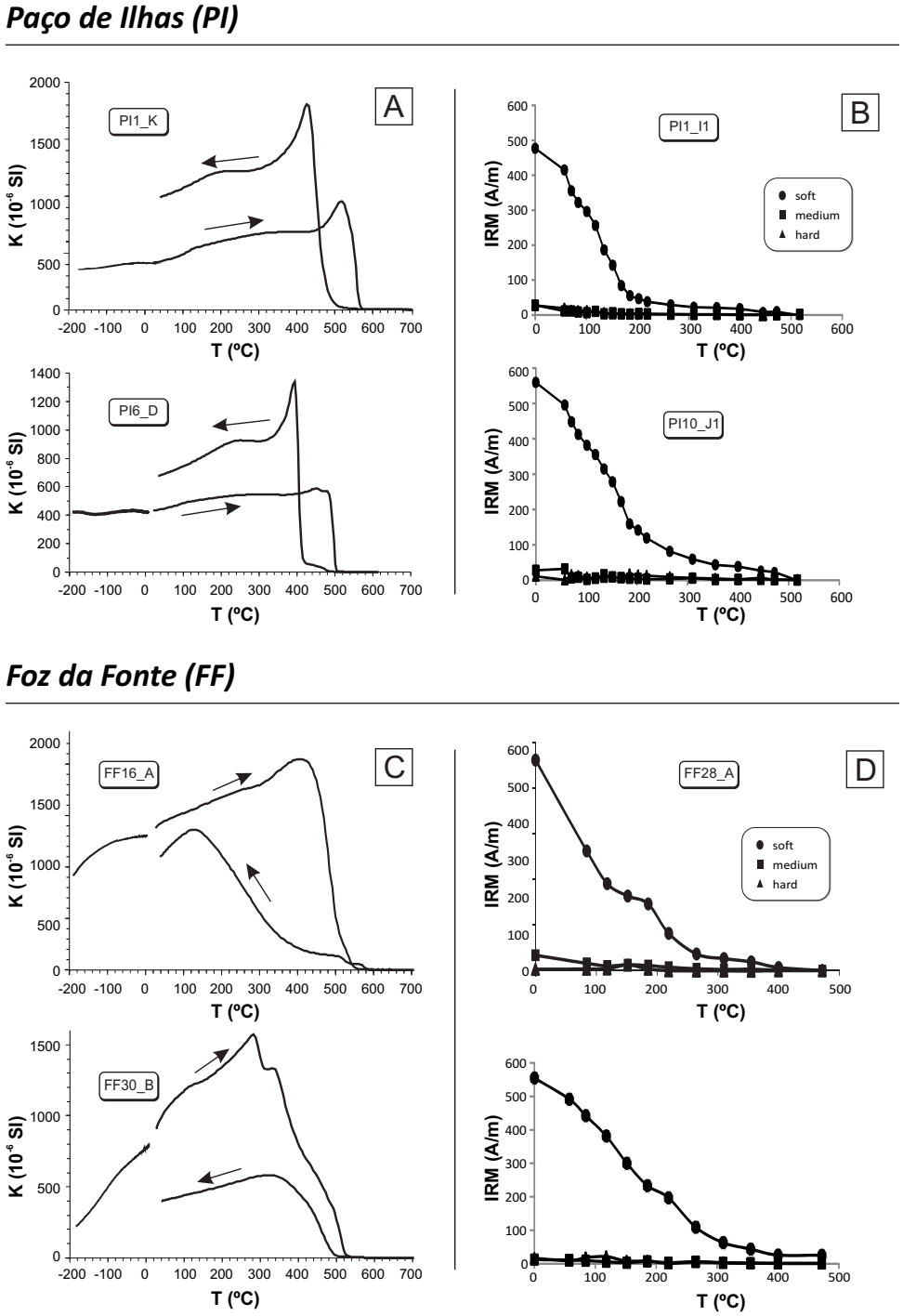

Figure 3.5: (a) Thermomagnetic susceptibility curves at low and high temperatures in an Argon controlled atmosphere for PI samples. (b) Thermal demagnetization of triaxial orthogonal IRM's [Lowrie, 1990] for PI samples. (c) Thermomagnetic curves in Ar-controlled atmosphere for FF samples. (d) Thermal demag-netization of triaxial orthogonal IRM's [Lowrie, 1990] for FF samples.

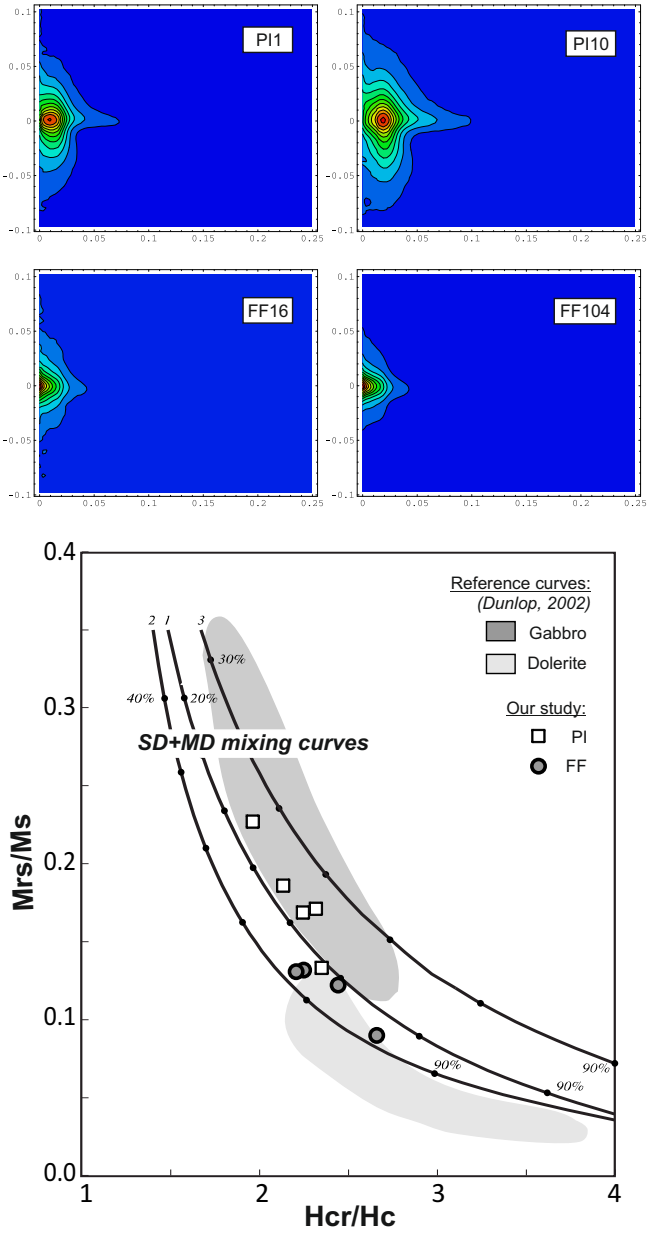

Figure 3.6: (top) FORC diagrams for PI and FF samples. (bottom) Modified Day plot showing hysteresis data from PI and FF samples compared to referenced data of gabbro and dolerite from Dunlop [2002b].

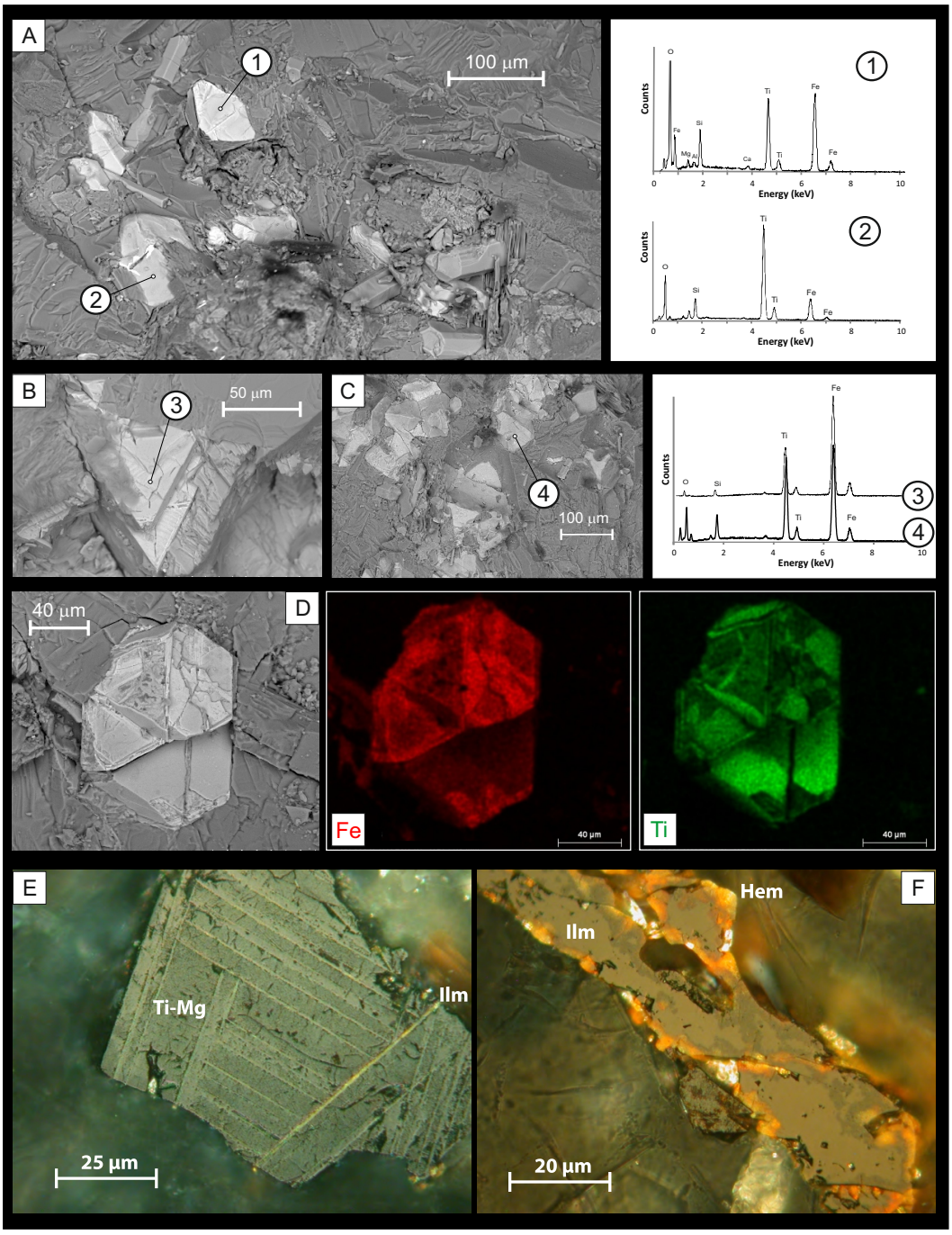

Figure 3.7: (a–d) Scanning Electron Microscopy (SEM) images coupled to Energy Dispersive Spectra (EDS) analyses of PI samples. Ti-Fe oxides are ubiquitous in the form of well-preserved crystals with spinel-like and cubic morphologies (see text for details). (e–f) Reflected light photo micrographs of sample PI1-A2 (Fig. 3.7e): Oil immersion, crossed nicols. Titanomagnetite with exsolved thin ilmenite lamellae (oxidation stages C3-C4). The ilmenite lamellae appear to be inhomogeneous with internal granulation and sample PI6-F1 (Fig. 3.7f): Oil immersion, crossed nicols. Subhedral ilmenite grain partially oxidized. The red internal reflections are characteristic of hematite.

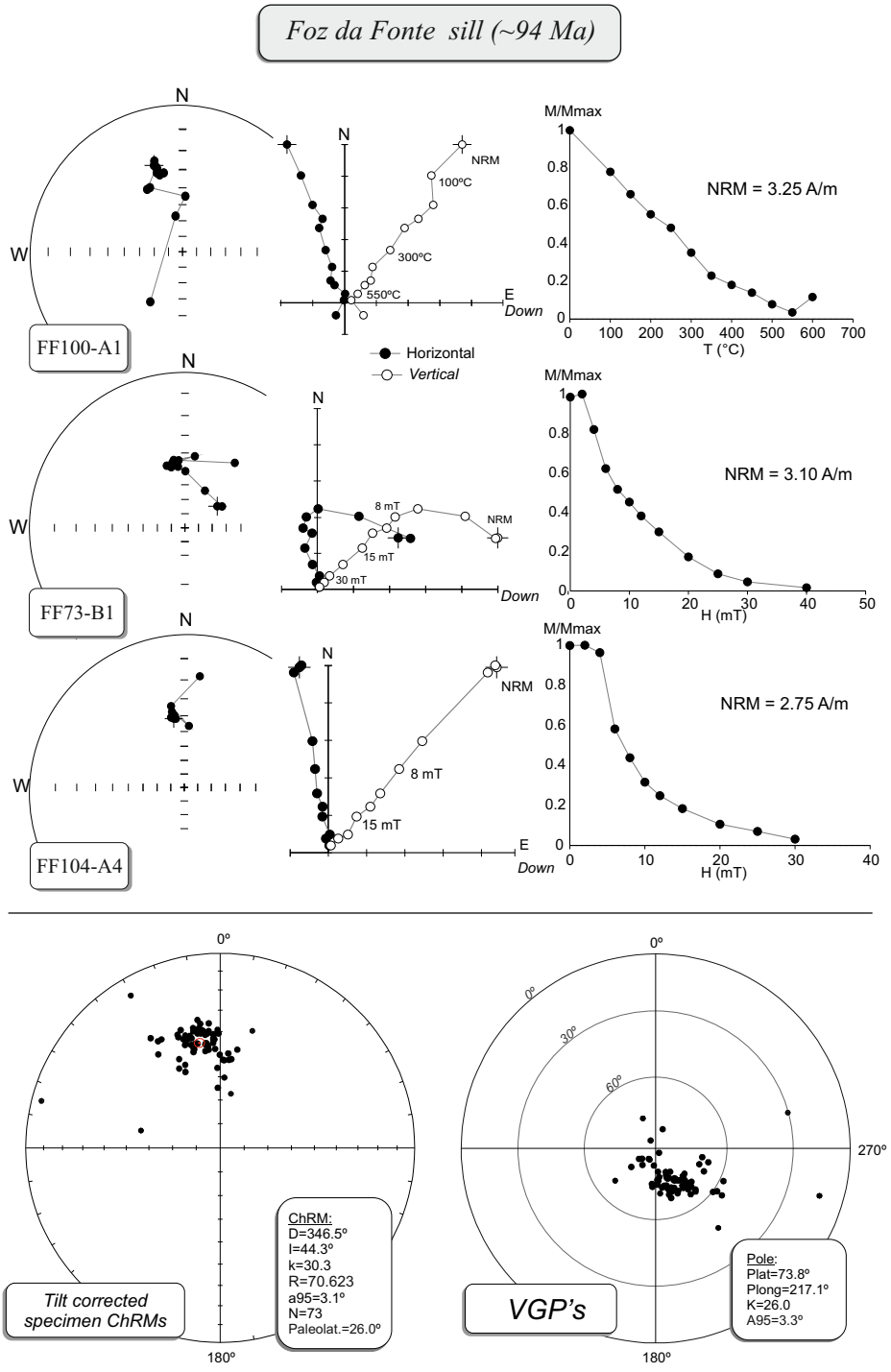

Figure 3.8: (top) Paleomagnetic results from FF sill. Stereographic and orthogonal projections and remanence intensity versus AF demagnetizing field or demagnetizing temperature diagrams. (bottom) ChRM after tilt correction (D = 230, I = 10°) and corresponding VGP's.

values between 400 and 800 Am^{-1}, $B_{1/2}$ between 20 and 30 mT, and DP around 0.2 to 0.3 mT. These results are indicative of a single low- to medium-coercive phase, with uniform grain-size distribution. The similarity to results obtained for PI samples indicates a similar magnetic mineralogy for both sills (Fig. 3.3). Once plotted on a Fuller et al. [2002] diagram, NRM-IRM ratios lie between the 10^{-1} and 10^{-2} thresholds, characteristic of rocks carrying a primary TRM origin for the remanence (Fig. 3.4b). The roughly linear shape of the curves indicates that no magnetically hard material is present.

No major transitions are observed at LT, while during HT analysis, unblocking temperatures fall between 520 and 560°C (Fig. 3.5c). Sample FF_16A exhibits Curie temperatures at 500-550°C and a Hopkinson peak that indicates mixture of fine magnetic particles (SD to PSD) [Dunlop & Ozdemir, 1997]. Sample FF_30B shows a more complex mineralogy, with Curie temperatures at ∼300°-400° and 520°C (Fig. 3.5c). These results indicate the presence of SD to MD titanomagnetite with different Ti-content. During cooling below 700°C, curves are irreversible indicating that authigenic magnetic minerals (probably magnetite) were generated during the heating process.

After thermal demagnetization of tri-axial orthogonal IRM, all samples show predominance of the softer magnetic fraction, whereas medium to hard fractions are undetectable (Fig. 3.5d). In the soft fraction, more than 90% of the induced remanence is demagnetized by ∼300°C. In sample FF_28A, three phases of T_B ∼120°C, ∼250°C and ∼400°C are identified. For sample FF_14B, only a T_B ∼300°C is clearly identified. As was the case for PI, these results confirm that titanomagnetite, with variable Ti-content is the principal magnetic carrier.

The magnetic domain state was checked using FORC measurements, which produced characteristic MD contours, all diverging from the origin (Fig. 3.6, top). Fig. 3.6 (bottom) shows that hysteresis ratios for FF samples lie close to the region expected for unremagnetized dolerites [Dunlop, 2002b], although, our data better fit the theoretical mixing curves and show a tendency toward a finer grain size than shown by Dunlop [2002a].

FF SEM and optical microscopic analyses

SEM photographs show the presence of numerous iron oxides identified by the association of O, Ti and Fe elements in the EDS spectra (Fig. 3.9a-e). Spinel-like and cubic morphologies, as well as the systematic association of Ti in EDS, indicate titanomagnetite as the principal magnetic carrier. These crystals exhibit well preserved euhedral shapes, with grain-sizes lying between 20 and 100 μm (Fig. 3.9a-e).

Thin section analyses by optical ore microscopy have confirmed the presence of subhedral grains of titanomagnetite, with oxy-exsolved ilmenite lamellae corresponding to

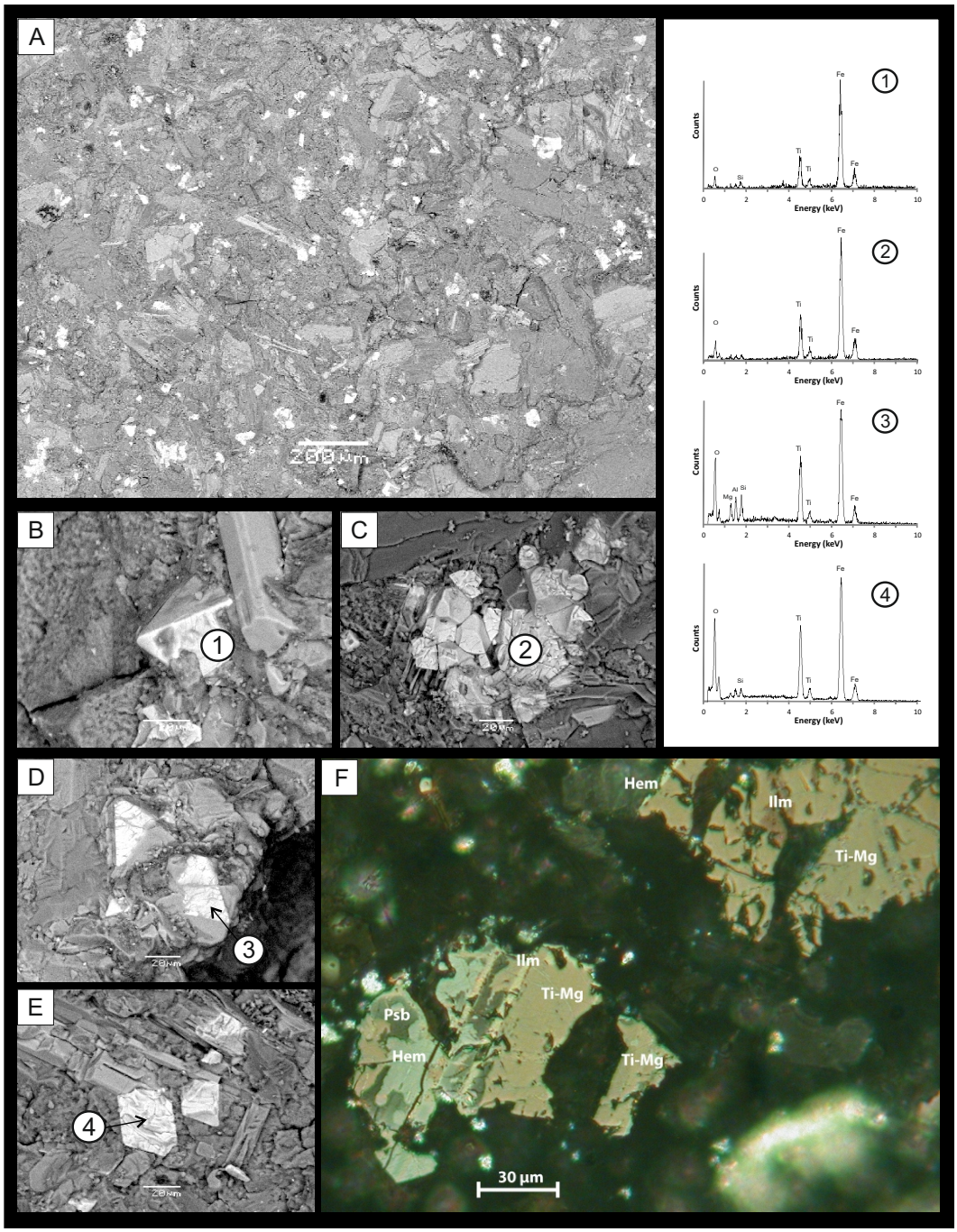

Figure 3.9: (a–e) SEM images coupled to EDS analyses of FF samples. Ti-Fe oxides are ubiquitous, in the form of well-preserved crystals with spinel-like and cubic morphologies (see text for details). (f) Reflected light photomicrograph (oil immersion) of a polished thin section from sample FF16-A2 showing different stages of high temperature oxidation. On the upper right part of the photo, a large homogeneous grain of Ti-magnetite with an anhedral ilmenite inclusion. On the lower left part of the photo, a single crystal showing, to the right, ilmenite intergrowths in titanomagnetite (oxidation stage C4) and to the left, areas of exsolved pseudobrookite, titanohematite and residual ilmenite (oxidation stage C6).

oxidation stage C3 of Haggerty [1991]. Our work also yielded evidence for more advanced stages of oxidation (C6), as illustrated in Fig. 3.9f. In contrast to PI samples, in FF samples ilmenite lamellae and crystals are well preserved. We also noted the sparsity of iron sulfides (three to four grains at thin section scale). Although not identifiable without further analyses, these are certainly non-magnetic as suggested by the results obtained in the Lowrie test. In addition, small veins of Ti-maghemite grains are present along the cracks of very few grains of Ti-magnetite, and may account for the irreversibility in the KT curves.

In summary, microscopic observations indicate that the FF sill preserves a primary magnetic mineralogy. This was acquired during cooling and supports a primary origin for the remanent magnetization.

3.5 Discussion

3.5.1 New paleomagnetic poles for Iberia at 88 and 94 Ma

The present paleomagnetic and rock magnetic study of the PI and FF sills provides two new important Cretaceous paleomagnetic poles for the Iberian Plate, at 88 Ma and 94 Ma, respectively. Stable demagnetization patterns, the presence of titanomagnetite as principal magnetic carriers, as well as absence of secondary oxides, indicate a primary (i.e., during cooling) origin for the isolated remanence. The corresponding paleopoles are classified by a Q factor [Van der Voo, 1990] of 5. However, as the ages of the PI and FF sills fall within the quiet zone of the CNPS, we have replaced the normally used reversal criteria with our very detailed magnetic mineralogical study, thus yielding a Q value of 6 for both poles.

Because thin magmatic bodies, particularly extrusive rocks such as basalts, have relatively short cooling times when compared to secular variation cycles ($\sim$10 kyr [Merrill & McFadden, 2003]), they can record a snapshot of the geomagnetic field. Therefore, we have attempted to evaluate the contribution of the PI and FF sills to the paleosecular variation during the CNPS. The most common and traditional method to study the PSV of the geomagnetic field is based on the analysis of the dispersion of VGPs determined from volcanic sites for a given latitude and age [Cox, 1970; Irving & Ward, 1964]. During the last 40 years, many PSV models have been proposed, among which the Model G [McFadden et al., 1988] and the TK03.GAD models [Tauxe & Kent, 2004] are the most recent and widely used (see Deenen et al. [2011] for a review). However, Linder & Gilder [2012] recently showed that the traditionally assumed latitudinal dependence of the VGP

dispersion parameters (i.e., S(λ) parameter) is a mathematical artifact resulting from the conversion from directions to poles. These new findings strongly question the validity of the methods used until now to estimate the PSV. An alternative method would be to use here directional distributions instead of VGP distributions. However, because most of PSV models are based on VGP distribution and not on directional distribution, there is no available database to use for comparison. In conclusion, the contribution of PSV in our data is difficult to evaluate but several hypothesis can be proposed. The first one is to consider that, despite their large and complex structure, the dense cluster of magnetic directions of the PI and FF sills indicate a record of a snapshot of the geomagnetic field. However, the fact that both corresponding poles well fit the global APWP at around 80 Ma and 100 Ma (Fig. 3.10) rather argue against such hypothesis. The second scenario is to consider that PSV was averaged out within individual samples. Actually, the PI sill corresponds to a large and thick intrusive layered-gabbroic complex with porphyritic textures, different lithology and presence of magmatic joins and syenites (Fig. 3.1) [Mahmoudi, 1991; Miranda, 2010]. This rather suggests a much longer cooling time than in the case of lava flows for example. Therefore we suggest that the dense clustering of magnetic directions could be partially or totally justified by the fact that each paleomagnetic sample has minimized PSV through a sufficiently long cooling time. This is plausible when variable Ti-content in titanomagnetite (i.e., variable unblocking temperatures and consequently lock-in time magnetization) and grain size (SD to MD) are observed in the rocks, as observed in the PI and FF sill. Moreover, this effect can also be amplified by the fact that PSV was lower during the quiet zone of the Cretaceous than for the last 5 Myr [Biggin et al., 2008]. These results may suggest that intrusive gabbroic rocks are excellent candidates to obtain reliable paleomagnetic pole in which the PSV has been minimized.

3.5.2 APWP of Iberia during the Mesozoic

Since the end of the 1950s, the motion of the Iberian Plate relative to Europe and Africa was extensively investi-gated, but is still a matter of debate. Carey [1958] was the first to propose, on the basis of geological data, a counterclockwise rotation of 30° to 40° linked to the opening of the Bay of Biscay during the Cretaceous. Bullard et al. [1965] further confirmed Carey's [1958] hypothesis from numerical paleogeographic modeling. Using analyses of seafloor magnetic anomalies from the Bay of Biscay, Scotese et al. [1988] suggested a counterclockwise rotation of 30° between 92 and 84 Ma, and 5° between 84 and 66 Ma, whereas Srivastava et al. [1990a] argued for a linear counterclockwise rotation of 30° between 125 and 83 Ma. However, in the broad transitional zone at magma-poor rifted margins, the seafloor-spreading origin of magnetic anomalies is still a matter of

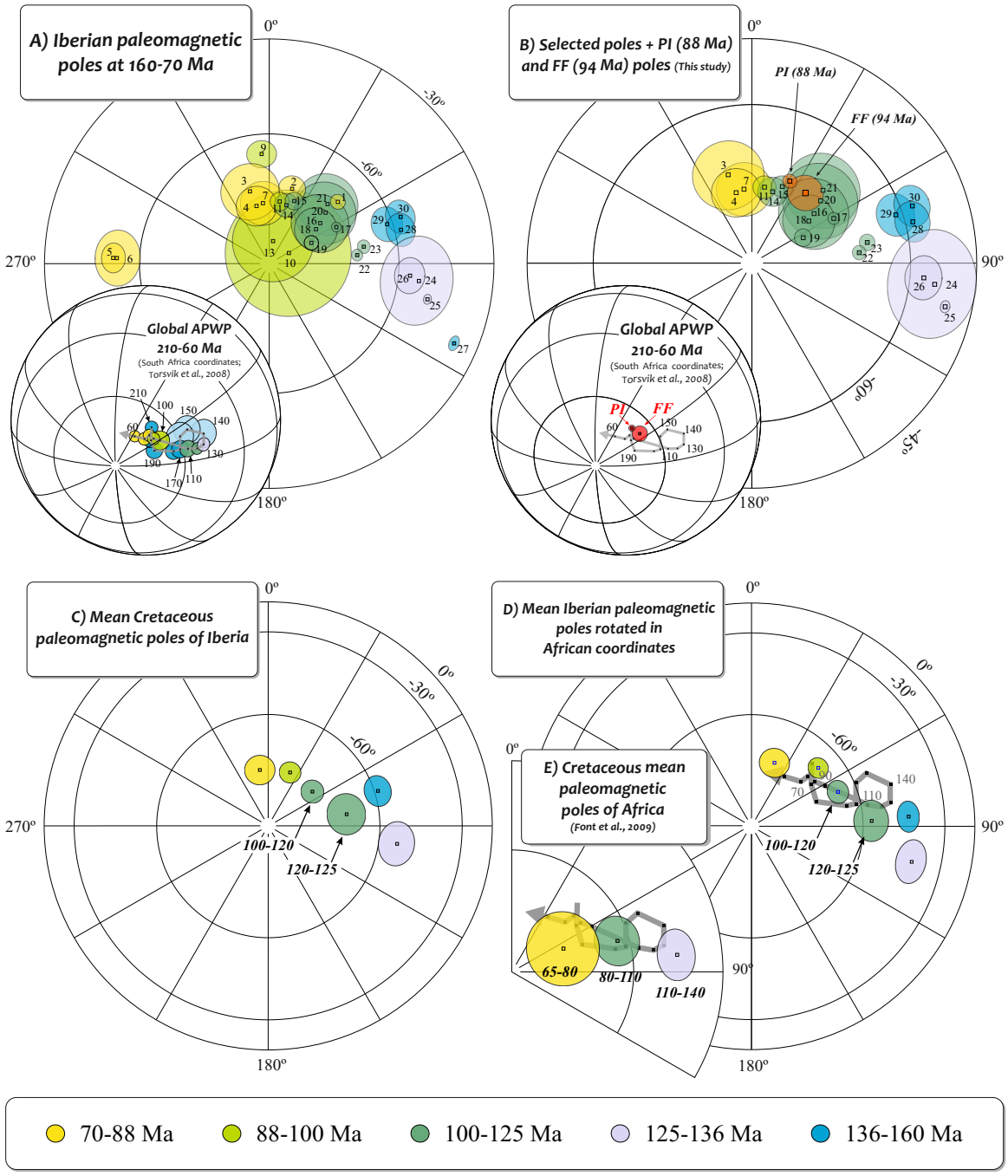

Figure 3.10: (a) Cretaceous paleomagnetic poles for Iberia (Table 3.1). (b) Selected paleomagnetic database and PI and FF (this study) poles (their position in African coordinates on the global APWP from Torsvik et al. [2008] is also shown). (c) Mean Cretaceous paleomagnetic poles for Iberia calculated from our paleomagnetic database (Table 3.1). (d) Mean Cretaceous paleomagnetic poles rotated into African coordinates compared to the global APWP. (e) Comparison with mean Cretaceous poles from Africa (compilation from Font et al. [2009]). All representations are in the southern hemisphere.

debate [Bronner et al., 2011; Sibuet et al., 2007; Tucholke et al., 2007]. Moreover, due to the presence of the CNPS, kinematic models based on seafloor magnetic anomalies are limited and paleomagnetic methods are then preferred.

Van der Voo [1969] was the first to provide paleomagnetic evidence for the counterclockwise rotation of Iberia of 35° since the Jurassic. Later paleomagnetic investigations of marine sediments from the Algarve and Lusitanian Basins by Galdeano et al. [1989] suggested a two-phase evolution with a relatively rapid phase of rotation of 26° during the Barremian Stage (125-110 Ma), and a slower phase of 13° from the Albian to Maastrichtian (110-83 Ma). Moreau et al. [1997] proposed a counterclockwise rotation of 22°±14° between 132 and 124 Ma. On the other hand, Storetvedt et al. [1987, 1990] suggest a more complex evolution involving clockwise and counterclockwise rotations before the coupling of Iberia to Europe. More recently, Gong et al. [2008b] suggested a single event of rotation, limited to the Aptian, based on new paleomagnetic data from the Organyà Basin, Spanish Pyrenees. It is important to note here that most of these interpretations have the severe limitation of being based on a low resolution and low quality paleomagnetic database. Their main problems are the paucity of precise radiometric dates, low age resolution of sampling, a small number of sites and samples, the absence of field tests and unknown paleo-horizontal corrections in the case of igneous rocks, and poorly defined inclination corrections for sedimentary rocks. Except for the Late Cretaceous, most of the Cretaceous paleomagnetic poles for the Iberian Plate were developed from sedimentary rocks (Table 3.2) that are known to be prone to remagnetization [e.g., Dinarès-Turell & Garcia-Senz, 2000; Font et al., 2006; Gong et al., 2008a, 2009; Jackson et al., 1992, 1993; McCabe & Elmore, 1989], and for which the magnetic inclination may be biased by depositional and post-depositional physical mechanisms [e.g., Tauxe & Kent, 2004]. Consequently, a re-examination of the paleomagnetic database for Iberia, as well as the acquisition of new paleomagnetic poles, preferentially from igneous rocks, is necessary.

Available Cretaceous paleomagnetic poles for Iberia between 158 and 68 Ma are shown in Fig. 3.10a and listed in Table 3.2. From the 30 paleomagnetic poles available for this period of time, 20 were selected for the calculation of mean paleopoles. Those paleopoles that were not used in the analysis are those obtained from the Salema intrusion (number 1 in Table 3.2 [Storetvedt et al., 1990]) and the Lisbon Volcanic Complex (LVC; number 2 [Van der Voo & Zijderveld, 1971]), which, despite their stable isolated magnetic remanence directions, show discrepancies relative to their age (Fig. 3.10a). The LVC passed a fold test [Van der Voo & Zijderveld, 1971] and was dated at 72.6±3.5 Ma (K-Ar on five whole-rock samples) [Ferreira & Macedo, 1979]. However, the position of the pole plots closer to the 100 to 88 Myr interval (Fig. 3.10a) than to the expected ∼73 Ma position, suggesting an

				Directions		Paleomagnetic Poles			
			Age	D	I	Lat	Long		
N°	Formation	Lo/Hi-Age	(Ma)	(°)	(°)	(°)	(°)	α95 (°)	Reference
1	Monchique - Salema intrusion*	72	68	341	42	-69.2	48.1	1.7	Storetvedt et al. [1990]
2	Lisbon Volcanic Complex*	70-74	72	352	40	-72.5	17.0	3	Van der Voo & Zijderveld [1971]
3	Monchique massif - syenites	70-74	72	181	-42	-76.9	357.5	4,5	Storetvedt et al. [1990]
4	Monchique Syenite	70-74	72	182	-37	-73.3	345.0	6.5	Van der Voo [1969]
5	Sines (Syenite, diabase, diorite)*	62-80	75	40.8	41.4	-53.0	272.0	3.3	Storetvedt et al. [1987]
6	Cabo da Roca*	75-78	75	39.4	43.4	-54.0	272.0	6.2	Storetvedt et al. [1987]
7	Sintra Granites	76-85	80	359	43.5	-76.5	354.0	5	Van der Voo [1969]
8	Paço d'Ilhas sill		88	350.0	42.4	-73.4	24.6	1.4	This study
9	Sintra Pluton (gabbros and diorites)*		90	358.0	27.3	-65.0	356.0	3.3	Storetvedt et al. [1987]
10	Organya Basin Sediments*	84-100	92	354,4	59.0	-85.1	62.0	14,1	Dinarès-Turell & Garcia-Senz [2000]
11	Organya Basin - Santa fè	92.5-96.5	94	357.7	47.2	-76.0	9.6	2.1	Gong et al. [2008b]
12	Foz da Fonte sill		94	346.5	44.3	-73.8	37.1	3.1	This study
13	Lisbon Area Sediments*	94-112	103	358	53	-85.0	9.7	9	Galdeano et al. [1989]
14	Organya Basin - Col d'Abella	108-109	108	356.0	48.1	-76.5	16.4	2.7	Gong et al. [2008b]
15	Organya Basin - Lluçà	109-112	110	354.1	46.8	-75	21.8	2.0	Gong et al. [2008b]
16	Algarve Basin Sediments	100-125	112	346.0	48.0	-75.5	51.7	6,5	Moreau et al. [1997]
17	Organya Basin - Font Bordonera	112-115	114	342.4	51.7	-72.9	61.6	1.1	Gong et al. [2008b]
18	Organya Basin Sediments	106-124	115	347.7	53.0	-77.1	53.9	4,8	Dinarès-Turell & Garcia-Senz [2000]
19	Organya Basin - Senyus top	115-118	116	348.4	56.3	-79.6	64.0	1.6	Gong et al. [2008b]
20	Lisbon Area Sediments	112-125	118	344.0	47.0	-73.0	48.0	7.0	Galdeano et al. [1989]
21	Iberian Chain	112-130	120	345.5	44.5	-71.3	44.5	7.0	Moreau et al. [1992]
22	Organya Basin - Senyus	118-121	121	334.9	56.5	-70.1	84.6	1.3	Gong et al. [2008b]
23	Organya Basin - Cabó	121-124	123	333.8	54.3	-68.3	80.0	1.5	Gong et al. [2008b]
24	Organya Basin Sediments	124-126	125	314.4	55.5	-54.5	96.7	9.9	Dinarès-Turell & Garcia-Senz [2000]
25	Organya Basin - Prada	124-126	125	308.8	57.5	-51.3	102.8	1.1	Gong et al. [2008b]
26	Lisbon Area Sediments	125-136	130	317	58	-57.0	95.0	4	Galdeano et al. [1989]
27	Organya Basin - Hostal Nou*	136-140	138	290.6	59.1	-39.1	113.4	1.7	Gong et al. [2008b]
28	Algarve Basin Sediments	136-151	142	324.0	46.0	-58.4	76.0	3.7	Moreau et al. [1997]
29	Algarve Limestones	140-150	145	328.0	45.9	-61.4	71.6	3.9	Galbrun et al. [1990]
30	Iberian Ranges	156-161	159			-57.4	70.5	3.8	Juárez et al. [1998]; Steiner et al. [1985]

* Poles excluded for mean calculations.

Table 3.2: Selected paleomagnetic poles of Iberia during Cretaceous and Late Jurassic.

error in age dating. Indeed, recent dates for several LVC sites indicate that this volcanic episode may have lasted much longer than previously thought and begun at around 100 Ma [R. Miranda, unpublished data]. The same argument applies to the Salema intrusion pole, for which a K-Ar whole-rock date gave an age of 72±2 Ma, but the paleomagnetic pole position plots closer to the 125 to 100 Ma interval (Fig. 3.10a). Other poles were excluded because of their inconsistent position and shallow inclination (Fig. 3.10a). These include the Sines, Cabo da Roca, Sintra Pluton (numbers 5, 6 and 9 [Storetvedt et al., 1987]), and Hostal Nou poles (number 27 [Gong et al., 2008b]). Finally, the Organyà basin (number 10 [Dinarès-Turell & Garcia-Senz, 2000]) and Lisbon area sediments (number 13 [Galdeano et al., 1989]) were not considered because of inconsistent pole positions and large $\alpha 95$ values (Table 3.2 and Fig. 3.10a). Before this study, of the 20 poles selected (Fig. 3.10b), only 3 were obtained from igneous rocks, while the rest were from sedimentary rocks. It is worth noting that between 100 and 88 Ma, only one selected pole, the Santa Fè sediments, Organyà Basin pole (number 11 [Gong et al., 2008b]), is reliable.

Once plotted on our selected database, the PI and FF poles are observed to consistently

Long (°)	Lat (°)	Angle (°)	Age (Ma)	Chrons	Reference
			Iberia - North America		
135.28	70.9	-16.09	65	c29	Luis & Miranda [2008]
135.65	69.7	-16.51	67	c30	Luis & Miranda [2008]
132.63	77.31	-18.48	72	c32	Luis & Miranda [2008]
118.5	85.33	-22.05	76	c33	Luis & Miranda [2008]
119.98	85.9	-23.22	82	c33r	Luis & Miranda [2008]
-9.4	76	-42.6	125	m0	Olivet [1996]
-7.4	73.1	-52.1	203	fit	Olivet [1996]
			North America- Africa		
-0.63	82.51	-20.96	65	c30	Klitgord & Schouten [1986]
-9.15	81.35	-22.87	71	c32	Klitgord & Schouten [1986]
-11.76	80.76	-23.91	73	c33y	Klitgord & Schouten [1986]
-18.35	78.3	-27.06	79	c33o	Klitgord & Schouten [1986]
-20.73	76.55	-29.6	84	c34	Klitgord & Schouten [1986]
-20.46	65.95	-54.56	125	m0	Labails [2007]
-19.24	65.92	-57.55	134	m10n	Labails [2007]
-18.08	66.57	-59.34	142	m16	Labails [2007]
-18.7	66	-62.29	148	m21	Labails [2007]
-18.44	66.08	-62.8	150	m22	Labails [2007]
-15.86	67.1	-70.55	154	m25	Labails [2007]
			Iberia - Africa		
-19.65	34.33	8.86	72		
-16.2	31.12	9.6	88		
-15.6	32.77	10.44	94		
-13.87	34.08	12.81	111		
-12.63	34.79	14.49	123		
-11.44	37.07	15.63	130		
-10.02	44.21	19.35	151		

* Isochron ages have been corrected from the original publications using Gradstein et al. [2004]. Finite rotations were interpolated for the plate pairs Iberia-North America and Africa-North America, for the corresponding ages of the paleomagnetic samples, before the computation of the Iberia-Africa finite rotations.

Table 3.3: Iberia-Africa Euler rotations.

fall between the 88-70 and 125-100 Ma intervals, but differ significantly from the Santa Fé pole (Organyà Basin, Pyrenees). We compared the PI and FF pole positions to the recent Global Apparent Polar Wander Path (GAPWP) of Torsvik et al. [2008] in African coordinates using the finite rotation poles listed in Table 3.3. The latter were calculated from the magnetic study made by Luis & Miranda [2008] up to chron C33r (83 Ma) for Iberia. During the Cretaceous superchron, it is not possible to compute intermediate finite rotation poles, and therefore we adopted the M0 rotation pole, determined by Olivet [1996], for our analysis. For the African-North American plate pair, we considered the finite rotation poles determined by Klitgord & Schouten [1986] up to chron 34, and the M0 rotation pole determined by Labails et al. [2010]. Both kinematic models were interpolated for the epochs under study (94 Ma and 88 Ma) to produce the two Iberian-African finite rotation parameters (Table 3.3). After rotation in African coordinates, the PI and FF

pole positions plot close to the reference GAPWP of Torsvik et al. [2008] at 100 and 80 Ma (Fig. 3.10b).

On the basis of the selected paleomagnetic pole positions, we discriminated time intervals for 160-136, 136-125, 125-100, 100-88, and 88-70 Ma, and then calculated corresponding mean paleomagnetic poles (Fig. 3.10c and Table 3.4). These mean poles show a coherent and quasi-linear path from 136 to 72 Ma, while during Jurassic-Cretaceous times (145-136 Ma) they depart westward. After rotating the mean poles into South African coordinates using selected and interpolated eulerian poles (Table 3.3), they fit with the GAPWP [Torsvik et al., 2008] for periods younger than 120 Ma. However, a significant misfit exists for older time intervals, i.e., those corresponding to rifting. The 136 to 125 Ma interval is the most critical because, even without rotation, the corresponding mean paleomagnetic pole is longitudinally distant from the GAPWP by $\sim$20° eastward (Fig. 3.10c). The use of alternative kinematic reconstructions for the Iberian and African plates does not show any improvement. One explanation for this is that, even if the GAPWP of Torsvik et al. [2008] is considered as the most reliable model for paleomagnetic reconstructions, it is not free of error. To test for such scenario, we plotted a recent compilation of African poles gathered by Font et al. [2009], which are only poles from igneous rocks, in order to minimize uncertainties in the paleomagnetic record of sedimentary rocks due to problems of inclination shallowing and time of magnetization acquisition. Fig. 3.10e shows that despite their lower quality (i.e., large α95 angles) in comparison to the Iberian poles, the African mean pole at 140 to 110 Ma is in agreement with the GAPWP [Torsvik et al., 2008]. A second explanation requires questioning the reliability of the paleomagnetic record for Iberia between 160 and 125 Ma, because it is based solely on six poles obtained from sedimentary rocks. It is worth noting that the misfit of the 160-125 Ma mean poles, in relation to the GAPWP, is essentially observed in the declination data set, suggesting that the magnetic inclination shallowing is not the

	Mean Cretaceous paleomagnetic poles of Iberia						Euler poles (Iberia-Africa)				
	Age (Ma)	Lat (°)	Long (°)	α95 (°)	N	Pole number	Age (Ma)	Long (°)	Lat (°)	Angle (°)	Reference
Late Cretaceous	70-88	-75.6	351.6	3.9	3	3-4;7	72	-19.65	34.33	8.86	Luis & Miranda [2008]; Klitgord & Schouten [1986].
	88-100	-75.1	22.6	2.8	5	8;11-12;14-15	94	-15.6	32.77	10.44	Luis & Miranda [2008]; Klitgord & Schouten [1986].
Early Cretaceous	100-120	-75.6	53.1	3	6	16-21	111	-13.87	34.08	12.81	Olivet [1996]; Labails [2007].
	120-125	-69.2	82.2	5.3	2	22-23	123	-12.63	34.79	14.49	Olivet [1996]; Labails [2007].
	125-136	-54.3	98.3	5.7	3	24-26	130	-11.44	37.07	15.63	Olivet [1996]; Labails [2007].
	136-160	-59	72.8	4	3	28-30	151	-10.02	44.21	19.35	Olivet [1996]; Labails [2007].

*See text for details.

Table 3.4: Mean Cretaceous paleomagnetic poles for Iberia and Iberia-Africa finite rotation Euler poles.

principal source of error. Recent developments in the assessment of magnetic anomalies older than M0 west of Iberia [Bronner et al., 2011] show that a re-evaluation is needed to better constrain the early drifting of Iberia from North America, and to improve our understanding of the kinematics of the Bay of Biscay. Moreover, existing M0 and pre-M0 magnetic reconstructions always show some level of lithospheric overlap or gaps, never geologically justified by the identification of the corresponding compressive or extensive processes [e.g., Srivastava et al., 1990a]. In view of the available paleomagnetic data and seafloor magnetic anomalies, we are not able to solve this problem and future investigations in the interval of 160 to 125 Ma are needed. For instance, kinematic models for Iberian Plate rotation, based on the declination and inclination of ChRM data [e.g., Gong et al., 2008b] are questionable until we are able to reconcile paleomagnetic data with seafloor magnetic anomalies.

3.6 Conclusions

Our paleomagnetic and rock magnetic investigations provide two new key poles for Iberia at about 88 and 94 Ma, located at Lat = 73.4° ; Long = 204.6° (A95 = 1.3° , k = 42.7) and Lat = 73.8° ; Long = 217.1° (A95 = 3.3° , k = 26.0), respectively. Once rotated into South African coordinates using selected and interpolated eulerian poles, they match the global Apparent Polar Wander Path at 80-100 Ma. On the basis of a rigorous selection of Cretaceous paleomagnetic poles from Iberia, we calculated mean paleomagnetic poles to test paleogeographic reconstructions. We conclude that from 120 to 70 Ma, paleomagnetic poles and magnetic anomaly reconstruction, when taken together, match well the global APWP, but are inconsistent when considering the interval of 160-120 Ma. Consequently, a coherent kinematic model for Iberian kinematics from 160 to 70 Ma will only be feasible after we are able to reconcile paleomagnetic data with kinematics of Iberia-Africa plate pair for the 160-120 Ma period.

3.7 Appendix: Supplementary tables

Specimen	D°	I°	MAD	Demag.
PI1_A1	341.2	35	4	AF
PI1_A2	39.1	10.7	9.1	AF
PI1_A4	346.6	45.5	2.2	AF
PI1_A5	344.8	45.3	2.6	AF
PI1_B1	348	42.7	1.2	AF
PI1_B2	350.7	46.8	3.3	AF
PI1_B4	351.1	46.4	2.2	AF
PI1_B5	355.7	45.1	2.2	AF
PI1_C1	358.6	59.2	8.2	AF
PI1_C2	337.6	42.6	2.6	AF
PI1_C3	341.1	48.2	6.7	thermal
PI1_C4	347.5	54.1	3.5	AF
PI1_D1	338.1	53.8	7.8	AF
PI1_D2	345.3	36.1	4.4	AF
PI1_D3	351.9	40.5	6.2	thermal
PI1_D4	357.4	50.4	2.1	AF
PI1_D5	349.8	50	2.3	AF
PI1_E1	357	26.5	2.7	AF
PI1_E2	346.7	37.9	2.8	AF
PI1_E3	347.4	37.8	5.5	thermal
PI1_E4	351.8	40.4	1.2	AF
PI1_E5	359.6	41.8	1.3	AF
PI1_F1	340.4	57.4	6.4	AF
PI1_F2	349.5	40.3	2.4	AF
PI1_F3	331.4	48.2	4.7	thermal
PI1_F4	352	44.8	2.8	AF
PI1_G1	3.3	17.5	2.7	AF
PI1_G2	352.3	29.4	4.5	AF
PI1_G3	354.1	35.4	3.7	thermal
PI1_G4	355.8	42.5	2.2	AF
PI1_H1	343.8	39.6	6.3	AF
PI1_H2	353.5	36.6	2	AF
PI1_H3	348.7	38	3.9	thermal
PI1_H4	352.3	38.4	2.7	AF
PI1_I1	15.3	19.7	6.6	AF
PI1_I2	-	-	-	AF
PI1_I3	342.1	34.9	3.1	thermal
PI1_I4	347.8	43.4	2.7	AF
PI1_J1	0	16.4	3.2	AF
PI1_J2	349.1	30.1	4.4	AF
PI1_J3	352.8	37.4	5	thermal
PI1_J4	354.5	37.9	1.9	AF

Specimen	D°	I°	MAD	Demag.
PI1_K1	-	-	-	AF
PI1_K2	349.9	40.6	4.2	AF
PI1_K3	347.5	48.4	5.7	thermal
PI1_K4	352.6	48.5	2.2	AF
PI1_K5	356.1	45.4	2.9	AF
PI1_L1	4.1	34.9	6.5	AF
PI1_L2	-	-	-	AF
PI1_L3	355.9	43.9	5.2	thermal
PI1_L4	358.2	45.1	3.1	AF
PI1_L5	346	48.1	3.8	AF
PI1_M2	357.9	36.8	2.4	AF
PI1_M3	351.1	42.4	3.3	thermal
PI1_N1	2.9	26	4.1	AF
PI1_N2	347.8	20.5	3.8	AF
PI1_N3	351.3	16.6	4.2	thermal
PI1_N4	359.8	29.6	4	AF
PI1_N5	356.5	42.4	3	AF
PI1_O1	352.7	29.9	3.4	AF
PI1_O3	347.5	50.4	3	thermal
PI1_O4	352	51.6	2.5	AF
PI1_O5	349	44.6	1.8	AF
PI1_P1	359.7	32.8	4.2	AF
PI1_P2	349.3	45.8	2.1	AF
PI1_P3	346.8	46.7	2.6	thermal
PI1_P4	354	48.2	2.5	AF
PI1_P5	348.6	43.3	1.6	AF
PI1_Q1	1.2	48.2	6.7	AF
PI1_Q2	353	32.9	3.1	AF
PI1_Q3	350.9	39.7	3.4	thermal
PI1_Q4	353.6	37.5	2.5	AF
PI1_Q5	348.9	45	2.9	AF
PI10_A1	352.9	48.5	1.6	AF
PI10_A2	348.8	39.2	2.8	thermal
PI10_A3	341.1	43.7	1.9	AF
PI10_B1	342.4	30	2.6	AF
PI10_B2	350.8	33	3.9	thermal
PI10_B3	333.4	47.8	3.8	AF
PI10_C1	349.9	51.4	1.9	AF
PI10_C2	344.4	50	3.1	thermal
PI10_C3	342.6	50.7	1.5	AF
PI10_C4	341.5	50.2	1.6	AF
PI10_D1	354.4	46.5	1.9	AF

Specimen	D°	I°	MAD	Demag.
PI10_D2	349.4	43.1	2.3	thermal
PI10_D3	92.7	-1.8	1.5	AF
PI10_E1	352	49.7	1.5	AF
PI10_E2	350.6	43	3.4	thermal
PI10_E3	89.6	-7.2	1	AF
PI10_F1	347.2	32.4	1.9	AF
PI10_F2	350.8	40.1	2.8	thermal
PI10_F3	356.3	44.8	2.5	AF
PI10_G1	352.3	19.8	3.7	AF
PI10_G3	350.5	44	2.3	AF
PI10_G4	351.8	44.6	2.2	AF
PI10_H1	317.2	46.8	4.9	AF
PI10_H2	347.6	40.7	3.7	thermal
PI10_H3	351.5	47.7	1.4	AF
PI10_I1	349.2	29	2.2	AF
PI10_I2	351.8	36.5	3.5	thermal
PI10_I3	343.2	51.1	3.6	AF
PI10_J1	340.8	29.1	1.8	AF
PI10_J2	350.2	38.8	2.7	thermal
PI10_J3	356.7	45.2	1.9	AF
PI10_J4	348.6	43	3.3	thermal
PI3_A0	352.2	40.7	5.7	thermal
PI3_A1	341.4	43.9	8.2	thermal
PI3_A2	-	-	-	thermal
PI3_A3	338.7	34.4	2	AF
PI3_A4	347.2	39.8	2.1	AF
PI3_A5	353.4	42.1	2	AF
PI3_B2	332	25.5	3	AF
PI3_B3	338.7	30	3.1	AF
PI3_B4	351.9	49.2	2	AF
PI3_B5	353.8	46.4	1.7	AF
PI3_C1	341.8	48.2	8.5	thermal
PI3_C2	-	-	-	AF
PI3_C3	336.7	35.6	3.1	AF
PI3_C4	344.6	46.4	3.5	AF
PI3_C5	354.1	47.9	1.7	AF
PI3_D1	340.7	27.5	7.3	thermal
PI3_D2	348.8	51.7	7	AF
PI3_D3	351.9	45	2.4	AF
PI3_D4	352.1	46	1.8	AF
PI3_D4	351.9	45.1	2.3	AF
PI3_E1	348.4	31.6	5.3	thermal

Specimen	D°	I°	MAD	Demag.
PI3_E2	350.1	47.9	5	AF
PI3_E3	344.5	39.4	2.2	AF
PI3_E4	343.3	45.9	2.5	AF
PI3_F2	341.6	19.2	4.4	AF
PI3_F3	342.7	37.7	3.1	AF
PI3_F4	348.9	44.5	2.9	AF
PI3_G1	336.9	33.3	3	thermal
PI3_G2	3.1	73.9	5.5	AF
PI3_G3	334.5	38.7	5.2	AF
PI3_G4	340.2	44.3	3.4	AF
PI3_H1	340.7	35.9	4.9	thermal
PI3_H2	359.5	56.5	4.1	AF
PI3_H3	344.8	40.4	1.8	AF
PI3_H4	356.5	46.2	2.2	AF
PI3_I1	341.2	34.7	3.5	thermal
PI3_I2	40.6	16.5	3.8	AF
PI3_I3	349.7	42.3	1.7	AF
PI3_I4	352.5	46.4	1.8	AF
PI4_A1	336.8	28.6	5.2	thermal
PI4_A2	351.5	22.9	3	AF
PI4_A3	350.5	43.3	3.6	AF
PI4_B1	348.9	33.7	3	thermal
PI4_B2	352.9	43	2.9	AF
PI4_C2	356.1	44.1	2.2	AF
PI4_D1	340.9	36.6	2.6	thermal
PI4_D2	338.7	35.2	3.6	AF
PI4_D3	345.7	47.7	3.2	AF
PI4_E1	0.5	32.7	2.8	thermal
PI4_E2	332.4	35.4	4.4	AF
PI4_E3	345.1	32.6	2.6	AF
PI4_E4	349.3	44.7	2.2	AF
PI4_E4	350.6	43.2	2.2	AF
PI4_F1	341.5	39.7	6	thermal
PI4_F2	333.6	33.7	4	AF
PI4_F3	357.2	38.2	4	AF
PI4_F4	356.4	44.5	2.9	AF
PI4_G1	348.4	40.5	3.2	thermal
PI4_G2	346.5	28.4	1.7	AF
PI4_G3	353.8	47.9	2.1	AF
PI4_H2	334.2	37.4	2.8	AF
PI4_H3	349.5	32.3	3.4	AF
PI4_H4	353.6	45.5	1.5	AF

Specimen	D°	I°	MAD	Demag.
PI4_I1	350.1	34.9	2.5	thermal
PI4_I2	341.5	31.8	1.9	AF
PI4_I3	343.3	33.1	2.8	AF
PI4_I4	348.2	34.8	1.9	AF
PI4_I5	354.3	45.3	2.4	AF
PI4_J1	352	37	2.2	thermal
PI4_J2	336.4	33.9	2.7	AF
PI4_J3	350.4	43.1	2.6	AF
PI4_J4	355	44.5	1.6	AF
PI4_J4	354.4	43.3	1.6	AF
PI6_A1	359.4	35.8	2.1	AF
PI6_A2	344.9	46.4	2.9	thermal
PI6_A3	350.9	47.3	1.7	AF
PI6_A4	336.5	49.6	2.4	thermal
PI6_B1	348.7	42.8	1.3	AF
PI6_B2	348.6	44.3	3	thermal
PI6_B3	349.6	43	2.3	AF
PI6_B4	346.1	47	2.6	AF
PI6_C1	330.3	39.9	1.3	AF
PI6_C2	347.3	43.5	4.4	thermal
PI6_C3	351	44.7	1.8	AF
PI6_C4	348.4	45.6	1.8	AF
PI6_D1	334.4	43.7	2	AF
PI6_D2	348.1	43.9	3	thermal
PI6_D3	351.6	46.6	1.5	AF
PI6_D4	347.1	47.2	1.3	AF
PI6_E1	350	43.4	1.6	AF
PI6_E2	353.8	46.7	2	AF
PI6_E3	349.3	49	1.3	AF
PI7_A1	347.1	49.6	1.8	AF
PI7_B1	347.6	33.9	1.2	AF
PI7_B2	347.8	38	4.1	thermal
PI7_B3	343	37.9	2	AF
PI7_B4	353.1	42	2.1	AF
PI7_B5	354.8	45.5	1.8	AF
PI7_C1	338.8	35.4	1.3	AF
PI7_C2	343.1	39.9	2.5	thermal
PI7_C3	349.1	44.2	2.3	AF
PI7_C4	352.6	49.3	1.8	AF
PI7_C5	350.1	50.7	2.4	AF
PI7_D1	345	44.1	1.7	AF
PI7_D2	349	43.8	2.9	thermal

Specimen	D°	I°	MAD	Demag.
PI7_D3	351.6	49.8	1.2	AF
PI7_D4	348.3	49.6	2.5	AF
PI7_E1	351.7	40.4	2.7	AF
PI7_E2	5.7	48.5	3.7	AF
PI7_E3	359.7	52.3	1.7	AF
PI7_E4	359.5	50.4	1.3	AF
PI7_F1	346	45.8	1.6	AF
PI7_F2	347.3	45.8	1.9	thermal
PI7_G1	345.6	49.8	1.7	AF
PI7_G2	347.9	44	2.2	thermal
PI7_G3	346.6	46.6	1.5	AF
PI7_H1	344.9	42.6	2.5	AF
PI7_H3	348	45.3	1.8	AF
PI7_H4	345.2	46.2	1.5	AF
PI7_I2	350.2	36.2	3	thermal
PI7_I3	359	41.7	2	AF
PI7_J1	328.9	34.4	3.1	AF
PI7_J2	339.2	45.8	2.2	thermal
PI7_J3	346.2	50.8	1.8	AF
PI7_K1	350.4	44.4	1.6	AF
PI7_K2	346.7	46	4.1	thermal
PI7_L2	347.9	47.4	2.5	thermal
PI7_L3	347.5	49.5	2.3	AF
PI7_M1	329.7	38.5	2.1	AF
PI7_M2	345.1	43.8	2.4	thermal
PI7_M3	351.3	46.9	2.3	AF
PI7_M4	351.2	46.6	1.8	AF
PI8_A1	344.7	34.9	3	AF
PI8_A2	345.5	34.1	3.4	thermal
PI8_B1	352.8	23.1	1.7	AF
PI8_B3	350.2	42.6	3	thermal
PI8_C1	322.6	49.1	3.1	AF
PI8_C2	342.2	48.8	4.2	thermal
PI8_C3	349.9	49.9	1.6	AF
PI8_D1	356.8	34.9	0.9	AF
PI8_E1	348.6	44.9	1	AF
PI8_E2	350.9	42.9	3	thermal
PI8_E3	354.5	47.4	1.2	AF
PI8_F1	333	43	2.3	AF
PI8_F2	351.2	45.7	3.1	AF
PI8_F3	354.8	48.9	1.3	AF
PI8_F4	350.2	44.7	2.3	AF

Specimen	D°	I°	MAD	Demag.
PI8_G1	346.7	39.5	1.6	AF
PI8_G2	348.8	33.4	2.8	thermal
PI9_A1	350.9	37.8	3.4	thermal
PI9_A3	355.4	49.5	2.5	AF
PI9_A4	349.5	48.7	3.6	AF
PI9_B1	355.3	54	1.9	AF
PI9_B2	346.4	47.8	2.4	thermal
PI9_B3	353.7	53.6	2.4	AF
PI9_B4	350.1	53.1	1.7	AF
PI9_C1	350	56.2	1.5	AF
PI9_C3	356.1	49.5	1.9	AF
PI9_C4	353	52.4	1.5	AF
PI9_D1	347.3	36.3	3.8	AF
PI9_D2	354.5	44.5	1.8	thermal
PI9_D3	359.2	49.3	1.9	AF
PI9_D4	357.8	50.6	0.9	AF
PI9_D5	353.9	46.5	2.3	AF
PI9_E1	353.5	35.4	5.6	AF
PI9_E2	352.8	35.8	4.8	thermal
PI9_E3	359.7	46.1	2.5	AF
PI9_E4	357.2	49.7	1.3	AF
PI9_F1	3.1	43.2	2.9	AF
PI9_F2	351.6	42.5	2.3	thermal
PI9_F3	355.9	48.7	1.7	AF
PI9_F4	358	48.4	2.8	AF
PI9_G1	357.5	45	1.6	AF
PI9_G2	356.5	40.2	4.1	thermal
PI9_G3	0.8	38.2	1.7	AF

Table 3.5: Characteristic mean directions of specimens from the PI sill

	Geographic		Tilt corrected (230°/10°)			
Specimen	D°	I°	D°	I°	MAD	Demag.
FF_12	-	-	-	-	-	AF
FF_16B	19.8	53.3	9.9	47.5	3.8	AF
FF_17A	9.7	63.5	357.7	56.2	2.3	AF
FF_19A	342.0	61.2	337.0	51.8	2.1	AF
FF_20B	-	-	-	-	-	AF
FF_20C	3.3	52.9	356.0	45.1	2.7	AF
FF_22C	333.3	46.3	331.4	36.6	1.6	AF
FF_23A	5.7	48.3	359.0	40.9	3.7	AF
FF_24	0.3	54.4	353.0	46.4	2.2	AF
FF_25A	358.3	53.7	351.5	45.4	1.9	AF
FF_26A	-	-	-	-	-	thermal
FF_26B	18.7	58.1	7.2	52.1	2.7	AF
FF_29A	34.8	71.5	11.1	66.9	8.7	AF
FF_30B	-	-	-	-	-	AF
FF_30C	356.0	47.0	350.9	38.7	4.6	AF
FF_31A	330.0	20.0	329.5	10.1	4.4	AF
FF_33A	331.2	46.5	329.6	36.7	5.7	AF
FF_34B	346.0	52.0	341.6	42.9	3.0	AF
FF_36A	350.5	55.0	344.9	46.1	3.6	thermal
FF_36B	3.1	49.1	356.6	41.4	2.2	AF
FF_37A	19.0	66.7	3.3	60.4	4.0	AF
FF_37C	327.6	51.9	326.3	41.9	4.7	AF
FF_38A	350.0	50.2	345.2	41.3	2.2	AF
FF_38B	345.1	49.8	341.1	40.6	1.7	AF
FF_40	-	-	-	-	-	AF
FF_41	354.5	46.1	349.7	37.7	1.9	AF
FF_42C	351.9	53.0	346.4	44.2	3.8	AF
FF_43A	22.6	42.9	15.4	37.7	5.4	AF
FF_46B	-	-	-	-	-	AF
FF_47A	-	-	-	-	-	AF
FF_47B	285.2	43.5	289.6	35.1	7.4	AF
FF_48B	350.2	56.5	344.3	47.6	2.7	AF
FF_49A	353.9	42.1	349.8	33.6	2.3	AF
FF_51A	-	-	-	-	-	AF
FF_51B	328.6	43.5	327.5	33.6	6.7	thermal
FF_52A	346.6	48.4	342.6	39.3	2.7	AF
FF_53A	345.4	52.6	341.0	43.4	3.1	AF
FF_54A	350.9	55.4	345.1	46.5	2.0	AF
FF_54B	270.6	62.9	282.3	55.6	5.8	AF
FF_55B	-	-	-	-	-	thermal
FF_56A	340.4	64.2	335.2	54.6	5.4	AF
FF_57A	353.5	53.0	347.7	44.3	2.4	AF

Continued on next page

Specimen	D°	I°	D°	I°	MAD	Demag.
FF_58A	5.2	55.3	356.9	47.8	3.2	AF
FF_59A	13.7	59.6	2.5	52.9	4.3	AF
FF_59B	-	-	-	-	-	AF
FF_60A	350.4	53.9	345.0	45.0	3.8	AF
FF_60B	15.1	56.1	4.9	49.7	4.3	AF
FF_61A	359.4	53.4	352.5	45.3	2.1	AF
FF_63A	349.1	53.2	344.0	44.2	2.0	AF
FF_63B	-	-	-	-	-	AF
FF_65A	358.7	56.6	351.2	48.3	2.4	AF
FF_65B	358.7	53.0	352.1	44.8	3.3	thermal
FF_66B	283.7	13.6	284.7	5.5	5.3	AF
FF_71A	-	-	-	-	-	AF
FF_71B	336.3	61.8	332.4	52.1	6.7	AF
FF_72A	15.9	71.8	357.5	64.8	3.7	thermal
FF_73B	0.9	56.0	353.2	48.0	4.8	AF
FF_76A	338.9	57.9	335.0	48.3	4.5	AF
FF_76B	-	-	-	-	-	AF
FF100_A1	344.7	45.5	341.3	36.3	3.2	thermal
FF100_A2	342.5	47.1	339.2	37.8	4.0	thermal
FF100_A3	346.2	50.0	342.1	40.8	4.5	thermal
FF100_A4	352.7	52.9	347.0	44.2	5.5	thermal
FF101_A1	342.6	48.4	339.2	39.0	6.6	thermal
FF101_A2	348.8	50.0	344.3	41.0	4.1	thermal
FF101_B1	354.8	46.7	349.9	38.2	4.4	thermal
FF101_B2	353.8	48.4	348.7	39.9	4.9	thermal
FF104_A1	351.4	45.6	347.1	36.9	3.9	AF
FF104_A2	359.8	43.8	354.7	35.9	4.1	AF
FF104_A3	355.3	44.1	350.8	35.7	5.0	AF
FF104_A4	357.2	47.8	351.8	39.5	1.9	AF
FF104_B1	358.1	49.3	352.3	41.1	4.3	AF
FF104_B2	347.7	50.3	343.2	41.3	3.1	AF
FF104_B3	355.5	48.5	350.2	40.1	1.1	AF
FF104_C1	4.9	46.7	358.6	39.2	3.5	AF
FF104_C2	359.9	47.5	354.2	39.5	3.9	AF
FF104_C3	2.6	48.7	356.3	41.0	2.3	AF
FF104_D1	3.9	51.2	356.8	43.5	3.4	AF
FF104_D2	359.2	48.7	353.4	40.6	2.5	AF
FF104_D3	356.3	47.3	351.1	38.9	2.2	AF
FF104_E1	17.2	58.8	5.7	52.5	3.7	AF
FF104_E2	12.8	59.5	1.9	52.7	1.9	AF
FF104_E3	9.2	57.6	359.5	50.4	3.9	AF
FF104_F1	3.0	50.9	356.2	43.2	6.3	AF
FF104_F2	351.3	47.2	346.8	38.4	3.9	AF
FF104_F3	349.2	49.1	344.7	40.1	4.6	AF

Continued on next page

Specimen	D°	I°	D°	I°	MAD	Demag.

Table 3.6: Characteristic mean directions (in-situ and after tilt correction) of specimens from the FF sill. D: declination I: inclination MAD: maximum angular deviation Demag: demagnetization method

Site	Latitude	Longitude
PI1	38°59'54.5"	9°24'2.0"
PI3	38°59'58.0"	9°24'3.5"
PI4	39°0'1.5"	9°24'2.5"
PI6	39°0'9.3"	9°23'49.2"
PI7	39°0'7.0"	9°23'49.0"
PI8	39°0'0.0"	9°23'53.5"
PI9	39°0'9.7"	9°24'26.4"
PI10	39°0'7.0"	9°24'31.0"
FF	38°27'3.5"	9°12'5.5"

Table 3.7: Geographic coordinates of PI sites and FF.

4. Testing Iberian Kinematics at Jurassic-Cretaceous times

Résumé

Au chapitre précédent, j'ai montré qu'il existe une incompatibilité entre les données paléomagnétiques ibériques d'âges pré-ouverture océanique (paléopôles moyens à 123, 130 et 151 Ma) et la courbe de dérive apparente des pôles (CDPA) pour ces mêmes intervalles de temps. Dans ce chapitre, je reprends cette question avec l'objectif de déterminer, pour chaque âge, la cause de ce désaccord. L'argumentation détaillée est présentée sous la forme d'un article publié dans *Tectonics* (M. Neres, J.M. Miranda et E. Font, 2013 : Testing Iberian kinematics at Jurassic-Cretaceous times, dont je donne ici un bref résumé.

Trois causes sont possibles pour expliquer l'origine de ce décalage entre les pôles paléomagnétiques de l'Ibérie et ceux de la CDPA : mauvaise calibration de la CDPA, pôles d'Euler et/ou données paléomagnétiques mal contraints. J'ai d'abord écarté l'hypothèse de la CDPA comme cause du problème, en testant les différents modèles de CDPA publiés jusqu'à maintenant, et en argumentant les raisons pour lesquelles j'ai considéré que le modèle de Torsvik et al. [2012] est le plus fiable. Puis, en utilisant les rotations d'Euler des modèles cinématiques de Olivet [1996] et de Vissers & Meijer [2012], les deux modèles les plus cités et aussi les plus discordants ("end-member models"), je montre que l'incompatibilité persiste indépendamment du modèle considéré (Fig. 4.1). La cause du problème réside donc dans la qualité des pôles paléomagnétiques ou dans celle des pôles d'Euler utilisés par les modèles cinématiques.

La méthode appliquée pour répondre à cette question est : (1) résoudre le problème inverse qui permet de trouver quels sont les pôles d'Euler de Ibérie par rapport à l'Afrique (IB/AF) capables de faire migrer les paléopôles moyens (à 123, 130 et 151 Ma) jusqu'aux pôles correspondants de la CDPA dans le référentiel Afrique (Fig. 4.2a) ; et (2) étudier quelles sont les implications d'utiliser ces pôles d'Euler pour déterminer la position de l'Ibérie aux âges correspondants. Pour effectuer l'opération (1), j'ai pris comme pôles potentiels (long./lat./angle) les points d'une grille couvrant tout le globe (Δlat, Δlong = 4° ou 6°, en fonction du temps de calcul) et, pour chaque point, j'ai pris des angles de rotation allant de 1° à 90°. Pour chaque âge, j'ai déplacé le pôle paléomagnétique moyen à l'aide de chaque pôle de rotation potentiel, et j'ai calculé la distance entre ce nouveau pôle paléomagnétique après rotation et la CDPA. Les pôles d'Euler dont les distances sont inférieures à 300 km (2.7°), correspondant aux losanges bleus en Fig. 4.2c, ont été acceptés pour effectuer l'opération suivante. Pour effectuer cette opération (2) les pôles IB/AF acceptés dans (1) ont servi à repositionner la plaque Ibérique (définie par la ligne de côte et les isobathes à -3000 m). Chaque reconstitution résultante a été évaluée en fonction de l'amplitude des recouvrements avec les continents voisins (paléo-positions de l'Afrique, de l'Amérique du Nord et de l'Eurasie). La présentation des résultats est donnée

en Fig. 4.2d (voir aussi l'annexe à la fin du chapitre, Section 4.6).

Ces résultats amènent les conclusions suivantes :

1. Les pôles paléomagnétiques de l'Ibérie au Crétacé Inférieur (123 et 130 Ma) sont incompatibles avec la CDPA global de Torsvik et al. [2012] : aucun pôle d'Euler n'est capable de placer ces pôles sur la CDPA pour les intervalles de temps considérés et simultanément placer l'Ibérie aux positions acceptables, car ils impliquent des superpositions ou au contraire des écarts injustifiables entre l'Ibérie et les plaques environnantes. Nous en concluons que c'est la qualité (au sens large) des données paléomagnétiques qui est la source du problème. Cette question est discutée au regard de la validité des tests de confiance et de l'histoire tectonique des régions concernées.

2. Le paléopôle du Jurassique Supérieur (à 151 Ma) est compatible avec la CDPA car il existe des pôles d'Euler IB/AF capables de rapprocher le paléopôle moyen de la CDPA, et simultanément de placer l'Ibérie dans des positions acceptables. Nous en concluons que les données paléomagnétiques correspondants au paléopôle à 151 Ma peuvent être considérées comme valables.

3. Cette compatibilité nous permet de présenter une nouvelle reconstitution de la plaque Ibérique à $\sim$150 Ma.

Compte-tenu la qualité douteuse des données paléomagnétiques existantes concernant l'Ibérie au Crétacé Inférieur, l'acquisition de nouveaux paléopôles et la ré-interprétation soigneuse des anomalies magnétiques s'avèrent indispensables.

Testing Iberian Kinematics at Jurassic-Cretaceous times

M. Neres,[1] **J. M. Miranda,**[1] **E. Font,**[1]

(This chapter is presented in a paper format, as published in *Tectonics*,
Neres et al., 2013, DOI:10.1002/tect.20074)

Abstract

Paleogeographic reconstructions of Iberia at the Mesozoic are still a matter of debate. The incompatibility between kinematic models and paleomagnetic data older than 120 Ma is a major problem for which no cause has yet been determined. Here, we use a new method to investigate the origin of this misfit. We solve the inverse problem of finding the Euler poles that fit paleomagnetic poles with the GAPWP and then test their implications on Iberian reconstructions. We show that Iberian poles from the Early Cretaceous (mean poles for 123 and 130 Ma) are incompatible with the GAPWP, bringing into question their validity. Contrarily, Late Jurassic data (mean pole at 151 Ma) are compatible with the GAPWP and thus can be considered reliable. Based on these results we propose a new magnetic reconstruction of Iberia and surrounding plates at ∼150 Ma (M22 anomaly). This work provides new constraints for the kinematic evolution of Iberia during Jurassic-Cretaceous. However, the development of a detailed and consensual model for the kinematic evolution of Iberia is dependent on the acquisition of new, high-quality paleomagnetic data and a reevaluation of seafloor magnetic anomalies.

[1]Instituto Dom Luiz, Universidade de Lisboa, Lisbon, Portugal.

4.1 Introduction

Iberian kinematics has been extensively investigated by several geological and geophysical approaches. However, no consensual model has yet been achieved, particularly for the Jurassic and Cretaceous. Paleogeographic reconstructions based on sea-floor magnetic chrons older than C34 have serious limitations. Firstly, the long-lived Cretaceous Normal Polarity Superchron (CNPS, from 125 Ma to 84 Ma [Gradstein et al., 2004]) prevents the use of magnetic reversals. Secondly, the absence of well-constrained M-chrons in the West Iberian Margin (WIM) and the Bay of Biscay, as well as uncertainties about the nature of the WIM [Bronner et al., 2011; Olivet, 1996; Rosenbaum et al., 2002; Russell & Whitmarsh, 2003; Sibuet et al., 2004, 2007; Srivastava et al., 2000], limit any kinematic reconstruction. This is emphasized by the fact that previous reconstructions systematically show lithospheric overlap or gap, for which geological evidences (corresponding compressive or extensive processes) are lacking (e.g. Srivastava et al. [1990a]). Alternatively, paleomagnetism has been used to assess relative movements between Iberia and surrounding plates. While some models defend a single rotation phase of Iberia [Gong et al., 2008b; Van der Voo, 1969] others favor a discontinuous two-stage counterclockwise rotation [Galdeano et al., 1989; Moreau et al., 1997] or a succession of clockwise and counterclockwise rotations [Storetvedt et al., 1987, 1990]. However, these models are based on low quality and low-resolution paleomagnetic data, particularly for the Jurassic-Early Cretaceous intervals [Neres et al., 2012; Osete et al., 2011; Osete & Palencia Ortas, 2006; Torsvik et al., 2012].

Recently, we published a revised paleomagnetic compilation of Iberia for the Late Jurassic to Cretaceous period [Neres et al., 2012]. After comparing Iberian mean paleomagnetic poles (IMPP) with those of the Global Apparent Polar Wander Path (GAPWP) of Torsvik et al. [2008] by using Euler poles from the literature [Labails et al., 2010; Olivet, 1996], we showed that GAPWP poles and IMPPs fit well together for time intervals younger than 120 Ma but are in disagreement for older periods. When using the Torsvik et al. [2012] (here referred as T12) GAPWP, the same conclusions are valid (Fig. 4.1, Table 4.1, Table 4.2). Furthermore, using Euler parameters from the alternative kinematic model synthetized by Vissers & Meijer [2012] (Table 4.1) maintains IMPPs closer to their non-rotated positions and originates larger incompatibilities, particularly at 123 Ma (Fig. 4.1). The origin of these misfits remains undetermined. Discrepancies linked to the referenced APWP are the less probable since few differences exist within the different models proposed in the literature [Besse & Courtillot, 2002; Kent & Irving, 2010; Schettino & Scotese, 2005; Torsvik et al., 2008, 2012] (cf. Section 4.6.1). Indeed, mean great circle distance of poles of the same age is less than 5° and may be due to

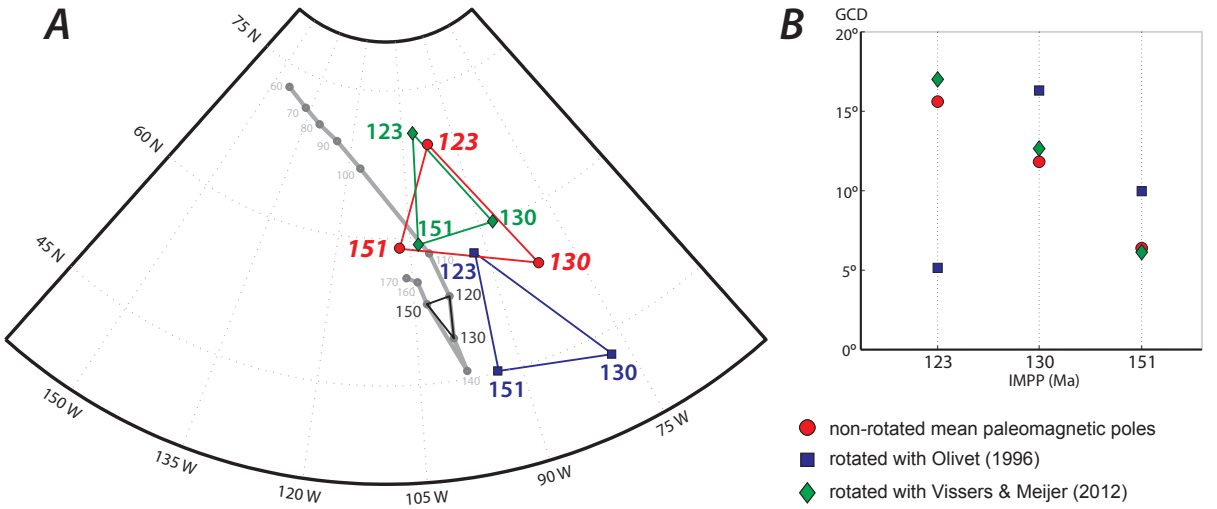

Figure 4.1: (a) Synthetic Global Apparent Polar Wander Path (GAPWP) of Torsvik et al. [2012] from 60 to 170 Ma in South African coordinates, together with Iberian mean paleomagnetic poles (IMPP) for 123, 130 and 151 Ma [Neres et al., 2012]. Paleomagnetic poles are shown in their non-rotated positions, and rotated using Euler poles from Olivet [1996] and Vissers & Meijer [2012] (Table 4.1). (b) Great circle distance (GCD) between IMPP (in-situ and rotated) and GAPWP poles (120, 130 and 150 Ma, respectively). The choice of Euler poles does not dramatically change the shape of the 123 - 130 - 151 Ma paths for non-rotated or rotated cases, and in neither case does it approximate the shape of GAPWP at the same time period. Such incompatibility between IMPP and GAPWP may be due either to the low quality of available paleomagnetic data or to erroneous Euler poles from kinematic models.

different paleomagnetic compilations and/or to different Euler parameters [Torsvik et al., 2012]. An exception to this is the APWP from Kent & Irving [2010], that shows considerable differences in both path and amount of APW, particularly at the Late Jurassic and Early Cretaceous. Therefore, the discrepancy must be linked to the low quality of paleomagnetic data and/or erroneous Euler poles.

In this work, we address the following questions: which Euler poles fit the IMPPs with the referenced GAPWP? What paleogeographic solutions do they imply and are they plausible with geological evidence? Our results show that coherent solutions only exist for the 150 Ma period, indicating that the paleomagnetic data are reliable, and allowing the development of a new magnetic reconstruction of Iberia for this period. These findings have crucial implications for the paleogeography of Iberia at the Jurassic-Cretaceous as well as for the calibration of GAPWP.

Mean Iberian paleomagnetic poles					
Age (Ma)	Plong (°)	Plat (°)	A95 (°)	N	Location
123	-97.8	69.2	5.3	2	Organyà Basin[1]
130	-81.7	54.3	5.7	3	Organyà Basin[1,2] ; Sediments near Sintra[3]
151	-107.2	59.0	4.0	3	Algarve Sediments[4,5]; Iberian Ranges[6]

IB-AF Euler rotation parameters				
Age (Ma)	Elong (°)	Elat (°)	Eangle (°)	Reference
123	16.967	53.731	-2.561	Vissers & Meijer [2012] (interpolated)
130	4.157	44.926	-7.959	
151	92.348	74.981	2.829	
123	34.79	-12.63	14.49	Olivet [1996]; Labails et al. [2010] (interpolated)
130	37.07	-11.44	15.63	
151	44.21	-10.02	19.35	

1 - Gong et al. [2008b]; 2 - Dinarès-Turell & Garcia-Senz [2000]; 3 - Galdeano et al. [1989]; 4 - Moreau et al. [1997]; 5 - Galbrun et al. [1990]; 6 - Juárez et al. [1998] and Steiner et al. [1985], after compilation from Osete et al. [2011]

Table 4.1: Iberian mean paleomagnetic poles (IMPP) and Iberia-Africa finite rotation parameters referenced in Fig. 4.1. IMPP from the compilation by Neres et al. [2012].

Age (Ma)	PLat (°)	Plong (°)	A95 (°)	Plate	Reference
120	53.6	261.3	2.6	SAF	Torsvik et al. [2012]
130	49.3	260.9	2.8		
150	53.1	257.2	6.4		
120	53.8	261.3	2.6	SAF	Torsvik et al. [2008]
130	50.6	260.0	2.9		
150	55.2	245.0	5.9		
120	54.0	261.1	2.7	SAF	Besse & Courtillot [2002]
130	50.0	262.1	2.9		
150	52.9	260.6	6.2		
120	55.1	263.1	-	SAF	Schettino & Scotese [2005]
130	52.2	265.6	-		
150	51.3	265.5	-		
120	74.2	192.2	2.7	NAM	Kent & Irving [2010]
130	71.7	193.4	2.4		
149	58.0	200.4	3.6		

Table 4.2: APWP poles considered in this work.

4.2 Method

Our approach is based on two steps: i) we solve the inverse problem of finding which Euler poles are able to fix IMPP with GAPWP's poles at 123, 130 and 151 Ma (Fig. 4.2a); and ii) we test if these hypothetical Euler poles bring the Iberian plate to reliable and coherent paleogeographic positions.

For the first step, we considered the APWPs from Besse & Courtillot [2002], Schettino & Scotese [2005] and Torsvik et al. [2012] in South African coordinates, and also the APWP from Kent & Irving [2010] in the North American frame (Table 4.2). We considered candidate Euler poles covering the whole globe in a grid with Δlat=Δlong=4° (in calculations for 123 and 130 Ma) or Δlat=Δlong=6° (for 151 Ma), and angles between -90° and 90° with steps of 1°. The grid spacing was chosen based on the computation time needed for calculations. For each age (123, 130 and 151 Ma), we rotated the IMPP (Table 4.1) with each candidate Euler pole and calculated the distance between the rotated IMPP and the respective APWP poles (120, 130 and 150 Ma poles of each considered APWP, as listed in Table 4.2). We accepted and kept for the next step the Euler poles that yielded a distance less than 300 km (2.7°).

In the second step, we first rotated the neighboring plates (NAM and EUR) to an AF-fixed frame in order to constrain the position of Iberia (Euler parameters in Table 4.3). We then rotated Iberia with each Euler pole accepted in step one and evaluated the resulting hypothetical paleogeographic solutions (cf. Section 4.6.2). For each plate, we used its respective coastline and -3000 m isobath (Fig. 4.2b).

All calculations and plots were made in Matlab. Rotation always stands for finite Euler rotation [Cox & Hart, 1986]. The magnetic reconstruction was made using Mirone [Luis, 2007] and Generic Mapping Tools (GMT) [Wessel & Smith, 1991] software, using data from the compilation of Luis & Miranda [2008].

4.3 Results

Results when considering the T12 GAPWP are summarized in Fig. 4.2. For each age we show the candidate Euler poles that bring IMPP close together with the GAPWP poles (Fig. 4.2c). Among them, the red-filled diamonds represent the best solutions, i.e. the solutions that maintain Iberia (IB) in the vicinity of Africa (AF, fixed), North America (NAM, rotated, in blue) and Europe (EUR, rotated, in green). We then represent the position of Iberia after rotation using the best solution Euler poles (Fig. 4.2d).

At 120 Ma, all simulated solutions imply a minimum overlap of 200 km between northwest IB and NAM, a gap of 200-300 km between IB and AF, and consequently a large overlap between IB and EUR (Fig. 4.2d). These gaps and overlaps increase dramatically at 130 Ma, yielding even more unrealistic solutions (Fig. 4.2d).

At 150 Ma, several solutions may be acceptable, with variable amounts of overlap of -3000 m isobaths in the north (overlap of Flemish Cap and Galicia Bank) (Fig. 4.2d).

For completeness, we also tested our approach using alternative APWPs [Besse & Courtillot, 2002; Kent & Irving, 2010; Schettino & Scotese, 2005]. Results using Besse & Courtillot [2002] and Schettino & Scotese [2005] are equivalent to those obtained by using the Torsvik et al. [2012] GAPWP. Using Kent & Irving [2010] APWP leads to unrealistic solutions for all time intervals.

4.4 Discussion

4.4.1 Testing Iberian Paleomagnetic Poles

In this study we evaluate the consistency between the IMPP compiled in our previous study [Neres et al., 2012], kinematic models and T12 GAPWP at around 123, 130 and 151 Ma, by simulating the paleogeographic solutions corresponding to IB-AF Euler poles able to fit the IMPP with GAPWP poles.

Our results show that there are no Euler poles able to fit the 123 and 130 Ma IMPPs with the T12 GAPWP, bringing into question the reliability of the corresponding paleomagnetic data.

The 123 Ma IMPP was calculated from two paleomagnetic poles from the Organyà Basin (Senyús and Cabó; [Gong et al., 2008b]) for which a primary character of the magnetization is argued by rock magnetic properties and by a positive fold test [Dinarès-Turell & Garcia-Senz, 2000; Gong et al., 2008b]. However, the reliability of these poles is still questionable: 1) They were not conducted on Cabó and Senyús, but on the overlying Font Bordanera and Santa Fé sites [Gong et al., 2008b]; 2) The positive fold test is not sufficient

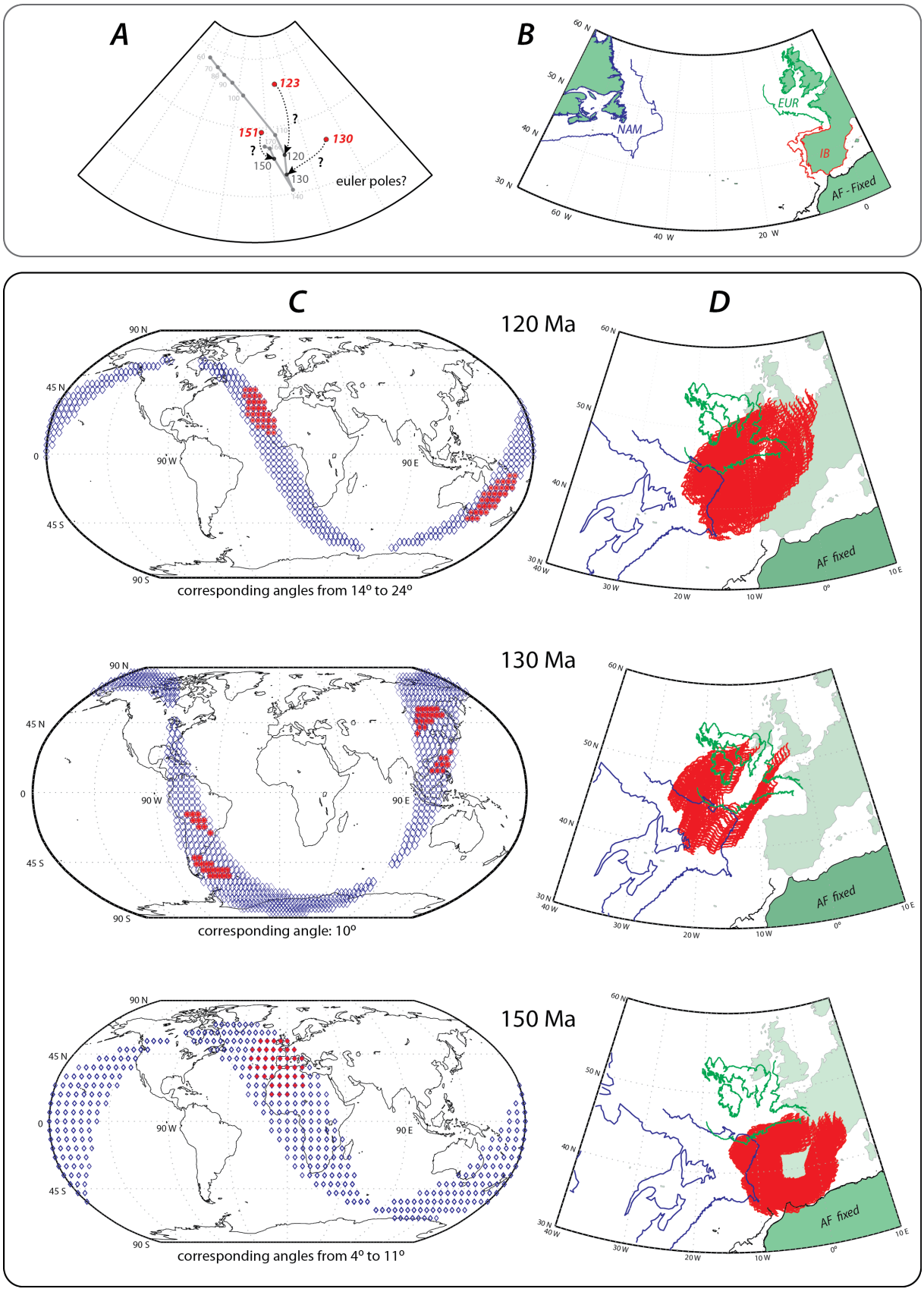
A
123
151
130
120
150
130
euler poles?
B
NAM
EUR
IB
AF - Fixed
C
D
120 Ma
corresponding angles from 14º to 24º
AF fixed
130 Ma
corresponding angle: 10º
AF fixed
150 Ma
corresponding angles from 4º to 11º
AF fixed

Figure 4.2

to exclude a remagnetization, but only to argue a pre-folding magnetization. Since the deformation of the Organyà Basin originates mostly from inversion during the Cenozoic compression [e.g., Garcia-Senz, 2002; Muñoz, 1992], a Cretaceous remagnetization (frequently reported for many Iberian basins [e.g., Galdeano et al., 1989; Gong et al., 2009; Juárez et al., 1998; Soto et al., 2008; Villalain et al., 2003]) would also yield a positive fold test and thus cannot be discarded. 3) The location of the Organyà Basin in an orogenic area such as the Pyrenees raises questions of its representativeness of stable Iberia: indeed, the Organya basin was completely detached and displaced southwards from its basement at the level of the Upper Triassic evaporites [e.g., Garcia-Senz, 2002; Muñoz, 1992; Oliva-Urcia et al., 2011]. For the sake of completeness, results presented at Fig. 4.1 suggest that the model of Olivet [1996] would be more suitable than the model of Vissers & Meijer [2012] for the M0 anomaly (125 Ma), if the paleomagnetic data were considered reliable. Indeed, after rotation using Euler parameters from [Vissers & Meijer, 2012], the 123 Ma IMPP remains close to its original location, whereas rotation using parameters from [Olivet, 1996] brings the 123 IMPP pole closer to the 120-130 Ma segment of the GAPWP.

The 130 Ma IMPP comprises two poles from the Organyà Basin: Prada site (Barremian-Aptian boundary, [Gong et al., 2008b]) and lowermost Aptian (sites 21-23, [Dinarès-Turell & Garcia-Senz, 2000]), as well as one pole from Lisbon area sediments (Hauterivian-Barremian, [Galdeano et al., 1989]). Although originally considered transitional or remagnetized, both poles from South Pyrenees are notably similar to the pole from Lisbon sediments, argued to be primary by a positive fold test. Moreover, even using only the pole from Galdeano et al. [1989], conclusions presented before remain valid as well. The strong incompatibility that exists between the 130 Ma IMPP and the corresponding GAPWP pole clearly highlights that the source of the incompatibility resides in the quality of the

Figure 4.2: (a) Conceptual representation of our inverse problem: non-rotated IMPP are plotted in the same representation as in Fig. 4.1a, and dashed paths illustrate the aim of our search: the IB-AF Euler poles that fit the paleomagnetic poles with the GAPWP. (b) Present-day coastlines and -3000 m isobaths used for simulations showed in 4.2d: IB (red), NAM (blue), EUR (green), and AF (black). (c) Results for the inverse problem: blue diamonds show the location of candidate Euler poles that bring together paleomagnetic and GAPWP poles in less than 2.7°. Among these, red-filled diamonds represent the best solutions: those that bring Iberia to the closest positions with respect to AF and NAM. (d) Position of the Iberian plate (red) after rotation using the best Euler poles (red-filled in 4.2c) For simplicity of representation, different solutions are shown as superimposed lines. Note that using the entire set of Euler poles (all blue diamonds in 4.2c) would result in a trajectory traveling across several regions of the globe. Plots are in Africa-fixed frame, with NAM (blue) and EUR (green) rotated with parameters from Table 4.3. Present-day configuration of EUR and IB is shown for reference.

Age (Ma)	Plates	long (°)	lat (°)	angle (°)	Reference
120	EUR-NAM	157.2	69.7	-22.8	Olivet [1996] (J anomaly)
	NAM-AF	-20.46	65.95	54.56	Labails et al. [2010] (M0)
	EUR-AF	-6.53	44.13	41.21	
130	EUR-NAM	157.2	69.7	-22.8	Olivet [1996] (J anomaly)
	NAM-AF	-19.77	65.93	56.22	Labails et al. [2010] (interpolated)
	EUR-AF	-5.88	44.96	42.74	
150	EUR-NAM	153.5	73	-25.2	Olivet [1996] (fit)
	NAM-AF	-18.44	66.08	62.8	Labails et al. [2010] (M22)
	EUR-AF	-4.32	46.26	46.44	

Table 4.3: NAM-AF and EUR-AF Euler poles used for Fig. 4.2d.

IMPP. As discussed before, a positive fold test for the Hauterivian-Barremian pole is not sufficient to prove a primary magnetization: this fold test compares directions from a horizontal site (site 5) and a tilted site (site 8). Site 8 is located in the southern limb of the Sintra anticline, a structure mainly originating from the local Tertiary inversion of the basin [Kullberg et al., 2011]. Therefore, a Cretaceous remagnetization cannot be excluded. Moreover, only positive polarities are reported by Galdeano et al. [1989], whilst inverse polarities should be expected for Hauterivian-Barremian ages. Furthermore, its proximity with the Late Cretaceous Sintra plutonic massif may have caused total or partial remagnetization. It is worth noting that the Galdeano et al. [1989] pole is the unique key pole to constrain the Iberian plate drift from the Hauterivian to the early Aptian [Gong et al., 2008a]. Because the quality of 130 Ma IMPP is strongly questioned, it is not possible to assess the quality of existing kinematic models at this period.

The IMPP at 151 Ma comes from Algarve sediments (Tithonian–Valanginian [Moreau et al., 1997] and Tithonian–Berriasian [Galbrun et al., 1990]) and Iberian Ranges [Juárez et al., 1998; Steiner et al., 1985]. The pole from the Iberian Ranges results from a rigorous selection of Jurassic paleomagnetic data made by Osete et al. [2011]. Poles from Algarve Basin show normal and inverse polarities that gave a positive reversal test, suggesting a primary origin for the magnetization. Furthermore, this region has been considered as part of stable Iberia [e.g., Osete & Palencia Ortas, 2006]. Therefore, the 151 Ma IMPP can be considered reliable and the results of our simulations can be used to constrain a finite plate reconstruction at 151 Ma.

4.4.2 New Reconstruction of Iberia at 150 Ma

In the absence of clear oceanic magnetic lineations, as is the case for the IB-NAM plate pair older than 84 Ma (C34 anomaly), plate reconstructions based on seafloor magnetic anomalies are severely handicapped. In this case, paleomagnetism is the most powerful alternative. For ages older than the C34 anomaly until the initial opening of Central Atlantic (195 Ma [Sahabi et al., 2004]), Iberian reconstructions can be two-fold constrained. On one hand, the kinematics of the AF-NAM plate pair (Central Atlantic domain, the southern neighboring region of Iberia) is constrained by the fit of seafloor magnetic anomalies (e.g. Labails et al. [2010]). On the other hand, paleomagnetic data of Iberia can be used to constrain IB-AF (and consequently IB-NAM) relative movement from the comparison with a GAPWP. For this purpose, it is imperative that paleomagnetic data are coherent with the GAPWP. We show here that regardless of the APWP considered, the 151 Ma IMPP is compatible with the GAPWP (Fig. 4.2d), which allows us to propose a new magnetic reconstruction of Iberia at these times (Fig. 4.3; respective Euler parameters are listed in Table 4.4).

The M22 finite Euler pole from the recent model of Labails et al. [2010] is used to reconstruct the Central Atlantic domain. To the north, the oceanic domain of the Bay of Biscay is closed. The implied finite rotation between IB and EUR from 150 Ma until present is of 28° about an Euler pole situated in central France (Fig. 4.3, Table 4.4). Some overlap between the Flemish Cap and Galicia Bank is resolved by partially closing the Galicia and Flemish Pass. Across NAM-EUR and IB-EUR plate pairs, a good agreement is verified between magnetic anomalies corresponding to Paleozoic orogenies and sutures, in particular the Ibero-Armorican arc [Silva et al., 2000] and the Iapetus suture. This suggests that, since the onset of the Pangaea breakup until 150 Ma, extension in these domains occurred with minor strike-slip component. However, no similar agreement between magnetic zones and lineations is verified across IB-NAM and IB-AF boundaries. This supports a more complex evolution of the southwestern and southern margins of Iberia. Indeed, the nature and evolution of the WIM, as well as the evolution of the IB-AF boundary is still a matter of debate. For example, Silva et al. [2000] verified a discontinuity of Paleozoic magnetic zones on the WIM, which is still not explained. Moreover, the nature of the WIM itself is discussed, with severe differences between published models [e.g., Afilhado et al., 2008; Bronner et al., 2011; Russell & Whitmarsh, 2003; Sibuet et al., 2007; Srivastava et al., 2000]. Several magnetic reconstructions failed to explain the large lithospheric gaps and overlaps observed at the IB-AF boundary [e.g., Sibuet et al., 2004; Srivastava et al., 1990a, 2000].

Fig. 4.4 shows the good agreement between parameters from our reconstruction and

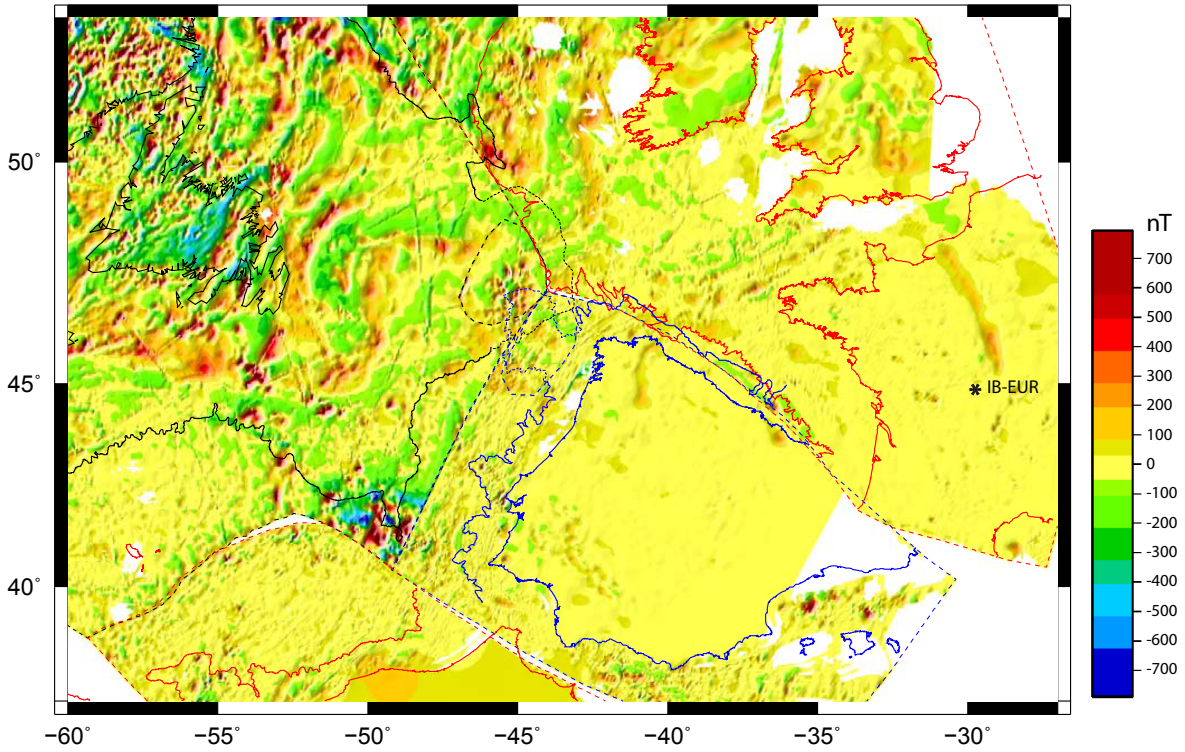

Figure 4.3: Magnetic reconstruction at 150 Ma (M22 anomaly). Africa is rotated with M22 parameters from Labails et al. [2010]. African (red), Iberian (blue), Eurasian (red) and North American (black) present-day 0 m and -3000 m isobaths are represented. Some overlap between Flemish Cap and Galicia Bank is resolved by partially closing the Galicia and Flemish Pass (dashed lines indicate the limits of the rotated blocks). Black asterisk shows location of finite IB-EUR pole (angle ∼28°). Reconstruction parameters are listed in Table 4.4.

Plates	long (°)	lat (°)	angle (°)
IB-NAM	-18.08	67.54	-57.72
EUR-NAM	308.70	85.46	-34.11
AF-NAM*	-18.44	66.08	-62.80
IB-EUR	2.08	46.55	-27.53
IB-AF	-7.55	51.55	5.29
GAL-IB	-7.78	37.28	-4.98
GAL-NAM	-19.38	65.12	-62.05
FLEM-NAM	-33.12	58.82	-1.13

Table 4.4: Finite Euler rotation parameters of the M22 reconstruction (150 Ma). *AF-NAM pole is the M22 pole from Labails et al. [2010]. Poles in italic result from sum of other indicated poles

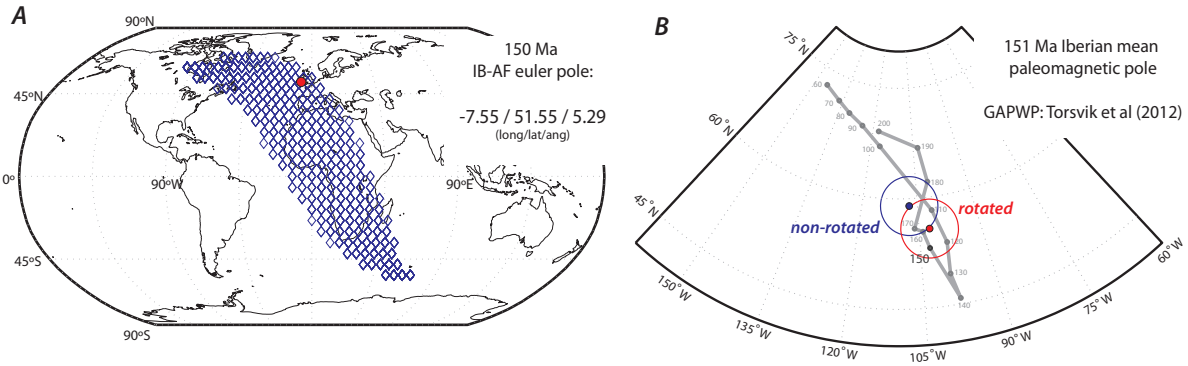

Figure 4.4: Compatibility between the presented reconstruction and Late Jurassic paleomagnetic data. (a) The IB-AF finite Euler pole from our 150 Ma reconstruction (red dot) belongs to the set of poles that bring together the IMPP to the GAPWP (see text and Fig. 4.2). (b) When rotated to African coordinates with our Euler pole, the 151 Ma mean paleomagnetic pole come closer to the GAPWP at corresponding ages. The distance from the rotated IMPP to the 150 Ma APWP pole (2.65°) is inferior to the A95 values of the IMPP and GAPWP pole.

paleomagnetic data. Our IB-AF finite Euler pole (Table 4.4) belongs to the set of poles that succeed in approximating the 151 Ma IMPP to the GAPWP (Fig. 4.4a). After rotation into African coordinates, the 151 Ma pole approximates the GAPWP at corresponding ages (Fig. 4.4b). The distance between the rotated IMPP and the 150 Ma APWP pole is now reduced to 2.65°, which is statistically satisfactory given the A95 values of IMPP and GAPWP poles (4.0° and 6.4° respectively).

4.5 Conclusions

Our results are three-fold:

- We show that Iberian mean paleomagnetic poles at 123 and 130 Ma are incompatible with GAPWP poles.
- The 151 Ma mean pole is compatible with the GAPWP, suggesting that the paleomagnetic data are reliable.
- We present a new magnetic reconstruction for Iberia at 150 Ma.

These findings provide new constraints for the kinematic evolution of Iberia at Jurassic-Cretaceous times but also highlight the need to acquire more high-quality paleomagnetic data for the Iberian plate, particularly at the Early Cretaceous.

4.6 Appendix: About the method

4.6.1 Comparison of results using BC02, SS05, KI10 and T12

In order to check if the misfit between paleomagnetic poles and Euler poles is linked to a miscalibration of the APWP, we tested the different APWPs from the literature: BC02, SS05, KI10 and T12, as defined before. This was done by repeating the calculations using the poles from each APWP, for each age. In the Results, we state that considering either B02, SS05 and T12 APWP poles leads to equivalent results (i.e. there are no reliable solutions for 120 or 130 Ma and there are acceptable solutions for 150Ma), and that using poles from KI10 APWP leads to unreliable solutions for the three ages.

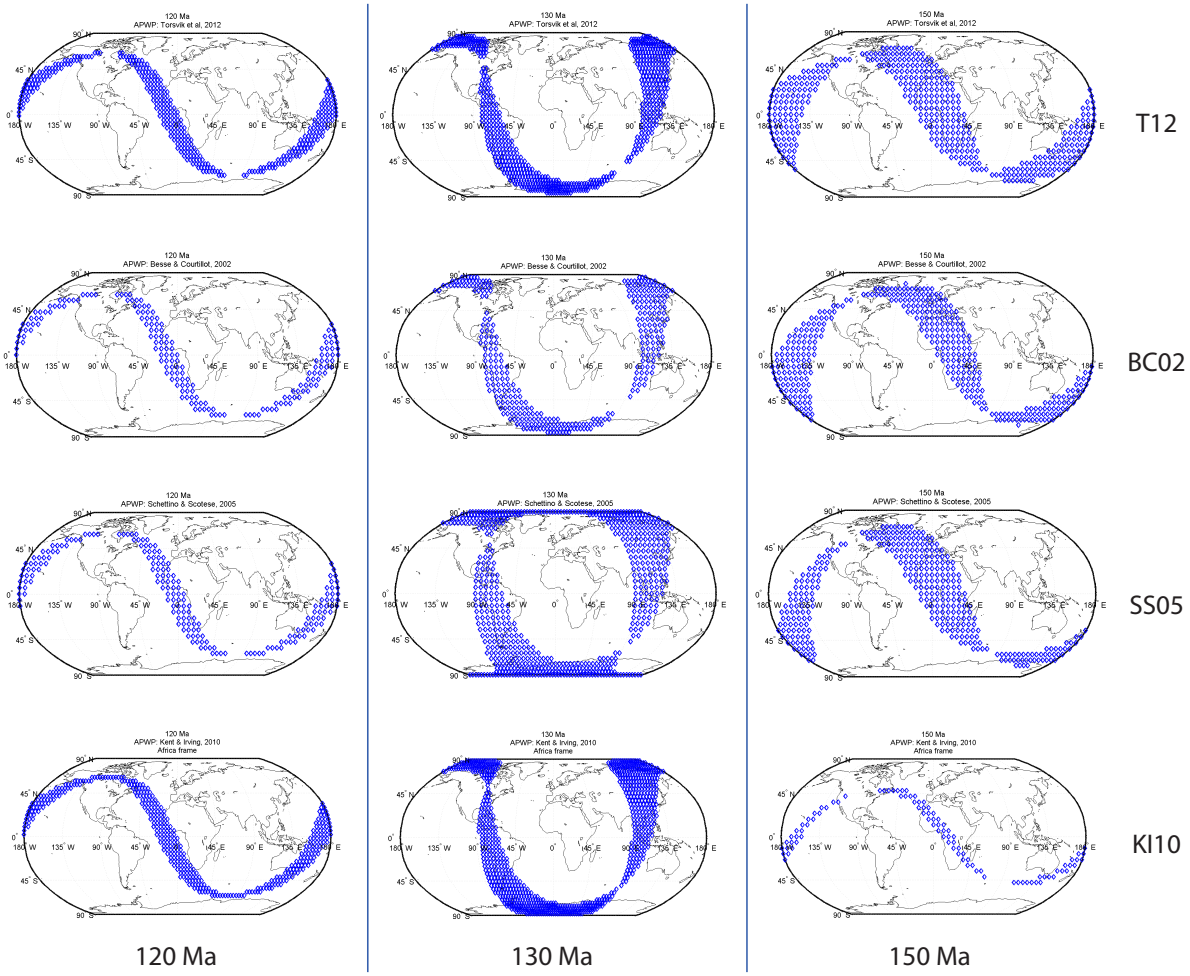

Figure 4.5: Euler poles accepted in the first step of the method (those that approximate the IMPPs to the APWP poles in less than 300 km), for each age and each APWP. Results considering poles from the different APWPs are equivalent, except for KI10 at 150 Ma.

A possible visualization of these results is here presented. Note that the choice of

APWP is done in the first step of the method (cf. Section 4.2). In Fig. 4.5 we represent the accepted Euler poles (those that approximate the IMPPs to the APWP poles in less than 300 km) at each age, when considering each APWP.

It can be observed that for 120 and 130 Ma, the accepted Euler poles are equivalent for all considered APWPs. The same is valid at 150 Ma for T12, BC02 and SS05, but not for KI10. For 150 Ma, the KI10 population of Euler poles is significantly different from the other three. Moreover and importantly, it does not contain the red-filled zone representative of the best solutions (cf. Fig. 4.2c and Section 4.6.2). This means that differences between poles from different APWPs at each age are not meaningful with respect to our analysis, except for the KI10 APWP at 150 Ma. In fact, this pole corresponds to the controversial Jurassic spike defended by Kent & Irving [2010], but argued by Torsvik et al. [2012] to be due to a low number of input poles.

4.6.2 Evaluation of the implied paleogeographic solutions

In the first step of our method (cf. Section 4.2), we find the rotation poles so that the distance between the rotated IMPP and the APWP poles is less than 300 km. This corresponds to a set of Euler poles spreading into several regions of the globe (blue diamonds in Fig. 4.2c). In the second step, we use these rotation poles to simulate the rotated positions for Iberia, and check if they are acceptable or not. This evaluation process will be illustrated here, in order to make it clearer.

Consider Fig. 4.6 and 4.7 that illustrate the results for 130 Ma and 150 Ma IMPPs, respectively, when using T12 APWP poles. The left and right parts of these figures are equivalent to Fig. 4.2c and 4.2d, respectively. In all cases, the population of blue diamonds (at the left) represents the entire set of Euler poles satisfying the criterion of step one. In the insets *a* of Fig. 4.5 and 4.6 (at the right) are plotted the rotated positions of Iberia corresponding to all this set of rotation poles. As referred in the caption of Fig. 4.2, this gives rise to completely implausible positions through different regions of the globe. Therefore, we select solutions that are more realistic: the "best" solutions, as named in the text. This corresponds to zooming on our region of interest, which is controlled by the paleogeographic positions of AF, EUR and NAM (as in Fig. 4.2d); Table 4.3, but also depends on the results of each simulation (compare Fig. 4.6 with Fig. 4.7). In practice, this was accomplished by defining a maximum allowed distance between the positions of one arbitrary point in Iberia, before and after rotation (dist_max). In insets *b*, *c* and *d* of Fig. 4.6 and 4.7, cases when considering different values for dist_max are represented. By comparing them, it can be seen that the choice of this computational parameter is not objective: it must be done a posteriori after each simulation, and different values can

be chosen depending if we want to plot more or less superimposed solutions. However, results and conclusions presented here are valid independently of the value of dist_max.

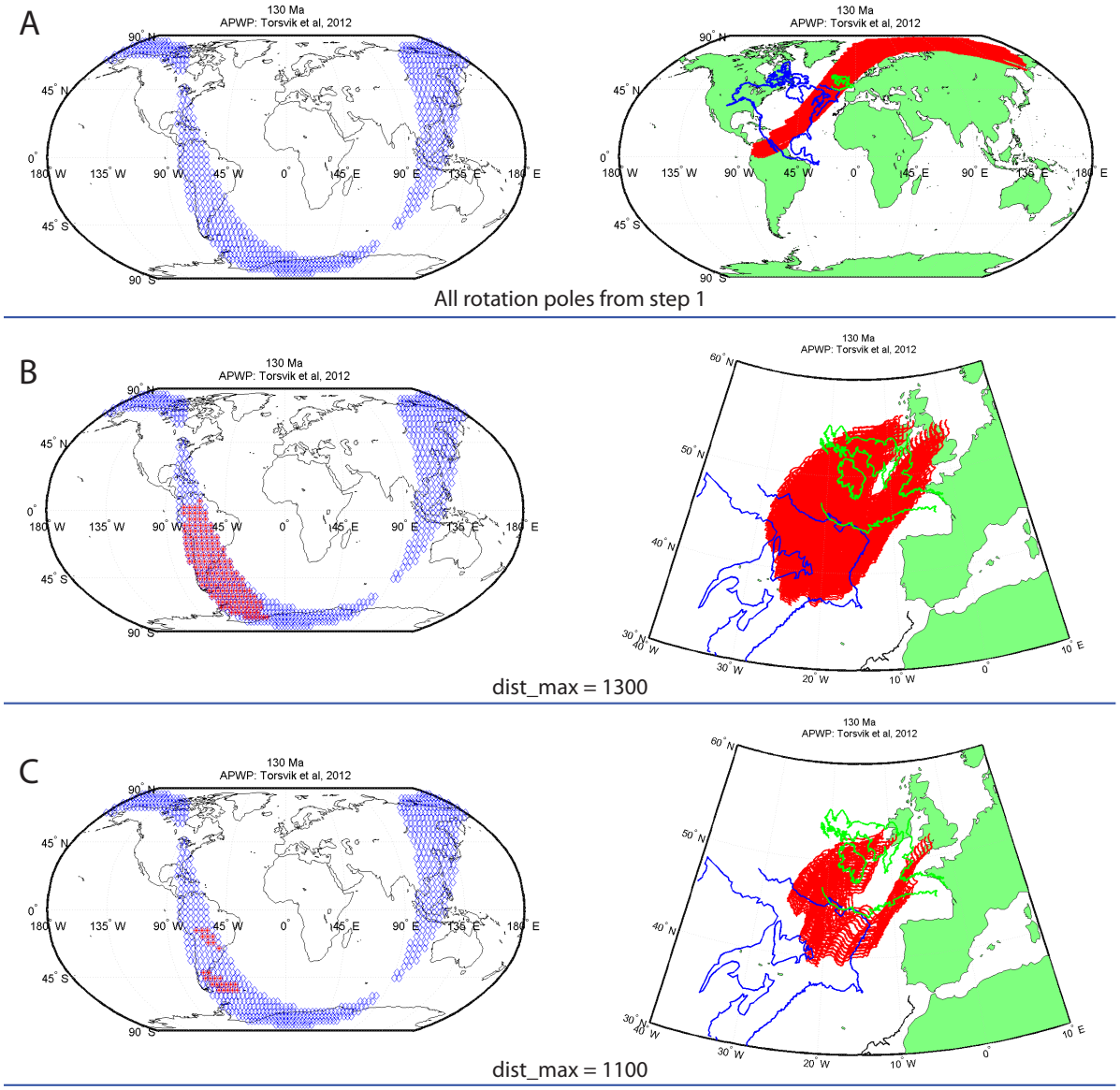

Figure 4.6: Illustration of the evalution of paleogeographic solutions achieved by using the potential Euler poles accepted on step one. Example for 130 Ma, using T12 APWP In A, at the right, are represented the solutions respective to all Euler poles (all blue diamonds at the left). In B (C), parameter dist_max (see text) was defined to 1300 km (1100 km), approximating to the region of interest (close to Africa, the fixed frame). The respective Euler poles are red-filled. No plausible solutions independently of the value of dist_max. See caption of Fig. 4.2.

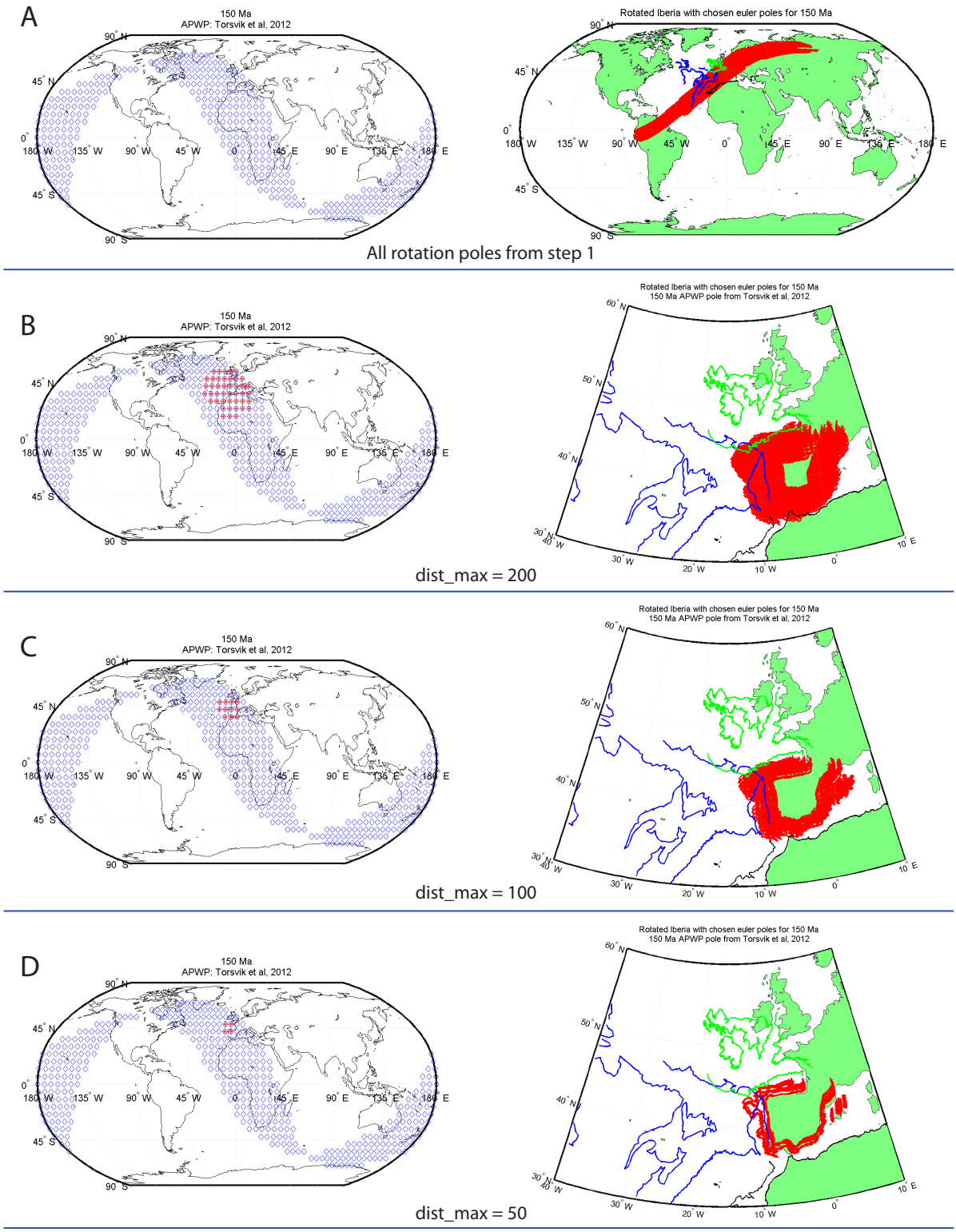

Figure 4.7: Illustration of evalution of paleogeographic solutions for 150 Ma, using T12 APWP In A, at the right, are represented the solutions respective to all Euler poles (all blue diamonds at the left). From B to D, solutions are restricted to smaller values of dist_max (200, 100 and 50 km, respectively), zooming to the region of interest. The respective Euler poles are red-filled. Acceptable solutions are found in this case.

5. Magnetic fabric in a Cretaceous sill (Foz da Fonte, Portugal): magmatic flow model and implications for regional magmatism

Résumé

Dans les chapitres précédents, j'ai présenté des résultats paléomagnétiques et des simulations numériques qui ont permis d'améliorer la compréhension de la cinématique de la plaque ibérique au Jurassique Supérieur et au Crétacé, et également de discuter les problèmes qui restent à résoudre. Dans ce chapitre, nous nous intéressons à un autre aspect des études magnétiques, ici appliqué à des sills d'âge Crétacé, celui de la caractérisation de certaines de leurs propriétés rhéologiques par l'étude de l'anisotropie de leur susceptibilité magnétique (ASM). Les roches que nous avons étudiées sont les magmas basiques (ou diabases) formant le sill de Foz da Fonte, daté d'environ 94 Ma et de 7 à 8 m d'épaisseur.

Affleurant dans la province magmatique portugaise du Crétacé Supérieur où plusieurs corps magmatiques intrusifs sont encore peu étudiés, ce sill constitue un véritable laboratoire naturel. Ce sill exposé en falaise sur la côte au Sud de Lisbonne, présente d'excellents affleurements. Grâce un pendage proche de l'horizontale, il a permis d'obtenir un échantillonnage vertical complet. Par ailleurs, des marqueurs macroscopiques du flux magmatique (vésicules carbonatées elliptiques) à proximité des contacts supérieur et inférieur avec les sédiments ont enregistré la direction de l'écoulement du magma (au moins au niveau de ces épontes).

Le mode de mise en place des sills et leur relation avec les autres structures magmatiques fait l'objet d'importantes discussions dans la littérature. Dans ce contexte, nous avons conduit une étude détaillée d'ASM afin de mieux comprendre l'écoulement du magma lors de la mise en place du sill, et de replacer cette mise en place dans le cadre du magmatisme régional. Cette étude est présentée sous la forme d'un article soumis à la revue *Geophysical Journal International*, par M. Neres, J.L. Bouchez, P. Terrinha, E. Font, M. Moreira, R. Miranda, P. Launeau, C. Carvallo (2013), sous le titre "Magnetic fabric in a Cretaceous sill (Foz da Fonte, Portugal) : magmatic flow model and implications for regional magmatism".

Nous avons échantillonné un profil vertical complet qui a montré des variations significatives des valeurs des paramètres d'AMS. Ces variations nous ont permis de définir cinq "couches" parallèles aux épontes du sill (Fig. 5.11 et 5.12), correspondant à trois domaines caractérisés par leur fabrique magnétique. Nous relions ces couches aux différents régimes de flux magmatique qui existent pendant l'intrusion (Fig. 5.15).

Ces domaines sont : (1) les zones figées, correspondant aux premiers ∼50 cm le long des épontes supérieure et inférieure du sill (ou mur et toît), sont caractérisées par un faible degré d'anisotropie, suggérant de faibles gradients de vitesse et un flux magmatique irrégulier le long des parois (probablement rugueuses) ayant lieu au cours des premiers stades de mise en place du sill ; (2) le cœur du sill, où de faibles anisotropies et grande

dispersion directionnelle sont observées, correspondant à la zone où le magma s'est écoulé plus librement, sous de faibles gradients de cisaillement et donc suivant un transport plutôt translatif ; et (3) les zones intermédiaires entre zones figées et cœur du sill, où on trouve les plus forts degrés d'anisotropie attribués aux zones où se développent les plus forts gradients de cisaillement.

Pour justifier ces interprétations, nous avons conduit plusieurs analyses. (1) La nature et l'homogénéité de la fabrique magnétique dans le sill, étudiés par les méthodes de la minéralogie magnétique (courbes thermomagnétiques, diagrammes de FORC et paramètres d'hystérésis) sur des échantillons régulièrement distribués dans le profil, ont montré que les porteurs magnétiques sont essentiellement des titanomagnétites multi-domaines avec un contenu variable en titane ; (2) La bonne corrélation entre la linéation magnétique (K_1) et l'axe long des vésicules a été vérifiée sur la surface structurale supérieure du sill, confirmant l'interprétation de l'ASM comme indicateur de la direction de l'écoulement magmatique ; et (3) La bonne correspondance entre la linéation magnétique et la fabrique de forme des minéraux opaques a été vérifiée par analyse d'image dans le plan du litage magmatique, montrant que l'ellipsoïde d'AMS correspond statistiquement à l'orientation préférentielle de forme des opaques. Par ailleurs, à partir des observations de microscopie électronique de deux échantillons (l'un situé près du toit et l'autre au milieu du sill) nous avons observé que les titanomagnétites sont de plus grande taille et plus agglomérées au coeur du sill qu'à proximité des épontes. Cette observation suggère que la "pression dispersive" (effet Bagnold) est effectivement minimum au cœur du sill, permettant aux petits grains de magnétite de former des agglomérats.

Les résultats directionnels de l'ASM nous ont permis de déterminer la direction de l'écoulement magmatique. Le sens de l'écoulement est donné par le pincement observé entre la foliation magnétique et les épontes du toit et du mur du sill. Le plan de foliation magnétique est partout subhorizontal avec une linéation d'orientation moyenne ∼N310°. Cette direction d'écoulement, et son sens vers le Sud-Est, suggèrent une localisation de la source magmatique au Nord-Ouest. Ces résultats nous conduisent à une interprétation géologique dans le cadre du magmatisme alcalin du Crétacé Supérieur de la marge ouest du Portugal. En intégrant les données issues des anomalies magnétiques, de la chronologie isotopique, de la sismique et de la tectonique, nous suggérons que l'anomalie du Cabo Raso (fortement positive) est la source magmatique du sill de Foz da Fonte. Ces mêmes données nous permettent de suggérer qu'une structure magmatique (de type faille ou dyke) d'environ 350 km de long, relie la marge portugaise (anomalies de la zone Sintra-Cabo Raso) au Tore Seamont situé 350 km plus au Nord-Ouest (Fig. 5.16).

Magnetic fabric in a Cretaceous sill (Foz da Fonte, Portugal): magmatic flow model and implications for regional magmatism

M. Neres,[12] **J.L. Bouchez,**[2] **P. Terrinha,**[13] **E. Font,** [1] **M. Moreira,** [14] **R. Miranda,** [5] **P. Launeau,** [6] **C. Carvallo,** [7]

(This chapter is presented in a paper format, as submitted to the *Geophysical Journal International*

Abstract

The intrusion mechanism and internal structure of sills are still not well understood. Here we present a detailed high resolution anisotropy of magnetic susceptibility (AMS) study and orientation of carbonate-filled vesicles of a Cretaceous sill from Portugal in order to better constrain the ∼7 metres along profile magmatic flow. Rock magnetic analyses were conducted in order to identify the nature and grain size of the magnetic carriers. According to their location in the profile, three magnetic fabric domains are identified: (1) at the borders (∼50 cm; chilled margins), low anisotropies suggest that low velocity gradients and heterogeneous flow paths took place during the initial emplacement stages; (2) in the center of the sill, where undisturbed magma flow is expected, low anisotropies are observed, suggesting low shear gradients and magma displacement close to pure translation; and (3) in-between, intermediate zones display high anisotropy values ascribed to maximum shear gradient zones. A mean orientation at ∼N310° of the magnetic lineations (K_1) agrees with the elongation direction of the vesicles and is interpreted as magma flow direction. In addition, a sense of flow toward the southeast is inferred from the mirror imbrication at the borders of the magnetic foliation plane and lineation. Implications of these results are discussed with respect to the West Iberian Late Cretaceous

[1]Instituto Dom Luiz, Universidade de Lisboa, Lisbon, Portugal.
[2]GET - OMP, Toulouse University, France.
[3]Instituto Português do Mar e da Atmosfera, Lisbon, Portugal.
[4]Instituto Superior de Engenharia de Lisboa, Lisbon, Portugal.
[5]Centro de Geologia da Universidade de Lisboa, Lisbon, Portugal.
[6]Laboratoire de Planétologie et Géodynamique de Nantes, France.
[7]Institut de Minéralogie et de Physique des Milieux Condensés, UPMC, Paris, France.

magmatism, by integrating magnetic anomalies, isotope chronology and tectonics. An offshore-onshore 350 km-long magmatic structure connecting the Tore Madeira Rise and the West Portuguese Margin is proposed, from where a >50 km-long connection with the sill is deduced.

5.1 Introduction

Sills are sheet-like magmatic intrusions concordant or parallel to layered host rocks. Their emplacement takes place in environments with a minimum principal stress (σ_3) close to vertical and/or with the presence of sub-horizontal discontinuities, such as sedimentary layers with significant rigidity contrasts [Kavanagh et al., 2006]. Despite the difficulty of studying sills, due to the low probability of their observation at surface level, significant results have been obtained concerning the geometry of magma flow and mode of emplacement. Most of these studies, such as those of Airoldi et al. [2012], Dragoni et al. [1997], Ferré et al. [2002] and Polteau et al. [2008a] are based on low-field anisotropy of magnetic susceptibility (AMS) measurements.

Analysis of the anisotropy of magnetic susceptibility (AMS) leads to determine the magnetic anisotropy ellipsoid, defined by three principal susceptibility axes ($K_1 > K_2 > K_3$) whose orientation is spatially related to the preferred orientation of the elongate magnetic particles, as first proposed by Khan [1962], or to the distribution of interacting particles according to Hargraves et al. [1991]. The first systematic study relating the magnetic fabric and the magmatic flow fabric was the seminal work of Knight & Walker [1988], who observed a strong correlation between the magnetic anisotropy axes and magma flow orientation as deduced from the orientation of elongated vesicles. Several further works used AMS to infer the direction and sometimes the sense of magma flow in dykes [e.g., Aubourg et al., 2008; Callot et al., 2001; Ernst & Baragar, 1992; Femenias et al., 2004; Raposo & Ernesto, 1995]. The flow direction is usually parallel to K_1 and its sense is deduced from the angular relation between K1 and the margins of the sill. It is well known, however, that the magnetic fabric depends on the magnetic mineralogy, on domain state of the grains [Potter & Stephenson, 1988; Rochette et al., 1992] and on the magnetic interactions between grains [Cañón-Tapia, 2001; Fanjat et al., 2012; Gaillot et al., 2006; Hargraves et al., 1991]. These effects will be evaluated hereunder.

Apart from magnetic studies, analogue and numerical models have been published to account for large-scale 3D-shapes and upward/outward propagation of sills, mostly from the continental Karoo-Ferrar formation [Airoldi et al., 2012; Galland et al., 2009; Polteau et al., 2008b], as well as 3D-seismic imaging from oceanic contexts [e.g., Thomson & Hut-

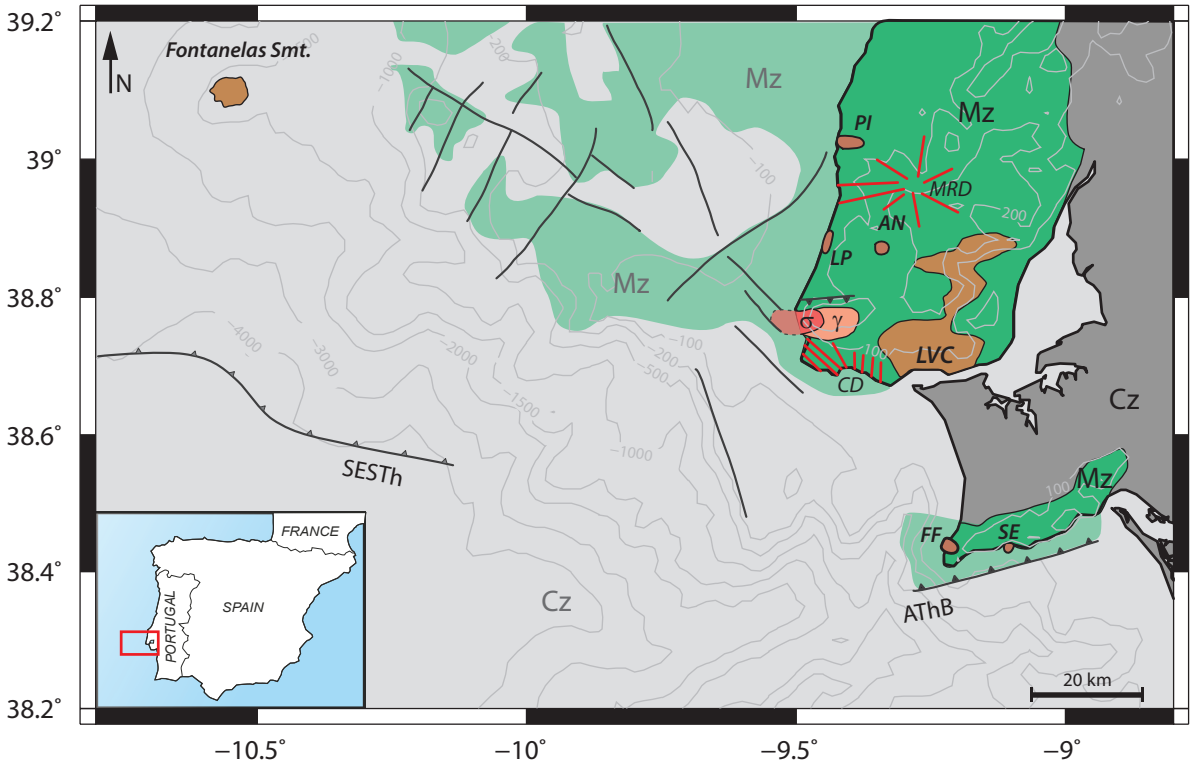

Figure 5.1: Schematic geological map of the study area. Late Cretaceous alkaline magmatic occurrences of the Lusitanian Basin and West Iberia Margin: Sintra igneous complex (γ: granite; σ: syenite); LVC (Lisbon Volcanic Complex); Fontanelas seamount; main sills: AN, Anços; FF, Foz da Fonte; LP, Lomba dos Pianos; PI, Paço de Ilhas; SE, Sesimbra. MRD: Mafra radial dyke complex; CD: Cascais dykes. Mz, Mesozoic sediments (Lusitanian Basin); Cz, Cenozoic sediments. AThB, Arrábida thrust belt of Miocene age; SESTh, Southern Estremadura Spur Thrust.

ton, 2004; Thomson, 2007]. Theoretical and experimental models discuss the propagation mechanisms of dykes, sills and laccoliths into sedimentary basins [Gressier et al., 2010; Kavanagh et al., 2006; Maccaferri et al., 2011; Menand, 2008, among others]. However, the question of how magma flows inside a sill remains, to our knowledge, unexplored. The main goals of this work are: i) to investigate magma flow patterns in a sill using AMS parameters and their variations across a vertical profile; and ii) to infer geological implications of our directional results in the study area.

In the region of Lisbon (Fig. 5.1), several mafic sills of the Late Cretaceous alkaline magmatism of west and south Portugal are accessible for observation and sampling along coastline cliffs or in quarries. In particular, the Foz da Fonte sill (FF-sill) allows a detailed sampling along a vertical section. A detailed AMS profile was conducted along with the study of the magnetic mineralogy which is used to strengthen the significance of the magnetic signal.

5.2 Geological setting

The FF-sill is located on the coastal cliff of the southernmost part of the Lusitanian Basin, a Mesozoic rift-basin located offshore and onshore western Iberia (Fig. 5.1). The rifting before oceanic spreading took place from the Early Triassic through Lower Cretaceous times, with the major extensional event during the Upper Jurassic [Kullberg et al., 2011; Soares et al., 2012; Wilson et al., 1989]. The nature of the Iberia (IAP) and Tagus (TAP) abyssal plains, located between the Tore-Madeira Rise and the Portuguese continental slope, remains under debate. Whether containing the ocean-continent transition or not, it consists of a highly stretched continental crust [e.g., Afilhado et al., 2008; Neves et al., 2009]. The IAP and TAP are separated by the Estremadura Spur that consists in a pop-up block bound by northward and southward directed thrusts (Fig. 5.2) that extend eastwards toward the Lusitanian Basin [Neves et al., 2009; Roque et al., 2009]. The FF-sill crops out at the northern edge of the Arrábida thrust belt, a Miocene structure located at the southern boundary of the Estremadura Spur.

Around Lisbon, a series of igneous bodies intruded the Lusitanian Basin during the Late Cretaceous (Fig. 5.1). Respective ages span from ∼94 to ∼80 Ma [Grange et al., 2010; Matos Alves, 1964; Matos Alves et al., 1980; Miranda et al., 2009; Miranda, 2010; Palácios, 1985; Terrinha et al., 2003, Miranda in prep.]. These bodies comprise lavas, dykes, plugs, sills and laccoliths, the largest volumes belonging to the Sintra Complex (84-79 Ma) and the Lisbon Volcanic Complex. Together with the Complexes of Sines (75 Ma) and Monchique (72 Ma) that outcrop further south (Fig. 5.2), these magmatic bodies constitute the majority of the Late Cretaceous Alkaline Province of Iberia, as defined by Rock [1982].

The FF-sill, dated at 93.8±3.9 Ma ($^{40}Ar/^{39}Ar$ on amphibole, [Miranda et al., 2009] is the oldest intrusive body of this magmatic event. It crops out ∼30 km south of Lisbon (38°27′3.5″N, 9°12′5.5″W) into Upper Albian limestones and claystones. Its exposure consists in a homogeneous fine-grained mafic rock with a maximum thickness of 8 m (Fig. 5.3) and a 150 m-stretch along the coast. The outcrop extends westward into the sea toward the azimuth 310°. The sill is parallel to the bedding of host sediments, the latter being gently tilted toward the NW (230° / 10°, strike / dip). The top part of the FF-sill was already the subject of a paleomagnetic study which revealed a stable natural remanent magnetization carried by titanomagnetite that allowed to define a primary paleomagnetic pole for Iberia at 94 Ma [Neres et al., 2012].

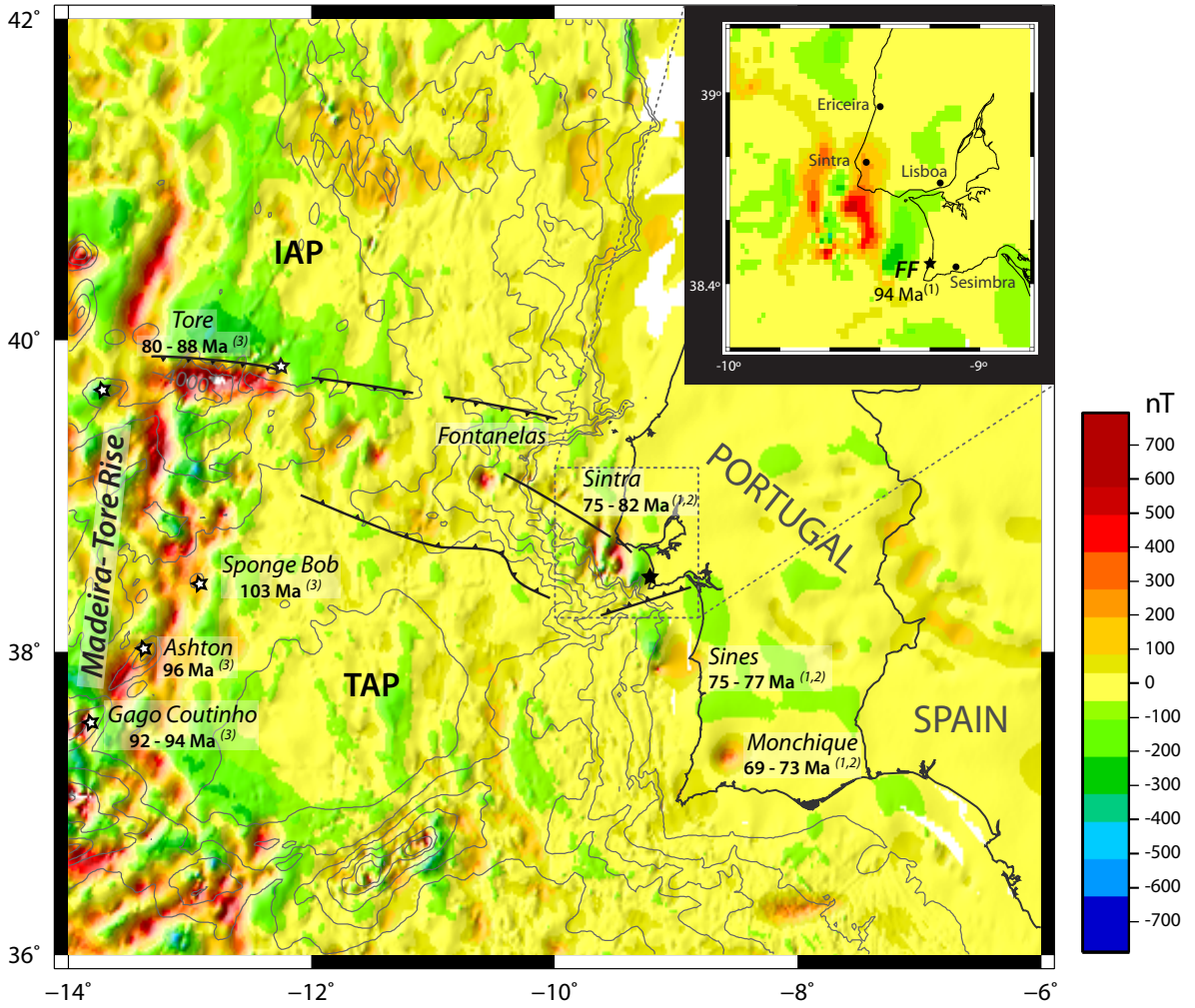

Figure 5.2: Magnetic anomalies of West Iberia (magnetic data from the compilation of Luis & Miranda [2008]). Ages of the Late Cretaceous onshore alkaline magmatism, as well as seamounts, are indicated. The onshore plutons (Monchique, Sines, Sintra) have strong magnetic signatures that extend offshore in the case of Sines and Sintra. Several punctual magnetic highs such as the Fontanelas Seamount form a lineament that extends from Sintra to the Tore Seamount. Inset: enlargement of the region of the Foz da Fonte (FF) sill; note the strong magnetic anomaly to the NW of FF-sill and south of Sintra (Cabo Raso anomaly). References for ages of Late Cretaceous onshore alkaline magmatism and seamounts: (1) Miranda et al. [2009], (2) Grange et al. [2008], (3) Merle et al. [2006].

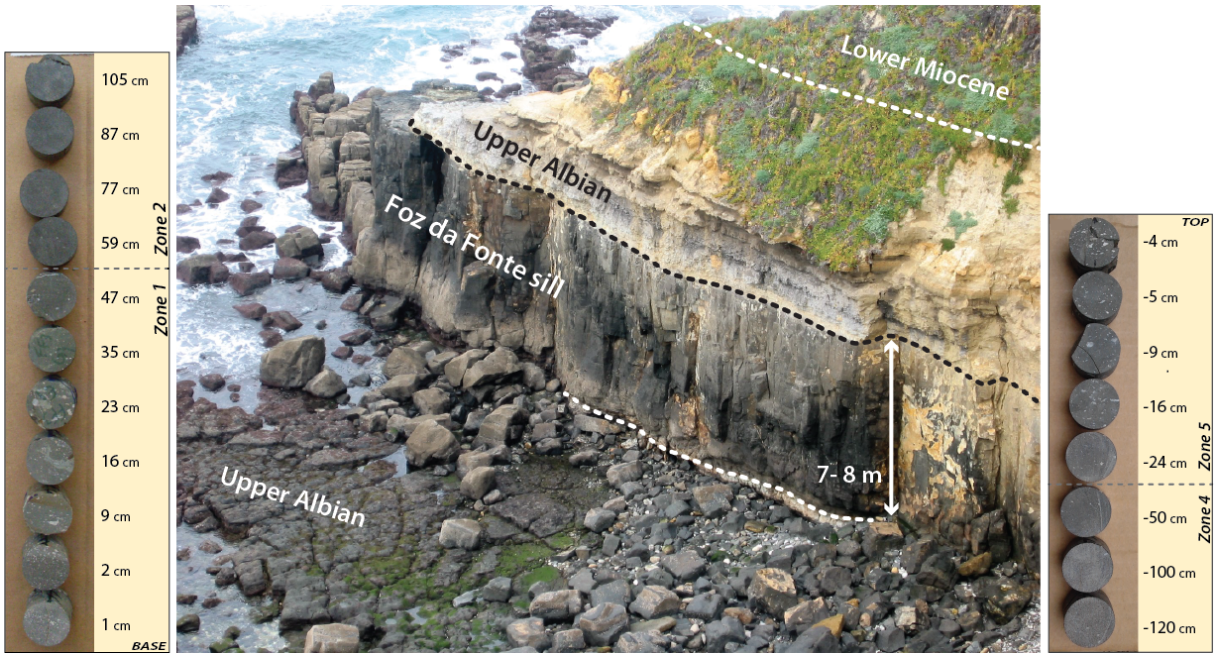

Figure 5.3: View from the south of the 7-8 m thick sill and the hosting Lower Cretaceous sediments unconformably overlain by the Lower Miocene. Columns on both sides show the aspect (colour, presence of vesicles) of specimens collected from the lower and upper contact zones: close to the sediments (zones 1 and 5) the specimens contain visible, sub-horizontally elongated vesicles filled with carbonate. See also Fig. 5.13.

5.3 Sampling and methods

Sampling of the FF-sill was realized during two sessions using a portable drilling equipment, the orientation being ensured by a solar compass. The first session [Miranda et al., 2006] concerned the upper exposed surface of the sill (from ∼50 cm to ∼1.5 m below the top contact) and provided 109 specimens from 19 sites. In the second session, a 7.2 m-high vertical profile was sampled in three different sites, a few meters apart from each other. The first site close to the basal contact (0 m to 1.1m) provided 11 cores; the second site provided 40 cores from 1.3 m to 6.7 m, and the third one gave 16 cores from 5.2 m up to the top (7.2 m). From this "vertical" sampling, 67 cores (171 specimens) were collected. Vertical spacing between samples is 10-30 cm, except near the base and top contacts where it is less than 10 cm. In the results section, the first and second sites will be presented as Profile A and the third site as Profile B.

Magnetic susceptibility and anisotropy of the specimens were measured with a MFK1 Kappabridge (AGICO) at the Instituto Dom Luiz (Lisbon University) under room temperature (applied field: 200 Am-1; frequency: 976 Hz). The *Anisoft* [Chadima & Jelinek, 2008] and *Stereonet* [Allmendinger et al., 2012] softwares were used for data processing. Scanning Electron Microscope (SEM) observations coupled with Energy Dispersive

Spectra (EDS) were performed on carbon-coated sections using the Jeol JSM-6360LV of the Geoscience Laboratory of Toulouse (France). We used complementary geochemical data (Loss on Ignition and Mg#) coming from analyses performed in the Universidad Autonoma de Madrid (Spain). Thermomagnetic susceptibility was measured in Ar-atmosphere by using a CS4 furnace (AGICO) coupled to the Kappabridge.

Hysteresis curves and First-order reversal curve (FORC) diagrams [e.g., Roberts et al., 2000] were measured in order to characterize the size of the magnetic carriers. The measurements were carried out at room temperature using a PMC μ-Vibrating Sample Magnetometer (μ-VSM) within the IPGP-IMPMC Mineral Magnetism Analytical Facility. For each sample, 100 FORCs were measured on a millimetric chip and the FORC distribution was calculated using a smoothing factor of 5 with the *Mathematica* program provided by Chris Pike [Pike et al., 1999].

5.4 Petrographic features

As described by Miranda [2010], the rock is a very fine-grained ultramafic alkaline tephrite (SiO_2 <45%) with pyroxene (Ti-augite), brown-amphibole (kaersutite), plagioclase, apatite and opaque minerals as the main phases (Fig. 5.4). Several carbonate-filled vesicles and ubiquitous felting of chlorite are particularly abundant toward the top and basal contacts. This makes the rock lighter in color, particularly at the lower contact (Fig. 5.3), a peculiarity attributed to the effect of fluids, due to magma-host interaction, larger in the lower contact than in the upper one. Chlorite is abundant around amphiboles and carbonate phases are ubiquitous, mainly inside vesicles and fractures (Fig. 5.4b,d,e). Interaction between the magma and the host sediments is also measured by the loss on ignition from conventional chemical analyses (LOI%: Fig. 5.5a). It varies from ∼5% toward the center of the sill to ∼15% close to the lower and upper contacts. Such a high interaction with the host sediments near the margins does not allow discussing chemical analyses in terms of within-profile magma differentiation. For example, the D-shape of the Mg-number (Mg# = Mg/(Mg+Fe_{tot}); Fig. 5.5b), discussed by some authors in terms of flow of melt within the sill [Aarnes et al., 2008] is attributed in our case to the mobility of elements in presence of fluids at the basal and top contacts. However, this late magmatic hydrothermalism has not (substantially) modified the original arrangement of the constituting minerals (Fig. 5.4).

The opaque minerals are homogeneously distributed in the rock and form either independent crystals of a few microns or variously elongate clusters of crystals some tens of microns in size (Fig. 5.4). Note that the opaque minerals are smaller and have a tendency

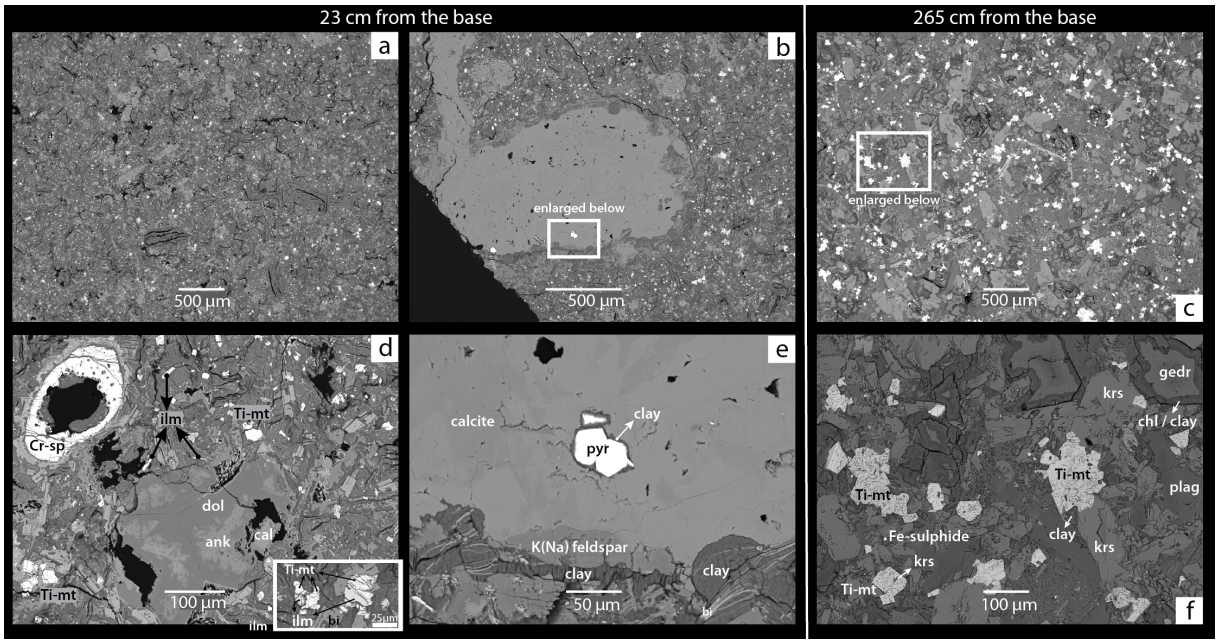

Figure 5.4: Scanning electron microscope (SEM) images of FF specimens. (a,b,d,e): specimen FF3-E2, located 23 cm from the base; (c,f): specimen FF4-K1, located 275 cm from the base. Close to the host-sediment (specimen FF3-E2), despite low- and high-temperature alterations, the primary rock texture is preserved. Inside of the sill, the crystals retain their magmatic composition, with the exception of some altered grain-boundaries. The well-preserved opaque minerals are smaller and more dispersed close to contact (specimen FF3-E2) than far from it (specimen FF4-K1) where they tend to form large clusters (compare (a) and (c) at identical scales). Ti-mt: titanomagnetite; ilm: ilmenite; Cr-sp: chromite-spinel; dol: dolomite; cal: calcite; ank: ankerite; bi: biotite; krs: kaersutite; gedr: gedrite; chl: chlorite; plag: plagioclase; pyr: pyrite.

to be more isolated from each other close to the borders of the sill (Fig. 5.4a,d), whereas clusters tend to reach sizes up to 100-200 microns at inner parts of the sill (Fig. 5.4c,f). As determined using SEM-EDS measurements, most opaque minerals are titanomagnetites with varying amounts of titanium, partly related to ilmenite exsolutions within titanomagnetite (inset of Fig. 5.4d). At inner regions of the sill, titanomagnetites are richer in Ti and with less variable Ti-content (TiO_2: ∼25-30%) than close to the borders (TiO_2: ∼15-35%). Chromium-bearing spinels (Fig. 5.4d) and small Ni-bearing iron-sulphides are also locally observed. Mineral species attributed to late-magmatic modifications are also observed: pyrite (Fig. 5.4e) and apatite, rutile, K-feldspar, biotite, chlorite and clay minerals (Fig. 5.4e, f).

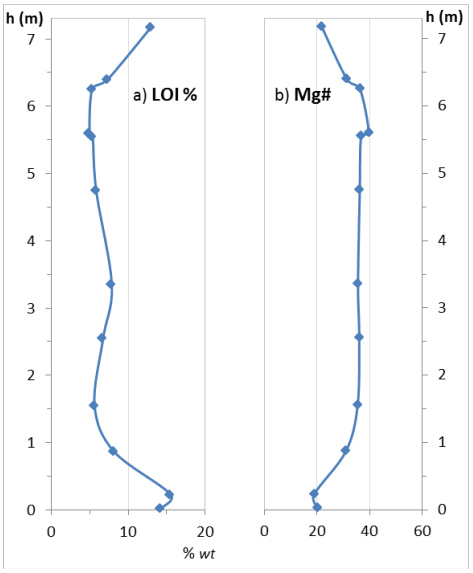

Figure 5.5: (a) Loss on ignition (LOI) and (b) magnesium number (Mg# = Mg/(Mg+Fe$_{tot}$)) from samples regularly distributed along the vertical profile. The high LOI values reflect the strong interaction between magma and host sediments at contact zones. For this reason the Mg# cannot be here interpreted in terms of magma differentiation.

5.5 Magnetic mineralogy

The detailed rock magnetic study from the upper part of the sill performed by Neres et al. [2012] revealed a primary (magmatic) magnetic mineralogy, corresponding to low-coercive pseudosingle-domain to multi-domain (PSD-MD) titanomagnetites. The variability of the magnetic mineralogy along the vertical profile is here studied on nine specimens regularly distributed along the profile. Temperature dependence of magnetic susceptibility K(T) from all specimens shows susceptibility drops from ∼350°C to ∼550°C, attributed to titanomagnetites with variable amounts of titanium (Fig. 5.6).

Specimens located in the ∼80 cm from the top and basal contacts (FF3-A, FF3-J and FF5-D) display the highest Curie temperatures (average T$_c$ around 560°C) and hence have compositions closer to pure magnetite. Inner specimens display a common susceptibility drop at T$_c$ ∼520°C, pointing to phases richer in Ti, in addition to other drops at lower temperatures. The FORC diagrams (Fig. 5.7) for the nine studied samples are all very similar and characteristic of PSD magnetic grains [Roberts et al., 2000]: the inner contours are closed but the outer contours are divergent. The coercivity for which the distribution is maximum around 10 mT, but contours extend up to 40 mT or even 60 mT for some samples (Fig. 5.7).

The hysteresis parameters Mrs (saturation remanent magnetization)/Ms (saturation magnetization) and Hcr (coercivity of remanence)/Hc (coercivity field) plotted on a Day-

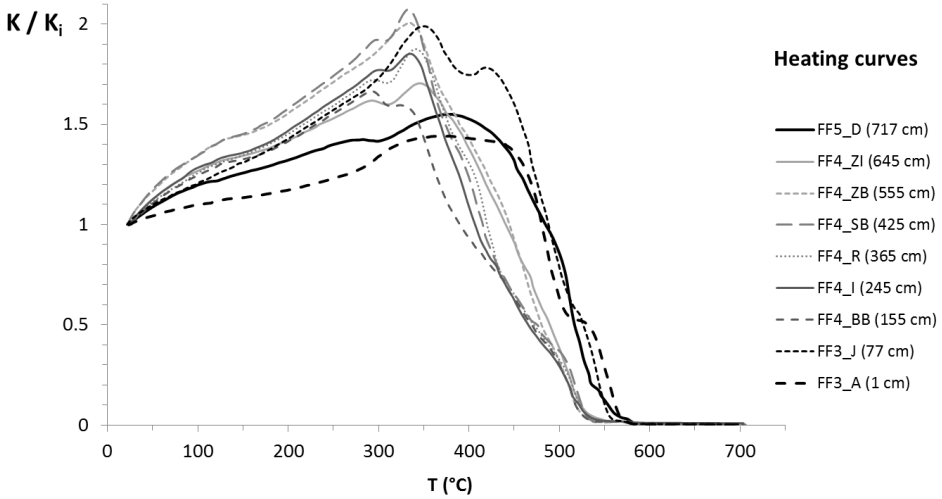

Figure 5.6: Thermomagnetic heating curves for samples regularly distributed along the profile of the sill. All curves are normalized to the respective initial susceptibility value.

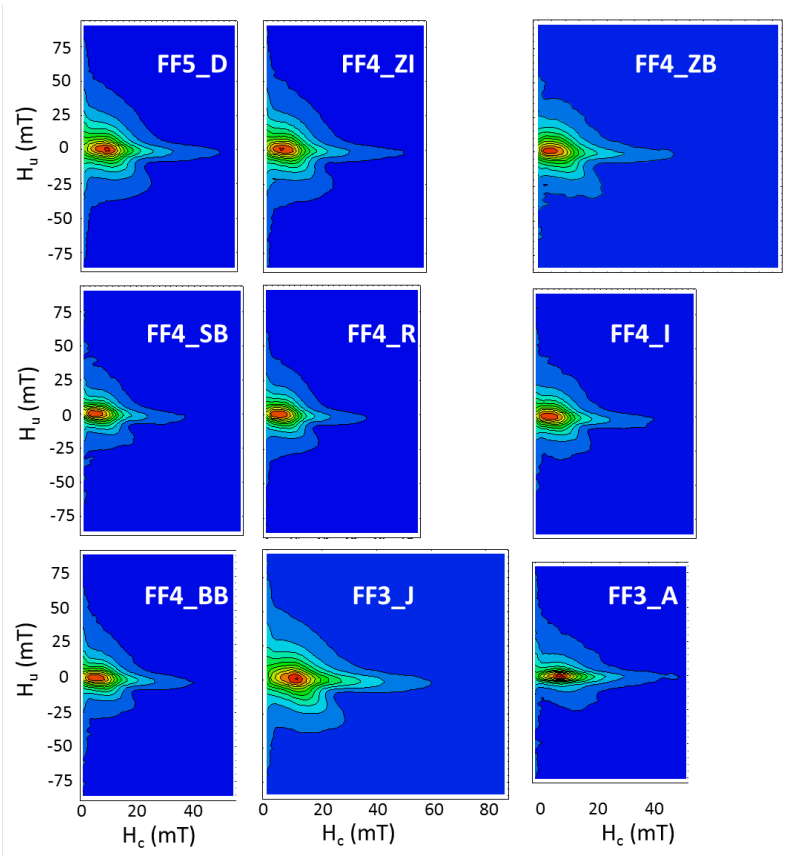

Figure 5.7: FORC (first order reversal curves) diagrams for the same set of samples as in Fig. 5.6. All diagrams are very similar and characterize PSD magnetic grains [Roberts et al., 2000].

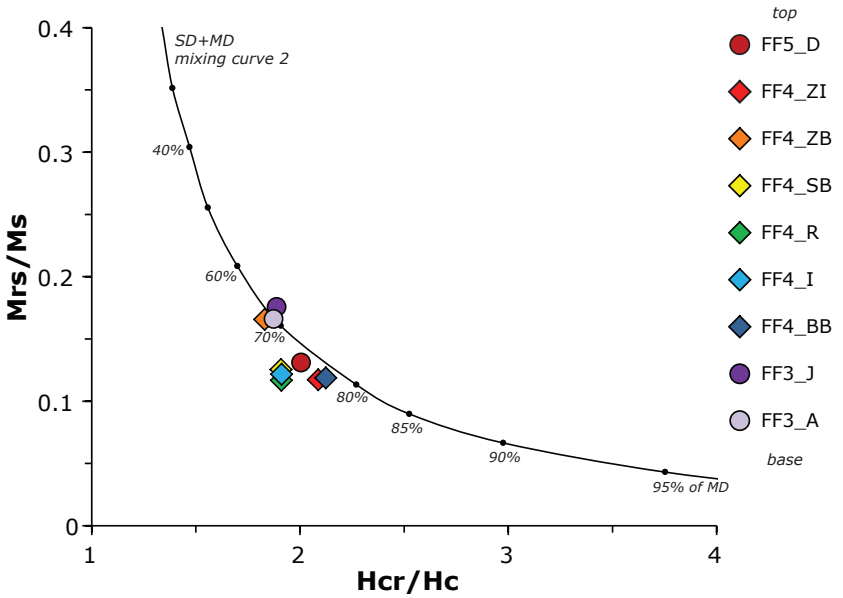

Figure 5.8: Day plot (ratio of saturation remanence to saturation magnetization, M_{rs}/M_s, against the ratio of remanent coercive force to ordinary coercive force, H_{cr}/H_c [Day et al., 1977]) for the same set of samples as in Figs. 5.6 and 5.7. The data plot in the PSD region and fit the theoretical curve #2 of Dunlop [2002b] in the 70-77% MD (multi-domain) segment, pointing to a high homogeneity of the domain states of the magnetic minerals of the sill.

plot (Fig. 5.8) are also consistent with PSD behaviour: they plot along the theoretical curve #2 of Dunlop [2002a,b] and cluster around 70% - 77% of MD-grains, pointing to a high homogeneity of the domain states of the magnetic carriers in the sill. In conclusion, these measurements show that MD-titanomagnetites are the dominant magnetic carriers throughout the section.

5.6 AMS results

The magnetic data under consideration will be as follows: bulk magnetic susceptibility (K_m=(K_1+K_2+K_3)/3), total (P = K_1/K_3), linear (L = K_1/K_2), planar (F = K_2/K_3) and shape (T = (2lnK_2-lnK_1-lnK_3)/(lnK_1-lnK_3)) anisotropy parameters; and azimuth/plunge of K_1 and K_3, the magnetic lineation and pole to magnetic foliation, respectively.

5.6.1 Bulk magnetic data

The magnetic data from the first sampling session integrates measurements from the upper part of the sill (∼0.5 – 1.5 m below the top contact), with bulk magnetic susceptibility values around 74±17 10^{-3} SI, a total anisotropy percentage (P%) spanning between 1%

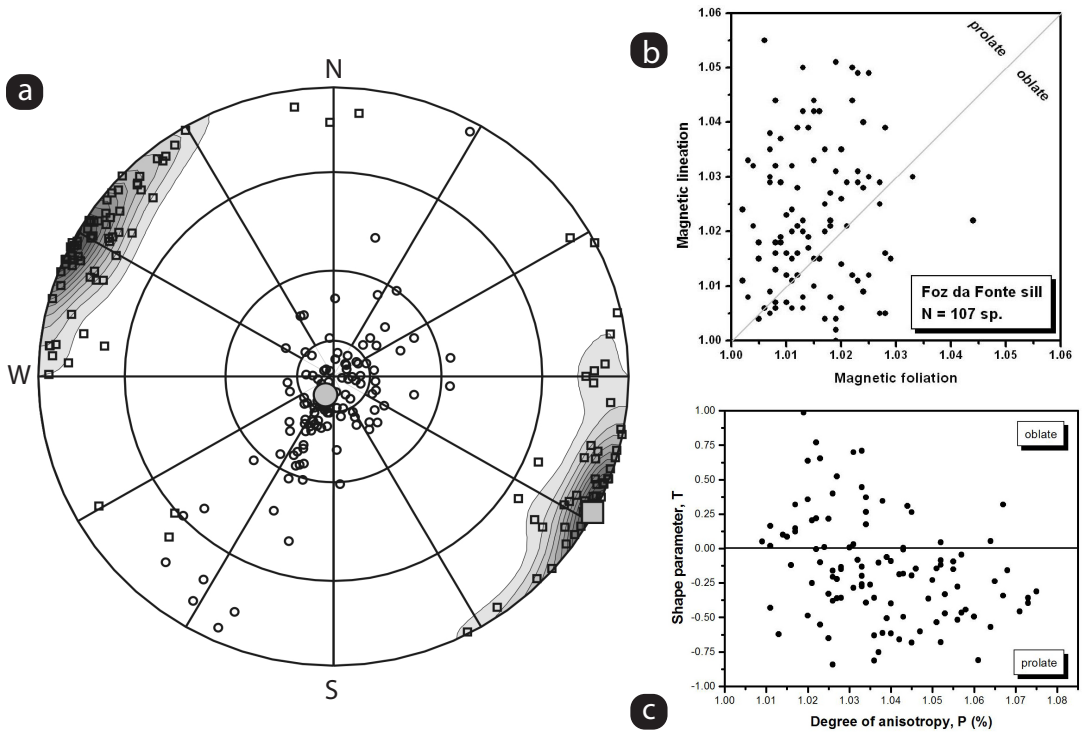

Figure 5.9: AMS results from the first sampling session (109 specimens on the exposed upper surface of the sill). (a) K_1 (squares) and K_3 (circles) axes, and density contours. Mean directions are represented with full symbols: $K_1 = 118° / 1°$ ($e_{31} = 1.3°$, $e_{12} = 3.0°$); $K_3 = 204° / 84°$ ($e_{31} = 1.3°$; $e_{23} = 3.1°$). Equal-area projection in geographical coordinates. (b) L (linear anisotropy) versus F (planar anisotropy) diagram. (c) T (shape parameter) versus P (total anisotropy diagram. The prolate shape (linear anisotropy) dominates the magnetic fabric.

and 7.5%, and a clear tendency for a linear anisotropy (average L% = 2.2 against average F% = 1.5) (Fig. 5.9). As expected, the magnetic foliation is close to horizontal (plunge of $K_3 = 84°$). The average magnetic lineation is extremely well defined, parallel to WNW-ESE (average $K_1 = 118°/01°$, trend/plunge) with confidence ellipses $e_{31} = 1.3°$ and $e_{12} = 3.0°$. The orientation of K_1 can therefore be interpreted with great confidence [Pueyo et al., 2005].

The magnetic data corresponding to the 67 core-samples (averages of 2 to 5 specimens/core) along the vertical profile (second sampling session) are reported in Table 5.2 (Section 5.9). The bulk magnetic susceptibility (K_m) for this profile varies from 30 to 67 10^{-3} SI with a mean value of 54 10^{-3} SI. The anisotropy percentage P% varies from 0.5 to 8.3% (mean: 3.1%), distributed into L%: 0.0 to 5.1% (mean: 1.5%) and F%: 2.0 to 4.6% (mean: 1.6%). The shape parameter T almost covers the whole range of values, from -0.8 to 0.97. Contour plots of the spatial orientation of K_1 and K_3 from all core-samples display remarkably well-defined sub-horizontal and sub-vertical distributions, respectively (Fig. 5.10). The average dip of all the magnetic foliations is a few degrees to the north

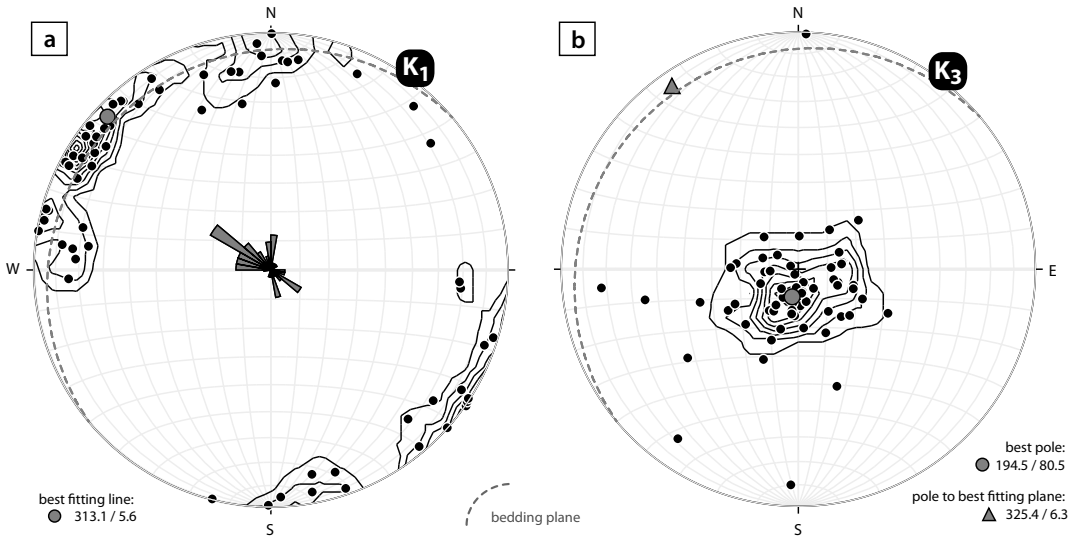

Figure 5.10: Directional AMS results for the second sampling session (67 core-samples along a vertical profile). Contour plots of K_1 (a) and K_3 (b) distributions. The rose diagram for K_1 (by 15° angular classes) is also represented as well as the bedding plane of the sill (230° / 10°; strike / dip; dashed great circle).

(best K_3 axis: 195°/81°). It reasonably agrees with the bedding plane, slightly dipping to the northwest (230°/10°, strike/dip or 320°/10°, strike of dip/dip). A trimodal distribution of the magnetic lineations (K_1 azimuths) is observed, made of a main sub-population trending around 300° and two minor ones around 285° and 0°. The average lineation corresponding to all samples slightly plunges to the northwest (best fitting line: 313°/06°) (Fig. 5.10a).

5.6.2 Along profile variations

The weighted arithmetic running means (using a double-weighted central value with respect to nearest neighbors) for K_m, P, L, F and T, as well as the azimuths of K_1 (K_1az, unweighted tensorial means of respective specimens) are given in Table 5.4 (Section 5.9). These data are plotted in Fig. 5.11 as vertical profiles, as a function of the elevation with respect to the floor of the sill. The top part comprises a partial sampling overlap between profiles A and B (from 5.2 m to 6.7 m), which will be used to discuss the directional variability of the magnetic lineation.

Based on the along-profile directional and scalar variations, five zones were defined. Stereoplots of K_1 and K_3 (in geographical coordinates, with indication of bedding plane) and anisotropy parameters biplots (L vs. F, and T vs. P) are represented in Fig. 5.12 for all specimens, and for each zone. The mean tensorial values are listed in Table 5.1 and given in both geographical and tilt-corrected (paleo-horizontal: bedding rotated into

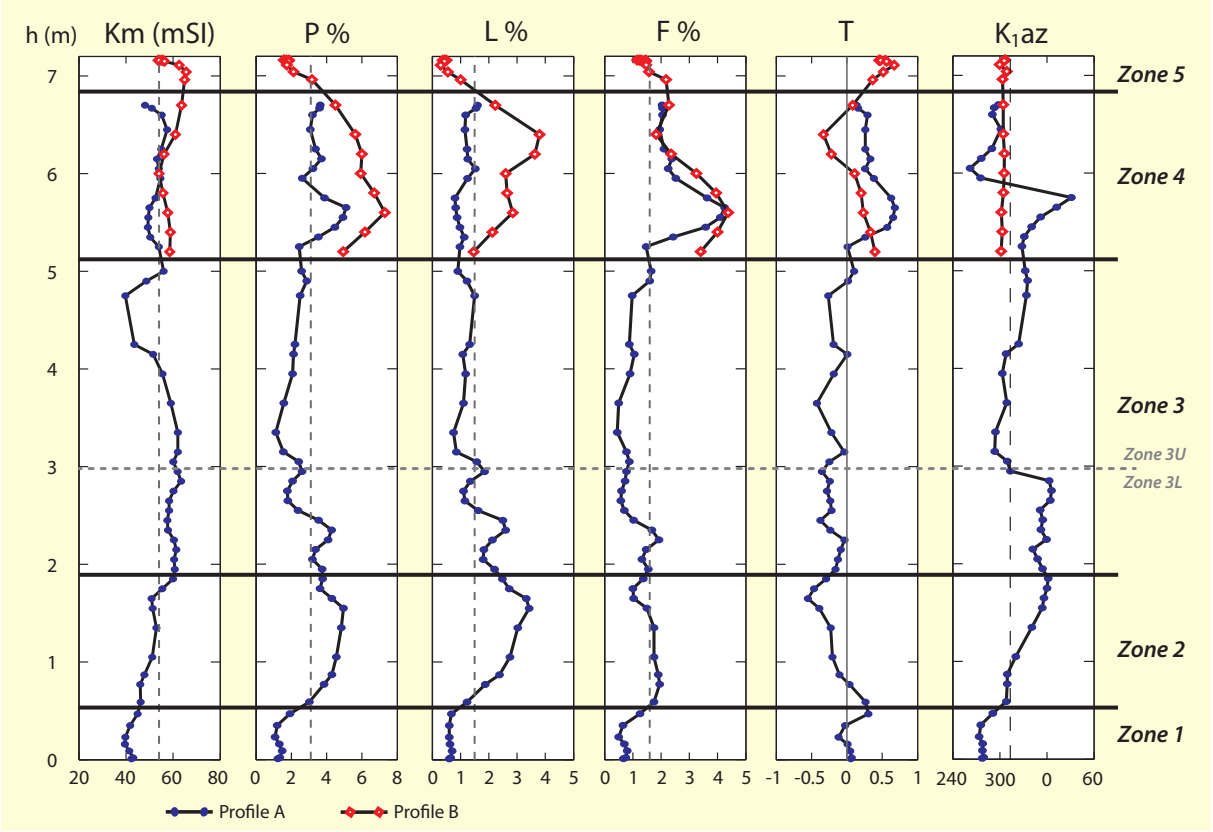

Figure 5.11: Vertical profile of the AMS in the Foz da Fonte sill. Bulk susceptibility Km (10^{-3} SI), linear (L), planar (F), total (P), shape (T) parameters, and azimuth of K_1 are represented as a function of the elevation from the base of the sill (h). Dashed lines represent the mean value for each parameter (54 mSI, 3.1%, 1.5%, 1.6%, and 330° for Km, P, L, F and K_1az, respectively), except for T, where the full line indicates T = 0.

			geographic				tilt corrected	
Zone	N	h (m)	K_1	e_{12} / e_{31}	K_3	e_{23} / e_{31}	K_1	K_3
5 (top)	14	6.9 - 7.2	127.2 / 1.4	15.2 / 6.7	223.5 / 77.2	9.4 / 5.3	126.9 / 11.2	263.3 / 74.7
4	48	5.1 - 6.9	304.2 / 3.8	14.4 / 5.3	195.3 / 78.3	8.7 / 5.8	124.2 / 5.8	248.8 / 79.9
3U	33	3.0 - 5.1	315.4 / 8.3	26.3 / 9.3	165.5 / 80.4	19.2 / 11.0	135.5 / 1.7	248.2 / 85.7
3L	34	1.9 - 3.0	354.9 / 4.7	19.9 / 8.9	251.7 / 70.1	30.7 / 10.4	174.8 / 3.5	272.3 / 64.7
3	67	1.9 - 5.1	342.2 / 6.1	30.5 / 13.7	210.1 / 81.0	23.4 / 12.5	162.1 / 3.2	269.0 / 79.1
2	24	0.5 - 1.9	337.5 / 2.2	30.7 / 7.4	82.4 / 81.7	9.8 / 6.3	157.7 / 7.4	12.2 / 81.1
1 (base)	18	0 - 0.5	277.4 / 16.3	8.5 / 5.1	130.2 / 70.9	9.4 / 5.1	278.9 / 8.8	120.0 / 80.6

Table 5.1: Directional AMS results per zone. N: number of specimens in each zone; h: vertical position in the sill; mean K_1 and K_3 orientation (dec / inc) in the geographical system and after tilt correction to the bedding plane (230° / 10°, strike / dip), and respective confidence ellipses. In bold, values showing the imbrication of magnetic foliation plane and lineation.

horizontal) frames.

Zones 5 and 1 correspond, respectively, to the first ∼40 cm under the top of the sill and to the ∼50 cm above its base. These zones are characterized by very low anisotropies ($P < 2\%$ and $L < 1\%$). The planar anisotropy is low in both zones, but slightly higher at the top (zone 5; $F > 1\%$) than at the base (zone 1; $F < 1\%$). Therefore, the shape fabric parameter is close to triaxial ($T \sim 0$) at the base and more oblate toward the upper contact ($T > 1$).

Zones 4 and 2 display the highest anisotropies. In zone 4, both profiles (A and B) display a strong planarity, the highest values being found in-between 5.5 and 6 m, but also a strong linearity in the case of profile B. In zone 2, the anisotropy is strongly linear. Similarly to what is observed in the marginal zones of the sill (zones 5 and 1), the anisotropy is more planar close to the top of the sill (zone 4, where the fabric is mainly planar, or oblate) than at its base (zone 2, linear or oblate fabric).

Zone 3 corresponds to the inner part of the sill (3.2 m in thickness), where rather low anisotropy is observed. However, two sub-zones can be distinguished: an upper zone 3U (∼2.2 m thick) where the anisotropy parameters are rather constant, and a lower one 3L (∼1 m thick) in which the anisotropy parameters are more variable. The limit between 3U and 3L is mainly characterized by a drastic change in the direction of the magnetic lineation (K_1), from 320° (3U) to 0° (3L) in average values.

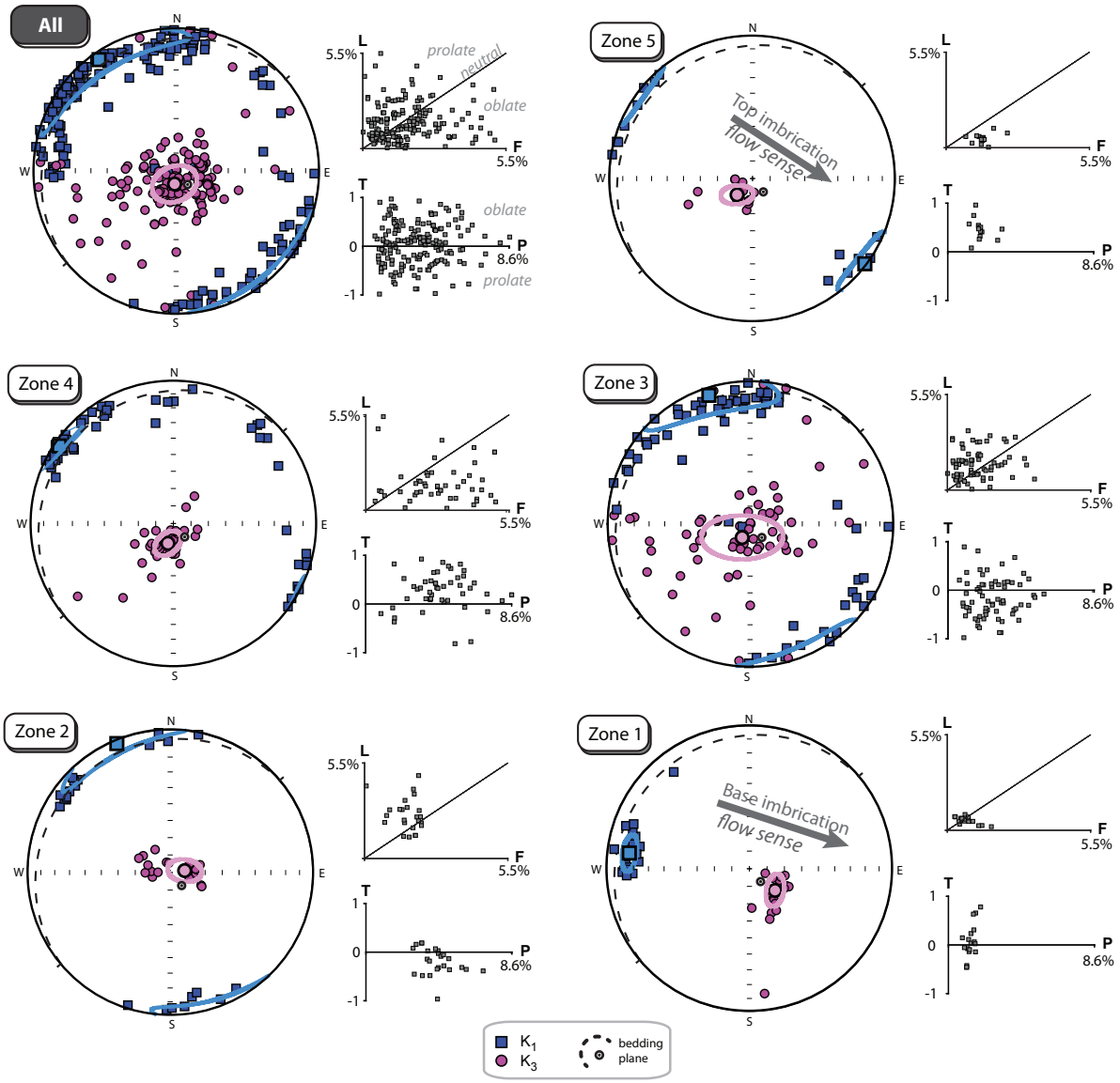

Figure 5.12: Along profile directional diagrams (K_1 and K_3 axes) and biplots of AMS parameters (L vs. F and T vs. P) of the FF-sill: all specimens (n = 171) and per zone. The bedding plane is the dashed great circle. An imbrication of the magnetic lineation (K_1) with respect to the bedding plane is observed between zones 1 (base) and 5 (top), and implies a magma flow sense toward the south-east. See also Table 5.1.

5.7 Discussion

5.7.1 Mineralogical variability

From our mineralogical observations using optical and electron microscopes, the main along-profile petrographic variations are concluded to come from the interaction with fluids extracted from the unmetamorphosed sedimentary rocks hosting the sill. The effect of fluids is witnessed by the carbonate-bearing vesicles, a few mm to 2 cm in length, that are present in ∼1 m close to both contacts (Figs. 5.3, 5.13). For example, specimen FF3-E (23 cm from the base) is invaded by carbonates, mostly found in vesicles and veinlets (Fig. 5.4b), and by clay minerals and chlorite attesting to the presence of hydrothermalism. Higher temperature transformations (biotite, K-feldspars, ilmenite exsolutions, etc) are also present (Fig. 5.4d,e). By contrast, specimen FF4-K (265 cm from base) is close to its primary (magmatic) mineralogy (kaersutite, gedrite, plagioclase, some Ni-Fe-bearing sulfides, etc), despite the presence of clay/chlorite along amphibole grain-boundaries (Fig. 5.4f) and occasional patches of carbonates.

Hydrothermal alteration is likely responsible for the rather low susceptibilities observed, in particular, close to the basal contact where light-colored specimens are present (Fig. 5.3). Susceptibility decrease may also be due to the larger dispersion of the individual magnetic grains against the contacts than inside the sill (compare Fig. 5.4a to Fig. 5.4c). The higher dispersion prevents magnetic interactions between grains, a mechanism responsible for the increase in magnetic susceptibility and anisotropy [Grégoire et al., 1995; Hargraves et al., 1991].

However, as already noted, the original magmatic texture has not been (substantially) modified, as attested for example by the primary arrangement of plagioclase laths (or ghosts of them) that are observed everywhere in the sill. It is also likely that the titanomagnetites, which form either isolated, euhedral and low shape ratio individuals, or clusters of grains which may be significantly elongated (Fig. 5.4), have their original (magmatic) shapes.

5.7.2 Linking AMS with direction and sense of magma flow

Close to the sill margins (zones 1 and 5) the rock displays a variable density of elongated vesicles into which carbonate grains have crystallized (Figs. 5.3, 5.4b,d and 5.13a). These vesicles, likely inherited from magma degasing, display ellipsoidal shapes due to magma deformation before solidification. The vesicles are therefore considered as passive markers, recording the strain that accumulated during the last stages of magma emplacement. This

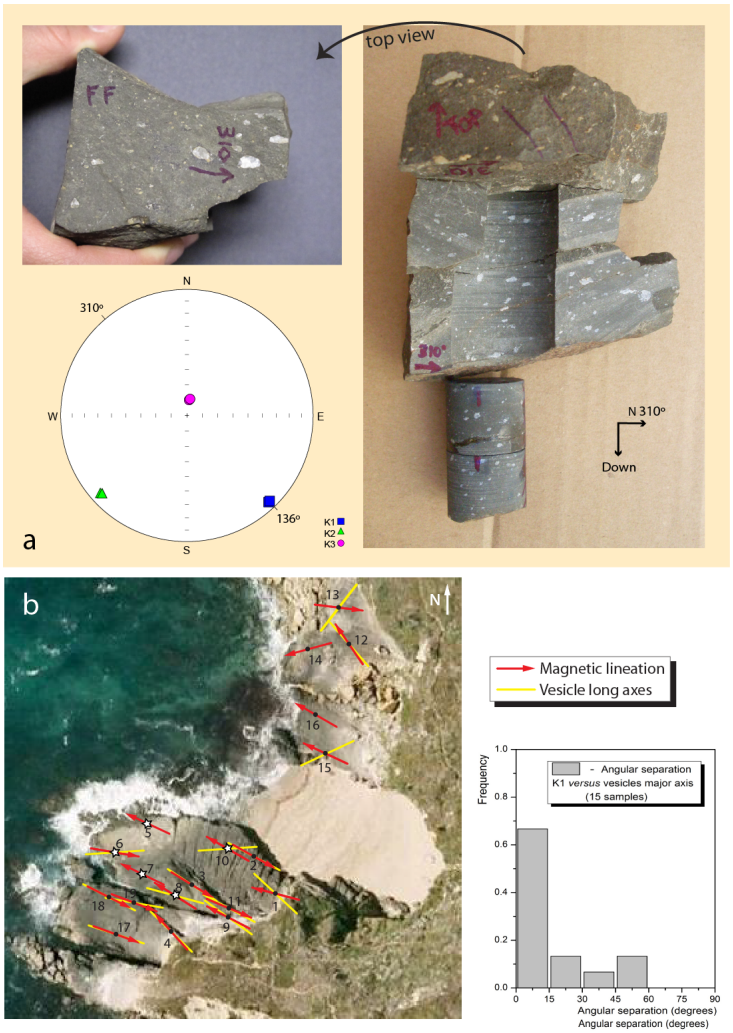

Figure 5.13: (a) Oriented photographs and stereographic plot of the magnetic fabric of a hand-sample from the upper surface of the FF-sill. The magnetic lineation (K_1), measured for specimens drilled from this rock, parallels the direction of maximum elongation of vesicles, a macroscopic indicator of magma flow direction. In this hand-sample, an imbrication of the vesicles (gently plunging toward the N130°) is remarkable and matches the plunge of K_1, pointing to a magma flow sense toward the south-east. (b) Vertical view of the FF-sill, showing the 19 sites from the first sampling session. For 15 sites, the elongation direction of the vesicle long axes (in yellow) is compared with the local magnetic lineation (K_1az, in red). Their angular separation is given in the histogram. Stars indicate locations from which the image analyses were undertaken (see Fig. 5.14).

is illustrated by an oriented hand-specimen coming from the exposed upper surface of the sill, in which aligned vesicles are elongated parallel to the 310 – 130° azimuth and plunge toward the southeast (130°) by an angle of ∼10° with respect to bedding (Fig. 5.13a). The AMS measurement from this specimen gives an azimuth of K_1 at 136°, with a plunge of 6° to the southeast, along with a subhorizontal magnetic foliation. Such a test reveals that the magnetic fabric agrees with macroscopic flow indicators, here represented by the vesicles. This test is strengthened by our systematic sampling of the upper part of the sill (first sampling session), which reveals that the vesicles long axes and the nearby measured K_1 azimuths are strongly correlated, being closer than 15° for 67% of the measurement sites, and closer than 30° for 83% of these sites (Fig. 5.13b).

A mirror imbrication, within both chilled margins, of the mean magnetic foliation and lineation with respect to the bedding plane is unequivocal (K_1 plunge: 11° toward N127° in zone 5 and 9° toward N279° in zone 1; Fig. 5.12, Table 5.1). This observation allows inferring the magma flow sense from the northwest to the southeast [Callot et al., 2001; Geoffroy et al., 2002; Knight & Walker, 1988]. Moreover, in addition to the azimuth agreement of vesicles long axes and magnetic lineation, an imbrication of the vesicles in some hand samples close to the contacts was also observed to be concordant with the imbrication of magnetic lineation. This is exemplified in Fig. 5.13a: the vesicles are gently plunging towards ∼N130°, matching the local imbrication of magnetic lineation and agreeing with a southeastward directed sense of flow.

In conclusion, our directional data can be interpreted in terms of flow fabric and sense of magma flow. The high statistical significance of the imbricated fabric prevents the need of using a deeper statistical analysis [e.g., Tauxe et al., 1998].

5.7.3 Linking the magnetic lineation with the shape fabric of the opaque grains

In order to ensure the significance of our AMS measurements in terms of shape fabric of the magnetic grains, an image analysis has been applied to specimens collected during the first sampling session (exposed surface of the sill). 44 images have been captured from 6 thin sections (cut parallel to the subhorizontal magnetic foliation) coming from the 5 sampling stations starred at Fig. 5.13b. One of these images along with the corresponding threshold image that allowed to sort the opaque grains, is represented at Fig. 5.14a,b. Application of the *Intercept* method of Launeau & Robin [1996] allowed to determine for each image the intercept rose and the respective shape preferred orientation of the opaque phase. A histogram of the angular difference between the preferred orientation of opaques

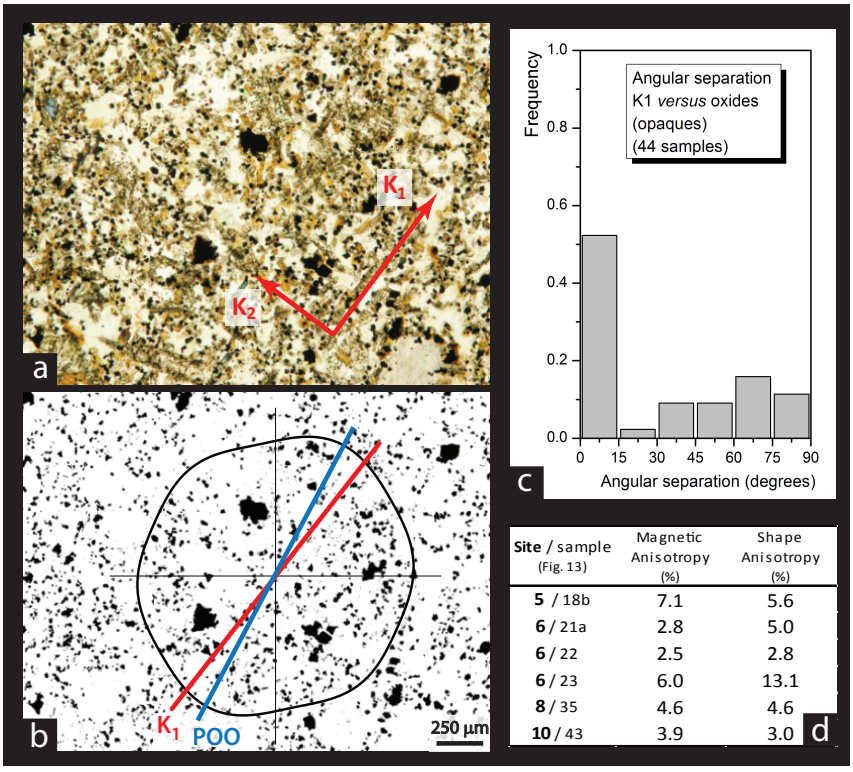

Figure 5.14: 2-D image analysis of opaque minerals, and comparison with magnetic lineation (K_1). (a) Oriented microphotograph taken from a section containing K_1 and K_2 (sample 18b, site 5, ∼70 cm below the top of the sill, zone 4). (b) Respective threshold image of opaque grains and rose of directions calculated by the Intercept method of Launeau & Robin [1996]. The shape preferred orientation of opaques (POO) is given by the maximum of the rose of directions. The difference, in the foliation plane, between the K_1 (38°) and POO (28°) of this image is 10°. This difference was calculated for 44 images (6 thin sections from 5 starred sites in Fig. 5.13) and is represented in (c). (d) Comparison between the total magnetic anisotropy (P%) and the shape anisotropy determined by image analysis.

and the local magnetic lineation is shown at Fig. 5.14c. A clear monomodal distribution is revealed, with angular deviations less than 15° in 53% of the cases. This mode reflects the strong coaxiality that exists, at least in the foliation plane, between the magnetic lineation K_1 and the shape fabric of the opaque grains. It is attributed to the clusters or aggregates of grains, which are principally responsible for the shape fabric. Note that deviations larger than 30° between K_1 and the grain-shape fabrics are rather equally distributed between 30° and 90°. These results strongly suggest that these weaker modes are mostly associated with the small, isolated and equant grains that are randomly or homogeneously distributed in the rock. In addition, with the exception of measurements from station #7, a rather good agreement is verified between the grain shape anisotropy deduced from these images and the magnetic anisotropy degree (Fig. 5.14d).

In conclusion, (i) the textural peculiarities of the sill exemplify the need of collecting a large number of images in order to obtain a representative result on image analysis; and (ii) the observed magnetic fabrics can be confidently interpreted in terms of shape anisotropy of the clusters of magnetic grains. However, in view of the small discrepancies existing between the grain shape fabrics and the magnetic anisotropy (Fig. 5.14d) some contribution of distribution anisotropy including magnetic interactions between grains cannot be excluded.

5.7.4 Interpreting the along-profile variations

In this section, it is attempted to interpret the magnetic anisotropy in terms of flow dynamics, through the shape fabrics of the opaque grains. The three principles of our reasoning are the following:

(1) The main carriers of the magnetic anisotropy are the aggregates of magnetic grains, which correspond to grains that got magnetically clustered at a given stage of magma flow;

(2) The non-clustered magnetic grains are made of minute ($\ll 10$ μm), close to cubic individuals that escaped clustering. The individual/cluster ratios as well as the grain density itself are variable: grain concentration appears to be lower against the boundaries of the sill (Fig. 5.4a) than at inner parts (Fig. 5.4c, 5.14). This phenomenon is attributed to the "dispersive pressure" (Bagnold effect [Bagnold, 1954]) at strong pressure gradient sectors. The non-clustered grains do not carry any significant magnetic anisotropy.

(3) The clustering of the individuals and the stretching of the clusters are triggered by the shear gradients due to the relative displacement of the individual grains or clusters of grains parallel to the shear plane. By contrast, at places where the flow is shearless, the magnetic markers are subjected to bulk translation and therefore may keep their former fabric. However it is suggested that this former fabric progressively vanishes during bulk

transportation.

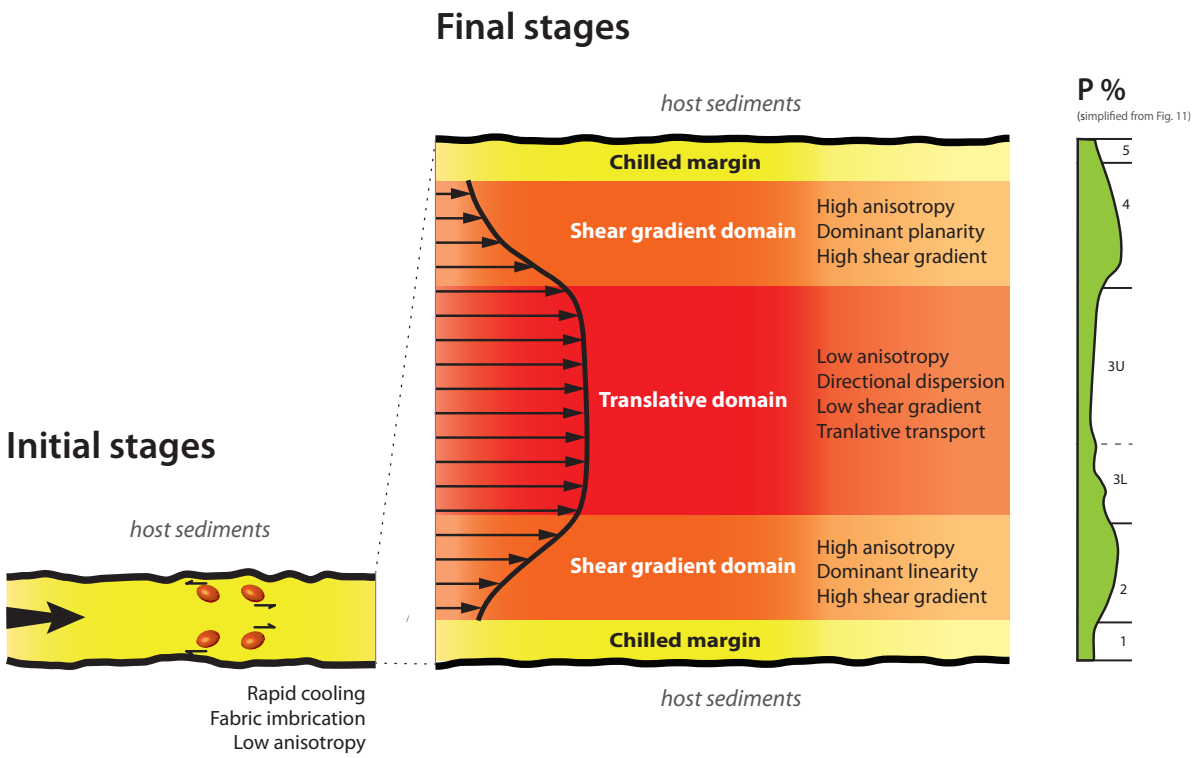

Figure 5.15: Model for magmatic flow during the emplacement of the FF sill. The chilled margins (zones 1 and 5) rapidly cooled during the first stages of magma emplacement into the host sediments. The inner zones of the sill (zones 2, 3 and 4) record the ultimate stages of magma emplacement. The velocity profile, based on the total anisotropy degree profile (see text) does not fit with a purely Newtonian flow behavior.

These considerations lead us to define three main domains into the vertical profile of the sill:

The chilled-margins: along the 30-50 cm-thick domains located at the roof and floor of the sill (zones 5 and 1), the magma displays low but stable anisotropy degrees. Thin section observations indeed indicate that the opaque grains are more dispersed than elsewhere (Fig. 5.4a), with fewer and smaller clusters attributed to the dispersive effect along the rigid boundary toward which magma velocity vanishes. This effect is enhanced by the rapid cooling along the borders: it increases magma viscosity, hence favours flow concentration towards the inside of the sill. Consequently, a slight susceptibility decrease may be observed at the borders of the sill, and the magnetic anisotropy remains modest in magnitude. The necessary shear gradients close to the borders are at the origin of the observed imbrications (Figs. 5.12, 5.15). Despite the low anisotropy, the AMS axes show little scattering (Fig. 5.11), a feature considered as an indication of a stable, i.e. not re-worked, fabric.

The translative domain: the internal part of the sill (zone 3U, particularly) is interpreted as such since it carries rather constant and low anisotropies for more than 3 meters, *i.e.* $>$ 40% of the sill thickness. The low anisotropies point to low differential movements inside the fluid layers. However, since there is some consistent anisotropy degree and magnetic lineation in zone 3U (P $\sim$ 1-3%; average $K_1 \sim 315°$), we assume that some shearing was present in this translative domain, able to record the flow direction (Fig. 5.11). Zone 3L, which is more fluctuating in both P% and azimuth of K_1, could be a transitional domain in which successions of shearing events took place in this globally translative domain.

The shear-gradient domains (zones 4 and 2): between the chilled-margins and the central parts of the sill, correspond to narrow slices (a few cm to 1 m) into which shear gradients (positive or negative) of the particles are present (Fig. 5.11, 5.15), making the anisotropy degree to increase or decrease, respectively. At the top of zone 4 and base of zone 2, the increase in anisotropy degree reflects the shear increase (positive shear gradient) of the particles when departing from the chilled-margins. When progressing toward the translative domain, within which the velocity gradient of the particles is low, the anisotropy degree decreases. Likewise, a decrease in the anisotropy degree is attributed to a decrease in the velocity gradient of the particles (negative shear gradient) (Fig. 5.15).

Variations of shape parameters L% and F% along profile (Figs. 5.11, 5.12), directly reflect the variations of P%, with the additional indication of more linearity or planarity of the fabric, also reflected by the T parameter. The latter is dominantly negative, thus prolate fabrics dominate, suggesting a rather well-defined (average) flow direction. However, this contrasts with the oblate top part of the profile (between 5 and 6 m; zone 4 *partim*) in which, in addition, the magnetic lineation greatly varies between profiles A and B. This planarity in the top part of the sill could be attributed to fabric flattening during the last stages of magma emplacement, when the magma pressure becomes equilibrated with the overburden pressure. Alternatively, it can be due to the fact that the sill inflation within the host sediments is mainly achieved against its deformable top rather than against its fixed base (Fig. 5.15), which could result on a higher lateral dispersion of the magma, and thus higher planarity in zone 4 than in zone 2.

5.7.5 Implications for regional tectonics and magmatism

Accepting that our data from the exposed surface of the sill and from the vertical profile provide the direction (∼310°) and sense (toward the southeast) of the magma flow, we are tempted to relate this local information with the regional geological context. Inspection of the geological features and magnetic anomalies of the study area underlines the close relationship that exists between the individual magnetic anomalies and the Late Cretaceous alkaline magmatism of West Iberia, whose age spans from 92 to 80 Ma (Fig. 5.1, 5.2). The neighboring Sintra complex (75-82 Ma) and the FF-sill (∼94 Ma) belong to this magmatism while, more to the south, the Sines and Monchique anomalies correspond to younger intrusive alkaline complexes.

Considering that most of the magnetic anomalies correspond to exposed magmatic bodies, it is here suggested that: i) the large magnetic anomaly to the south of Sintra (known as the Cabo Raso anomaly, Fig. 5.2) may correspond to a Late Cretaceous alkaline intrusion buried under Mesozoic and Cenozoic sediments, as also supported by the seismic reflection profile (Fig. 5.16a,b); and ii) the various intrusions between the Tore seamount and the FF-sill define a tectono-magmatic lineament of intrusive alkaline bodies of a Late Cretaceous age (Fig. 5.16c and d). These intrusions and volcanoes intruded along the fault that separates the Tore seamount and the TAP [Roque et al., 2009], and eastward across the Fontanelas seamount towards the continental shelf (Cabo Raso anomaly area, cf. Figs. 5.1, 5.2, 5.16d). This fault zone, arcuate shaped in map view, is buried under Pliocene-Quaternary sediments south of Sintra but is well exposed at the front of the Arrábida fold and thrust belt. We also note that the NW-SE striking vertical faults south of Sintra are systematically intruded by basic dykes (Fig. 5.1).

Based on these evidences it is suggested that the NW-SE directed magmatic flux found in the FF-sill can be viewed as the south-easternmost prolongation of the buried basic intrusion corresponding to the Cabo Raso anomaly (Fig. 5.16c and d). Based on the thickness of the sill, the ∼50 km displacement that the magma may have suffered is compatible with the model of Bunger & Cruden [2011](Fig. 5.16e).

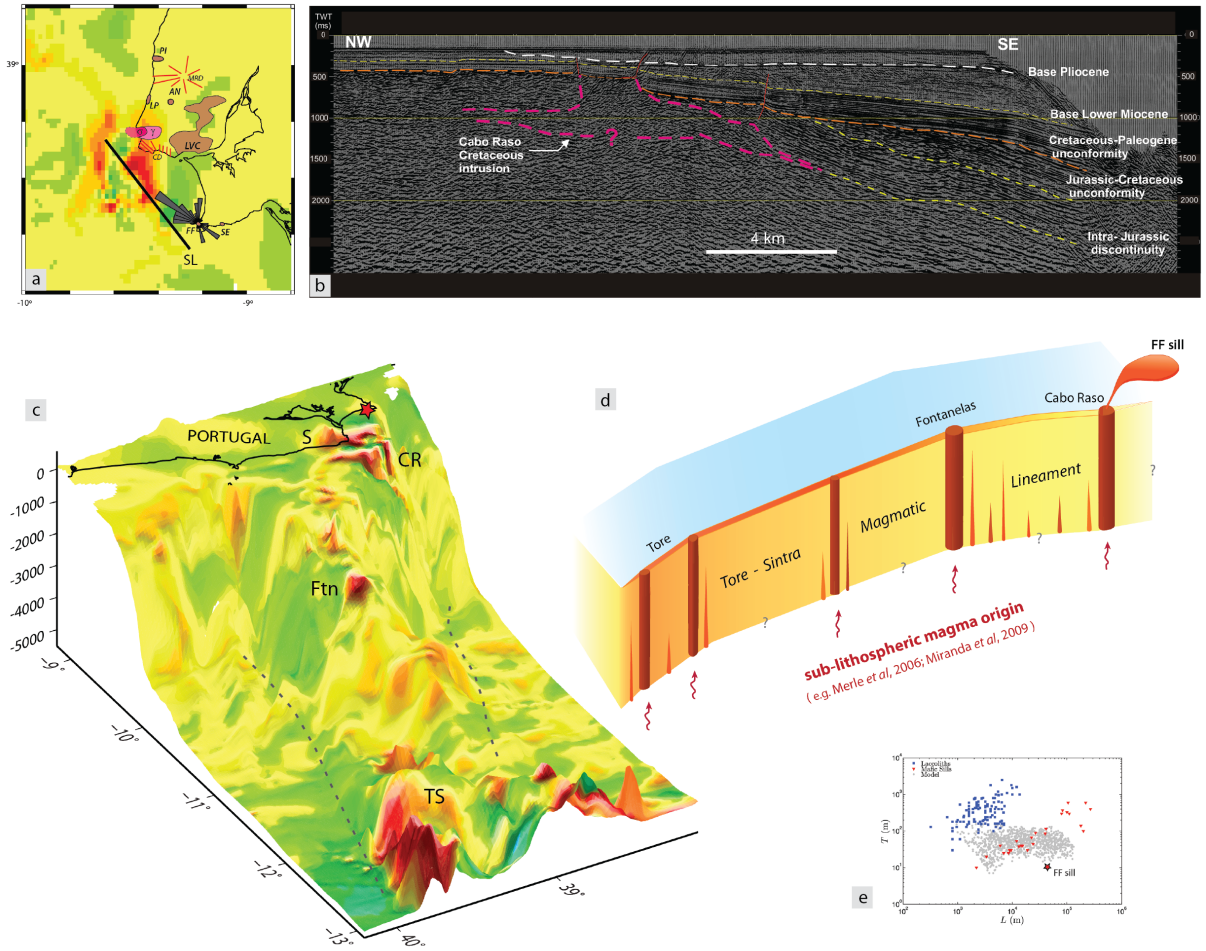

Figure 5.16: Tectonic and magmatic implications. (a) Detail of the Cabo Raso magnetic anomaly, with location of the onshore alkaline magmatic bodies (see Fig. 5.1 for description) and of the reflection line (SL) shown in (b). Also shown is the azimuth of the magnetic lineation (K_1) of the FF sill. (b) Multichannel seismic reflection profile; stratigraphy calibrated using oil exploration boreholes. The contoured area with no reflection in the Cretaceous coincides with the Cabo Raso magnetic anomaly, in agreement with the existence of a Cretaceous magmatic body. (c) Three-dimensional view from NW of the Estremadura Spur bathymetry overlain with the magnetic anomalies from Fig. 5.2 [Luis & Miranda, 2008]. The marked magnetic anomalies TS and Ftn (Tore and Fontanelas seamounts) coincide with dredged volcanic edifices (see text and Fig. 5.2 for details). CR: Cabo Raso anomaly; S: Sintra; red star: Foz da Fonte sill. (d) Schematic model for the possible connection of the Tore-Sintra-Cabo Raso intrusion and the Foz da Fonte sill (see text for description); Drawing not to scale; for horizontal length (∼350km) compare with (c). (e) Plot of the FF sill in a thickness versus length plot by Bunger & Cruden [2011]. Length measured from the centre of the Cabo Raso anomaly to Sesimbra; thickness ∼10m.

5.8 Conclusions

This work led us to the following conclusions:

- The magnetic mineralogy is primary and homogeneous across the sill.
- The magnetic fabric is dominantly carried by the shape anisotropy of clusters of multi-domain titanomagnetite grains.
- The correlation between the elongation of vesicles, magnetic fabric and shape preferred orientation allows the interpretation of the magnetic fabric in terms of magmatic fabric and indicates a magma flow toward the south-east.
- The along-profile magnetic fabric records five zones of flow regimes more-or-less symmetrical with respect to the middle of the profile: (i) two chilled margins, (ii) two high shear gradient domains, and (iii) a central channel of translational flow.
- Combining the interpretation of the magnetic anomalies (off and onshore) with the age of the alkaline magmatism of West-Iberia and Tore-Madeira Rise, and the structure of the continental margin, we suggest the existence of a 350 km-long dyke-like structure running from the Tore seamount to the Cabo Raso magnetic anomaly.
- The Cabo Raso intrusion is likely the magmatic source of the Foz da Fonte sill, for which a >50 km length is inferred.

5.9 Appendix 1: Tables

Sample	h (cm)	K_m (mSI)	P	L	F	T	K_1az	$k_1$pl	$k_3$az	$k_3$pl
				Profile A						
FF3_A	1	40.79	1.012	1.006	1.006	0.018	282.9	19.5	105.7	70.6
FF3_B	2	45.47	1.013	1.006	1.008	0.135	277.6	23.1	114.6	66.0
FF3_C	9	40.43	1.016	1.008	1.008	-0.019	277.1	12.0	157.0	66.5
FF3_D	16	39.48	1.014	1.006	1.008	0.086	276.3	16.7	137.9	68.4
FF3_E	23	38.98	1.009	1.005	1.004	-0.111	273.4	18.3	132.0	66.6
FF3_G	35	41.49	1.011	1.008	1.004	-0.338	267.7	15.4	162.0	47.2
FF3_H	47	45.17	1.017	1.003	1.014	0.690	300.2	13.3	107.6	76.0
FF3_I	59	48.06	1.032	1.013	1.018	0.179	303.7	11.3	79.7	74.6
FF3_J	77	43.72	1.040	1.020	1.020	0.010	311.9	9.3	80.1	75.0
FF3_K	87	48.57	1.042	1.022	1.020	-0.054	310.4	8.2	82.0	75.3
FF3_L	105	50.41	1.048	1.031	1.016	-0.322	305.6	8.5	85.7	79.0
FF4_A	135	55.08	1.044	1.026	1.018	-0.123	161.2	3.4	266.8	78.2
FF4_BB	155	51.25	1.057	1.038	1.018	-0.354	356.3	4.5	304.5	81.0
FF4_BA	165	47.91	1.040	1.035	1.006	-0.726	177.7	5.0	105.6	77.7
FF4_CA	175	56.60	1.035	1.025	1.011	-0.402	168.8	13.5	313.3	73.5
FF4_CB	185	60.81	1.035	1.024	1.012	-0.335	194.6	0.6	288.3	76.9
FF4_D	195	61.71	1.046	1.026	1.020	-0.106	180.8	1.2	294.9	86.8
FF4_E	205	58.61	1.023	1.012	1.010	-0.100	128.8	13.6	215.7	13.4
FF4_F	215	62.90	1.036	1.022	1.013	-0.201	350.7	16.2	144.8	72.6
FF4_G	225	60.93	1.040	1.017	1.023	0.156	169.6	5.7	275.8	68.3
FF4_H	235	56.57	1.047	1.029	1.018	-0.247	7.2	11.3	182.7	79.1
FF4_I	245	57.34	1.037	1.029	1.008	-0.610	162.5	11.9	271.9	66.4
FF4_J	255	59.08	1.021	1.013	1.007	-0.035	357.3	10.2	259.0	34.2
FF4_K	265	57.93	1.016	1.010	1.006	-0.193	2.9	12.3	240.3	61.8
FF4_L	275	58.27	1.019	1.013	1.004	-0.517	4.4	12.7	240.3	61.8
FF4_M	285	66.35	1.017	1.008	1.010	0.102	297.0	86.7	1.7	0.5
FF4_N	295	62.73	1.030	1.025	1.005	-0.655	1.2	21.9	264.8	17.4
FF4_O	305	55.94	1.027	1.016	1.011	-0.201	122.1	6.1	0.3	78.4
FF4_P	315	65.59	1.013	1.006	1.008	0.061	95.3	21.0	182.2	10.2
FF4_Q	335	60.93	1.009	1.006	1.004	-0.072	131.8	0.7	37.2	72.7
FF4_R	365	60.64	1.014	1.012	1.002	-0.802	318.8	5.6	50.0	63.3
FF4_S	395	54.16	1.026	1.014	1.012	-0.023	300.5	8.7	66.2	75.0
FF4_SA	415	53.26	1.017	1.007	1.010	0.108	283.4	1.6	187.7	74.3
FF4_SB	425	45.38	1.025	1.015	1.010	-0.168	140.0	3.6	231.7	39.9
FF4_T	475	30.28	1.021	1.016	1.005	-0.523	336.5	27.0	116.0	55.7
FF4_U	490	53.13	1.033	1.013	1.019	0.160	340.9	13.6	109.1	70.3
FF4_V	500	58.16	1.028	1.007	1.021	0.265	321.4	10.9	197.3	68.7
FF4_W	525	54.39	1.014	1.009	1.005	-0.284	328.0	5.0	224.5	63.7
FF4_X	535	48.82	1.042	1.014	1.028	0.340	350.0	29.3	201.7	56.6
FF4_ZA	545	49.35	1.043	1.008	1.036	0.641	328.2	11.2	190.6	75.0
FF4_ZB	555	49.58	1.051	1.009	1.043	0.661	348.5	15.4	185.5	74.2

Continued on next page

Sample	h (cm)	K_m (mSI)	P	L	F	T	K_1az	$k_1$pl	$k_3$az	$k_3$pl
FF4_ZC	565	49.41	1.052	1.009	1.042	0.659	40.8	9.2	178.0	77.7
FF4_ZD	575	51.40	1.049	1.006	1.043	0.739	23.5	10.4	250.5	76.0
FF4_ZE	595	58.06	1.005	1.011	1.017	0.372	308.6	2.2	201.5	64.0
FF4_ZF	605	50.75	1.046	1.022	1.024	0.040	93.4	21.7	242.0	65.0
FF4_ZG	615	56.40	1.032	1.006	1.025	0.580	51.3	15.1	214.7	74.1
FF4_ZH	625	49.45	1.038	1.016	1.021	0.129	109.3	5.5	216.3	72.7
FF4_ZI	645	64.66	1.027	1.011	1.017	0.208	318.4	4.8	216.3	72.7
FF5_C	660	51.21	1.031	1.008	1.023	0.500	295.4	10.2	175.5	70.0
FF5_B	667	53.64	1.039	1.020	1.019	-0.046	106.8	2.6	210.4	79.1
FF5_A	670	45.35	1.035	1.014	1.021	0.227	300.1	3.8	190.9	78.4
Profile B										
FF7_L	520	57.56	1.044	1.013	1.030	0.394	305.9	3.7	161.2	85.5
FF7_K	540	60.56	1.060	1.018	1.042	0.407	297.5	4.6	170.9	82.4
FF7_J	560	56.98	1.083	1.036	1.046	0.128	124.8	0.1	224.4	87.9
FF7_I	580	56.59	1.066	1.024	1.041	0.266	300.8	7.8	167.3	78.9
FF7_H	600	52.52	1.053	1.022	1.030	0.143	306.9	13.7	111.8	75.8
FF7_G	620	54.52	1.065	1.036	1.029	-0.113	307.4	7.8	142.0	82.0
FF7_F	640	63.31	1.057	1.051	1.006	-0.795	123.8	0.8	211.6	73.4
FF7_E	670	62.87	1.046	1.014	1.032	0.382	297.8	2.0	189.1	83.9
FF7_D	696	65.45	1.031	1.010	1.021	0.354	316.4	3.4	213.4	75.6
FF7_C	704	65.92	1.019	1.006	1.013	0.368	297.4	4.2	190.0	76.0
FF7_B	711	65.09	1.016	1.000	1.016	0.965	285.1	3.0	173.5	82.0
FF5_D	715	54.41	1.019	1.006	1.014	0.385	123.0	1.2	223.2	81.2
FF7_AD	716	51.52	1.019	1.005	1.015	0.508	137.4	16.1	251.9	53.8
FF7_AC	716	58.70	1.018	1.004	1.014	0.507	282.5	2.0	189.6	74.7
FF7_AB	716	53.88	1.014	1.005	1.009	0.328	279.7	0.3	267.1	80.0
FF7_AA	716	53.53	1.017	1.003	1.014	0.649	285.3	1.6	267.9	80.1
Mean		54.03	1.031	1.015	1.016	0.032	313.1	5.6	194.5	80.5

Table 5.2: Per core data of the AMS vertical profile (second sampling session): bulk susceptibility ($M_m = (K_1+K_2+K_3)/3$) in 10^{-3} SI units, total ($P = K_1/K_3$), linear ($L = K_1/K_2$), planar ($F = K_2/K_3$) and shape anisotropy parameters ($T = (2\ln K_2 - \ln K_1 - \ln K_3)/(\ln K_1 - \ln K_3)$), and azimuth and plunge of K_1 and K_3 (maximum and minimum susceptibility axes). h, in cm, indicates the vertical distance from the base of the sill.

Sample	h (cm)	K_m (mSI)	P	L	F	T	K_1az
Profile A							
FF3_A	2	43.040	1.014	1.007	1.008	1.067	279.2
FF3_B	9	41.455	1.015	1.007	1.008	1.046	277.7
FF3_C	16	39.594	1.013	1.006	1.007	1.011	278.1
FF3_D	23	39.731	1.011	1.006	1.005	0.882	273.5
FF3_E	35	41.779	1.012	1.006	1.007	0.976	275.8
FF3_G	47	44.970	1.019	1.007	1.013	1.305	291.0
FF3_H	59	46.250	1.030	1.012	1.018	1.265	308.4
FF3_I	77	46.016	1.039	1.019	1.020	1.036	309.6
FF3_J	87	47.818	1.043	1.024	1.019	0.895	309.5
FF3_K	105	51.118	1.046	1.028	1.018	0.795	320.4
FF3_L	135	52.957	1.048	1.030	1.018	0.770	341.0
FF4_A	155	51.375	1.050	1.034	1.015	0.611	354.2
FF4_BB	165	50.917	1.043	1.033	1.010	0.448	356.1
FF4_BA	175	55.477	1.036	1.027	1.010	0.534	360.3
FF4_CA	185	59.981	1.038	1.025	1.014	0.706	361.8
FF4_CB	195	60.712	1.038	1.022	1.016	0.838	354.4
FF4_D	205	60.459	1.032	1.018	1.013	0.873	348.1
FF4_E	215	61.334	1.034	1.018	1.015	0.914	342.1
FF4_F	225	60.332	1.041	1.021	1.019	0.966	359.6
FF4_G	235	57.851	1.043	1.026	1.017	0.763	352.3
FF4_H	245	57.579	1.036	1.025	1.010	0.625	354.7
FF4_I	255	58.354	1.024	1.016	1.007	0.782	351.3
FF4_J	265	58.299	1.018	1.012	1.006	0.766	364.4
FF4_K	275	60.201	1.018	1.011	1.006	0.719	365.8
FF4_L	285	63.422	1.021	1.014	1.007	0.758	363.0
FF4_M	295	61.938	1.026	1.019	1.008	0.648	313.5
FF4_N	305	60.052	1.024	1.016	1.009	0.751	309.6
FF4_O	315	62.013	1.016	1.009	1.008	0.962	293.5
FF4_P	335	62.021	1.011	1.008	1.005	0.779	294.5
FF4_Q	365	59.091	1.016	1.011	1.005	0.575	308.8
FF4_R	395	55.557	1.021	1.012	1.009	0.815	303.1
FF4_S	415	51.517	1.021	1.011	1.011	1.006	308.1
FF4_SA	425	43.576	1.022	1.013	1.009	0.812	324.0
FF4_SB	475	39.768	1.025	1.015	1.010	0.737	333.9
FF4_T	490	48.674	1.029	1.012	1.016	1.016	335.3
FF4_U	500	55.959	1.026	1.009	1.017	1.102	332.5
FF4_V	525	53.938	1.025	1.010	1.015	1.009	328.2
FF4_W	535	50.341	1.035	1.011	1.024	1.259	331.2
FF4_X	545	49.273	1.045	1.010	1.036	1.571	340.6
FF4_ZA	555	49.480	1.049	1.009	1.041	1.656	351.9
FF4_ZB	565	49.950	1.051	1.008	1.043	1.680	372.4
FF4_ZC	575	52.568	1.039	1.008	1.036	1.627	391.3
FF4_ZD	595	54.570	1.026	1.013	1.025	1.381	275.5

Continued on next page

Sample	h (cm)	K_m (mSI)	P	L	F	T	K_1az
FF4_ZE	605	53.992	1.032	1.015	1.023	1.258	262.2
FF4_ZF	615	53.251	1.037	1.013	1.024	1.332	276.2
FF4_ZG	625	54.992	1.034	1.012	1.021	1.262	289.9
FF4_ZH	645	57.497	1.031	1.012	1.020	1.261	301.3
FF4_ZI	660	55.179	1.032	1.012	1.021	1.291	290.5
FF5_C	667	50.956	1.036	1.016	1.021	1.159	293.0
FF5_B	670	48.109	1.036	1.016	1.020	1.136	298.4
			Profile B				
FF7_L	520	58.559	1.049	1.015	1.034	0.398	301.7
FF7_K	540	58.914	1.062	1.021	1.040	0.334	303.2
FF7_J	560	57.779	1.073	1.029	1.044	0.232	302.0
FF7_I	580	55.672	1.067	1.027	1.040	0.201	304.6
FF7_H	600	54.035	1.059	1.026	1.033	0.110	305.7
FF7_G	620	56.213	1.060	1.036	1.024	-0.220	305.8
FF7_F	640	60.998	1.056	1.038	1.018	-0.330	304.3
FF7_E	670	63.621	1.045	1.022	1.023	0.081	304.3
FF7_D	696	64.921	1.032	1.010	1.022	0.365	303.6
FF7_C	704	65.594	1.021	1.006	1.016	0.514	309.0
FF7_B	711	62.626	1.018	1.003	1.015	0.671	299.9
FF5_D	715	56.356	1.018	1.004	1.015	0.561	305.6
FF7_AD	716	54.036	1.019	1.005	1.015	0.477	306.7
FF7_AC	716	55.700	1.017	1.005	1.013	0.463	306.7
FF7_AB	716	54.999	1.016	1.004	1.012	0.453	306.7
FF7_AA	716	53.649	1.016	1.004	1.012	0.542	306.7

Table 5.4: Running means of AMS parameters represented in Fig. 5.11 (see text for details).

5.10 Appendix 2: AMS from other sills of the Lusitanian Basin

During this thesis, we sampled and conducted AMS studies on other magmatic bodies from the Lusitanian Basin. In this section we present AMS results obtained from three other sills: Paço de Ilhas (PI), Lomba dos Pianos (LP) and Anços (AN). All these sills crop out north of Lisbon and Sintra, in a region where several subvolcanic structures have been mapped and associated with the Late Cretaceous magmatism of west Iberia (sills, dykes, plugs, necks; see Fig. 2.14 of Miranda [2010]). In Fig. 5.17 and Table 5.5 are presented the AMS results of PI, LP and AN sills, and in Fig. 5.18 are plotted the average directions of K_1 (magnetic lineation) of FF, PI, LP and AN sills.

These results should be improved, and carefully analyzed and interpreted by future studies.

Paço de Ilhas sill

The Paço de Ilhas sill was, together with the Foz da fonte sill, the subject of the paleomagnetic study presented in the Chapter 3. AMS data come from the same sites (see Fig. 3.1h), thus cover the outcropping area of the sill. Only inner parts of the sill were sampled, and not the contacts. The fabric has high significance [Pueyo et al., 2005]. The magnetic foliation is subhorizontal and the magnetic lineation is well constrained to the ∼N160° direction.

Lomba dos Pianos sill

The Lomba dos Pianos sill was sampled both in its center and close to the contacts, in a almost complete vertical profile. However, data presented here do not include the contacts and are restricted to $L \geqslant 5\%$. The fabric shows significant directional dispersion. Nevertheless, the average foliation is sub-horizontal despite high confidence angles, and the average lineation (∼N5°) is in the limit for statistical significance. A larger amount and wider sampling could homogenize the results.

Anços sill

The Anços sill was sampled in a single site. The fabric is highly oblate, with well defined sub-horizontal foliation and dispersion of the lineation within the horizontal plane, despite a tendency to cluster around the average (∼N150°). Given the large size and exposure of the sill, we believe that more and wider sampling could unravel a significant fabric.

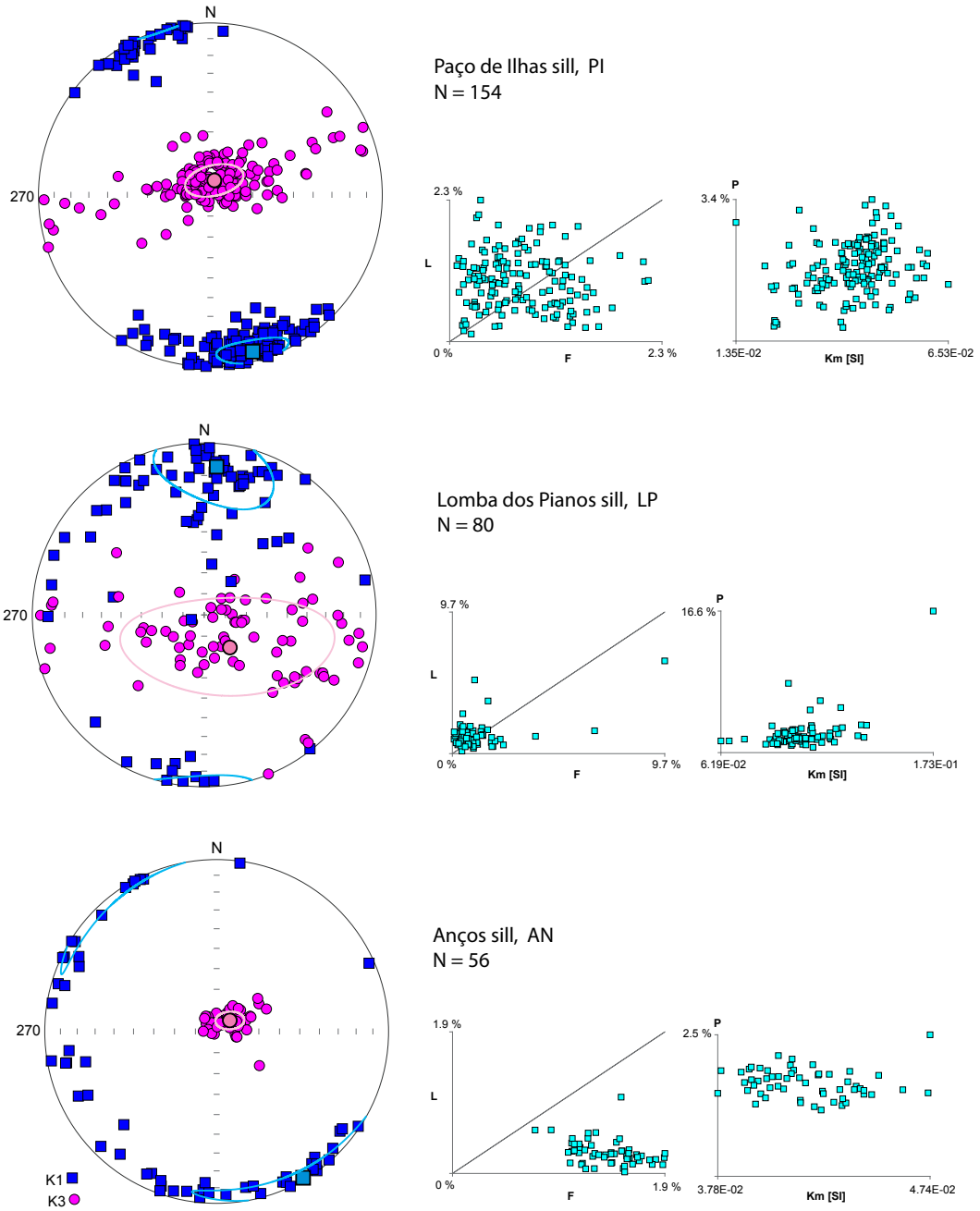

Figure 5.17: AMS results for Paço de ilhas (PI), Lomba dos Pianos (LP) and Anços (AN) sills.

Sill	N	K_1	e_{12} / e_{31}	K_3	e_{23} / e_{31}
PI	154	164.9 / 6.1	13.1 / 7.0	15.1 / 82.9	14.0 / 7.2
LP	80	4.8 / 14.6	25.5 / 18.8	141.7 / 70.3	52.3 / 23.3
AN	56	149.4 / 1.3	39.5 / 4.8	50.1 / 81.9	6.8 / 4.2

Table 5.5: AMS data of PI, LP and AN sills

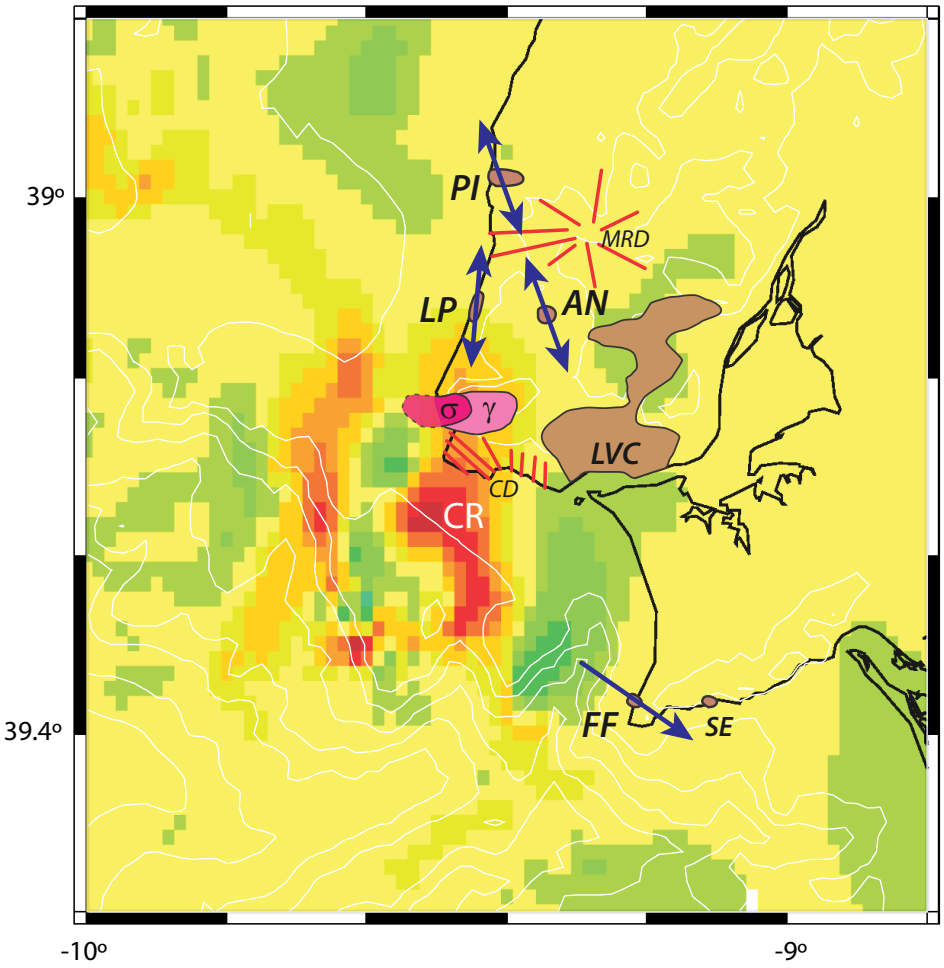

Figure 5.18: Map of magnetic anomalies showing location of some Late Cretaceous magmatic occurrences (see caption of Fig. 5.1). The azimuth of magnetic lineation of sampled sills is indicated by blue arrows. CR: Cabo Raso magnetic anomaly.

6. Final Synthesis and Conclusions

6.1 Iberian kinematics

- We showed that sills may be good targets for paleomagnetic studies, in which secular variation is averaged out and the primary magnetization is preserved.
- We contributed for the calibration of the Late Cretaceous APWP of Iberia by providing two new high-quality paleomagnetic poles:

  PI pole ~88 Ma: PLat=73.4°; PLong=204.6°; A95=1.3°; k=42.7.

  FF pole ~94 Ma: PLat=73.8°; PLong=217.1°; A95=3.3°; k=26.0.

- We made a rigorous selection of Iberian paleomagnetic data and provided a synthetic APWP for the Late Jurassic-Cretaceous of Iberia, constituted by mean poles calculated for several time periods. The paucity of good paleomagnetic data for Iberia became clear during this analysis. Low age resolution, lack of confidence tests and structural control are the main problems.
- We showed that paleomagnetic data for ages younger than 120 Ma agree with the global APWP after being rotated with rotation parameters from kinematic models. These ages correspond in general to times when the oceanic spreading is well recorded on the seafloor magnetic anomalies.
- We showed that, once assumed the validity of the global APWP, paleomagnetic data and Euler rotations deduced from magnetic anomalies are inconsistent for pre-oceanic spreading ages (older than 120 Ma)
- We developed a method to determine the cause of that incompatibility, and concluded:

  123 Ma mean paleomagnetic pole These data, coming from the Organyà Basin, Southern Pyrenees, are incompatible with the APWP and their validity is strongly questioned. We suggest some possible explanations: the fold test does not exclude a Cretaceous remagnetization; the geological setting may not be part of stable Iberia.

  130 Ma mean paleomagnetic pole These data show even greater incompatibility with the APWP and are thus considered unreliable. Once again, remagnetization or tectonic issues are the most probable causes.

  151 Ma mean paleomagnetic pole These data are compatible with the APWP: there are IB-AF euler rotation poles that match them together and that deliver plausible paleogeographic solutions.

- We proposed a new magnetic reconstruction for Iberia at 150 Ma, compatible with Late Jurassic paleomagnetic data. The respective rotation poles are:

  IB-NAM long=-18.08°; lat=67.54°; angle=-57.72°.

  IB-AF long=-7.55°; lat=51.55°; angle=5.29°.

- The construction of a consensual kinematic model for Iberia since the Pangean breakup is dependent not only on the acquisition of more paleomagnetic data or on the reevaluation of marine magnetic anomalies, but more importantly on the compatibility between both types of data. The new method developed here can be used by future studies as a tool to test that compatibility.

6.2 Magmatic flow

- We showed that the anisotropy of magnetic susceptibility measured in sills may be insightful for the understanding of the flow, preserving information about emplacement times. A correlation between the magnetic lineation, shape preferred orientation of opaques and elongation of vesicles allows interpreting the magnetic fabric in terms of magmatic fabric.

- The shape anisotropy of clusters of multi-domain titanomagnetite grains is the main source for the magnetic anisotropy.

- We identified five zones within the vertical profile of FF sill, corresponding to different types of magnetic fabric, which we relate with different flow regimes:

  Chilled margins ∼50 cm apart from the margins, where low anisotropies suggest low velocity gradients and heterogeneous flow paths during initial emplacement stages

  Shear gradient domains where high anisotropy values are ascribed to maximum shear gradient zones

  Translative domain where low anisotropies suggest low shear gradients and magma displacement close to pure translation

6.3 Iberian Late Cretaceous Magmatism

- We determined the direction of magma flow in the FF sill to be ∼310°(average lineation), directed from NW to SE (deduced from the imbrication of magnetic

lineation and foliation close to the borders).

- We suggest that the Cabo Raso anomaly is the most probable magmatic source for the FF sill.
- Based on the joint interpretation of off- and onshore magnetic anomalies, geochronological data, and the structure of the continental margin, we suggest the existence of a magmatic structure connecting the onshore Sintra-Lisbon region with the Tore seamount, ∼350 km to the WNW.

7. Suggestions for Future Work

Given the results and problems unraveled by this work, we suggest the following important further work.

7.1 Iberian kinematics

- Acquire new paleomagnetic data for Iberia, especially for the Early Cretaceous. Preference should be given to intrusive magmatic rocks, namely sills, but data from sedimentary basins, based on magnetostratigraphic studies will also be of great value. In all cases, special attention should be given to eventual remagnetization or structural problems.

- Acquire more paleomagnetic data for older ages since the Pangean breakup ($\sim$200 Ma) and integration with published data [e.g., Osete et al., 2011], aiming to a better calibration of the pre-drift Iberian APWP.

- After accomplishment of previous objectives, use the improved Iberian APWP to constrain pre-drift continental fits of Iberia and surrounding plates. During this, special care should be given to the interpretation of resulting kinematics, namely in terms of reconstruction of magnetic anomalies and justification of implied geological processes.

7.2 Magmatic flow

- Continue exploring AMS as a tool to inform about about how magma flows within sills and the relation between flow, AMS and preferred orientation of minerals:

- Conduct similar studies in other sills, in order to verify if the same characteristics of the magnetic fabric are found within them. This should be done in other sills from the Lusitanian Basin but also from other geological contexts. When possible, integrate geochemical data to study eventual correlations between the rheological properties and the flow regime suggested by magnetic data.

- Evaluate the 3D shape preferred orientation of opaque grains in FF samples. Although attempted during this work, it was not possible so far to accomplish it, due to the small size and low anisotropy of the grains. It is thus likely that, similarly to what was presented here for 2D, in which a statistical integration of tens of images was necessary to accomplish a significant interpretation, a more thorough statistical integration will also be needed for the 3D analysis.

7.3 Iberian Late Cretaceous Magmatism

- Determine the AMS in other sills of the Lusitanian Basin, with the aim to unravel the direction of magma flow during emplacement. Sampling should be as wide as possible in the horizontal plane in order to determine possible variations of direction within the sills. The AMS of other dykes and within the Lisbon Volcanic Complex would also be insightful. Integration of results will ultimately allow to estimate the location of magma suppliers and emplacement mechanisms.

- Study the offshore magmatism. In this work we suggested that exists a magmatic connection between the Tore seamount and the Sintra-Lisbon region. This hypothesis should be tested by inspection of seismic profiles, improved maps of magnetic anomalies, gravimetry, in order to search for the mechanism of this connection. The role of the Late Cretaceous magmatism and related structures on the Cretaceous geodynamical evolution of Iberia will then be much better understood.

List of Figures

1.1 Map of magnetic anomalies of the Iberian plate and surroundings 6
1.2 Kinematic model of Olivet [1996] 8
1.3 Kinematic model of Vissers & Meijer [2012] 10
1.4 Kinematic models of Olivet [1996], Vissers & Meijer [2012] and Sibuet et al. [2012] 11
1.5 Central Atlantic kinematics 12
1.6 Offshore Late Cretaceous magmatism 14
1.7 Onshore Late Cretaceous magmatism 15

2.1 Types of spin alignment in ferromagnetism (*s.l.*) 20
2.2 Super-exchange ferromagnetic coupling 21
2.3 Ternary diagram of iron oxides and variation of parameters 22
2.4 Internal and external magnetic fields in an elliptic ferromagnetic crystal 25
2.5 Magnetic domains and walls 26
2.6 Hysteresis curve for a ferromagnetic material 30
2.7 States of magnetization along the hystersis curve 31
2.8 IRM unmixing of magnetic components 31
2.9 Experimental procedure for the Lowrie test 32
2.10 Day diagram 33
2.11 FORC diagrams 34
2.12 AMS ellipsoid and fabric diagrams 36

3.1 Geological settings and field photos of PI and FF sills 51
3.2 Paleomagnetic results from the PI sill 55
3.3 IRM acquisition for PI and FF samples 57
3.4 Fuller et al. [2002] test for PI and FF samples 59
3.5 Thermomagnetic curves and Lowrie test for PI and FF samples 61
3.6 FORC diagrams for PI and FF samples 62
3.7 SEM photos from PI samples 63
3.8 Paleomagnetic results for the FF sill 64
3.9 SEM photos from FF samples 66

3.10 Implications for the Iberian APWP 69

4.1 Relation between Iberian paleomagnetic data, kinematic models and global APWP 89
4.2 Finding and testing potential IB-AF Euler poles 93
4.3 Magnetic reconstruction at 150 Ma 97
4.4 Compatibility between the 150 Ma reconstruction and paleomagnetic data 98
4.5 Comparison of results when using different APWPs 99
4.6 Evaluation of results: example for 130 Ma, T12 APWP 102
4.7 Evaluation of results: example for 150 Ma, T12 APWP 103

5.1 Geological setting of FF sill 111
5.2 Magnetic anomalies of West Iberia 113
5.3 Field photo from the southern outcrop of FF sill 114
5.4 SEM photos of FF specimens 116
5.5 Geochemical data along the vertical profile 117
5.6 Thermomagnetic curves for specimens along the vertical profile 118
5.7 FORC diagrams for specimens along the vertical profile 118
5.8 Day plot for specimens along the vertical profil 119
5.9 AMS results from the first sampling session 120
5.10 AMS results from the second sampling session 121
5.11 Variation of AMS parameters along the vertical profile 122
5.12 Variation of AMS along the vertical profile of FF sill 124
5.13 Magnetic lineation versus elongation of vesicles 126
5.14 Magnetic lineation versus shape preferred orientation of opaque grains 128
5.15 Magmatic flow model 130
5.16 Tectonic and magmatic implications 133
5.17 AMS results from PI, LP and AN sills 140
5.18 Magnetic lineation of FF, PI, LP and AN sills on a regional frame 141

List of Tables

2.1 Magnetic properties of some minerals 23

3.1 Paleomagnetic results for PI and FF sills 60
3.2 Selected paleomagnetic poles of Iberia during Cretaceous and Late Jurassic . . . 71
3.3 Iberia-Africa Euler rotations 72
3.4 Mean paleomagnetic poles for Iberia and Iberia-Africa rotation poles 73
3.5 ChRM of PI specimens 79
3.6 ChRM of FF specimens 82
3.7 Geographic coordinates of PI sites and FF 82

4.1 Iberian mean paleomagnetic poles and Iberia-Africa rotation parameters 90
4.2 APWP poles considered in this work 90
4.3 NAM-AF and EUR-AF Euler poles 95
4.4 Euler rotation parameters for the 150 Ma reconstruction 97

5.1 Per zone AMS results of FF sill 123
5.2 Per core AMS data of FF sill 136
5.4 Per core running means of AMS data from ff sill 138
5.5 AMS data of PI, LP and AN sills 141

Bibliography

Aarnes, I., Podladchikov, Y. Y., & Neumann, E. R., 2008. Post-emplacement melt flow induced by thermal stresses: Implications for differentiation in sills, *Earth and Planetary Science Letters*, **276**(1-2), 152–166.

Afilhado, A., Matias, L., Shiobara, H., Hirn, A., Mendes-Victor, L., & Shimamura, H., 2008. From unthinned continent to ocean: The deep structure of the West Iberia passive continental margin at 38 degrees N, *Tectonophysics*, **458**(1-4), 9–50.

Airoldi, G., Muirhead, J. D., Zanella, E., & White, J. D. L., 2012. Emplacement process of Ferrar Dolerite sheets at Allan Hills (South Victoria Land, Antarctica) inferred from magnetic fabric, *Geophysical Journal International*, **188**(3), 1046–1060.

Allmendinger, R. W., Cardozo, N. C., & Fisher, D., 2012. *Structural Geology Algorithms: Vectors & Tensors*, Cambridge University Press, Cambridge, England.

Argand, E., 1924. La tectonique de l'Asie. Conférence faite á Bruxelles, le 10 août 1922, *Compte-rendu du XIII^o Congrès géologique international (XIIIe session)-Belgique 1922*, , 171–372.

Aubourg, C., Tshoso, G., Le Gall, B., Bertrand, H., Tiercelin, J.-J., Kampunzu, A., Dyment, J., & Modisi, M., 2008. Magma flow revealed by magnetic fabric in the Okavango giant dyke swarm, Karoo igneous province, northern Botswana, *Journal of Volcanology and Geothermal Research*, **170**(3), 247–261.

Bagnold, R. A., 1954. Experiments on a Gravity-Free Dispersion of Large Solid Spheres in a Newtonian Fluid under Shear, *Proceedings of the Royal Society of London. Series A. Mathematical and Physical Sciences*, **225**(1160), 49–63.

Bernard-Griffiths, J., Gruau, G., Cornen, G., Azambre, B., & Mace, J., 1997. Continental lithospheric contribution to alkaline magmatism: Isotopic (Nd, Sr, Pb) and geochemical (REE) evidence from Serra de Monchique and Mount Ormonde complexes, *Journal of Petrology*, **38**(1), 115–132.

Besse, J. & Courtillot, V., 2002. Apparent and true polar wander and the geometry of the geomagnetic field over the last 200 Myr, *Journal of Geophysical Research-Solid Earth*, **107**(B11).

Biggin, A. J., van Hinsbergen, D. J. J., Langereis, C. G., Straathof, G. B., & Deenen, M. H. L., 2008. Geomagnetic secular variation in the Cretaceous Normal Superchron and in the Jurassic, *Physics of the Earth and Planetary Interiors*, **169**(1-4), 3–19.

Bronner, A., Sauter, D., Manatschal, G., Peron-Pinvidic, G., & Munschy, M., 2011. Magmatic breakup as an explanation for magnetic anomalies at magma-poor rifted margins, *Nature Geoscience*, **4**(8), 549–553.

Bullard, E., Everett, J. E., & Smith, A. G., 1965. The fit of the continents around the Atlantic, *Philosophical Transactions of the Royal Society of London. Series A, Mathematical and Physical Sciences*, **258**(1088), 41–51.

Bunger, A. P. & Cruden, A. R., 2011. Modeling the growth of laccoliths and large mafic sills: Role of magma body forces, *Journal of Geophysical Research-Solid Earth*, **116**(B2), B02203.

Butler, R. F., 1992. *Paleomagnetism: Magnetic Domains to Geologic Terranes*, Blackwell Scientific Publications, Boston.

Callot, J. P., Geoffroy, L., Aubourg, C., Pozzi, J. P., & Mege, D., 2001. Magma flow directions of shallow dykes from the East Greenland volcanic margin inferred from magnetic fabric studies, *Tectonophysics*, **335**(3-4), 313–329.

Cande, S. C. & Kristoffersen, Y., 1977. Late Cretaceous magnetic-anomalies in North-Atlantic, *Earth and Planetary Science Letters*, **35**(2), 215–224.

Carey, S., 1958. A tectonic approach to continental drift, in *Symposium on Continental Drift*, vol. , p. 177–355.

Cañón-Tapia, E., 2001. Factors affecting the relative importance of shape and distribution anisotropy in rocks: theory and experiments, *Tectonophysics*, **340**(1), 117–131.

Chadima, M. & Hrouda, F., 2006. Remasoft 3.0 a user-friendly paleomagnetic data browser and analyzer, *Travaux Géophysiques*, **XXVII**, 20–21.

Chadima, M. & Jelinek, V., 2008. Anisoft 4.2 - Anisotropy data browser, *Contributions to Geophysics & Geodesy*, **38**, 41.

Choukroune, P., Le Pichon, X., Seguret, M., & Sibuet, J.-C., 1973. Bay of biscay and pyrenees, *Earth and Planetary Science Letters*, **18**(1), 109–118.

Cloetingh, S., Gallart, J., de Vicente, G., & Matenco, L., 2011. TOPO-EUROPE: From Iberia to the Carpathians and analogues, *Tectonophysics*, **502**(1-2), 1–27.

Cox, A., 1970. Latitude dependence of the angular dispersion of the geomagnetic field, *Geophysical Journal of the Royal Astronomical Society*, **20**(253-269).

Cox, A. & Hart, R., 1986. *Plate Tectonics: How It Works*, Blackwell Scientific Publications, Oxford.

Day, R., Fuller, M., & Schmidt, V. A., 1977. Hysteresis properties of titanomagnetites: Grain-size and compositional dependence, *Physics of the Earth and Planetary Interiors*, **13**(4), 260–267.

Deenen, M. H. L., Langereis, C. G., van Hinsbergen, D. J. J., & Biggin, A. J., 2011. Geomagnetic secular variation and the statistics of palaeomagnetic directions, *Geophysical Journal International*, **186**(2), 509–520.

Dinarès-Turell, J. & Garcia-Senz, J., 2000. Remagnetization of Lower Cretaceous limestones from the southern Pyrenees and relation to the Iberian plate geodynamic evolution, *Journal of Geophysical Research-Solid Earth*, **105**(B8), 19405–19418.

Dinis, J. L., Rey, J., Cunha, P. P., Callapez, P., & Pena dos Reis, R., 2008. Stratigraphy and allogenic controls of the western Portugal Cretaceous: an updated synthesis, *Cretaceous Research*, **29**(5-6), 772–780.

Dragoni, M., Lanza, R., & Tallarico, A., 1997. Magnetic anisotropy produced by magma flow: theoretical model and experimental data from Ferrar dolerite sills (Antarctica), *Geophysical Journal International*, **128**(1), 230–240.

Dunlop, D. J., 2002a. Theory and application of the Day plot (M-rs/M-s versus H-cr/H-c) 1. Theoretical curves and tests using titanomagnetite data, *Journal of Geophysical Research-Solid Earth*, **107**(B3).

Dunlop, D. J., 2002b. Theory and application of the Day plot (M-rs/M-s versus H-cr/H-c) 2. Application to data for rocks, sediments, and soils, *Journal of Geophysical Research-Solid Earth*, **107**(B3).

Dunlop, D. J. & Ozdemir, O., 1997. *Rock Magnetism: Fundamentals and Frontiers*, Cambridge Studies in Magnetism, Cambridge University Press, Cambridge.

Ernst, R. E. & Baragar, W. R. A., 1992. Evidence from Magnetic Fabric for the Flow Pattern of Magma in the Mackenzie Giant Radiating Dyke Swarm, *Nature*, **356**(6369), 511–513.

Fanjat, G., Camps, P., Shcherbakov, V., Barou, F., Sougrati, M. T., & Perrin, M., 2012. Magnetic interactions at the origin of abnormal magnetic fabrics in lava flows: a case study from Kerguelen flood basalts, *Geophysical Journal International*, **189**(2), 815–832.

Femenias, O., Diot, H., Berza, T., Gauffriau, A., & Demaiffe, D., 2004. Asymmetrical to symmetrical magnetic fabric of dikes: Paleo-flow orientations and Paleo-stresses recorded on

feeder-bodies from the Motru Dike Swarm (Romania), *Journal of Structural Geology*, **26**(8), 1401–1418.

Ferreira, M. & Macedo, C., 1979. K-Ar Ages of the Permian-Mesozoic Basaltic Activity in Portugal, *Abstracts VI. Europ. Col. Geochron., Cosmochron. and Isotope Geology*, , 26–27.

Ferré, E. C., Bordarier, C., & Marsh, J. S., 2002. Magma flow inferred from AMS fabrics in a layered mafic sill, Insizwa, South Africa, *Tectonophysics*, **354**(1-2), 1–23.

Fidalgo González, L., 2001. *La cinématique de l'Atlantique Nord: la question de la déformation intraplaque*, Ph.D. thesis, Université de Bretagne Occidentale-Brest.

Fisher, R., 1953. Dispersion on a sphere, *Proceedings of the Royal Society of London. Series A. Mathematical and Physical Sciences*, **217**(1130), 295–305.

Font, E., Trindade, R. I. F., & Nedelec, A., 2006. Remagnetization in bituminous limestones of the Neoproterozoic Araras Group (Amazon craton): Hydrocarbon maturation, burial diagenesis, or both?, *Journal of Geophysical Research-Solid Earth*, **111**(B6).

Font, E., Ernesto, M., Silva, P. F., Correia, P. B., & Nascimento, M. A. L., 2009. Palaeomagnetism, rock magnetism and AMS of the Cabo Magmatic Province, NE Brazil, and the opening of South Atlantic, *Geophysical Journal International*, **179**(2), 905–922.

Font, E., Nascimento, C., Omira, R., Baptista, M., & Silva, P., 2010. Identification of tsunami-induced deposits using numerical modeling and rock magnetism techniques: A study case of the 1755 Lisbon tsunami in Algarve, Portugal, *Physics of the Earth and Planetary Interiors*, **182**(3), 187–198.

Fuller, M., Cisowski, S., Hart, M., Haston, R., Schmidtke, E., & Jarrard, R., 1988. NRM-IRM(s) demagnetization plots - An aid to the interpretation of Natural Remanent Magnetization, *Geophysical Research Letters*, **15**(5), 518–521.

Fuller, M., Kidane, T., & Ali, J., 2002. AF demagnetization characteristics of NRM, compared with anhysteretic and saturation isothermal remanence: an aid in the interpretation of NRM, *Physics and Chemistry of the Earth*, **27**(25-31), 1169–1177.

Gaillot, P., de Saint-Blanquat, M., & Bouchez, J.-L., 2006. Effects of magnetic interactions in anisotropy of magnetic susceptibility: Models, experiments and implications for igneous rock fabrics quantification, *Tectonophysics*, **418**(1–2), 3–19.

Galbrun, B., Berthou, P. Y., Moussin, C., & Azema, J., 1990. Magnetostratigraphy of the Jurassic-Cretaceous boundary in carbonate marine shelf - the Bias do Norte section (Algarve, Portugal), *Bulletin De La Societe Geologique de France*, **6**(1), 133–143.

Galdeano, A., Moreau, M. G., Pozzi, J. P., Berthou, P. Y., & Malod, J. A., 1989. New paleomagnetic results from Cretaceous sediments near Lisbon (Portugal) and implications for the rotation of Iberia, *Earth and Planetary Science Letters*, **92**(1), 95–106.

Galland, O., Planke, S., Neumann, E.-R., & Malthe-Sorenssen, A., 2009. Experimental modelling of shallow magma emplacement: Application to saucer-shaped intrusions, *Earth and Planetary Science Letters*, **277**(3-4), 373–383.

Garcia-Senz, J., 2002. *Cuencas extensivas del Cretácico inferior en los Pirineos Centrales, formación y subsecuente inversión*, Ph.D. thesis, Universitat de Barcelona.

Geldmacher, J., Hoernle, K., Klügel, A., Wombacher, F., Berning, B., et al., 2006. Origin and geochemical evolution of the madeira-tore rise (eastern north atlantic), *Journal of Geophysical Research: Solid Earth (1978–2012)*, **111**(B9).

Geoffroy, L., Callot, J. P., Aubourg, C., & Moreira, M., 2002. Magnetic and plagioclase linear fabric discrepancy in dykes: a new way to define the flow vector using magnetic foliation, *Terra Nova*, **14**(3), 183–190.

Gong, Z., Dekkers, M. J., Dinares-Turell, J., & Mullender, T. A. T., 2008a. Remagnetization mechanism of Lower Cretaceous rocks from the Organya Basin (Pyrenees, Spain), *Studia Geophysica Et Geodaetica*, **52**(2), 187–210.

Gong, Z., Langereis, C. G., & Mullender, T. A. T., 2008b. The rotation of Iberia during the Aptian and the opening of the Bay of Biscay, *Earth and Planetary Science Letters*, **273**(1-2), 80–93.

Gong, Z., van Hinsbergen, D. J. J., & Dekkers, M. J., 2009. Diachronous pervasive remagnetization in northern Iberian basins during Cretaceous rotation and extension, *Earth and Planetary Science Letters*, **284**(3-4), 292–301.

Gradstein, F. M., Ogg, J. G., & Smith, A. G., 2004. A Geologic Time Scale 2004, *Lethaia*, **37**(2), 175–181.

Grange, M., Scharer, U., Cornen, G., & Girardeau, J., 2008. First alkaline magmatism during Iberia-Newfoundland rifting, *Terra Nova*, **20**(6), 494–503.

Grange, M., Scharer, U., Merle, R., Girardeau, J., & Cornen, G., 2010. Plume-Lithosphere Interaction during Migration of Cretaceous Alkaline Magmatism in SW Portugal: Evidence from U-Pb Ages and Pb-Sr-Hf Isotopes, *Journal of Petrology*, **51**(5), 1143–1170.

Gressier, J.-B., Mourgues, R., Bodet, L., Matthieu, J.-Y., Galland, O., & Cobbold, P., 2010. Control of pore fluid pressure on depth of emplacement of magmatic sills: An experimental approach, *Tectonophysics*, **489**(1–4), 1–13.

Grégoire, V., Blanquat, M. D., Nedelec, A., & Bouchez, J. L., 1995. Shape anisotropy versus magnetic-interactions of magnetite grains - experiments and application to AMs in granitic-rocks, *Geophysical Research Letters*, **22**(20), 2765–2768.

Haggerty, S. E., 1991. Oxide textures; a mini-atlas, *Reviews in Mineralogy and Geochemistry*, **25**(1), 129–219.

Hargraves, R. B., Johnson, D., & Chan, C. Y., 1991. Distribution anisotropy - the cause of AMS in igneous rocks, *Geophysical Research Letters*, **18**(12), 2193–2196.

Harrison, R. J. & Feinberg, J. M., 2008. FORCinel: An improved algorithm for calculating first-order reversal curve distributions using locally weighted regression smoothing, *Geochemistry Geophysics Geosystems*, **9**.

Heslop, D., McIntosh, G., & Dekkers, M. J., 2004. Using time- and temperature-dependent Preisach models to investigate the limitations of modelling isothermal remanent magnetization acquisition curves with cumulative log Gaussian functions, *Geophysical Journal International*, **157**(1), 55–63.

Hoffman, K. A., Singer, B. S., Camps, P., Hansen, L. N., Johnson, K. A., Clipperton, S., & Carvallo, C., 2008. Stability of mantle control over dynamo flux since the mid-Cenozoic, *Physics of the Earth and Planetary Interiors*, **169**(1-4), 20–27.

Irving, E. & Ward, M. A., 1964. A statistical model of the geomagnetic field, *Pure and Applied Geophysics*, **57**(47-52).

Jackson, M., Sun, W. W., & Craddock, J. P., 1992. The rock magnetic fingerprint of chemical remagnetization in midcontinental Paleozoic carbonates, *Geophysical Research Letters*, **19**(8), 781–784, Times Cited: 20.

Jackson, M., Rochette, P., Fillion, G., Banerjee, S., & Marvin, J., 1993. Rock magnetism of remagnetized Paleozoic carbonates - low-temperature behavior and susceptibility characteristics, *Journal of Geophysical Research-Solid Earth*, **98**(B4), 6217–6225, Times Cited: 45.

Juárez, M. T., Osete, M. L., Melendez, G., Langereis, C. G., & Zijderveld, J. D. A., 1994. Oxfordian magnetostratigraphy of the Aguilon and Tosos sections (Iberian Range, Spain) and evidence of a Preoligocene overprint, *Physics of the Earth and Planetary Interiors*, **85**(1-2), 195–211.

Juárez, M. T., Lowrie, W., Osete, M. L., & Melendez, G., 1998. Evidence of widespread Cretaceous remagnetisation in the Iberian Range and its relation with the rotation of Iberia, *Earth and Planetary Science Letters*, **160**(3-4), 729–743.

Kavanagh, J. L., Menand, T., & Sparks, R. S. J., 2006. An experimental investigation of sill formation and propagation in layered elastic media, *Earth and Planetary Science Letters*, **245**(3–4), 799–813.

Kent, D. V. & Irving, E., 2010. Influence of inclination error in sedimentary rocks on the Triassic and Jurassic apparent pole wander path for North America and implications for Cordilleran tectonics, *Journal of Geophysical Research-Solid Earth*, **115**.

Khan, M. A., 1962. The anisotropy of magnetic susceptibility of some igneous and metamorphic rocks, *Journal of Geophysical Research*, **67**(7), 2873–2885.

Kirschvink, J. L., 1980. The least-squares line and plane and the analysis of paleomagnetic data, *Geophysical Journal of the Royal Astronomical Society*, **62**(3), 699–718.

Klitgord, K. D. & Schouten, H., 1986. *Plate Kinematics of the Central Atlantic*, vol. The Western North Atlantic Region, Geol Soc Am Bull, Boulder, Colorado.

Knight, M. D. & Walker, G. P. L., 1988. Magma flow directions in dikes of the Koolau Complex, Oahu, determined from magnetic fabric studies, *Journal of Geophysical Research-Solid Earth and Planets*, **93**(B5), 4301–4319.

Kruiver, P. P., Dekkers, M. J., & Heslop, D., 2001. Quantification of magnetic coercivity components by the analysis of acquisition curves of isothermal remanent magnetisation, *Earth and Planetary Science Letters*, **189**(3-4), 269–276.

Kruiver, P. P., Langereis, C. G., Dekkers, M. J., & Krijgsman, W., 2003. Rock-magnetic properties of multicomponent natural remanent magnetization in alluvial red beds (NE Spain), *Geophysical Journal International*, **153**(2), 317–332.

Kullberg, J. C., Rocha, R., Soares, A., Rey, J., Terrinha, P., Azerêdo, A., Callapez, P., Duarte, L., Kullberg, M. C., Martins, L. T., Miranda, J. R., Alves, C., Mata, J., Madeira, J., Mateus, O., Moreira, M., & Nogueira, C. R., 2011. *A Bacia Lusitaniana: Estratigrafia, Paleogeografia e Tectónica*, p. 989–1141, Escolar Editora, Lisboa.

Labails, C., 2007. *La marge sud-marocaine et les premières phases d'ouverture de l'océan Atlantique Central*, Ph.D. thesis, Université de Bretagne Occidentale-Brest.

Labails, C., Olivet, J. L., Aslanian, D., & Roest, W. R., 2010. An alternative early opening scenario for the Central Atlantic Ocean, *Earth and Planetary Science Letters*, **297**(3-4), 355–368.

Launeau, P. & Robin, P. Y. F., 1996. Fabric analysis using the intercept method, *Tectonophysics*, **267**(1–4), 91–119.

Le Pichon, X. & Sibuet, J. C., 1971. Evolution of North-East Atlantic, *Nature*, **233**(5317), 257–&.

Linder, J. & Gilder, S. A., 2012. Latitude dependency of the geomagnetic secular variation S parameter: A mathematical artifact, *Geophysical Research Letters*, **39**.

Lowrie, W., 1990. Identification of ferromagnetic minerals in a rock by coercivity and unblocking temperature properties, *Geophysical Research Letters*, **17**(2), 159–162.

Luis, J. F., 2007. Mirone: A multi-purpose tool for exploring grid data, *Computers and Geosciences*, **33**(1), 31–41.

Luis, J. F. & Miranda, J. M., 2008. Reevaluation of magnetic chrons in the North Atlantic between 35 degrees N and 47 degrees N: Implications for the formation of the Azores Triple Junction and associated plateau, *Journal of Geophysical Research-Solid Earth*, **113**(B10).

Maccaferri, F., Bonafede, M., & Rivalta, E., 2011. A quantitative study of the mechanisms governing dike propagation, dike arrest and sill formation, *Journal of Volcanology and Geothermal Research*, **208**(1–2), 39–50.

Macintyre, R. M. & Berger, G. W., 1982. A note on the geochronology of the Iberian alkaline province, *Lithos*, **15**(2), 133–136.

Mahmoudi, A., 1991. *Quelques intrusions alcalines et basiques du Cretacé Superieur au Portugal*, Ph.D. thesis, Université Nancy I.

Martins, L. T., 1991. *Actividade Ignea Mesozóica em Portugal*, Ph.D. thesis, Universidade de Lisboa.

Martins, L. T., Madeira, J., Youbi, N., Munha, J., Mata, J., & Kerrich, R., 2008. Rift-related magmatism of the Central Atlantic magmatic province in Algarve, Southern Portugal, *Lithos*, **101**(1-2), 102–124.

Matos Alves, C. A., 1964. Estudo petrológico do maciço eruptivo de Sintra, *Revista da Faculdade de Ciências de Lisboa*, **2**, 123–289.

Matos Alves, C. A., Rodrigues, B., Serralheiro, A., & Faria, A., 1980. O complexo basáltico de Lisboa, *Comunicações dos Serviços Geológicos de Portugal*, **66**, 111–134.

McCabe, C. & Elmore, R. D., 1989. The occurrence and origin of late Paleozoic remagnetization in the sedimentary-rocks of North-America, *Reviews of Geophysics*, **27**(4), 471–494.

McFadden, P. L., Merrill, R. T., & McElhinny, M. W., 1988. Dipole/quadrupole family modelling of paleosecular variation, *Journal of Geophysical Research-Solid Earth and Planets*, **93**(B10), 11583–11588.

Menand, T., 2008. The mechanics and dynamics of sills in layered elastic rocks and their implications for the growth of laccoliths and other igneous complexes, *Earth and Planetary Science Letters*, **267**(1–2), 93–99.

Merle, R., Schärer, U., Girardeau, J., & Cornen, G., 2006. Cretaceous seamounts along the continent–ocean transition of the Iberian margin: U–Pb ages and Pb–Sr–Hf isotopes, *Geochimica et cosmochimica acta*, **70**(19), 4950–4976.

Merle, R., Jourdan, F., Marzoli, A., Renne, P. R., Grange, M., & Girardeau, J., 2009. Evidence of multi-phase Cretaceous to Quaternary alkaline magmatism on Tore-Madeira Rise and neighbouring seamounts from Ar-40/Ar-39 ages, *Journal of the Geological Society*, **166**, 879–894.

Merrill, R. T. & McFadden, P. L., 2003. The geomagnetic axial dipole field assumption, *Physics of the Earth and Planetary Interiors*, **139**(3-4), 171–185.

Miranda, J. M., 2011. *Introduçao ao Geomagnetismo*, Instituto Dom Luiz, Universidade de Lisboa.

Miranda, R., 2010. *Petrogenesis and geochronology of the Late Cretaceous alkaline magmatism in the west Iberian Margin*, Ph.D. thesis, Universidade de Lisboa.

Miranda, R., Moreira, M., Valadares, V., Terrinha, P., & Kullberg, J. C., 2006. Magmatic flow pattern of the Foz da Fonte sill (Upper Cretaceous) by AMS: implications for the understanding of the last cycle of mesozoic magmatic activity in the West Iberian Margin., in *Abstracts of the Lasi II: Physical geology of subvolcanic systems: Laccoliths, Sills, and Dykes*, p. 48–50, Visual Geosciences.

Miranda, R., Valadares, V., Terrinha, P., Mata, J., Azevedo, M. R., Gaspar, M., Kullberg, J. C., & Ribeiro, C., 2009. Age constraints on the Late Cretaceous alkaline magmatism on the West Iberian Margin, *Cretaceous Research*, **30**(3), 575–586.

Moreau, M. G., Canerot, J., & Malod, J. A., 1992. Paleomagnetic study of Mesozoic sediments from the Iberian chain (Spain) suggestions for Barremian remagnetization and implications for the rotation of Iberia, *Bulletin De La Societe Geologique De France*, **163**(4), 393–402.

Moreau, M. G., Berthou, J. Y., & Malod, J. A., 1997. New paleomagnetic Mesozoic data from the Algarve (Portugal): Fast rotation of Iberia between the Hauterivian and the Aptian, *Earth and Planetary Science Letters*, **146**(3-4), 689–701.

Moskowitz, B. M., 1991. Hitchhiker's guide to magnetism, in *Environmental Magnetism Workshop (IRM)*, vol. 279, p. 48.

Muñoz, J. A., 1992. Evolution of a continental collision belt: ECORS-Pyrenees crustal balanced cross-section, in *Thrust tectonics*, p. 235–246, Springer.

Márton, E., Abranches, M. C., & Pais, J., 2004. Iberia in the Cretaceous: new paleomagnetic results from Portugal, *Journal of Geodynamics*, **38**(2), 209–221.

Neres, M., Font, E., Miranda, J. M., Camps, P., Terrinha, P., & Mirao, J., 2012. Reconciling Cretaceous paleomagnetic and marine magnetic data for Iberia: New Iberian paleomagnetic poles, *Journal of Geophysical Research-Solid Earth*, **117**.

Neres, M., Miranda, J., & Font, E., 2013. Testing Iberian Kinematics at Jurassic-Cretaceous times, *Tectonics*.

Neves, M. C., Terrinha, R., Afilhado, A., Moulin, M., Matias, L., & Rosas, F., 2009. Response of a multi-domain continental margin to compression: Study from seismic reflection-refraction and numerical modelling in the Tagus Abyssal Plain, *Tectonophysics*, **468**(1-4), 113–130.

Nogueira, C. R., 2008. *Fluxo magmático em diques do Cortejo Radial de Mafra (sector NW), Bacia Lusitaniana*, Msc.

Oliva-Urcia, B., Casas, A. M., Soto, R., Villalaín, J. J., & Kodama, K., 2011. A transtensional basin model for the Organyà basin (central southern Pyrenees) based on magnetic fabric and brittle structures, *Geophysical Journal International*, **184**(1), 111–130.

Olivet, J. L., 1996. Kinematics of the Iberian Plate, *Bulletin Des Centres De Recherches Exploration-Production Elf Aquitaine*, **20**(1), 131–195.

Omira, R., Baptista, M. A., & Miranda, J. M., 2011. Evaluating Tsunami Impact on the Gulf of Cadiz Coast (Northeast Atlantic), *Pure and Applied Geophysics*, **168**(6-7), 1033–1043.

Osete, M. L. & Palencia Ortas, A., 2006. Polos Paleomagnéticos de Iberia de los últimos 300 millones de años, *Física de la Tierra*, **18**, 157–181.

Osete, M. L., Gomez, J. J., Pavon-Carrasco, F. J., Villalain, J. J., Palencia-Ortas, A., Ruiz-Martinez, V. C., & Heller, F., 2011. The evolution of Iberia during the Jurassic from palaeomagnetic data, *Tectonophysics*, **502**(1-2), 105–120.

Palencia Ortas, A., Osete, M. L., Vegas, R., & Silva, P., 2006. Paleomagnetic study of the Messejana Plasencia dyke (Portugal and Spain): A lower Jurassic paleopole for the Iberian plate, *Tectonophysics*, **420**(3-4), 455–472.

Palácios, T., 1985. *Petrologia do Complexo Vulcânico de Lisboa*, Ph.D. thesis, Universidade de Lisboa.

Pike, C. R., Roberts, A. P., & Verosub, K. L., 1999. Characterizing interactions in fine magnetic particle systems using first order reversal curves, *Journal of Applied Physics*, **85**(9), 6660–6667.

Polteau, S., Ferre, E. C., Planke, S., Neumann, E. R., & Chevallier, L., 2008a. How are saucer-shaped sills emplaced? Constraints from the Golden Valley Sill, South Africa, *Journal of Geophysical Research-Solid Earth*, **113**(B12).

Polteau, S., Mazzini, A., Galland, O., Planke, S., & Malthe-Sorenssen, A., 2008b. Saucer-shaped intrusions: Occurrences, emplacement and implications, *Earth and Planetary Science Letters*, **266**(1-2), 195–204.

Potter, D. K. & Stephenson, A., 1988. Single-domain particles in rocks and magnetic fabric analysis, *Geophysical Research Letters*, **15**(10), 1097–1100.

Pueyo, E. L., Roman-Berdiel, M. T., Bouchez, J. L., Casas, A. M., & Larrasoana, J. C., 2005. Statistical significance of magnetic fabric data in studies of paramagnetic granites, *Magnetic Fabric: Methods and Applications*, **238**, 395–420.

Rabinowitz, P. D., Cande, S. C., & Hayes, D. E., 1978. Grand Banks and J-anomaly ridge, *Science*, **202**(4363), 71–73.

Raposo, M. I. B. & Ernesto, M., 1995. Anisotropy of magnetic-susceptibility in the Ponta-Grossa Dyke Swarm (Brazil) and its relationship with magma flow direction, *Physics of the Earth and Planetary Interiors*, **87**(3-4), 183–196.

Ribeiro, P., Silva, P. F., Moita, P., Kratinová, Z., Marques, F. O., & Henry, B., 2013. Palaeomagnetism in the Sines massif (SW Iberia) revisited: evidences for Late Cretaceous hydrothermal alteration and associated partial remagnetization, *Geophysical Journal International*, **195**(1), 176–191.

Roberts, A. P., Pike, C. R., & Verosub, K. L., 2000. First-order reversal curve diagrams: A new tool for characterizing the magnetic properties of natural samples, *Journal of Geophysical Research-Solid Earth*, **105**(B12), 28461–28475.

Robertson, D. J. & France, D. E., 1994. Discrimination of remanence-carrying minerals in mixtures, using Isothermal Remanent Magnetization acquisition curves, *Physics of the Earth and Planetary Interiors*, **82**(3-4), 223–234.

Rochette, P., Jackson, M., & Aubourg, C., 1992. Rock magnetism and the interpretation of anisotropy of magnetic susceptibility, *Reviews of Geophysics*, **30**(3), 209–226.

Rock, N. M. S., 1982. The late Cretaceous alkaline igneous province in the Iberian Peninsula, and its tectonic significance, *Lithos*, **15**(2), 111–131.

Roque, C., Terrinha, P., Lourenço, N., & M., P. d. A., 2009. Morphostructure of the Tore seamount and evidences of recent tectonic activiy (West Iberian Margin), in *Nuevas contribuiciones al Margen Ibérico Atlantico 2009*, p. 33–36, Universidad de Oviedo.

Rosenbaum, G., Lister, G. S., & Duboz, C., 2002. Relative motions of Africa, Iberia and Europe during Alpine orogeny, *Tectonophysics*, **359**(1-2), 117–129.

Ruiz-Martínez, V. C., Torsvik, T. H., van Hinsbergen, D. J., & Gaina, C., 2012. Earth at 200 Ma: Global palaeogeography refined from CAMP palaeomagnetic data , *Earth and Planetary Science Letters*, **331–332**(0), 67 – 79.

Russell, S. M. & Whitmarsh, R. B., 2003. Magmatism at the west Iberia non-volcanic rifted continental margin: evidence from analyses of magnetic anomalies, *Geophysical Journal International*, **154**(3), 706–730.

Sahabi, M., Aslanian, D., & Olivet, J. L., 2004. A new starting point for the history of the central Atlantic, *Comptes Rendus Geoscience*, **336**(12), 1041–1052.

Schettino, A. & Scotese, C. R., 2005. Apparent polar wander paths for the major continents (200 Ma to the present day): a palaeomagnetic reference frame for global plate tectonic reconstructions, *Geophysical Journal International*, **163**(2), 727–759.

Schott, J. J. & Peres, A., 1987. Paleomagnetism of the lower Cretaceous redbeds from northern Spain - evidence for a multistage acquisition of magnetization, *Tectonophysics*, **139**(3-4), 239–253.

Scotese, C. R., Gahagan, L. M., & Larson, R. L., 1988. Plate tectonic reconstructions of the Cretaceous and Cenozoic ocean basins, *Tectonophysics*, **155**(1-4), 27–48.

Sibuet, J. C., Srivastava, S. P., & Spakman, W., 2004. Pyrenean orogeny and plate kinematics, *Journal of Geophysical Research-Solid Earth*, **109**(B8).

Sibuet, J. C., Srivastava, S., & Manatschal, G., 2007. Exhumed mantle-forming transitional crust in the Newfoundland-Iberia rift and associated magnetic anomalies, *Journal of Geophysical Research-Solid Earth*, **112**(B6).

Sibuet, J.-C., Rouzo, S., Srivastava, S., Dehler, S., Deptuck, M., & Karim, A., 2012. Plate tectonic reconstructions and paleogeographic maps of the central and north atlantic oceans, *Canadian Journal of Earth Sciences*, **49**(12), 1395–1415.

Silva, E. A., Miranda, J. M., Luis, J. F., & Galdeano, A., 2000. Correlation between the Palaeozoic structures from West Iberian and Grand Banks margins using inversion of magnetic anomalies, *Tectonophysics*, **321**(1), 57–71.

Soares, D. M., Alves, T. M., & Terrinha, P., 2012. The breakup sequence and associated lithospheric breakup surface: Their significance in the context of rifted continental margins (West Iberia and Newfoundland margins, North Atlantic), *Earth and Planetary Science Letters*, **355–356**(0), 311–326.

Soto, R., Villalaín, J. J., & Casas-Sainz, A. M., 2008. Remagnetizations as a tool to analyze the tectonic history of inverted sedimentary basins: A case study from the Basque-Cantabrian basin (north Spain), *Tectonics*, **27**(1), TC1017.

Srivastava, S. P., Roest, W. R., Kovacs, L. C., Oakey, G., Levesque, S., Verhoef, J., & Macnab, R., 1990a. Motion of Iberia since the late Jurassic - results from detailed aeromagnetic measurements in the Newfoundland basin, *Tectonophysics*, **184**(3-4), 229–260.

Srivastava, S. P., Schouten, H., Roest, W. R., Klitgord, K. D., Kovacs, L. C., Verhoef, J., & Macnab, R., 1990b. Iberian Plate kinematics - a jumping plate boundary between Eurasia and Africa, *Nature*, **344**(6268), 756–759.

Srivastava, S. P., Sibuet, J. C., Cande, S., Roest, W. R., & Reid, I. D., 2000. Magnetic evidence for slow seafloor spreading during the formation of the Newfoundland and Iberian margins, *Earth and Planetary Science Letters*, **182**(1), 61–76.

Steiner, M. B., Ogg, J. G., Melendez, G., & Sequeiros, L., 1985. Jurassic magnetostratigraphy, 2. Middle-late Oxfordian of Aguilon, Iberian Cordillera, northern Spain, *Earth and Planetary Science Letters*, **76**(1-2), 151–166.

Storetvedt, K. M., Mogstad, H., Abranches, M. C., Mitchell, J. G., & Serralheiro, A., 1987. Paleomagnetism and isotopic age data from upper Cretaceous igneous rocks of W Portugal - geological correlation and Plate Tectonic aspects, *Geophysical Journal of the Royal Astronomical Society*, **88**(1), 241–263.

Storetvedt, K. M., Mitchell, J. G., Abranches, M. C., & Oftedahl, S., 1990. A new kinematic model for Iberia - further paleomagnetic and isotopic age evidence, *Physics of the Earth and Planetary Interiors*, **62**(1-2), 109–125.

Tarling, D. & Hrouda, F., 1993. *The Magnetic Anisotropy of Rocks*, Chapman and Hall, London.

Tauxe, L., 2010. *Essential of Paleomagnetism*, University of California Press.

Tauxe, L. & Kent, D. V., 2004. A simplified statistical model for the geomagnetic field and the detection of shallow bias in paleomagnetic inclinations: Was the ancient magnetic field dipolar?, *Timescales of the Paleomagnetic field*, **145**, 101–115.

Tauxe, L., Gee, J. S., & Staudigel, H., 1998. Flow directions in dikes from anisotropy of magnetic susceptibility data: The bootstrap way, *Journal of Geophysical Research-Solid Earth*, **103**(B8), 17775–17790.

Terrinha, P., Aranguren, A., Kullberg, M. C., Pueyo, E., Kullberg, J. C., Casas-Sainz, A., & Rillo, C., 2003. Complexo Ígneo de Sintra—um modelo de instalação constrangido por novos dados de gravimetria e ASM, in *Ciências da Terra*, vol. Especial V, VI. Congresso Nacional de Geologia, pp. 58–59.

Thinon, I., Matias, L., Rehault, J. P., Hirn, A., Fidalgo-Gonzalez, L., & Avedik, F., 2003. Deep structure of the Armorican Basin (Bay of Biscay): a review of Norgasis seismic reflection and refraction data, *Journal of the Geological Society*, **160**, 99–116.

Thomson, K., 2007. Determining magma flow in sills, dykes and laccoliths and their implications for sill emplacement mechanisms, *Bulletin of Volcanology*, **70**(2), 183–201.

Thomson, K. & Hutton, D., 2004. Geometry and growth of sill complexes: insights using 3D seismic from the North Rockall Trough, *Bulletin of Volcanology*, **66**(4), 364–375.

Torsvik, T. H., Mueller, R. D., Van der Voo, R., Steinberger, B., & Gaina, C., 2008. Global plate motion frames: Toward a unified model, *Reviews of Geophysics*, **46**(3).

Torsvik, T. H., Van der Voo, R., Preeden, U., Mac Niocaill, C., Steinberger, B., Doubrovine, P. V., van Hinsbergen, D. J. J., Domeier, M., Gaina, C., Tohver, E., Meert, J. G., McCausland, P. J. A., & Cocks, L. R. M., 2012. Phanerozoic polar wander, palaeogeography and dynamics, *Earth-Science Reviews*, **114**(3-4), 325–368.

Tucholke, B., Sawyer, D., & Sibuet, J.-C., 2007. Breakup of the Newfoundland–Iberia rift, *Geological Society, London, Special Publications*, **282**(1), 9–46.

Van der Voo, R., 1969. Paleomagnetic evidence for the rotation of the Iberian Peninsula, *Tectonophysics*, **7**, 5–56.

Van der Voo, R., 1990. The reliability of paleomagnetic data, *Tectonophysics*, **184**, 1–9.

Van der Voo, R. & Zijderveld, J., 1971. Renewed paleomagnetic study of the Lisbon volcanics and implications for the rotation of the Iberian Peninsula, *Journal of Geophysical Research*, **76**(17), 3913–3921.

Verati, C., Rapaille, C., Feraud, G., Marzoli, A., Bertrand, H., & Youbi, N., 2007. (40)Ar/(39)Ar ages and duration of the Central Atlantic Magmatic Province volcanism in Morocco and Portugal and its relation to the Triassic-Jurassic boundary, *Palaeogeography Palaeoclimatology Palaeoecology*, **244**(1-4), 308–325.

Vergés, J., Fernàndez, M., & Martínez, A., 2002. The Pyrenean orogen: pre-, syn-, and post-collisional evolution, *Journal of the Virtual Explorer*, **8**, 57–76.

Villalain, J. J., Fernadez-Gonzalez, G., Casas, A. M., & Gil-Imaz, A., 2003. Evidence of a Cretaceous remagnetization in the Cameros Basin (North Spain): implications for basin geometry, *Tectonophysics*, **377**(1-2), 101–117.

Vissers, R. L. M. & Meijer, P. T., 2012. Mesozoic rotation of Iberia: Subduction in the Pyrenees?, *Earth-Science Reviews*, **110**(1–4), 93–110.

Wessel, P. & Smith, W., 1991. Free software helps map and display data, *Eos, Transactions, American Geophysical Union*, **72 (441)**, 445–446.

Whitmarsh, R. B., Miles, P. R., Sibuet, J.-C., & Louvel, V., 1996. Geological and geophysical implications of deep-tow magnetometer observations near sites 897, 898, 899, 900 and 901 on the West Iberia continental margin, *Proceedings of the Ocean Drilling Program, Scientific Results*, **149**, 665–674.

Wilson, R., Hiscott, R., Willis, M., & Gradstein, F., 1989. The Lusitanian Basin of west-central Portugal: Mesozoic and Tertiary tectonic, stratigraphic, and subsidence history, *Extensional tectonics and stratigraphy of the North Atlantic margins. AAPG Mem*, **46**, 341–361.